FACULTY OF SCIENCES

Synthesis and Characterization of Self-Assembly-Based Mesoporous Organosilica Films for Low-k Dielectric Application

Murad Aydan Redzheb
Student number: 01210640

Supervisors: Prof. Dr. Pascal Van Der Voort, Dr. Silvia Armini

A dissertation submitted to Ghent University in partial fulfilment of the requirements for the degree of Doctor in Sciences - Chemistry

Academic year: 2017 – 2018

GHENT UNIVERSITY

imec

FACULTY
OF SCIENCES

FACULTY OF SCIENCES

Table of Contents

FACULTY OF SCIENCES

ACKNOWLEDGEMENTS

Before starting my doctoral studies, I had the chance to spend nine months in imec. During this period, I got an impression of a collaborative atmosphere created and maintained by people who were always ready to respond to a request for help and eager to explain in detail the source of and the solutions to my problems. These impressions convinced me that imec would be a wonderful place to conduct a PhD research.

My PhD experience, however, was made possible by my promotor Prof. Dr. Pascal Van Der Voort, my former co-promotor Dr. Mikhail R. Baklanov and my current co-promotor Dr. Silvia Armini. Therefore, I would like to thank them for giving me the opportunity to start this PhD research and for their guidance during my studies.

In addition to the discussions with promotors, my PhD activities were significantly influenced by discussions with and contributions from PhD colleagues whose work involved development of low-k materials. In particular, I thank Mikhail Krishtab, Liping Zhang, Oguzhan Orkut Okudur, and Chen Wu. I am also grateful for the feedback which I received during the regular low-k meetings from the usual attendees Quoc Toan Le, Patrick Verdonck, Jean-Francois de Marneffe, and Kris Vanstreels. Furthermore, I thank the colleagues and friends Marcus Heyne, Yiting Sun, Ivan Zyulkov, Sebastiaan Herregods, Benjamin Groven, Davide Tierno, Abhitosh Vais, Sebastien Moitzheim, and Tsvetan Ivanov with whom we shared many lunches and interesting conversations.

As a part of the PhD experience, I had the chance to enjoy the mentoring of internship and thesis students. This experience made me appreciate the various motivations and the associated attitudes toward scientific contributions students can have. I thank Henry Hopkins, Tom Berger, Mathias Jacobs, Laura Garcia Gonzalez, and Jens Van Nerum for their contributions.

Imec has an exceptionally rich portfolio of characterization techniques which enable fast material characterization which is crucial for a material development research. These techniques are mainly operated by the colleagues at the material and components analysis department of which I would like to thank Johan Meersschaut, Olivier Richard, Thierry Conard, and Alexis Franquet.

Another rare opportunity accessible to PhD students at imec is the access to clean rooms equipped with not only the tools which are employed for the production of the current generation of integrated circuits but also with the tools which will be required for the future generation technology nodes. However, getting familiar with the tool capabilities and process peculiarities would be challenging were it not for the integration engineers and the managers. In this respect, I thank Gayle Murdoch, Hirohisa Uchida, Juergen Boemmels, Zsolt Tokei, and Herbert Struyf for their support.

In spite of being a Ghent University student, due to my accommodation in Leuven, I did not have too many opportunities to interact with my UGent colleagues. However, I would like to thank Frederik Goethals, Els De Canck, and Sander Clerick for their assistance and their readiness to help a distant colleague.

Apart from the two main institutions which enabled my PhD studies, I was fortunate enough to collaborate with the Leibniz Institute of Surface Modification in Leipzig, Germany. This collaboration was made possible by Lutz Prager who readily agreed to host me for a week of UV cure experiments in his lab. I thank Dr. Prager for his hospitality and for the delightful tour of the Leipzig centre. I also thank Sergej Naumov for his quantum chemical calculations which helped us better understand the UV cure results.

SBA Materials, Inc. are acknowledged for providing films for investigation of the effect of the UV cure on the low-k properties as well as for their financial support in meeting the cost associated with the trip to Leipzig. In particular, I thank Hash Pakbaz, James Hickman, and Nigel Hacker.

Ultratech, Inc. are acknowledged for performing laser anneal experiments on the low-k films. In particular, I thank Michael Awdshiew, Yun Wang, Shaoyin Chen, and Van Le.

The grazing-incidence small-angle x-ray scattering (GISAXS) experiments in the ELETTRA synchrotron facility in Trieste, Italy are another memorable experience from my PhD years. In this regard, I would especially like to thank Sigrid Bernstorff who agreed to collaborate with people (me and Silvia) who had no experience with GISAXS measurements or GISAXS data analysis. I thank Dr. Bernstorff for accommodating us on two occasions in her personal beam time which allowed us to prepare a successful proposal for a comprehensive GISAXS study. I also thank Krunoslav Juraic and Barbara Sartori without whom the GISAXS experiments wouldn't have been possible.

Finally, I thank my mother, Sevil Keskin, and my best friend and partner in life Fevi for their loving support.

FACULTY OF SCIENCES

SCIENTIFIC ACTIVITIES

Peer Reviewed Journals

1. ***M. Redzheb**, L. Prager, S. Naumov, M. Krishtab, S. Armini, P. Van Der Voort, M. R. Baklanov, Effect of the C-bridge length on the ultraviolet-resistance of oxycarbosilane low-k films, Applied Physics Letters, 108(1), 012902 (2016)*

2. ***M. Redzheb**, L. Prager, M. Krishtab, S. Armini, K. Vanstreels, A. Franquet, P. Van Der Voort, M.R. Baklanov, UV cure of oxycarbosilane low-k films, Microelectronic Engineering, 156, 103-107 (2016)*

3. ***M. Redzheb**, S. Armini, T. Berger, M. Jacobs, M. Krishtab, K. Vanstreels, S. Bernstorff and P. Van Der Voort, On the mechanical and electrical properties of self-assembly-based organosilicate porous films, Journal of Materials Chemistry C, 5, 8599-8607 (2017)*

4. ***M. Redzheb**, S. Bernstorff, B. Sartori, P. Van Der Voort, S. Armini, Periodic Mesoporous Organosilica Films with a Tunable Steady-State Mesophase, ChemPhysChem, 18, 20, 2846–2849 (2017)*

5. ***M. Redzheb**, P. Van Der Voort, S. Armini, Template dependent hydrophobicity in mesoporous organosilica films, Microporous and Mesoporous Materials, In press, Available online 7 October 2017*

Conference Proceedings

1. ***M. Redzheb**, L. Prager, M. Krishtab, S. Armini, K. Vanstreels, A. Franquet, P. Van Der Voort, M.R. Baklanov, Impact of UV wavelength and curing time on the properties of spin-coated low-k films, 2015 IEEE International Interconnect Technology Conference and 2015 IEEE Materials for Advanced Metallization Conference (IITC/MAM), 99-102 (2015)*

2. ***M. Redzheb**, S. Armini, K. Vanstreels, J. Meersschaut, M. R. Baklanov, Y. Wang, S. Chen, V. Le, M. Awdshiew, P. Van Der Voort, Laser anneal of oxycarbosilane low-k film, 2016 IEEE International Interconnect Technology Conference / Advanced Metallization Conference (IITC/AMC), 156-158 (2016)*

Patents

1. ***M. Redzheb**, S. Armini, Selective deposition of dielectric materials, EP 17169473, Priority date 04.05.2017*

Conferences

1. ***M. Redzheb**, S. Armini, M. Baklanov, P Van Der Voort, Characterization of advanced k 1.9, 2.0 and 2.2 ultra-porous SiOC(H) films deposited by Plasma-Enhanced Chemical Vapor Deposition, Science and Application of Thin Films, 2014, Çeş me, Turkey (oral)*

2. ***M. Redzheb**, L. Prager, M.Krishtab, S. Armini, K. Vanstreels, Alexis Franquet, P. Van Der Voort, and M.R. Baklanov, Impact of UV wavelength and curing time on the properties of spincoated low-k films, International Interconnect Technology Conference / Materials for Advanced Metallization 2015, Grenoble, France (poster)*

3. ***M. Redzheb**, S. Armini, O. O. Okudur, K. Vanstreels, S. Bernstorff, P. Van Der Voort and M. Baklanov, Gemini-templated PMO low-k films, Materials for Advanced Metallization, 2016, Brussels, Belgium (oral)*

4. ***M. Redzheb**, S. Armini, K. Vanstreels, J. Meersschaut, M.R. Baklanov, Y. Wang, S. Chen, V. Le, M. Awdshiew, P. Van Der Voort, Laser anneal of oxycarbosilane low-k film, International Interconnect Technology Conference / Advanced Metallization Conference 2016, San Jose, California, USA (poster)*

5. ***M. Redzheb**, S. Armini, B. Sartori, S. Bernstorff, P. Van Der Voort, Time-resolved GISAXS investigation of the self-assembly of spin-coated PMO films, XXV International Materials Research Congress, 2016, Cancun, Mexico (oral)*

6. ***M. Redzheb**, O. O. Okudur, P. Van Der Voort, S. Armini, Periodic Mesoporous Organosilica Films for Low-k Application: Promises and Challenges, MRS Spring Meeting and Exhibit, 2017, Phoenix, AZ, USA (oral)*

7. ***M. Redzheb**, P. Van Der Voort, S. Armini, Template-dependent hydrophobicity in mesoporous organosilica films, 5th International Conference on Multifunctiona, Hybrid and Nanomaterials, 2017, Lisbon, Portugal (oral)*

ENGLISH SUMMARY

In the last twenty years, the microchip performance has been dominated by the interconnect (RC) signal delay. Moreover, in contrast to the delay associated with the transistor switching, the RC delay has steadily increased with each technology node. Thus, various materials have been investigated to enable faster signal propagation through the interconnects. These efforts can be divided into two main research areas – conductors and dielectrics. The dielectrics are in the spotlight of this work. While the insulating properties of the dielectrics, quantified by the dielectric constant or k-value, are important for the signal delay, the microchip manufacturing processes impose additional requirements on the insulators, such as mechanical and electrical reliability, chemical stability, hydrophobicity, thermal stability, and others. Many of these requirements can be met by self-assembly-based organosilicate dielectrics. In particular, oxycarbosilane (OCS) and periodic mesoporous organosilica (PMO) films are considered as promising low-k candidates. Therefore, in this work, we provide additional insight into the properties of self-assembly based organosilicate films in order to elucidate their applicability as low-k dielectrics.

Oxycarbosilanes are SiO_2-based materials in which some of the Si-O-Si groups have been replaced by Si-$(CH_2)_x$-Si groups. In OCS films, the UV and VUV irradiation has more detrimental effect on ethylene-bridged (x=2) oxycarbosilane films as compared to those containing methylene (x=1) groups. The concentration of the bridging ethylene groups is reduced by the 222 nm light. In contrast, the bridging methylene groups are not affected by the 222 nm light. The difference in the stability of these two alkylene groups is more pronounced when the films are exposed to 172 nm light. The ethylene groups are depleted by more than 75% while methylene loss is limited to only 40%. Comparable k and Young's modulus (YM) values ($k \leq 2.3$, YM≥7.5 GPa and k=2.07, YM=5.5 GPa) are obtained following 1 min 172 nm and 20 min 222 nm irradiations but the latter produces superior low-k films because of a complete template removal without any induced hydrophilization. On the other hand, laser anneal can be applied to as-deposited OCS films for template removal and to improve the YM of the porous films. Within a narrow processing window, 13% improvement of the YM value as compared to the reference films annealed in a furnace at 400°C with no impact on the k-value of 2.25 can be achieved. However, extensive bond rearrangements, mostly related to the removal or reorganization of the organic content of the organosilicate matrix, make this approach rather unattractive.

The replacement of some of the Si-O-Si by Si-CH_2-Si functionalities in a porous organosilica film results in a smaller improvement of the YM than previously thought. For instance, at a density of ~0.87 g/cm^3, the film containing methylene groups has an YM of 6.6 GPa, while the one without – 5.3 GPa. This effect is counteracted by a higher dielectric constant for the films containing

methylene groups – 2.27 with and 2.12 without the Si-CH_2-Si groups at the same density due to an increase in the matrix density when Si-O-Si are replaced by Si-CH_2-Si groups. Therefore, depending on the integration scheme, if processing damage to the low-k can be avoided, low carbon content dielectrics might be more suitable for integration due to lower porosity required to achieve low dielectric constant.

In the organosilica films, the self-hydrophobization reaction in which a bridging methylene group is transformed into a methyl group can occur at a temperature as low as 200°C, significantly lower than previously reported in literature. Additionally, the hydrophobization reaction in the presence of a template requires higher activation energy than in porous materials. Furthermore, in methylene-bridged organosilica films, the degree of self-hydrophobization depends on the employed template. The films templated by cetyltrimethylammonium chloride (CTAC) are more hydrophilic when compared to films templated by BrijL4 and BrijS10. The template-dependent hydrophobicity is attributed to the blocking of the silanol condensation by the polyethylene oxide chains in the Brij-type surfactants leading to a higher concentration of Si-OH groups with respect to CTAC. The extra silanols are consequently available for self-hydrophobization reactions.

PMO films are OCS films in which control over the pore arrangement allows obtaining pore structure which belongs to one of the crystallographic groups. We have synthesized and characterized an ethane-PMO film templated with the ionic Gemini 16-12-16 surfactant. Following a thermal template removal, the PMO film has a distorted 2D hexagonal pore organization with a pore size distribution centred at 2 nm. The Gemini-templated PMO films meet the material specifications for low-k dielectric layers. The Gemini surfactants are an exciting class of templating molecules because their packing parameter can be relatively easily controlled, opening the possibility for a systematic engineering of the mesophase of PMO films with a small pore size.

A tunable steady state (TSS) exists in spin-coated PMO films. During the TSS, the surfactant self-assembly can be directed by the ambient conditions, such as humidity and temperature, resulting in a desired mesophase. At a relative humidity of 70%, films with 3D or 2D hexagonal phases depending on the surfactant to organosilica molar ratio have been obtained. However, the high humidity has competing effects on the mesophase which can be understood in the context of the charge density matching mechanism. On the one hand, the interaction between the H_2O and the surfactant molecules leads to an increase of the micelle surface curvature, while on the other hand, the H_2O molecules cause depolymerization of the siloxane bonds creating conditions which favor the decrease of the micelle surface curvature. The polycondensation degree of the organosilica oligomers also affects the formed mesophases. For instance, 3D hexagonal phase is obtained after 20 min solution aging, 2D hexagonal after 40 min aging and no ordered mesophase

if the solution is aged for longer than 70 min. Additionally, cubic mesophases are observed when the water to organosilica molar ratio is reduced from 30 to 14. A PMO film with a 2D hexagonal pore order possesses 1.7 GPa lower Young's modulus than a film with a disordered porosity while both have the same dielectric constant of 2.30. Experiments to deposit PMO film in narrow 45 nm trenches reveals that high surface energy of the substrate is required in order to obtain a well-ordered PMO.

Contrary to expectations, the ionic surfactant CTAC is a suitable templating agent for low-k films. The use of CTAC does not result in a significantly higher leakage current density or lower breakdown field when compared to a film with a non-ionic surfactant. In particular, the leakage current density of the CTAC-templated film at 1MV/cm is 1.6×10^{-9} A/cm^2 while the breakdown field is 5.7 MV/cm. At the same time, CTAC-templated PMO films have a small pore size of about 2 nm and a narrow pore size distribution both of which are very important for a low-k application.

NEDERLANDSE SAMENVATTING

In de afgelopen twintig jaar werd de prestatie van de microchip beperkt door de interconnect (RC) signaalvertraging. Bovendien is de RC-vertraging, in tegenstelling tot de vertraging die gepaard gaat met het schakelen van de transistor, gestaag toegenomen met elk technologieknooppunt. Om hier aan tegemoet te komen zijn er verschillende materialen onderzocht om een snellere signaalverspreiding door de interconnecties mogelijk te maken. Deze inspanningen kunnen worden onderverdeeld in twee belangrijke onderzoeksgebieden: geleiders en dielectrica. Dielectrica zijn de focus van dit werk. Waar de isolerende eigenschappen van de dielectrica, gemeten door de permittiviteit (diëlektrische constante) of k-waarde, belangrijk zijn voor de signaalvertraging, stellen de microchip-productieprocessen extra eisen aan de isolatoren zoals mechanische en elektrische betrouwbaarheid, chemische stabiliteit, hydrofobiciteit, thermische stabiliteit en andere. Aan veel van deze eisen kan worden voldaan door self-assembly dieletricia op basis van organosilicaten. Met name oxycarbosilaan (OCS) en periodieke mesoporeuze organosilica films (PMO-films) worden beschouwd als veelbelovende kandidaten voor low-k dielectrica. Daarom geven we in dit werk extra inzicht in de eigenschappen van op self-assembly gebaseerde organosilicaatfilms om hun toepasbaarheid als low-k dielectrica te verduidelijken.

Oxycarbosilanen zijn materialen op basis van SiO_2, waarbij sommige Si-O-Si groepen zijn vervangen door Si-$(CH_2)_x$-Si groepen. In OCS-films hebben UV- en VUV-straling een schadelijker effect op ethyleen gebrudgde (x=2) oxycarbosilaanfilms dan op methyleen houdende (x=1) groepen. Fotonen met een energie lager dan 6,2 eV (bv. λ= 222 nm) kunnen de methyleenbrugverbinding niet vernietigen. De concentratie van de overbruggende ethyleengroepen wordt daarentegen wel door het 222 nm licht verlaagd. Het verschil in stabiliteit van deze twee alkyleengroepen is meer uitgesproken wanneer de films worden blootgesteld aan 172 nm licht. De ethyleengroepen zijn voor meer dan 75% uitgeput, terwijl het methyleenverlies beperkt is tot slechts 40%. Vergelijkbare k- en Young's modulus (YM)-waarden ($k \leq 2.3$, YM $\geq$ 7.5 GPa en $k = 2.07$, YM = 5.5 GPa) worden verkregen na bestraling door 172 nm gedurende 1 minuut of door bestraling 222 nm bestraling gedurende 20 minuten. Deze laatste produceert superieure low-k films dankzij een complete templaat verwijdering zonder geïnduceerde hydrofilisatie. Anderzijds kan laser annealing worden toegepast op de vers afgezette OCS-films voor het verwijderen van templates en ter verbetering van de YM van de poreuze films. In het strike productieproces kan een verbetering van 13% van de YM-waarde worden bereikt ten opzichte van de referentiefilm die in een oven bij 400 °C is gebakken en die verder geen invloed heeft op de k-waarde van 2,25. Door de uitgebreide herschikking van de

verbindingen, die meestal verband houdt met het verwijderen of reorganiseren van de organische inhoud van de organosilicaatmatrix, is deze aanpak echter weinig aantrekkelijk.

De vervanging van een deel van de Si-O-Si door Si-CH_2-Si functionaliteiten in een poreuze organosilica film resulteert in een kleinere verbetering van de YM dan eerder gedacht. Bijvoorbeeld, bij een dichtheid van ~0,87 gcm^{-3} heeft de film met methyleengroepen een YM van 6,6 GPa, terwijl de film zonder een YM heeft van 5,3 GPa. Dit effect wordt gecompenseerd door een hogere permittiviteit (diëlektrische constante) voor de films die methyleengroepen bevatten - 2,27 met en 2,12 zonder Si-CH_2-Si-groepen bij dezelfde dichtheid respectievelijk als gevolg van een toename van de matrixdichtheid wanneer Si-O-Si groepen worden vervangen door Si-CH_2-Si-groepen. Daarom, afhankelijk van het integratie schema, als tijdens het productieproces schade aan de low-k dielectrica kan worden vermeden, zouden dielectrica met een laag koolstofgehalte meer geschikt kunnen zijn voor integratie vanwege de lagere porositeit die nodig is om een lagere permittiviteit te bereiken.

In de organosilica films kan de zelf-hydrofobiseringsreactie waarbij een overbruggende methyleengroep wordt omgezet in een methylgroep reeds plaats vinden bij een temperatuur vanaf 200°C, beduidend lager dan eerder vermeld in de literatuur. Bovendien vereist de hydrofobiseringsreactie in aanwezigheid van een template een hogere activeringsenergie dan in poreuze materialen. Voorts is de mate van zelf-hydrofobiseringsreactie in methyleen-gebridde organosilica films afhankelijk van de gebruikte template. De films die door cetyltrimethylammoniumchloride (CTAC) gebruiken als template, zijn hydrofieler dan films waarbij BrijL4 en BrijS10 gebruikt werden als template. De template-afhankelijkheid van de hydrofobiciteit wordt toegeschreven aan het blokkeren van de silanolcondensatie door de polyethyleenoxideketten in oppervlakteactieve stoffen van het Brij type, wat leidt tot een hogere concentratie van Si-OH-groepen ten opzichte van CTAC. De extra silanolen zijn bijgevolg dus beschikbaar voor zelf-hydrofobiseringsreacties.

PMO-films zijn OCS-films waarbij de controle over de porieopstelling het mogelijk maakt poriestructuur te verkrijgen die behoort tot één van de kristallografische groepen. We hebben een ethaan-PMO film gesynthetiseerd en gekenmerkt waarbij de oppervlakteactieve stof Gemini 16-12-16 als template werd gebruikt. Na het thermisch verwijderen van de template, heeft de PMO-folie een vervormde 2D zeshoekige poriën sturctuur met een poriëngrootteverdeling gecentreerd rond 2 nm. De Gemini-gelamineerde PMO-films voldoen aan de materiaalspecificaties voor low-k diëlektrische lagen. De Gemini oppervlakteactieve stoffen zijn een interessante klasse van template moleculen omdat hun pakking parameter relatief eenvoudig te controleren is, waardoor de mogelijkheid ontstaat voor een systematische engineering van de mesofase van PMO-films met een kleine poriëngrootte.

In PMO-films met spincoating bestaat een tunable steady state (afstelbare steady state) (TSS). Tijdens de TSS kan self-assembly door de omgevingscondities, zoals luchtvochtigheid en temperatuur, gestuurd worden, wat resulteert in een gewenste mesofase. Bij een relatieve vochtigheid van 70% zijn films met 3D of 2D zeshoekige fasen, afhankelijk van de molaire verhouding van oppervlakteactieve stof tot organosilica, verkregen. De hoge luchtvochtigheid heeft echter concurrerende effecten op de mesofase, die kunnen worden begrepen in het kader van het afstemmingsmechanisme voor de laaddichtheid. Aan de ene kant leidt de interactie tussen de H_2O en de oppervlakteactieve moleculen tot een toename van de kromming van het micel oppervlak, terwijl aan de andere kant de H_2O moleculen leiden tot een depolymerisatie van de siloxaanbindingen waardoor omstandigheden worden gecreëerd die de afname van de kromming van het micelle oppervlak bevorderen. De polycondensatiegraad van de organosilica oligomeren beïnvloedt ook de gevormde mesofasen. Zo wordt bijvoorbeeld een 3D zeshoekige fase verkregen na 20 min. rijpen van de oplossing, 2D zeshoekig na 40 min. rijpen en geen geordende mesofase indien de oplossing ouder dan 70 min. is. Bovendien worden kubieke mesofasen waargenomen wanneer de molaire verhouding van water ten op zichte van organisch-silica van 30 tot 14 wordt verlaagd. Een PMO-film met een 2D zeshoekige poriënorde heeft een 1,7 GPa lagere Jonge modulus dan een film met een ongeordende porositeit, terwijl beide dezelfde permittiviteit van 2,30 hebben. Experimenten om PMO-films te deponeren in smalle 45 nm geulen tonen aan dat een hoge oppervlakte-energie van het substraat nodig is om een goed geordend PMO te verkrijgen.

In tegenstelling tot de verwachtingen is de ionische oppervlakteactieve stof CTAC een geschikt template voor low-k films. Het gebruik van CTAC leidt niet tot een significant hogere lekstroomdichtheid of een lager afbraakveld in vergelijking met een film met een niet-ionogene oppervlakteactieve stof. Met name de lekstroomdichtheid van de CTAC-templated film bij 1MVcm^{-1} is 1,6 x 10^{-9} Acm^{-2} terwijl het afbraakveld 5,7 MVcm^{-1} is. Tegelijkertijd hebben PMO-films waarbij CTAC als template werd gebruikt, een kleine poriegrootte van ongeveer 2 nm en een smalle poriëndistributie, die beide zeer belangrijk zijn bij low-k toepassingen.

ABBREVIATIONS

AFM	Atomic force microscopy
AUC	Area under the curve
B3LYP	Becke, 3-parameter, Lee-Yang-Parr density functional
BTESE	1,2-Bis(triethoxysilyl)ethane
BTESM	1,2-Bis(triethoxysilyl)methane
CDO	Carbon-doped oxide
CMP	Chemical-mechanical polishing
CTAB	Cetyltrimethylammonium bromide
CTAC	Cetyltrimethylammonium chloride
CTE	Coefficient of thermal expansion
DEMS	Diethoxymethylsilane
DFT	Density functional theory
DNA	Deoxyribonucleic acid
EISA	Evaporation-induced self-assembly
EP	Ellipsometric porosimetry
ERD	Elastic recoil detection
EtLK	Low-k containing ethylene bridges
FER	Ferrierite
FinFET	Fin Field Effect Transistor
FTIR	Fourier-transform infra-red
FWHM	Full Width at Half Maximum
GISAXS	Grazing-incidence small-angle x-ray scattering
HMDS	Hexamethyldisilazane
IBM	International business machines
IC	Integrated circuit
ITO	Indium-Tin-Oxide
LA	Laser anneal
LP	Low pressure
LTA	Linde Type A
MEL	ZS**M-EL**even
MeLK	Low-k containing methylene bridges
MFI	ZS**M-FI**ve
MOSFET	Metal-Oxide-Semiconductor Field Effect Transistor
MPMOC	Methane PMO templated by CTAC

MPMOL4	Methane PMO templated by BrijL4
MPMOS10	Methane PMO templated by BrijS10
MSE	Mean square error
MSQ	Methylsilsesquioxane-like film
MSQF127	Methylsilsesquioxane templated by PluronicF127
MSQL4	Methylsilsesquioxane templated by BrijL4
MSQS10	Methylsilsesquioxane templated by BrijS10
MSSQ	Methylsilsesquioxane
MTES	Methyltriethoxysilane
NASA	National Aeronautics and Space Administration
NI	Nanoindentation
OCS	Oxycarbosilane
OCSF127	Oxycarbosilane templated by PluronicF127
OCSC	Oxycarbosilane templated by CTAC
OCSL4	Oxycarbosilane templated by BrijL4
OCSS10	Oxycarbosilane templated by BrijS10
OMCTS	Octamethylcyclotetrasiloxane
PECVD	Plasma-enhanced chemical vapor deposition
PEO	Polyethylene oxide
PID	Plasma-induced damage
PMO	Periodic mesoporous organosilica
PMS	Periodic mesoporous silica
PSD	Pore size distribution
PSZ	Pure silica-zeolite
RC	Resistance x Capacitance
RH	Relative humidity
RI	Refractive index
RT	Room temperature
SAWS	Surface acoustic wave spectroscopy
SE	Spectroscopic ellipsometry
TDS	Thermal desorption spectroscopy
TEM	Transmission electron microscopy
TEOS	Tetraethoxy silane
TMCS	Trimethylchlorosilane
TMS	Trimethylsilyl
TMCTS	1,3,5,7-tetramethylcyclotetrasiloxane

ToF-SIMS	Time-of-flight secondary ion mass spectroscopy
TPAOH	Tetrapropylammonium hydroxide
ULSI	Ultra-large-scale integration
UV	Ultra-violet
VUV	Vacuum ultra-violet
WCA	Water contact angle
XPS	X-ray photoemission spectroscopy
XRD	X-ray diffraction
YM	Young's modulus
ZSM	Zeolite Socony Mobil

CHAPTER 1. INTRODUCTION

1.1. Ultra-large scale integrated circuits, Back-End-Of-Line and low-k materials

What if Moore's law applied to transportation or to agricultural productivity, or to space travel? Then, by the year 2017 we would have been able to travel to the Sun on a single gallon of fuel or feed the world's population with 1 km^2 of land, or travel 300 times faster than the speed of light.[1] Interestingly, in spite of the excitement that the Moore's law has created among technology enthusiasts, it does not anymore correspond to the fastest scientific and technological development. In the past fifteen years, the Moore's law has been outpaced by the genome sequencing innovations and technological advances (Figure 1.1). Nevertheless, while the societal impact of the genome sequencing technology is still to be appreciated, the effect of Moore's law on society, which has been consistently observed for longer than fifty years, is easy to recognize. One telling example is the fact that any smartphone today has more computing power than all of NASA in 1969 when they sent astronauts to the Moon.[2] More importantly, Moore's law has enabled numerous exciting technological and scientific advances including machine learning, self-driving cars, self-landing rockets,[3] robotics, brain-machine interfaces, virtual reality, supercomputers used for theoretical simulations, as well as the aforementioned genome sequencing which takes advantage of the available computing power to piece together and analyze the sequenced genome fragments, i.e. within the bioinformatics category.[4]

Moore's law is not a physical law but rather it has been referred to as a "social fact" which is continually made into an empirical fact by the actors' perceptions.[5] The "law" is an observation made in 1965 by one of the founders of Intel Corporation, Gordon E. Moore, pointing out that for the 6 years prior, the number of transistors on a computer chip has doubled every year.[6]

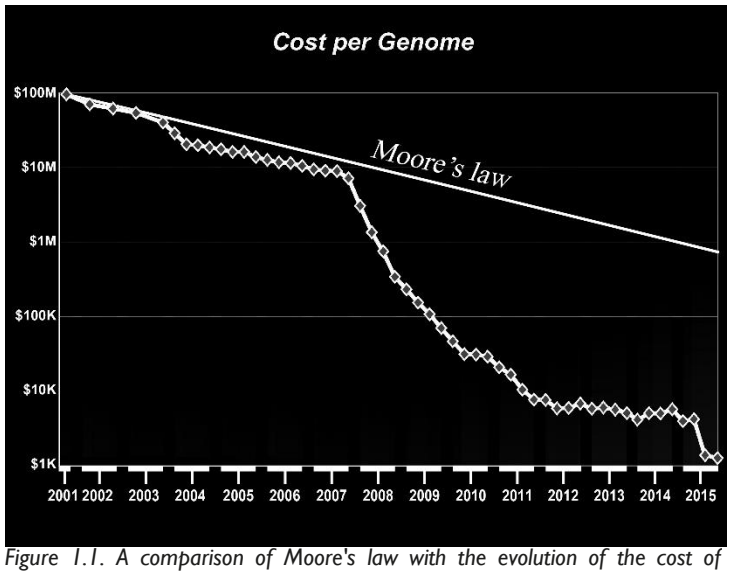

Figure 1.1. A comparison of Moore's law with the evolution of the cost of sequencing a complete human genome in the period 2001-2015. Source: National Institute of Health, USA

Consequently, Moore predicted that this trend would continue in the next 10 years. In 1975, he revised his prediction by stating that he expected each next doubling to take 2 years[7] and the trend has been mostly maintained for the last 40 years.

Therefore, the number of transistors on a chip has increased from about 50 in 1965[6] to more than twenty billion in 2017.[8] The "cramming" of transistors has been possible by the downscaling of their dimensions in each new generation, the most recent of which is the 10 nm technology node (Figure 1.2).[9–11] Nevertheless, the label of the technology node does not refer to the physical dimensions of the transistors, anymore. Starting with the 45 nm node, the gate dimension could not be further reduced without a severe performance penalty. Therefore, at the 22 nm node, the transistor density was increased by the introduction of the FinFET (Fin Field Effect Transistor) technology, where a silicon "fin" serves as the body of the MOSFET (Metal-Oxide-Semiconductor FET) instead of the silicon wafer,[12] but the gate dimensions remained relatively constant. Still, with accordance to Moore's law, each new generation contained about 2 times more transistors. Therefore, the label of the technology node refers loosely to a gate pitch dimension of a planar transistor which would result in a similar number of transistors to the produced microchip. Nevertheless, among the chip manufacturers, there is no agreement on a precise definition.

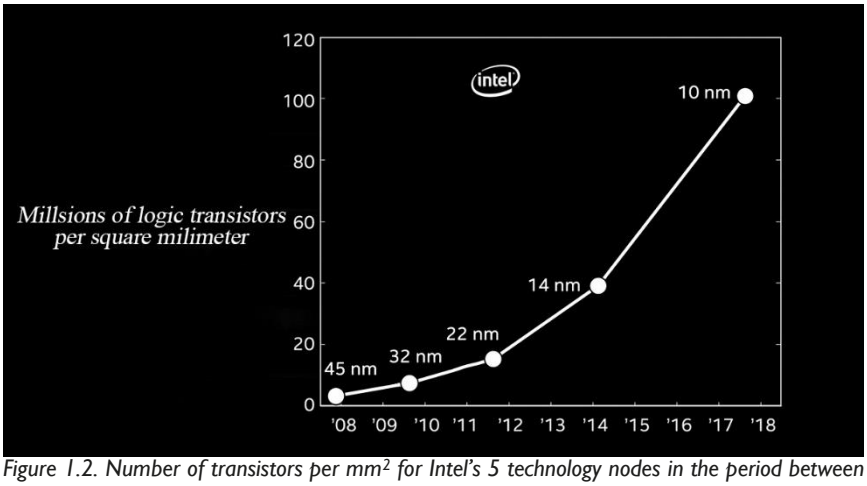

Figure 1.2. Number of transistors per mm² for Intel's 5 technology nodes in the period between 2008 and 2017.[11]

In spite of the attention which the transistor density has received, the interconnects have been the dominant factor limiting the chip performance since the 130 nm technology node (Figure 1.3). The term interconnects refers to the wires, together with the accompanying insulation and barrier materials, which connect the transistors to one another. The interconnect signal delay together with the gate signal delay comprise the total signal delay, i.e. the time it takes for the output voltage to reach 50% of its final output level when the input voltage changes to 50% of its final input level, associated with an integrated circuit. While the gate delay decreases with the smaller transistor size, the interconnect delay, known also as RC delay, increases. The RC denotes the two contributions to the interconnect signal delay, namely the resistance (R) of the

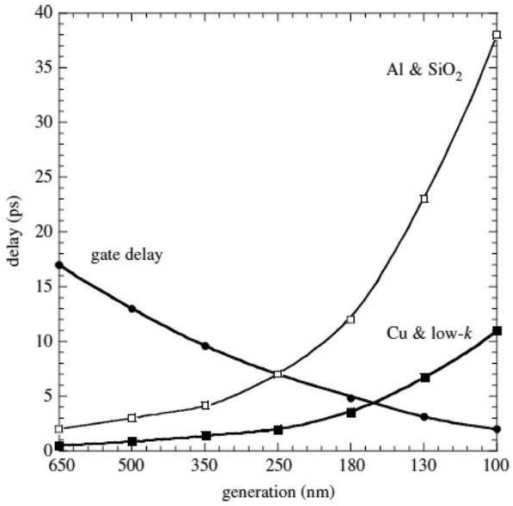

Figure 1.3. Comparison of the gate signal delay with the interconnect signal delay for different interconnect metallization schemes.[2 10]

conductive metal wires and the capacitance (C) between them. In particular the RC delay is given by:

$$RC = 2\rho\kappa\varepsilon_0(4\frac{L^2}{P^2} + \frac{L^2}{T^2}),$$

where ρ is the metal resistivity, ε_0 is the vacuum permittivity, κ is the relative permittivity (or dielectric constant) of the interlayer dielectric, P is the metal line pitch (sum of line width and line spacing), T is the metal thickness, and L is the metal line length.[13] Therefore, the RC delay increases when the metal line pitch is decreased and the metal lines become longer both of which are required as a consequence of the transistor downscaling. At the same time, the RC delay can be reduced by decreasing the resistivity of the metal lines and the dielectric constant of the insulating layers. The reduction of the metal resistivity was achieved in 1997 by replacing the Al (ρ = 2.7 μΩ.cm) metal wires with Cu (ρ = 1.7 μΩ.cm).[14] Nevertheless, the continued scaling of the metal dimensions has renewed the urgency to discover a better conducting material for the smallest metal pitch dimensions at which the bulk resistivity values are not informative anymore. On the other hand, the reduction of the dielectric constant of the insulator has been ongoing since 2000 when the first material with a dielectric constant lower than that of SiO_2 was integrated in a high-volume manufacturing.[15] The challenges to reduce the dielectric constant have been related to the consequences of the replacement of Al with Cu as the conducting metal. In particular, in an aluminum metallization scheme, the metal was deposited and then patterned by reactive ion etching (RIE). In contrast, in a copper metallization scheme, a new process had to be developed since Cu cannot be patterned by traditional RIE because of the very low vapor pressure of the reaction products.[16] As a result, the damascene process has emerged as the industry standard (Figure 1.4).[15] In a damascene process, the dielectric layer is deposited and patterned first before the metal deposition. Therefore, the dielectric has become

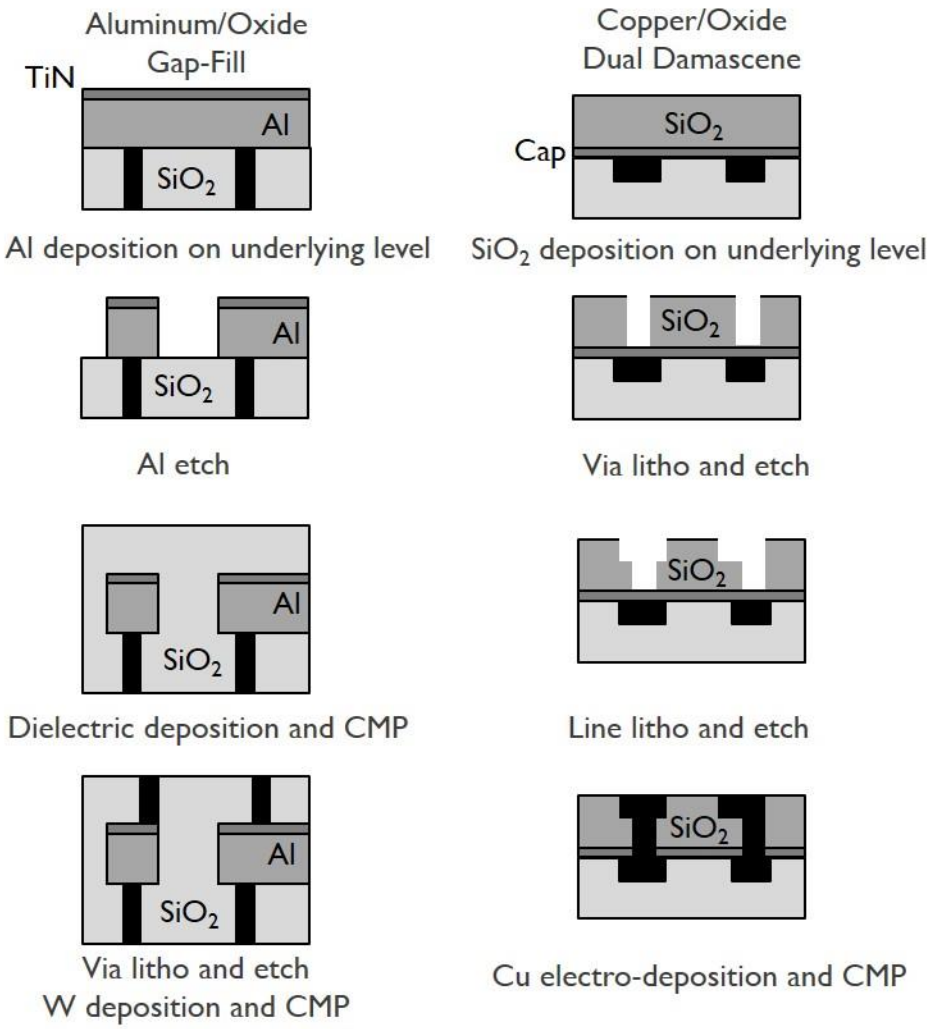

Figure 1.4. Schematic representation of the conventional Aluminum/oxide gap-fill approach versus dual damascene Copper/oxide integration. Adapted from [15]

subject to various processing damage mechanisms which have made the decrease of the dielectric constant challenging.

In addition to reducing the RC signal delay, the low-k materials are also needed in order to reduce the power consumption:

$$Power = CV^2f,$$

where V is the driving voltage of the transistor devices, f is the operational frequencies, and C is the capacitance.[13] Therefore, by decreasing the dielectric constant of the insulating media, faster chips running at lower power can be produced.

1.2. Dielectric constant

The dielectric constant (k) describes the macroscopic polarization response of a dielectric material and can be expressed in the following way[13]:

$$k = \frac{\boldsymbol{D}}{\boldsymbol{E}},$$

where **D** is the electric displacement vector and **E** is the electric field vector. When considered microscopically, three polarization mechanisms exist: 1) electronic; 2) ionic, also known as nuclear or distortion; and 3) dipolar polarization. The microscopic and the macroscopic polarization phenomena are linked via the modified Clausius-Mossotti relation known as the Debye equation:[15]

$$\frac{k-1}{k+2} = \frac{4\pi}{3} N(\alpha_e + \alpha_d + \frac{\mu^2}{3k_bT}),$$

where k is the dielectric constant, N is the number of atoms, α_e is the electronic polarizability, α_d is the distortion or nuclear polarizability and $\frac{\mu^2}{3k_bT}$ is the orientational or dipolar polarizability, where μ is the dipole moment, k_b is the Boltzmann constant, and T is the temperature. The electronic polarizability, α_e, accounts for the displacement of the cloud of bound electrons with respect to the nucleus under an applied electric field. The nuclear polarizability describes the distortion of the nuclei position when an electric field is applied. Finally, the dipolar polarizability corresponds to the response of permanent dipoles to the applied electric field.

Each microscopic polarization mechanism is associated with response time proportional to the mass of the electrons, the nuclei, and the dipoles, respectively. Therefore, in an alternating electric field, the polarization phenomenon exhibits a frequency dependence. Consequently, the dielectric constant is frequency dependent. Figure 1.5 shows the typical cut-off frequencies for each microscopic polarizability contribution. The dielectric constant which includes all three polarization contributions is referred to as a static dielectric constant. In a typical microprocessor, the clock frequency is several gigaherz (10^9 Hz) which means that the dipolar polarizability is mostly screened out. However, in the low-k research, usually, the static dielectric constant at 100 kHz or 1 MHz is reported in order to provide deeper insight in the material properties.

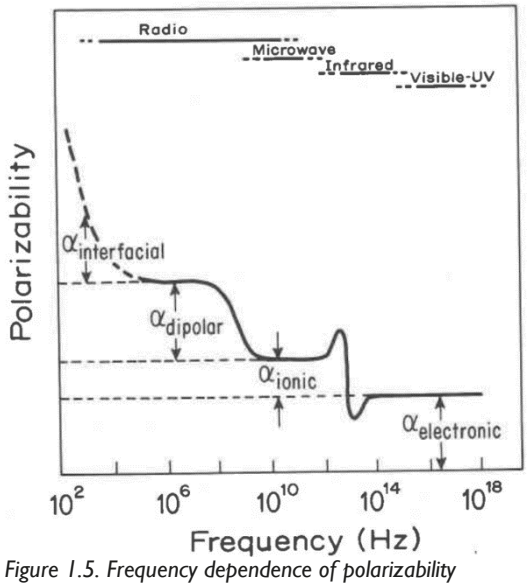

Figure 1.5. Frequency dependence of polarizability

1.3. Historical overview of low-k materials

Amorphous hydrogenated silica was the BEOL dielectric insulator for the majority of the IC technology nodes down to 180 nm.[13,15] The reason had to do with the exceptional properties of silicon dioxide. The SiO_2 can be obtained quite dense (2.2-2.3 g/cm^3) with high network connectivity and few dangling bonds.[15] In terms of thermal stability, it softens and melts without decomposition above 1500°C, a temperature much higher than the BEOL limit of ca. 400°C.[17] The dielectric breakdown of bulk silica is greater than 10 MV/cm, an electrical stress beyond what would be experienced in modern chip operation.[15] Mechanically, silicon dioxide is stiff with an elastic modulus between 55 and 74 GPa, a hardness of ~10 GPa, and a critical fracture energy of 4.4 J/m^2.[13,15] Its coefficient of thermal expansion (CTE) is only 0.5 ppm/K.[17] The dielectric constant of a thermally grown silica depends on the mode of deposition and processing and can vary between 3.7 and 4.5.[13,15,17]

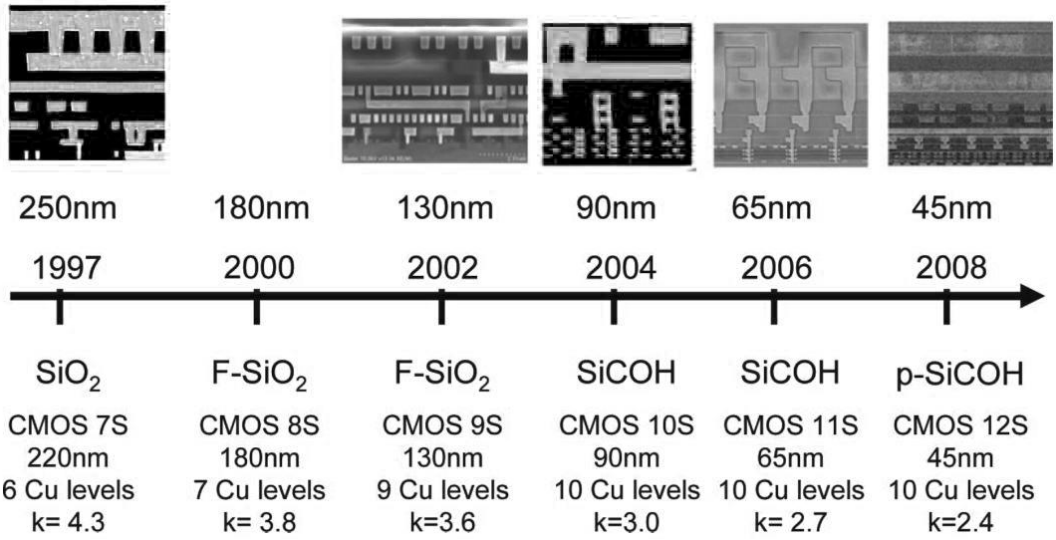

Figure 1.6. Electron microscopy micrographs of the IBM BEOL for the technology nodes from 250 to 45 nm.[15]

In anticipation of the dominant role of the interconnect delay in the overall signal delay beyond the 250 nm technology node, the 1994 American National Technology Roadmap for Semiconductors (NTRS) pointed out the need for new dielectric materials expecting the introduction of a dielectric with k<3.0 at the 180 nm technology node.[18] Furthermore, according to the 1997 NTRS, the implementation of a low-k with k between 2.0 to 2.5 was expected to happen in 2001. However, the first dielectric with a k=3.7 was introduced at the 180 nm technology node in 2000 (Figure 1.6).[15] Later, insulators with k=3.0 and k=2.7 were implemented at the 90 nm and the 65 nm technology nodes in 2004 and 2006, respectively.[15] Next, porous low-k films with k=2.4 appeared in high-volume manufacturing in the 45 nm technology in 2008.[15] In spite of the challenge to further decrease the dielectric constant of the insulators, in the 14 nm technology node demonstrated in 2015, Intel reported the introduction of air gaps in two of its thirteen interconnect levels (Figure 1.7).[19] In the air gap technology no

dielectric is present between the metal lines, i.e. the metal lines are separated mostly by air which is the ultimate low-k dielectric with a k≈1.0.

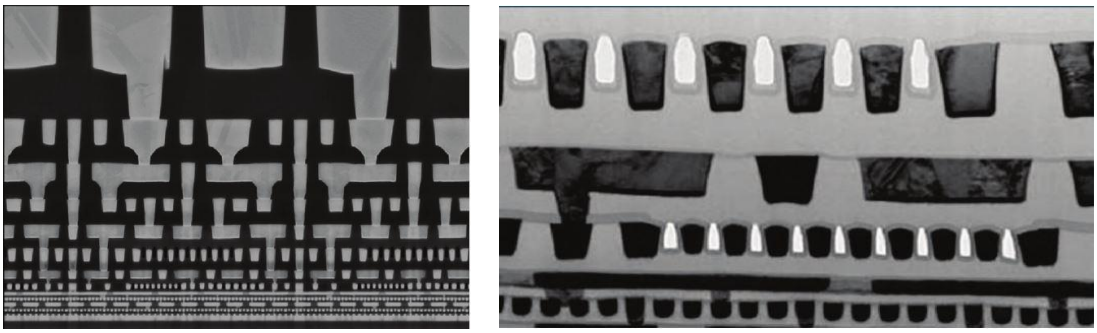

Figure 1.7. a) Intel's BEOL stack at the 14 nm technology node. b) Metal levels 4 and 6 contain air gaps.[19]

The first material with a dielectric constant lower than SiO_2, i.e. a low-k material, to be introduced at the 180 nm technology node was F-doped SiO_2 which is denoted fluorosilicate glass or FSG. Compared to the Si-O bond, the Si-F bond is less polarizable and therefore the FSG has a lower dielectric constant. Also, the Si-F bond is a strong bond (129 kcal/mol)[15] making it highly thermally stable and resistant to homolytic scission and oxidation. The FSGs were also attractive from engineering perspective since the same deposition methods as for SiO_2 could be employed and only required the further inclusion of fluorine-containing precursors such as C_2F_6 or SiF_4. Additionally, the interaction of the FSGs with plasmas is very similar to that of SiO_2 with the only difference of an increased etch rate due to the presence of fluorine.[20] Although the breakdown fields vary for FSG films, even the lower values (~3MV/cm) were compatible with chip-operation requirements for the 180 and 130 nm technology nodes.[15] Nevertheless, one substantial problem for FSG films is that Si–F bonds have a hygroscopic nature and are not very stable.[21] Even if the higher fluorine concentration in the FSG film can reduce the dielectric constant, the FSG film (> 10 at. %) readily absorbs moisture while stored in a clean room and therefore has a higher dielectric constant. Water adsorption influences not only the dielectric constant of low-k films, but also their integrity. In fluorinated silica, water reacts with Si–F bonds according to the following:[22]

$$Si–F + H_2O \rightarrow Si–OH + HF$$

Such a reaction can occur at room temperature and leads to both the formation of undesirable hydrophilic Si–OH bonds and hydrofluoric acid which attacks the Si–O bond. Hence, fluorinated silica glasses cannot contain more than 10%–12% of fluorine (which corresponds to a k value of 3.3–3.4).[20] Thermal desorption spectroscopy (TDS) investigations have shown that the FSG film with high fluorine concentration can desorb more fluorine than the film with low fluorine concentration.[21] Furthermore, the amount of water desorbed out of the FSG film with low fluorine concentration is much smaller than the films with higher than 10% fluorine.[21] The small loss of fluorine in TDS spectra for the low fluorine FSG film indicates good stability for low-temperature annealing (< 450°C).

Due to the limitations of the fluorine-doped silica films in their ability to achieve and maintain k values below 3.0, carbon-doped silica (carbon-doped oxides or CDO, SiCOH, SiOC, or organosilicate glasses, OSG) films were investigated. The integration of CDO films in interconnect structures is facilitated by the similarity of their chemical composition and structure to that of the SiO_2. They were implemented in the technology nodes below 130 nm. Doping the silica films with C by introducing -CH_3 groups lowers the dielectric constant since it causes an increase of the interatomic distances creating free volume in the silica.[20] Typical densities of CDOs are between 1.2 and 1.4 g/cm^3,[20] significantly lower than SiO_2. CDO films have dielectric constants down to 2.6.[20] The dielectric constant of the film depends on the number of methyl groups in the film's matrix since they lower both the polarity and the density of the material by a steric effect. Additionally, the Si-CH_3 groups make the low-k hydrophobic preventing water adsorption and an increase of the k value. The plasma conditions necessary to deposit CDO films are the key parameters to optimize film properties, the boundaries of which are controlled by the precursor structure and chemical composition. For instance, the deposition temperature plays a key role in determining the thermal stability of the as-deposited PECVD film. It has been demonstrated that films deposited at 250-300°C lost 5 at.% of hydrogen after an anneal at 450°C for 4-8 h in nitrogen.[23] Subsequently, stable films deposited at 400°C with a dielectric constant of 2.7-2.8 have been reported.[24] Furthermore, when a high power plasma is used, the film structure becomes more uniform and precursor structure is less important. These films are more extensively cross-linked, resulting in an improvement of mechanical properties due to higher connectivity of the matrix network.[25] In contrast, in a low-fragmentation-regime plasma, the ring structure of cyclic precursors can be preserved in the as-deposited film.[26] CDO dielectrics can be prepared from a variety of pure precursors or precursor mixtures with or without an additional reactive gas. As a general rule, precursors with less than one oxygen atom per silicon in their structure are deposited in the presence of an oxidant in the plasma feed, e.g. O_2.[15] Although the presence of an oxidant is necessary to form Si-O-Si network bonds, when depositing low oxygen content organosilanes, this can lead to the oxidation of sensitive bonds (e.g., C-H). This undesired oxidation makes it difficult to control the ratio of Si-Me/Si-O bonds incorporated in the film. These issues have been solved by designing precursors which contain more Si-O bonds in their structure and therefore do not require an oxidant. Films with dielectric constants ranging from 3.0 to 2.7 with suitable mechanical properties have been obtained from both linear and cyclic molecules, with diethoxymethylsilane (DEMS) and 1,3,5,7-tetramethylcyclotetrasiloxane (TMCTS) being the most popular choices.[15] The mechanical properties of the CDO films are inferior to those of the SiO_2 or FSG dielectrics and they usually decrease with decreasing k values.[13] The CTE of the CDO film with k = 2.8 spans a range of 11.8–12.3×10^{-6}/K.[13] These values are very close to that of copper (17 × 10^{-6} /K),[15] with which

they are integrated. The CDO films with k = 2.8 have low leakage current, reaching a value of 2 × 10^{-10} A/cm^2 at a field of 1 MV/cm.[13]

Starting with the 45 nm technology node, the device performance was further improved by the integration of materials with a dielectric constant of about 2.4. To lower the dielectric constant below 2.6, part of the solid network is replaced with air (k ≈ 1.0). This modification results in a decrease of the film density, thus reducing the total number of dipoles N present in the film and the dielectric constant. The fraction of the material which is filled with air is referred to as porosity, i.e. $p=V_p/V$, where V_p is the pore volume and V is the total material volume. Nevertheless, porosity is not straightforward to define and measure since most materials are to some extent porous. IUPAC divides the porous materials into three categories:[27] 1) crystalline materials with molecular dimension pores, e.g. zeolites; 2) materials with constitutive porosity which is the result of loose packing of "small particles" as in inorganic gels and ceramics; 3) materials with subtractive porosity in which the pores are created by the selective removal of some elements of the original structure. The CDO dielectrics described above contain constitutive porosity which is partly imparted by the bulky methyl groups. Nevertheless, the decrease of the dielectric constant below 2.6 requires higher porosity which can be achieved by a subtractive approach. One subtractive approach is to employ a matrix precursor with a functional group, e.g. a vinyl group, which will generate a second labile phase during the deposition. In an alternative subtractive approach, a sacrificial phase, usually a polymer called porogen, is deposited together with the CDO matrix precursor(s), e.g. DEMS or TMCTS, and is later selectively decomposed. The porogen can be an unsaturated polymer or it may contain reactive functionality such as an epoxide group. The porogen can be removed by a thermal decomposition at about 400°C which usually requires several hours or by a shorter UV cure for less than 15 min at 400°C.[15] The properties of the porous films depend upon several factors: nature of the precursor and the porogen, deposition conditions, and method of porogen removal. The incorporation of the porogen in the hybrid film (before porogen removal) does not guarantee the formation of porosity after the decomposition. Rather, it depends on the degree of interconnectivity of the organosilicate matrix. Beyond a certain porosity limit, any matrix will collapse due to an insufficient connectivity. As a result, the introduction of groups which do not contribute to the matrix connectivity, such as the methyl group, lower the porosity limit at which the film collapse is observed.[28] Furthermore, the matrix connectivity becomes important for the mechanical properties of the film when their integrity is compromised by the increased pore volume. The matrix connectivity or the average network connectivity of a material with a structural formula $Si_xO_y(CH_3)_z$ where all carbon atoms are assumed to be in the form of methyl groups bound to silicon, can be given by[25]

$$\langle r \rangle = \frac{(4x-z)+2y}{x+y}.$$

For an optimal Young's modulus (E value) at a certain density or a dielectric constant, the $\langle r \rangle$ must be above the rigidity percolation threshold of 2.4.[25] Therefore, for optimal mechanical stability, at most one methyl group must be bonded to a Si atom. On the other hand, the porogen, rather its incomplete removal, affects mostly the electrical properties of the low-k. The porogen residues, in particular the remaining sp^2 C species, have been linked to an increase of the electronic and dipolar contribution of the permittivity.[28] They have also been linked to a leakage current increase and a deterioration of the breakdown field as compared to films where a virtually complete removal of the porogen has been achieved.[29]

With the tighter dimensions at the 32 nm technology nodes and below, the plasma-induced damage (PID) had to be limited as much as possible. This is why, for the layers with the narrowest dimensions, low porosity dielectrics with k≈2.55 were investigated and implemented.[30] Another successful strategy to reduce the PID has been the introduction of carbon-bridged PECVD precursors which results in films with higher carbon content.[30,31] A methane-bridged precursor has been used in combination with DEMS and bicyclohexadiene to prepare porous films, which exhibit k = 2.4 and 2.2.[31] Furthermore, using the methane-bridged precursor leads to films with a network with high average connectivity number and therefore the elastic modulus is higher compared to films obtained without the use of the methane-bridged precursor.[30]

The ultimate insulator, air gap, was introduced in high volume manufacturing by Intel in the BEOL stack of their 14 nm technology node (Figure 1.7). Two main integration schemes for air-gap formation have been reported.[32] The first approach uses a sacrificial material that can be removed at late process steps to create air-gaps. The second approach, employed by Intel, involves a non-conformal deposition of dielectric inside patterned trenches to form air-gaps. The basic idea of this approach is first to remove dielectric material between metal interconnect lines and then use a non-conformal dielectric deposition to form air-gaps by pinch-off of the dielectric layer. The shape of the air-gap depends very much on the aspect ratio, defined as the ratio between the height and the width of the trenches. The pinch-off profile is more difficult to achieve as the trench width increases or the aspect ratio decreases. The non-conformal dielectric deposition technique to form air-gaps offers more mechanical integrity at higher manufacturing costs. One of the serious concerns related to the BEOL stack containing air gap dielectric is the mechanical reliability of the interconnects. Finite element model simulations have demonstrated that the sidewall dielectric liner is a critical location where high tensile stress concentration can result in a failure under thermo-mechanical loads. The stresses can be mitigated without compromising the capacitance by implementing the thinnest metal barrier and thickest liner possible within the iso-capacitance design space for a target capacitance.[33] On the other hand, electromigration (EM) experiments have revealed that air-gapped Cu lines without a dielectric liner fail early by voiding due to oxidation and deterioration of the interfacial adhesion

at the Cu interfaces. Therefore, Cu encapsulation using a conformal dielectric liner is necessary in order to ensure hermeticity and provide endurance to the thermal and EM induced extrusive stresses. However, the tensile stress in Cu lines increases linearly with the thickness of the dielectric liner. Therefore, increasing the thickness of the dielectric liner beyond the minimum thickness required for hermeticity is not desirable.[34] Another reason to reduce the thickness of the dielectric barrier is its high dielectric constant. For instance, the predominant dielectric barriers used by the industry SiN and SiCN have k values of 7 and 5.3, respectively.[35] An additional issue is that the air-gap fabrication typically requires more process steps, which means higher manufacturing costs.

1.4. Low-k deposition methods

1.4.1. Plasma-enhanced chemical vapor deposition (PECVD)

All of the dielectric materials discussed so far, from silica to porous SiCHO, have been deposited by PECVD (Figure 1.8). In a chemical vapor deposition (CVD),[20] active intermediates are formed in the gas phase by thermal initiation followed by a chain-branch reaction. The lifetime and concentration of the active intermediates in the gas phase is proportional to the reactor volume (V) and inversely proportional to its surface area (S). Furthermore, increasing the temperature to the self-ignition point results in the increase of the reaction rate for the kinetics of the exothermic reactions. The acceleration of the reaction rate results in a faster temperature rise leading to an autocatalytic process. Therefore, important parameters in CVD are the S/V ratio, the deposition temperature, pressure, and reactants concentration. Similar phenomena are observed during PECVD. An important distinction is that, in a PECVD process, films can be deposited at much lower temperatures than in a thermal CVD process because the electron energy in the plasma controls the dissociation of the precursors into active radicals. Additionally, the concentration of active intermediates in the gas phase depends on the plasma power. Therefore, as a function of plasma power and geometrical factors of the reactor, it is possible

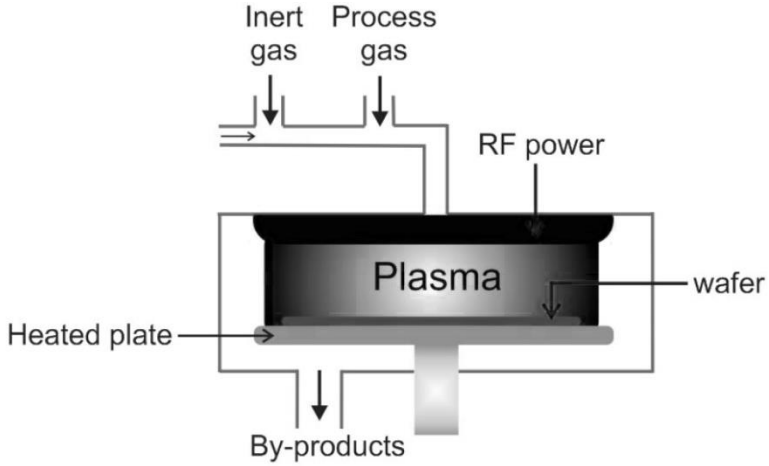

Figure 1.8. Schematic representation of a Plasma Enhanced CVD reactor

to observe regions of nonstable discharge (low concentration of intermediates), powder, high density, and low-density film formation. The dissociation of the precursors in the plasma is a complex phenomenon involving considerable bond breaking and the formation of high-energy species. In this regard, the bonding arrangement in the product is often very different from that in the starting materials. Related to a low-k film deposition, there are only a few studies devoted to the understanding of molecule dissociation mechanisms. In one such study[36] on the dissociation of mixtures of decamethylcyclopentasiloxane (DMCPS) and cyclohexene oxide (CHO), the dissociation of a cyclic molecule has been shown to occur through C–H and Si–CH_3 bonds breaking, whereas the Si–O–Si ring was mostly preserved and then incorporated in the film. The study also found that CHO dissociated into H, C_xH_y and CO radicals. Furthermore, the exact link between the porogen and the final pore size remains unclear since the porogen molecular weight has been shown not to correlate with the low-k's pore size.[37] A low substrate temperature during PECVD can result in a greater incorporation of porogen from the same reactant mixture but also results in a weaker SiCOH skeleton.[38] As a result, films deposited at lower temperatures can shrink more during the curing process and have a larger k value after curing. Therefore, to strengthen the hybrid film structure and avoid pore collapse, a higher deposition temperature (below porogen degradation) has been used. For the deposition of SiC and SiOCH films from trimethylsilane (3MS), for instance, it has been observed that the dielectric constant increases with increasing the total flow, the rf power, and decreasing the 3MS concentration.[20] The dependence of the dielectric constant on pressure goes through a maximum above which the dielectric constant decreases again.[20]

Finally, it is often pointed out that the PECVD approach is ill-suited for integration schemes where a dielectric gap fill is required.[13] Nevertheless, there have been recent reports showing the possibility to perform a gap fill with a PECVD low-k.[39,40] However, PECVD seems to be unsuitable to achieving films with a porosity of more than 50% and an appropriate mechanical stability.[41,42] Therefore, there has been ever increasing interest in the spin-deposited low-k films for high porosity and extreme low dielectric constant films.

1.4.2. Spin-on deposition

In spite of the fact that the PECVD has so far been the low-k deposition method of choice in large volume production, the IC industry has a very extensive experience with the spin-on deposition which is employed primarily for the application of liquid photoresists and consistently delivers high-quality coatings of controlled thickness.[13] The spin-on deposition is particularly suitable when a good planarization and gap fill properties are required. The generation of ultra-low-k porous materials with dielectric constants below 2.0 and good mechanical and electrical properties is problematic by CVD, but easily achievable by spin-on.[13,41] The deposition of thermally sacrificial layers and features is often more easily accomplished with spin-on materials

since the deposition is performed at room temperature. Additionally, the equipment for spin-on deposition is cheaper than that for PECVD, but the materials are more expensive and there is more waste associated with spin-on. Typical spin coating processes utilize only 2–5% of the material dispensed onto the substrate, while the remaining 95–98% is flung off in to the coating bowl and disposed.[43]

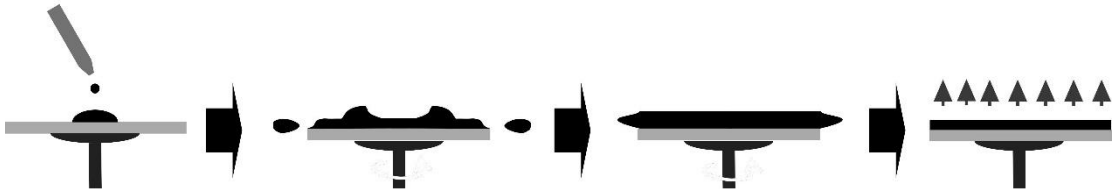

Figure 1.9. Spin-on deposition sequence consisted of 1) Dispensing sol on a substrate; 2) Spin-up; 3) Spin-off; 4) Evaporation

Bornside et al.[44,45] divide the spin-coating into four stages: deposition, spin-up, spin-off and evaporation, although for sol-gel coating, evaporation normally overlaps the other stages (Figure 1.9). In the deposition stage, a solution is deposited on the substrate. Then, at the spin-up stage, the substrate is accelerated to the desired rotation rate and the liquid flows radially, owing to the action of centrifugal force. In the spin-off stage, the excess liquid is ejected off the edge of the substrate. The film continues to thin slowly until disjoining pressure effects cause the film to reach an equilibrium thickness or until it turns solid-like due to a dramatic rise in viscosity from solvent evaporation. In the final stage, the thinning of the film is due solely to solvent evaporation. A model first proposed by Meyerhofer[46] has been found to capture much of the essential characteristics of the spin coating process even though it decouples evaporation and flow. This model captures the experimentally observed scaling of the final thickness $h_f \sim \eta_0^{1/3}\omega^{-1/2}$, where η_0 is the initial solution viscosity, and ω is the final rotation speed.[47] After spinning, the sol undergoes a sharp increase in viscosity and transforms into a "wet gel." The wet gel is a somewhat rigid substance yet consisting of a liquid and a solid component. The solid part is formed by a three dimensional network of linked polymers spanning throughout the film, while the liquid fills the free space surrounding the solid part. As the film dries, it shrinks in volume. Once the film is attached to the substrate and unable to shrink in that direction, the reduction in volume is accommodated completely by a reduction in thickness. When the film has solidified and stresses can no longer be relieved by flow, tensile stresses develop in the plane of the substrate. It is commonly observed that cracking of films does not occur if the film thickness is below a certain critical thickness $h_c \approx$ 0.5-1 μm.[48] Subsequently, the gel is dried by a thermal step at a moderate temperature (bake). During the bake step, the original solvents are removed and the film undergoes a major weight and volume loss of up to 50%. Based on the technique used for drying, a distinction between xerogels and aerogels can be made.[49] Xerogels are formed through conventional drying by evaporation, while aerogels use supercritical drying of solvents. Finally, a sintering at temperatures varying from 350 to 600°C (cure) is required to

obtain a stable film. The cure step induces the final cross-linking of the polymer chains and results in a mechanically stable film structure.

During the spin-coating process, the evaporation of solvent takes place at the top surface of the flowing fluid, thus a concentration profile for the solute species will exist within the flowing solution. Since the solute species in sol-gel solutions undergo polycondensation reactions, it is possible for the top surface to experience a rapid increase in viscosity and potentially to act as a barrier to further evaporation. It has been shown that the evaporation rate applicable through the entire first stage of spin coating is nearly the same as that for pure solvent.[50] Thus the top surface composition does not deviate greatly from its starting value until very near the end of coating formation process, when flow has effectively ceased and the coating drying stage begins.[50] Solvent evaporation leads to localized surface tension gradients which in turn drive a non-uniform film distribution at the surface. It has been demonstrated that the evaporation of solvents from the spin-on solution has significant impact upon the development of striations in spin-on films. The striation defect appears as radially oriented regions of thicker film that often develop in a corrugated, spoke-like profile across the surface of spin-on films. The primary driving force behind striation growth is capillary induced lateral fluid migration at the fluid/atmosphere interface.[51–54] This thin film spreading due to surface tension imbalance is most commonly referred to as the "Marangoni effect".[55] A decrease in height and an increase in spacing of the striations have been observed when alcohols of high boiling points are used.[56] Another strategy to minimize the striations has been to employ a mixture of solvents in which the more volatile solvent possesses higher surface tension with the air.[57]

In contrast to the PECVD, for spin-on materials, the basic structure and bonding arrangement of the initial material are usually maintained to a large degree in the product. Spin-on organosilicate materials are usually prepared by sol–gel processing. This method is generally associated with the preparation of glasses or ceramic materials derived from metal alkoxides.[49] Sols are dispersions of solid, colloidal particles (1–100 nm in diameter) in a liquid resulting from the initial hydrolysis and condensation of silica precursors. The sol represents the processable state of these materials. Gels, on the other hand, are interconnected rigid network structures characterized by the lack of tractability and solubility. Thus, silica gels may be produced from the growth of discrete colloidal particles or by the simultaneous hydrolysis and condensation of a suitable precursor, generally an alkoxysilane. The latter approach does not need to exhibit a distinct colloidal stage and condensation is preferably, temporarily arrested while still in the soluble stage. The typical preparation of these materials by the sol–gel process involves the hydrolysis and polycondensation of alkoxy- and/or halogenated silanes in the presence of water and a suitable catalyst. The catalyst is typically a mineral acid (HCl, HNO_3, etc.), which promotes the hydrolysis reaction to yield silanols. On the other hand, basic catalysts tend to favor the

polycondensation reaction. The silanol functionality readily reacts with itself or an alkoxy/chloro group in a condensation step, which forms siloxane groups and eliminates water or alcohol/HCl. In this fashion, a highly cross-linked network is ultimately formed. The sol–gel approach is subject to many variables, such as the nature of the catalyst, the amount of water relative to alkoxide groups and the reaction temperature. These will be discussed more in detail in the section dedicated on the spin-on silsesquioxane-based low-k candidates.

1.5. Low-k candidates

As the IC industry is interested in implementing dielectric materials with ultra-low k value, i.e. k<2.4, in this section, we will consider the low-k candidates with a dielectric constant lower than 2.4 which have received the most attention. We will consider their appealing properties and the issues which need to be resolved before they can be integrated as an inter-layer dielectric. The introduction of porosity in organic and ceramic materials is ubiquitous throughout the literature as the only viable method to obtain ultra-low-k materials. A distinguishing feature here is that the porosity for dielectric applications must be nano-sized, should be evenly distributed, must be produced under typical BEOL conditions and must be generated in thin films. As compared to interconnected pores, the presence of isolated pores is more compatible with integration demands, even if this is hard to achieve at pore volumes above 25% usually required to achieve an ultra-low k value.

Candidates	**k @ 100 kHz**	**YM (GPa)**	$\bar{d}$**, nm**	**Breakdown field, MV/cm**	**Thermal stability, °C**	**CTE, ppm/K**
SiO2	3.70-4.50	55-74	-	>10	>1500	0.5
HSSQ	1.85-2.80	<2-8.3	<1-3.5	<5	<350	20
MSSQ	2.0-2.80	3.8-4.5	3.5	~5	~550	80-110
Aerogels	1.03-2.10	<2	5-20	<0.5	Unstable	High
Xerogels	1.70-2.30	<4	<1.5-30	0.5-2	~450	62.2
Zeolites	1.70-3.10	7-54	<1-70	<3	>1000	57.4-71.7
PMS	1.5-2.6	1.5-14.4	3.4-9.0	3-4	>450	?
CDO	1.95-2.80	4-8.5	2-4	5-6	>450	12
PMO	1.7-2.9	1.86-20	2-4	>5	>450	10
Polymers	2.2-2.80	2.45	<1-15	4	300-500	40-100
MOF	1.2-4.8	4.7-8.6	<1-?	?	~450	-75-11.7
BC:H	>2.6	126	-	<2	~1500	Low?

Table 1.1. Overview of the low-k properties of the low-k candidates described in this chapter.

1.5.1. Silicates and zeolites

1.5.1.1. Hydrogen silsesquioxane (HSSQ)

One of the earliest and most extensively studied silicates targeted for dielectric applications was hydrogen silsesquioxane (HSSQ). HSSQ is an analogue of SiO_2 where one of the four oxygen atoms bonded to Si has been replaced with a hydrogen atom.[15] Thus, the empirical structure is generally designated as $(HSiO_{1.5})_n$ or $(HSiO_{1.5})_{2n}$ (n = 2, 3...) in order to indicate the polyhedral nature of the precursor oligomers. In the HSSQ materials, the Si and O atoms are arranged in the form of a cage or a ladder (Figure 1.10).[58] The cage can include eight (T8), ten (T10), twelve (T12) or more silicon atoms. The cages in polymerized HSSQ are connected to each other through oxygen atoms while other cage corners are terminated by hydrogen. The cage structure creates free volume, decreasing the material's density and, therefore, its k value. For coatings cured to the thermal limit of 400°C in inert ambient, the dielectric constant of HSSQ is approximately 2.8 with a Young's modulus of 8.3 GPa and a tensile stress of approximately 70 MPa.[59] On the other hand, porogen-based HSSQ have been reported to reach a dielectric constant as low as 1.85 at a 50% porosity and a pore size of 3.5 nm.[60] Additionally, the films have low stress values, 20 ± 5 MPa. The films are also sensitive to an exposure to oxidizing plasmas during the deposition of a sealing layer resulting in an increase of the dielectric constant with time. While a sealing layer containing no oxygen, such as the SiC:H is shown to have no detrimental effect on the low-k properties, the large pore size required the deposition of at least 25 nm thick sealing layer due to a significant penetration into the pores.[61]

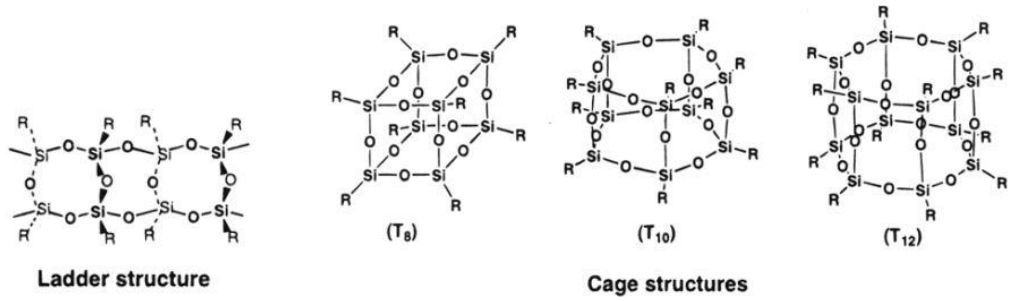

Figure 1.10. Structures of silsesquioxanes

One of the issues encountered with HSSQ materials is their thermal stability.[62] At temperatures between 250 and 350°C, the cage-like structure transforms into a more randomly cross-linked network structure. At temperatures higher than 350 °C, the evolution of SiH_4 and H_2 is observed. At temperatures ranging from 350 to 400 °C, the HSSQ film expands, while from 400 to 450 °C, it contracts.[63] Consistently, the refractive index and the dielectric constant first decrease due to formation of free pore volume and then increase due to densification.[64] On the other hand, a steady increase of the dielectric constant with the temperature has also been

reported,[62] possibly, showing the dependence of the HSSQ response on the distribution of the cage sizes, information which is not always available when proprietary low-k films are evaluated. Another issue preventing the integration of the HSSQ films is their chemical stability.[15] When exposed to oxidizing plasmas, utilized for photoresist striping, the HSSQ readily oxidizes and forms silanols upon subsequent exposure to ambient moisture. This leads to increased leakage current and offers a pathway for fast environmental stress cracking.[65]

1.5.1.2. Aerogels

Aerogels are sol-gel derived materials with extremely high porosities of up to 95%, large open pores, and a high internal surface area which may exceed 1000 m^2/g.[49] The large pore volume is made possible due to a procedure which allows the removal of the pore fluid from wet gels minimizing the capillary forces during the drying stage. One of the most often employed drying method is the supercritical drying that minimizes the capillary forces and conserves the pore structure of the wet gels with a minimal shrinkage. In one of the first studies, the dielectric constant of a 3.4 μm thick silica aerogel was reported to be 1.79 (78% porosity).[66] Nevertheless, due to the presence of residual silanols after the supercritical drying, water is adsorbed inside the pores resulting in an increase of the dielectric constant and the leakage current.[67] If the aerogel is consequently annealed at 450°C, a lower dielectric constant (k=2.0) and leakage current ($J = 10^{-5}$ A/cm^2 at 1 MV/cm) are obtained as compared to the as-synthesized material (k = 2.1, $J = 10^{-4}$ A/cm^2 at 1 MV/cm).[68] A similar effect, 12% lower k-value and almost 2 orders of magnitude lower leakage current, is observed after silylation using trimethylchlorosilane.[69]
While ultralow-k aerogel films can be successfully prepared, the processing conditions are not easily adaptable to continuous thin-film-forming operations and would lead to higher production costs. In terms of material properties, the big pores (10-20 nm), the extremely poor mechanical properties, and the hydrophilicity, if no silylation is performed, make the aerogels challenging to integrate in the back-end-of-line of microchips.[15]

1.5.1.3. Xerogels

The preparation of xerogels employs a drying procedure which does not require supercritical conditions resulting in lower pore volume than aerogels. Therefore, xerogels have lower production costs and better mechanical properties making them more interesting for a low-k application. There are two main procedures for the preparation of xerogels – a two-step acid-catalyzed scheme and a two-step acid-base-catalyzed scheme. Due to the low condensation rate associated with the two-step acid-catalyzed procedure, the solvent removal from the gel results in a significant shrinkage leading to a monolith/film with a very fine texture where about 65% of the pores have a radius smaller than 1.5 nm.[70] On the other hand, the higher condensation rate at the second step of the acid-base-catalyzed procedure leads to more highly branched oligomers

preventing interpenetration and therefore during the solvent removal, the shrinkage stops at an earlier stage due to the stiffness of the impinging clusters. This results in larger pores, so that the maximum capillary pressure is reduced compared to the previous example. This xerogel has less microporosity and a broader distribution of larger pores.[70] An important final step is the immersion of the film in a nonpolar solvent, e.g., n-hexane, to allow the replacement of ethanol and subsequent surface modification with a silylation agent such as hexamethyldisilazane (HMDS) or trimethylchlorosilane (TMCS). Capping the reactive hydroxyl groups in the ambient drying process makes the shrinkage upon drying reversible since the organosilyl-functionalized pore surfaces cannot participate anymore in the condensation reaction or hydrogen bonding when the gel collapses due to the capillary tension developed during drying; therefore, the shrunken network elastically springs back to its original porous state. The silylation of xerogel films is important to maintain a high porous volume and is also beneficial for the dielectric constant through removal of polar Si-OH groups.[15,21] The two-step acid-base-catalyzed procedure results in films with significantly higher pore volumes and has therefore received more attention from the IC industry. The relationship between the structure of the gel and xerogel is shown schematically in Figure 1.11.

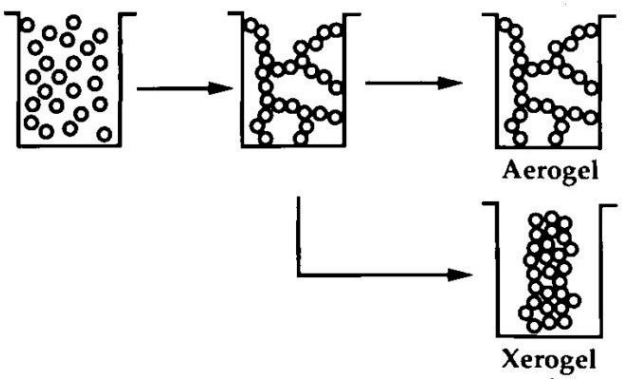

Figure 1.11. Structural relationship between the sol, gel and the final aerogel/xerogel[49]

Using the acid-base-catalyzed procedure, films with porosities between 45 to 90% and dielectric constants at optical frequencies between 2.5 and 1.14 have been reported.[71,72] The aging time can be used to tailor the porosity of the xerogel films since dissolution and re-precipitation reactions cause neck formation between the particles. The time and temperature of the aging, the pH of the medium, and the solvent influence these reactions. The porosity first increases with time, reaches a maximum, and then decreases.[73] The aging time also affects the fracture toughness of xerogel films and there may be an optimal aging time and temperature for maximum fracture toughness.[74] The contact angle of water on the xerogel films annealed in forming gas at 450°C for 30 min is 100°. The anneal in forming gas significantly reduces the leakage current measured at 1MV from 3.21 × 10^{-5} A/cm^{-2} (before anneal) to 6-8 × 10^{-6} A/cm^{-2} (after anneal).[75] The stress of a 50% porosity xerogel film is below the detection limit (38.6 MPa) and the stress

of the sample after 450°C annealing (60% porosity) is 40.5 MPa.[72] Silica xerogel films display relatively low dielectric strength with a breakdown field close to 2 MV/cm.[71]

Because control of the solvent evaporation is not always easy, another approach has been developed where a nonvolatile co-solvent (ethylene glycol) is added to the sol, allowing spin-coating in an open, ambient atmosphere.[76] Compared to the controlled evaporation process, porosity is now determined by the ethylene glycol/TEOS volume ratio. In this case, a narrower pore size distribution is obtained as compared to the film made with only ethanol as a solvent, resulting in higher hardness and modulus.[77] Nevertheless, the average pore size increases exponentially with increasing porosity.[76] The Young's modulus has been found to have a power law dependence on the porosity in the range between 25 and 75%.[77]

While low dielectric constants can be obtained in the case of xerogels, control of the pore size is difficult and the processing conditions are not always compatible with mainstream manufacturing. The reported pore sizes between 10 and 30 nm[78,79] make the integration of these materials and improved formulations in a real structure extremely challenging.[15] Another issue is related to the low Young's modulus of E<4 GPa[80] while a minimum value of 4 GPa has been reported to be required if a low-k dielectric is to survive the chemical mechanical polishing (CMP) step.[81] Additionally, the film is also significantly damaged during the photoresist strip. If an integration scheme is designed in order to prevent the interaction of the plasma reactive species with the xerogel material then an improvement of the breakdown voltage has been observed.[82]

1.5.1.4. Zeolites

Zeolites are microporous crystalline materials that consist of open aluminosilicate frameworks derived from $[SiO_4]^{4-}$ and $[AlO_4]^{5-}$ tetrahedra linked to form cages, channels or cavities of various sizes.[83] In contrast to the classical aluminosilicate zeolites, the pure silica-zeolites (PSZ) consist of only silica tetrahedra and therefore do not contain framework charges or cations that would be detrimental for electronic applications. The PSZs which have received most attention from the IC industry for low-k application are silicalite-1[84] and silicalite-2[85] (Figure 1.12). Due

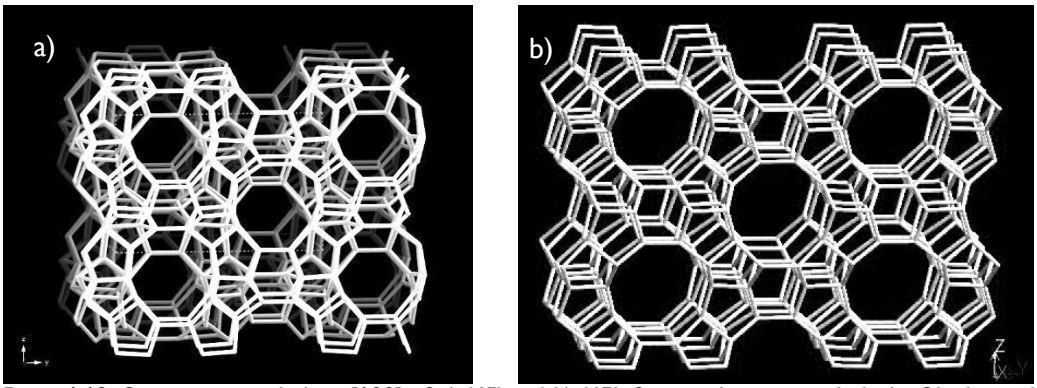

Figure 1.12. Structures viewed along [100] of a) MFI and b) MEL framework types to which the Silicalite and Silicalite-2 pure silica zeolites (PSZ) belong

to their microporous crystalline structure, better mechanical properties as well as reduced barrier and/or metal in-diffusion are expected.[16] Indeed, a nanoindentation investigation of a single PSZ FER crystal provided evidence for a significantly superior elastic modulus as compared to amorphous silica at a given density reporting an experimental YM of 49.4 GPa and a calculated k of 1.78.[86]

Two main strategies have been employed for the preparation of PSZ films:[86,87] 1) in situ crystallization in an autoclave of a solution composed of tetrapropylammonium hydroxide (TPAOH), tetraethoxysilane (TEOS) and water, and 2) spin-coating of a solution containing silicalite nanocrystals. The porosity in the zeolite films originates from the intra-particle porosity within the zeolite nanoparticles and the inter-particle porosity owing to the packing of the near-spherical nanoparticles in thin film morphology. In order to produce films with a reasonable quality, good particle size monodispersity is required.

In-situ crystallized films possess excellent mechanical properties with YM=30–40 GPa for dielectric constants ranging from 2.7 to 3.1.[16] Impressive low-k properties, k=1.7 and YM=54 GPa, have been reported for an MFI PSZ obtained following a low temperature synthesis in combination with a non-thermal photochemical activation.[88] The k and the YM are close to the theoretically predicted values for the single-crystal MFI. The hydrophilicity and the dielectric constant of the films has been shown to decrease with the increase of the water in the starting mixture.[89] Nevertheless, a significant increase in leakage current has been observed. It has additionally been shown that the in situ crystallized film's hydrophilicity increases with exposure to water vapor.[90]

On the other hand, silicalite spin-on films present lower dielectric constants (k = 1.8–2.1) due to the additional porosity gained from inter-nanocrystal packing voids.[87] By increasing the Silicalite-1 nanocrystals content, the crystallinity, hydrophobicity, roughness and porosity increase while YM and dielectric constant decrease. Additionally, a better cohesion is observed for films with a lower nanocrystal content due to the absence of large interstitial voids between the nanoparticles which in films with higher nanocrystal content often result in cracks.[91] The presence of larger mesopores also affects the adhesive properties of these films, leading to failure during CMP.[92] The pore size evolves with crystallization time. A crystallization time of up to 4 days results in micropores of 0.55 nm and 2-5 nm mesopores while a longer crystallization leads to pores with a size of tens of nanometers.[91,93] While the films with lower nanocrystal content possess better cohesion, they are hydrophilic which has a detrimental effect on the k value which increases from 2.1 to 4 within minutes.[94] This has been resolved by silylation treatments. A silylation with TMCTS results in a film with an elastic modulus of 7.03 GPa and a dielectric constant of 1.94 for which the mean-time-to-failure lifetime of time-dependent dielectric breakdown has been estimated to be longer than ten years at 125°C under the electric field of

3.4 MV/cm.[95] Additionally, the dielectric constant and the leakage current become lower as the synthesis temperature increases.[95] The silylation results in a YM as high as 18 GPa for a dielectric constant at an optical frequency of 2.1.[94] Nevertheless, the silylation decreases the porosity. The incorporation of trimethylsilyl (TMS) groups decreases the porosity by 26-56%, depending on the initial pore size distribution. The smaller the pores, the larger is the impact of the incorporation of TMS groups.[96] Furthermore, a combination of UV cure and silylation treatments have been employed in order to improve the low-k properties. A calcination, followed by a silylation, a UV cure with λ=254 nm and another silylation with TMCTS results in a PSZ film with a YM of 10 GPa and k value of 2.18.[97] On the other hand, a UV cure with a λ=172 nm combined with a silylation with TMCTS results in MEL-type PSZ films with a YM=5.7, k=1.9, and a leakage current density of 10^{-9} A/cm^2 at 2MV/cm.[98] Unexpectedly, a UV cure (λ=200-400 nm) at 425 °C hydrophobizes spin-on Silicalite-1 films by grafting the silanols with the organic template. Moreover, the silanol condensation enhances the fusion of the grains, minimizing the intergrain voids and as a result the mesopore size decreases from larger than 50 nm to 2-8 nm. The film has a dielectric constant of 2.16 and an elastic modulus of 10.7 GPa.[99]

In order to achieve a k value in an even lower range, additional mesoporosity has been introduced by the incorporation of organic labile molecules in the zeolite suspension. For instance, the inclusion of 5–15 wt % of cyclodextrin in the synthesis procedure leads to a controllable interparticle pore size ranging from 2.71 to 3.29 nm.[100] A k value of 1.8 is obtained for a 15 wt % porogen loading, while the mechanical properties for this film remain excellent, YM = 14.3 GPa. When the surfactant Tween 80 is included in the suspension, the resulting films have uniform and smooth surfaces, an average mesopore size of 4.5 nm, a k values <2, low leakage current density (i.e., 6×10^{-9} A/cm^2), and an elastic modulus of 13.4 GPa.[101] Furthermore, the surfactant Pluronic F127 has been employed to obtain films with porosities between 9 and 60% and k values between 2.9 and 1.9 while the elastic moduli are in the range of 13-20 GPa.[102] Importantly, the addition of methyl triethoxysilane to the deposition solution results in hydrophobic films which do not require a post-silylation treatment and the k value does not change after exposure to air with a relative humidity of 40-60%. Nevertheless, this approach retards the crystal growth of the zeolites.[102]

Organic-inorganic hybrid zeolite materials have not yet received attention from the IC industry but their organic framework might be beneficial for their chemical and electrical stability.[103] In organic-inorganic hybrid zeolite materials some of the oxygen atoms are replaced by a methylene group. The use of methylene-bridged organosilane as a silicon source gives zeolite materials containing an organic group as lattice, with several zeolitic phases such as the MFI and the LTA structures. The material is not a physical mixture of conventional zeolite and amorphous organic-containing material but contains a genuine organic-inorganic hybrid zeolite. Some of the

methylene frameworks (Si-CH_2-Si) are partly cleaved to give rise to methyl groups[103] which is expected to hydrophobize the zeolites making them more suitable for low-k application.

Recently, Poloni et al. performed DFT simulations in order to screen for the most promising low-k candidates among the known and some hypothetical pure-silica zeolites. They recommend six zeolites within the IZA database (JSR, IRR, OBW, BOZ, OSO, and NPT) exhibiting both ultra-low-k (2.27, 2.33, 2.34, 2.37, 2.39, and 2.49, respectively) and relatively large bulk modulus (47.0, 42.1, 65.1, 57.6, 64.6, and 72.9 GPa, respectively).[104]

In spite of the impressive k and YM values reported (Figure 1.13), zeolite films suffer from a variety of problems arising from the particulate nature and the unwanted large, non-ordered mesoporosity caused by irregular nanoparticle shapes. Particle size of the crystallites may also be a problem as feature size dimensions approach 10 nm and below. Non-uniformities within films results in poor etch rates or variations and difficulties at CMP steps.[105] The films have high surface roughness that is difficult to reduce as polishing will generally result in pull-out of individual nanoparticles. Furthermore, the interparticle voids will also become problematic during the patterning of the dielectric layers and also at the seeding barrier layer integration steps.[105] For these reasons, the use of silicalite films as low-k materials in semiconductor manufacturing currently does not seem realistic.[16]

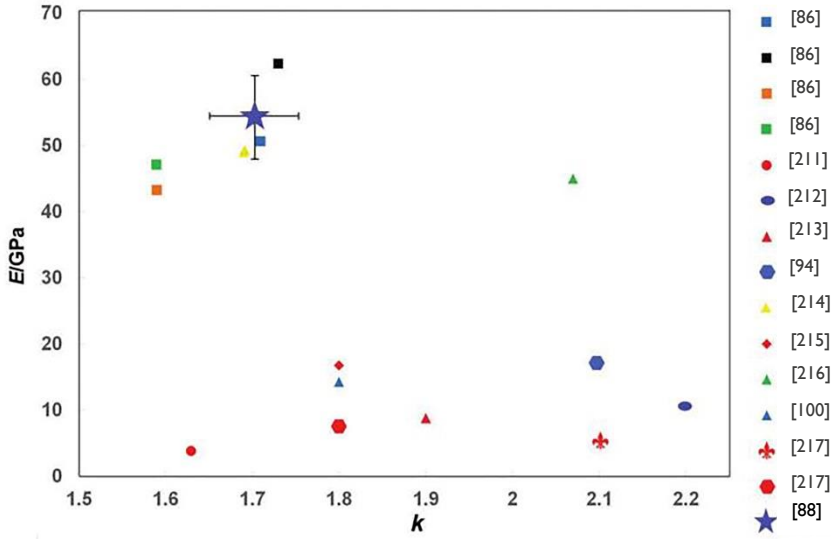

Figure 1.13. Comparison of the YM and the k-values of the reported zeolite films.[88] *Color code for zeolite type—Blue: MFI, Red: MEL, Black: FER, Green: BEA, Orange: CHA, Yellow: LTA.*

1.5.2. Polymers

Organic polymers have been receiving a decreasing interest from the low-k community judged by the way they have been presented in the last 15 years in the comprehensive reviews on the advances in the low-k research.[13,15,16,20] Organic polymers can be divided into two different groups with respect to their dielectric response: non-polar (low-loss) and polar polymers. Non-polar polymers contain molecules with almost purely covalent bonds. Low-loss polymers have

dielectric constants which are independent of frequency. On the other hand, polar polymers contain heteroatoms which contain different electronegativity giving rise to an asymmetric charge distribution. Therefore, polar polymers have higher dielectric constant which is frequency dependent. While saturated hydrocarbons have a lower polarizability than unsaturated, conjugated and aromatic hydrocarbons, the aliphatic C-C, C-H, and C-N bonds are generally not stable at T≥300-400°C. The polymers with a sufficient thermal stability (450-500°C) usually contain aromatic, cross-linked or ladder structures. The thermal stability can also be improved by fluorination which additionally decreases the dielectric constant. Nevertheless, most of the organic low-k films with sufficient thermal stability have dielectric constants close to 2.6-2.8.[20] Therefore, the applicability of majority of the organic polymers for low-k is limited because of their low thermal stability, softness and high CTE. The large CTE of polymers, on the order of 40-100 ppm/K,[15] is unsuitable since repeated thermal cycling causes a stress buildup due to the thermal mismatches with the neighboring materials which can lead to delamination and adhesive failure.

One class of organic polymers that have acceptable thermal stability are polyarylene materials (Figure 1.14). These materials are marketed under the trade name of SiLK™. These materials have been reported to have T_g values in excess of 450°C with a dense dielectric constant of 2.65 and excellent thermal stabilities.[106] Therefore, in order to meet the needs for the 10 nm technology node and beyond of a dielectric with k<2.4, the SiLK needs to be made porous. Nevertheless, the low k value of the dense SiLK means that a lower pore volume will need to be introduced as compared to silica in order to reach a k<2.4. The SiLK needs to be annealed at a T>325°C before it acquires high enough elastic modulus to prevent a collapse of the material due to capillary pressures during the porogen decomposition.[15] As a result, the porogen needs to have a decomposition temperature higher than 325°C. Polystyrene has been employed as a porogen together with the B-staged[1] SiLK resin resulting in a film with a mean pore size of ~40

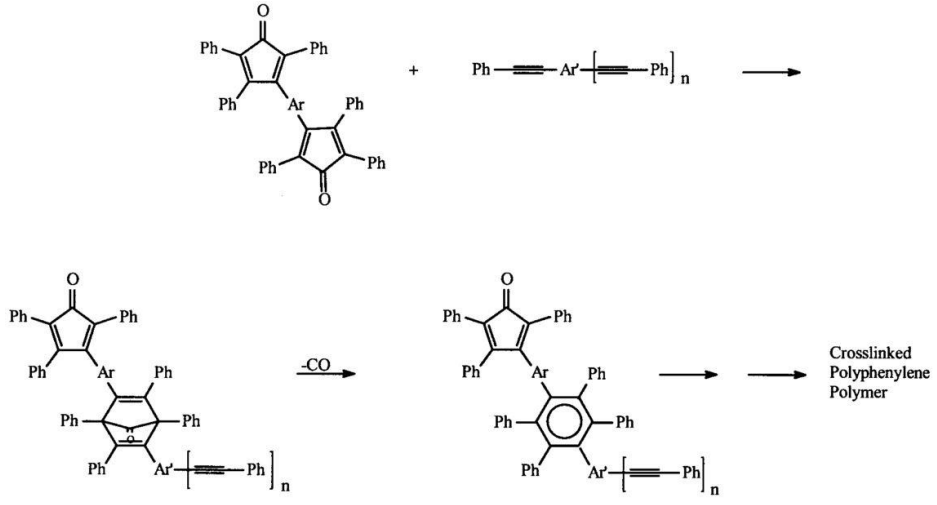

Figure 1.14. The polymerization reaction leading to the SiLK

[1] B-staging refers to the partial cure (i.e. oligomerization) of the polymer[107]

nm and dielectric constants in the 2.2-2.3 range.[107] A polyarylene film with a dielectric constant below 2.0 has been reported to have a bimodal pore size distribution centered around 5 Å and 80 Å.[108,109] A k ~ 2.2 can be achieved by a thermally initiated graft of polyethyleneglycol methacrylate onto a SiLK film resulting in pore sizes in 10-15 nm range.[110] It is clear that pore sizes in this range are unsuitable for integration into the 10 nm and beyond. Nevertheless, the average pore size has been decreased to <2 nm while also improving the CTE from ~ 65 to ~45 ppm in the SiLK Y formulation.[15] The porous SiLK is the only porous organic material for which integration studies have been reported, both single and dual damascene but it has not been employed in a large scale manufacturing.[15]

1.5.3. Organosilicates

This section considers the main low-k candidates for future generation technology nodes, the organosilicates. We have divided the organosilicate low-k films into three categories: 1) porous SiCHO (pSiCHO) dielectrics obtained from a PECVD process; 2) spin-coated methylsilsesquioxane (MSSQ) materials and their derivatives; 3) spin-coated and PECVD oxycarbosilanes (OCS). The pSiCHO are the dielectrics employed so far in chip manufacturing which makes them the most seriously considered low-k candidates. The interest towards the MSSQs have diminished due to their insufficient mechanical properties and therefore we will also consider their derivatives with improved mechanical stability. Finally, the OCS films contain bridging alkylene groups ($Si(CH_2)_nSi$) which allow the introduction of carbon in the low-k matrix without having a detrimental effect on the matrix connectivity and the Young's modulus.

1.5.3.1. PECVD pSiCHO dielectrics

The PECVD porous SiCHO films can be generated either by using a precursor containing a functional group that will generate a second phase during deposition or by mixing a matrix precursor with a reactive hydrocarbon molecule, also called a porogen. Typical precursors selected for the former approach are vinylmethylsilanes. For precursors containing more than one vinyl group per silicon, the organic phase formed during deposition becomes less volatile due to a higher degree of cross-linking.[111] While dielectric constants as low as 2.0 can be obtained with vinyltrimethylsilane, no convincing integration results have been presented.[15]

On the other hand, the porogen (subtractive) approach is the more versatile way to obtain pSiCHO films.[38] In the first step of the porogen approach, matrix and porogen precursors are transformed into species that eventually lead to the formation of a 'hybrid' film composed of an organosilicate matrix enclosing organic inclusions. The porogens need to have some weak bonds that are easily dissociated in the low-power plasma such as unsaturated cyclic hydrocarbons like terpinenes or norborenes; linear alkenes; or molecules with strained rings like cycloalkene oxides or butadiene monoxide.[38] In the second step of the porogen approach, the porogen

molecule fragments are removed. At this point, the film usually becomes porous and has low-k properties.[28] The removal of the porogen can be done by annealing the films at ca. 400°C in an inert ambient, or using electron beam (e-beam) or UV irradiation. The latter two techniques are much faster than the thermal anneal, can enhance the matrix cross-linking and improve the mechanical properties of the pSiCHO films.[112,113] Additional ways to remove the porogen include H_2 plasma and supercritical CO_2.[114,115]

The most often used curing approach in research labs, is the thermal anneal. However, the thermal anneal of 4 h at 400°C in He[116,117] is usually insufficient to remove completely the porogen. An anneal at a temperature higher than 430°C is not suitable since this is the upper limit for an integration with Cu metallization. That is why the e-beam cure and the UV cure have been investigated. Both types of cure are done at temperatures of ~400°C for durations of minutes. Both e-beam and UV cure remove porogen from the deposited films but can also remove some skeleton bonds such as Si-CH_3, Si-H, and Si-OH, leading to the formation of new Si-O-Si cross-links. E-beam cure is performed with electrons at energies of ~2 to ~10 keV, the energy of the beam needed for curing scales with film thickness.[112,118] The e-beam can induce damage in the active devices during integration processing.[38] The degree of damage induced by the e-beam cure increases with the thickness of the gate oxide and with the dose of the e-beam and is more likely to occur at higher electron energies.

As a result, the UV cure is the preferred technique for curing pSiCHO films. In order to elucidate the effect of the photon energy during the UV cure, some authors have used monochromatic UV light,[119,120] while in high volume manufacturing, UV cure is performed by the use of broadband UV lamps.[38] During UV irradiation, the porosity is created through a combination

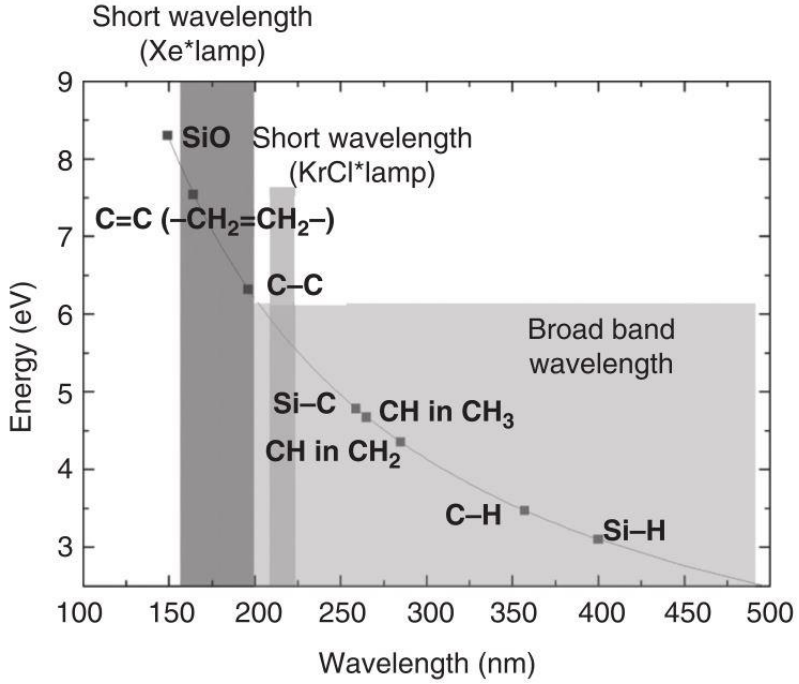

Figure 1.15. Bond dissociation energies of different structures in the SiOCH material[28]

of the photonic breaking effect (Figure 1.15) and thermally activated degradation of porogen. Thanks to this double effect, the porogen is removed from the film within a few minutes.[28] The initial porogen removal makes the film porous resulting in a decrease in Young's modulus as compared to the as-deposited film. A continued exposure to UV causes a densification of the film resulting in increase in modulus owing to an enhanced cross-linking.[38] This densification is a result of the breaking of Si-CH_3 bonds and rearrangement of the skeleton by increased cross-linking. The lowest achievable dielectric constant in pSiCOH films depends on both the porogen and the matrix precursor. For instance, at high fractions of porogen incorporated in the as-deposited films, the removal of the porogen may result in a collapse of the thickness rather than in enhancing porosity. As a result, the dielectric constant does not decrease with increasing the relative amount of porogen beyond the value corresponding to the minimum k.[117] On the other hand, if the matrix of the as-deposited film is strong enough, ultra-low-k films with k=2.1 can be achieved by increasing the relative amount of the porogen.[117] In the latter case, the shrinkage reaches a plateau and therefore the increase of the porogen content results in continuous increase in the porosity of the film and corresponding decrease in its dielectric constant.[13] In order for the matrix to be mechanically strong enough to avoid collapse after the removal of the porogen, it should be minimally bonded to the porogen species to avoid forming dangling bonds or other defect sites.[121] In terms of structure, the SiCHO constituted by silicon bonded to more than one methyl group are not able to prevent significant film shrinkage. This behavior has been discussed using percolation of rigidity arguments.[25] Networks below the percolation threshold are more deformable than those above the percolation point and the maximization of O_3-Si- and O_4-Si- units is necessary to avoid the film collapse.[28]

The increase of the C content from 0 to 19 at.% in pSiCHO films leads to a decrease in the ionic contribution to the dielectric constant from 1.86 to 0.25 and a much smaller reduction of the electronic contribution from 2.10 to 1.90.[122] The dipolar contribution becomes negligible as the C content increases. Therefore, the reduction of the ionic contribution, owing to the decreases in the film density and in the number of Si-O groups in the films, is the predominant factor in the reduction of the overall dielectric constant.[122] Furthermore, porous SiCHO films with low leakage currents of less than 10^{-8} A/cm^2 at fields below 2 MV/cm[1] have been reported making them suitable for integration in a chip interconnect.[38] The porous SiCHO dielectrics have intrinsic tensile stresses in the range of 35 MPa to 55 MPa depending on the deposition and curing conditions. The stress values increase with UV cure time and, for the same chemistry, will normally be smaller for films of lower k and corresponding lower E values.[38] One factor which determines the strain and stress in the low-k during the thermal cycling in the integration process is the CTE. The reported CTE values of ~12 ppm/°C for pSiCHO with k = 2.1[117] are suitable since they are similar to that of copper. Interestingly, no correlation of pore size with

the molecular volume of the porogen has been established. The pores seem to be formed by a species larger than one porogen precursor molecule, which could be created either in the plasma phase, on the film surface or even in the bulk of the film during the curing stage.[37] Nevertheless, even though the porogen nature seems not to determine the pore size in a simple way, it has an impact on the film properties because it modifies the structure of the produced organosilicate network.[37] For example, when a deuterated porogen is used with DEMS, extensive hydrogen and deuterium scrambling is observed between the porogen and the inorganic network.[123] Furthermore, it is a common observation that with the increase in the pore volume of pSiCHO films, the pore size increases making them unacceptably large when porosity values of 40% or higher are achieved.[124,125]

Dense SiCHO films prepared from cyclic siloxane precursors possess superior mechanical properties to those prepared from linear methylsilanes.[13] Nevertheless, it is difficult to incorporate porogen in films deposited with cyclic matrix precursors, such as TMCTS or octamethylcyclotetrasiloxane (OMCTS), and large porogen to skeleton flow ratios have to be used to fabricate pSiCOH films.[126] Lower flow ratios have to be used with non-cyclic skeleton precursors, such as the branched DEMS.[38] Additionally, an efficient incorporation of the C_xH_y porogen fractions in the deposited films requires the use of porogen molecules with at least two reactive bonds, such as double C=C bonds or strained bonds such as in the bicycloheptadiene or a-terpinene.[30,127] Nevertheless, the presence of such bonds in the porous film[112,128] has been linked to a deterioration of the electrical reliability.[129] Even if the presence of sp^2-carbon in the pSiCHO films is not considered to be the result of the use of porogens with double bonds,[112] it has not been ruled out. Rather, such structures are thought to arise from the degradation of the porogen under energetic conditions in the plasma, this signal being observed in the hybrid film and not in a matrix film.[112] These types of graphitic-like residues are not observed in spin-on films after UV curing.[130] The presence of porogen residues leads to an increase of the electronic and dipolar contribution of the permittivity.[28] These structures hold a permanent dipolar moment and non-localized valence electrons. Moreover, these graphitic-like structures are more conductive than the SiCHO skeleton and as a result, a correlation between porogen residue and leakage current has been shown.[29] The breakdown field is also affected by the presence of these residues. When a H_2 plasma treatment is combined with a UV cure, a pSiCHO film with undetectable porogen residues is obtained.[131] The limitation of this approach is that the film must be thinner than 200 nm. Otherwise, hydrogen treatment can densify the top layer, which induces inhomogeneity and prevents the porogen extraction.[28]

1.5.3.2. Methyl Silsesquioxanes (MSSQ)

Silsesquioxanes are polymers with the empirical formula $(R–SiO_{3/2})_n$. These compounds derive their name from the one-half (3/2) or sesquistoichiometry of oxygen bound to silicon. In

particular, the methyl silsesquioxanes (MSSQs) are analogous to the orthosilicate structure, where one of the four oxygen atoms bonded to silicon has been replaced by a methyl group. The most common representatives are a ladder-type structure, and a cage structure containing eight silicon atoms placed at the vertices of a cube (T8 cube).[20] MSSQs are prepared by a sol-gel chemistry. Here, we will consider the MSSQ polymeric films reported from methyltrialkoxysilanes and their copolymers with the tetraalkoxysilanes with a dielectric constant below 2.4.

Compared to the HSSQ films, MSSQ-based films show better thermo-oxidative stability. Under inert atmosphere, MSSQ demonstrates high thermal stability of ~550°C and low oxygen sensitivity to 300-350°C.[15] "Dense" MSSQ films have a dielectric constant of 2.7-2.8 and breakdown field higher than 4 MV/cm. The low dielectric constant is a result of the low electronic polarizability of the methyl substituent along with the presence of constitutive porosity estimated to be 6.7%.[15] Relatively low YM values, ranging from 3.8 to 4.5 GPa, have been reported while the CTE tends to be fairly high, in the range of 80-110 ppm/°C, compared to SiO_2 with a CTE of approximately 0.50 ppm/°C.[132]

The presence of Si-Me groups in the MSSQ, while necessary to achieve lower k, disrupts the connectivity of the silicate network and deteriorates the film mechanical properties. Therefore, in order to increase the network connectivity, copolymers derived from MSSQ with other monomers have been explored. For instance, porous films have been deposited from methyltrimethoxysilane (MTMS) and TEOS with molar ratios from 0 to 9 and cetyltrimethylammonium bromide (CTAB) as the porogen.[133] Films with 60% porosity could be obtained without pore collapse. In order to ensure the hydrophobicity of the films, the MTMS needs to be at least 50 mol% in TEOS. Furthermore, at a constant porogen loading, the dielectric constant decreases when the ratio of MTMS in TEOS increases. Surprisingly, partial crystallinity in the matrix of the mesoporous films could be observed, although the mechanism of crystallization could not be established. The small pore diameter of only 3 nm at 50% porosity is an advantage for low-k application and cannot be achieved by a PECVD method.[134] Small pore size of up to 3.5 nm at porosities higher than 50% can be obtained by various tetraalkylammonium bromide porogens.[135] Additionally, a YM of ca. 4 GPa, sufficient to survive a CMP step, for a film with a k of 2.0 has been demonstrated.[135]

Interestingly, there seem to be no systematic studies which have evaluated the impact of the MSSQ synthesis conditions on the low-k properties even if the hydrolysis and condensation of alkoxysilicates have been extensively researched and it has been shown that different oligomers and polymers are obtained depending on the pH and the H_2O:Si ratio, r. Next, we will review the main pH regions as well as r values above and below 4, the stoichiometric ratio for tetraalkoxysilanes, and their effect on the polymer morphology.

Below pH 2, the rate of hydrolysis of tetraalkoxysilanes is large compared to the rate of condensation. Additionally, for r values greater than 4, the hydrolysis is expected to be essentially complete at an early stage of the reaction. In these conditions, the condensation occurs by reaction-limited cluster-cluster aggregation leading to weakly-branched structures. On the other hand, when the hydrolysis reaction is performed with understoichiometric amounts of water ($r < 4$), condensation commences before hydrolysis is complete. Unhydrolyzed alkoxy groups promote the formation of more weakly-branched structures. Because the ether-forming condensation reaction is unlikely, unhydrolyzed extended structures can be highly concentrated without gelling. These concentrated systems exhibit high viscosities suitable for spinnability.[136]

Above pH 7, and for r values greater than 4, the hydrolysis of all polymeric species formed by tetraalkoxysilanes is expected to be complete. Dissolution reactions that occur preferentially at weakly-branched sites provide a continual source of monomers while redistribution reactions can produce unhydrolyzed monomers. Under these conditions, growth occurs primarily by monomer-cluster aggregation because condensation occurs preferentially between weakly acidic species that tend to be protonated and strongly acidic species that are deprotonated. When the amount of water is understoichiometric ($r << 4$) the unhydrolyzed sites get incorporated in the growing clusters. The probability of condensation at these sites is less than at hydrolyzed sites. Finally, under the conditions used by Stöber,[137] high pH and $r>20$, primary particles formed by nucleation, growth, and ripening undergo an ordered aggregation process to form monosized spherical particles.[136]

At intermediate values of pH (3-8), a spectrum of transitional structures are expected from tetraalkoxysilanes. The dissolution and condensation rates smoothly increase with pH, whereas the hydrolysis rate goes through a minimum at approximately neutral pH. Increased H_2O:Si ratios, r, increase the dissolution and hydrolysis rates at any particular pH value. At a neutral pH and $r << 4$, the condensation reaction initially proceeds between incompletely hydrolyzed species. Depolymerization and redistribution reactions provide an additional source of monomers. The hydrolyzed species are more likely to condense with a larger cluster than with themselves. Increasing the value of r causes an increase in the hydrolysis and dissolution rates, both of which promote the formation of more compact structures. Below pH 7 the hydrolysis rate increases and the rates of dissolution and condensation decrease. Hydrolysis occurs by an acid-catalyzed mechanism involving a basic, protonated alkoxy substituent while condensation occurs by a base-catalyzed mechanism involving an acidic deprotonated silanol. Therefore hydrolysis occurs preferentially on monomers and weakly branched oligomers that subsequently condense preferentially with clusters. However, the availability of monomers at later stages in the reaction decreases with pH; therefore, the predominant growth mechanism changes from monomer-cluster to cluster-cluster with decreasing pH and increasing time of reaction. Below

pH 4 the condensation process becomes essentially irreversible and more weakly branched structures predominate. From pH 7 to pH 8, the dissolution and hydrolysis rates increase. Restructuring reactions provide a continual supply of monomers and insure that reaction-limited conditions are achieved. At sufficiently high r, the process is akin to aqueous silicate polymerization, and smooth colloidal particles should form.[136]

Steric factors exert the greatest effect on the hydrolytic stability of alkoxysilanes. Any complication of the alkoxy group retards the hydrolysis of alkoxysilanes, but the hydrolysis rate is lowered the most by branched alkoxy groups. The substitution of alkyl groups for alkoxy groups increases the electron density on the silicon increasing the stability of positively charged transition states. Conversely, hydrolysis or condensation decreases the electron density on silicon which increases the stability of negatively charged transition states. Under acidic conditions, the hydrolysis rate increases with the degree of substitution, of electron-providing alkyl groups, whereas under basic conditions the reverse trend is observed. Under acidic conditions, the hydrolysis rate decreases with each subsequent hydrolysis step, whereas under basic conditions, the increased electron-withdrawing capabilities of OH (and OSi) compared to OR establishes a condition in which each subsequent hydrolysis step occurs more quickly as hydrolysis and condensation proceed.[136]

The overall condensation rate is minimized at about pH 2 and maximized at intermediate pH. The minimum corresponds to the isoelectric point of silica: surface silanol groups are protonated and deprotonated at lower and higher pH values, respectively. The pH-dependence suggests that for more highly cross-linked systems, protonated and deprotonated silanols are involved in the acid- and base-catalyzed condensation mechanisms at pH < 2 and pH > 2, respectively.[136]

In organosilanes organic substituents influence the acidity of silanols involved in condensation. Electron-providing alkyl groups reduce the acidity of the corresponding silanol. This should shift the isoelectric point toward higher pH values, significantly influencing the pH-dependence of the condensation mechanism. Conversely, electron-withdrawing groups (-OH or -OSi) increase the silanol acidity, and the minimum condensation rate for oligomeric species occurs at about pH 2. Thus, the extent of both hydrolysis and condensation and, in organoalkoxysilanes [$R_xSi(OR)_{4-x}$], the value of x determine the reaction mechanism and define what is meant by acid- or base-catalyzed condensation. In general, base-catalyzed condensation occurs when the pH is above about 2.[136]

The most widely accepted mechanism for the condensation reaction involves the attack of a nucleophilic deprotonated silanol on a neutral silicate species and this reaction pertains above the isoelectric point of silica (pH>2-4.5, depending on the extent of condensation of the silicate species), where surface silanols may be deprotonated. Therefore, the mechanism favors reactions between larger, more highly condensed species, which contain acidic silanols, and

smaller, less weakly branched species. On the other hand, the acid-catalyzed condensation mechanism involves a protonated silanol species. Protonation of the silanol makes the silicon more electrophilic and thus more susceptible to nucleophilic attack. The most basic silanol species (silanols contained in monomers or weakly branched oligomers) are the most likely to be protonated. Therefore, condensation reactions may occur preferentially between neutral species and protonated silanols situated on monomers, end groups of chains, etc. [136]

1.5.3.3. Oxycarbosilanes

In this section, we will consider a class of organosilicate materials in which carbon atoms are present as bridging groups between two silicon atoms (Figure 1.16). These hybrid organic–inorganic materials are known in the literature under different names: bridged polysilsesquioxanes,[138] oxycarbosilanes[139,140] and carbosiloxanes.[141] These materials are obtained from the same precursor molecules as the periodic mesoporous organosilica (PMO) materials which will be presented later but the pore structure was either not investigated or no presence of pore organization was reported. Additionally, since the bridged silsesquioxane precursors are often mixed with alkylalkoxysilanes, we will distinguish between *neat* oxycarbosilanes obtained only using a bridged precursor and copolymers which contain more than one matrix precursor. Theoretical studies predict that organosilicate films containing alkylene-bridging units should deliver higher modulus compared to films where the carbon is introduced only in the form of methyl groups.[142][143]

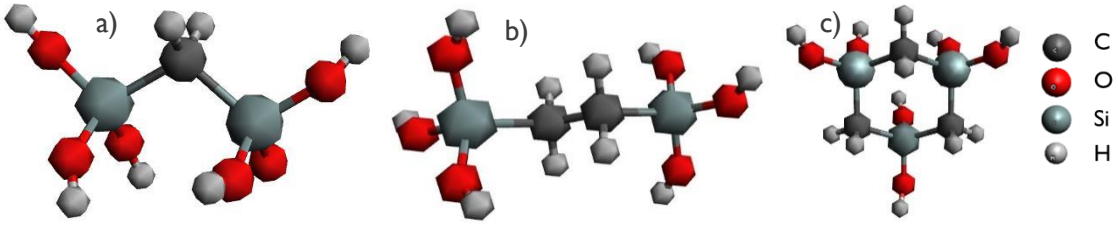

Figure 1.16. Typical PMO precursors: a) methylene-bridged precursor $_3$(RO)Si-CH$_2$-Si(OR)$_3$; b) ethylene-bridged precursor $_3$(RO)Si-CH$_2$-CH$_2$-Si(OR)$_3$; c) ring precursor, 1,1,3,3,5,5-Hexaalkoxy-1,3,5-trisilacyclohexane

Considering films obtained without the use of a porogen, the ethylene-bridged oxycarbosilane has a Young's modulus of 30 GPa while a film obtained from methyltrimethoxysilane (MTMS) has a YM of 5GPa. This is explained with the various large and flexible Si-O-Si cage structures formed by the MTMS during the polycondensation combined with the loss of the small strained cages during the high-temperature vitrification which reduces the density of the film. At the same time, the addition of 1,2-Bis(triethoxysilyl)ethane (BTESE) results in smaller cages and strained cycles with more rigid Si-O-Si microstructures and allows for the covalent incorporation of the cages in the film.[144] The higher modulus in the oxycarbosilanes is also partly due to a denser matrix with a mass density of 1.6 g/cm^3 while the film composed entirely of the MTMS has a density of 1.2 g/cm^3. As a result, the dielectric constant of the former is 3.14 while k=2.75 in the latter case. Importantly, the CTE of 10ppm/K of the oxycarbosilanes is 10 times lower than that

of the MSSQ film.[144] These findings have been corroborated by several studies[145,146] with the additional finding that when the 1,2-Bis(trimethoxysilyl)ethane (BTMSE) content in MTMS is increased from 0 to 47%, the residual stress in the film increases from 54 to 117.5 MPa.[146] When porogen is introduced in the copolymeric films, a dielectric constant as low as 1.92 has been reported[147] but the modulus has been reported to be only 1.86 GPa. Importantly, for all these films, a power law decay of the modulus as a function of porosity was observed.[147]

The YM of neat oxycarbosilanes are 4-5 times higher than the MSSQs of similar densities and k-values.[139,140] Additionally, unlike the MSSQs and the copolymeric oxycarbosilanes, the YM decreases linearly with decreasing density. The adhesive fracture resistances of the methylene- and ethylene-bridged systems are 15 and 17 J/m^2, respectively, compared to 10 J/m^2 for SiO_2.[139] The YM are 72, 20, and 17 GPa for silica, methylene-, and ethylene-bridged films, respectively, whereas the fracture resistance of these materials follows the reverse order.[139] Furthermore, recent computational modeling has established that the bulk modulus of ethylene-bridged oxycarbosilanes scales as $(p - 0.6)^{1.92}$ and the fracture energy scales as $(p - 0.55)$, where p is the network connectivity.[148]

Another strategy to prepare porous carbon-bridging containing materials relies on methane-bridged hyperbranched carbosiloxanes (HBCSO). HBCSO films with dielectric constants ranging from 3.0 to ~ 1.8 were obtained using Pluronic 123 as a porogen. Over the entire range, the Young's moduli of the films are largely superior to the MSSQ samples, but inferior to methylene-bridged oxycarbosilanes films.[141] For example, Young's moduli of 17-22 GPa are obtained for films with dielectric constants ranging from 2.6 to 3.1. These materials have breakdown fields higher than 5MV/cm, and leakage currents $<10^{-8}$ A/cm^2 at 2 MV/cm.

The strategy to increase the carbon content in the silica-based low-k materials has culminated in the investigation of polycarbosilane films in which all of the oxygen atoms are replaced by carbon atoms. Polycarbosilanes cross-linked at 300°C are thermally stable to more than 450°C.[149,150] They are hydrophobic and insensitive to moisture-assisted cracking, since no siloxane bonds susceptible to moisture-attack are present.[150,151] Nonporous films with a dielectric constant as low as 2.32 have been reported.[149] Their elastic moduli are superior to typical MSSQ materials but inferior to the OCS.[151] The polycarbosilanes are also resistant to Cu diffusion because of the hydrophobicity of the polymer which prevents the Cu ionization through metal oxidation at the metal–polymer interface.[149]

A number of requirements have been asserted for a sol-gel formulation to be compatible with the current integration scheme. For instance, the surfactant has to be nonionic and thermally decomposed (rather than using solvent washing), high-quality films without defects should be spin-coated on 300 mm wafers (low boiling alcohols cannot be used as a solvent), halogenated

acids like HCl need to be replaced by HNO_3 to prevent chloride ion contamination and, finally, sol solutions should be stable for at least one month at room temperature.[16]

1.5.4. Non-silicon-based low-k dielectrics

1.5.4.1. MOF and COF

Metal-organic frameworks (MOFs) have emerged in the past few years as a class of materials with a wide spectrum of applications. Their properties arising from the self-assembly of metal ions/clusters with electron-donating organic linkers, enables ordered frameworks with high uniform porosities, low densities and high thermal stabilities to be created.[152,153] MOFs have been proposed as possible candidates for low-k dielectrics since some of the MOFs are thermally stable at temperatures of up to 400°C, show electrically insulating behavior, high mechanical strength and chemical stability.[152] The potential of MOFs for low-k applications was initially proposed by Zagorodniy et al.[154] through theoretic evaluation of the dielectric constant of a range of MOFs. The first experimental evidence for such a device was based on ZIF-8 (Figure 1.17) films which had an effective k value of 2.3 with good mechanical properties and hydrophobicity.[155] A strontium-based MOF[156], after a dehydration, has a dielectric constant of 2.4 with a low dielectric loss (0.026) and a low leakage current of 1.69×10^{-9} A/cm^2. Nevertheless, since the measurements were performed on pressed pellets, interstitial gaps and interfaces could interfere with the data interpretation and further work is needed to benchmark these materials. The dehydrated compound was thermally stable at temperatures up to 420°C. A spectroscopic ellipsometry study of the optical constants of HKUST-1 films after full dehydration revealed a refractive index of 1.39 which is in a good agreement with the predicted dielectric constant of 1.7. Importantly, such studies take into account only the electronic polarization while the contribution from the other polarization mechanisms (ionic and dipolar) still needs to be demonstrated. On the other hand, Zn-based MOF nanocrystals have been used to form films on an ITO glass by dip coating and secondary growth resulting in continuous MOF-3, MOF-5 and MOF-10 films with dielectric constants of 1.2, 2.1 and 4.8 at 2 MHz respectively. The films also have good mechanical strength (YM=4.7-8.6 GPa), adhesion, and hydrophobicity.[157]

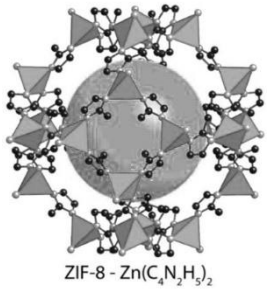

Figure 1.17. Unit cell of ZIF-8

MOF films are usually deposited from a solution via dip- or spin-coating. On the other hand, atomic layer deposition has been reported using the trimethylamuminium (TMA) and various

saturated and unsaturated, linear carboxylic acids.[158,159] Attractive features of some of the obtained films are smoothness (RMS < 0.5 nm), hydrophobicity, and transparency in the optical range. Nevertheless, the films are amorphous with a RI>1.5 indicating dense films with high electronic polarizability. Employing the ALD/MLD route, highly crystalline copper(II)terephthalate (Cu-TPA) films have been reported. If considered for low-k application, however, a significant drawback of the Cu-TPA films is the fact that they readily adsorb moisture.[160] Furthermore, a chemical vapor deposition process (MOF-CVD) has enabled high-quality films of ZIF-8 with a uniform and controlled thickness, even on high-aspect-ratio features.[161] The demonstration of vapor-phase deposition of MOF is likely to increase the interest in these materials from the IC industry.

Covalent organic frameworks (COFs) are a new class of porous covalent organic structures whose backbone is composed entirely of light elements (B, C, N, O, Si). COFs are made by combination of organic building units covalently linked into extended structures to make crystalline materials. The attainment of crystals is done by several techniques in which a balance is struck between the thermodynamic reversibility of the linking reactions and their kinetics.[162] There have been no reports investigating these materials for a low-k application but given their similarity to the MOFs in terms of porosity and crystallinity combined with the lack of any metals, the COFs might be more suitable for a low-k application than the MOFs.

1.5.4.2. Boron carbide

A recent report has investigated amorphous BC:H films for low-k application.[163] Dielectric constant values as low as 2.6 have been demonstrated. Additionally, options for further improvement of k have been proposed such as decreasing oxygen content or stiffening the lattice. Furthermore, no subtractive porosity has been introduced in the reported films and therefore, it has been suggested as a possible avenue for further lowering of k. Nevertheless, the electrical reliability seems to be severely compromised for the lowest density films since the dielectrics break below 2MV/cm. Interestingly, the YM has been measured to be as high as 126 GPa for a film with a k=3.0.

1.6. Periodic mesoporous silica-based materials

According to IUPAC, mesopore denotes the pore size range between 2 and 50 nm.[164] A significant advance in the synthesis of mesoporous materials was achieved in 1992 when Mobil scientists synthesized MCM (Mobil Composition of Matters)-41/48.[165,166] The MCM materials, in particular, are porous silicas but the reported synthesis was clearly generalizable to other matrix compositions. The extendibility was evident from the fact that the synthesis relied on surfactant self-assembly which is a universal surfactant behavior, influenced but not determined by the silica oligomers. The surfactant self-assembly and the mechanism of how it determines

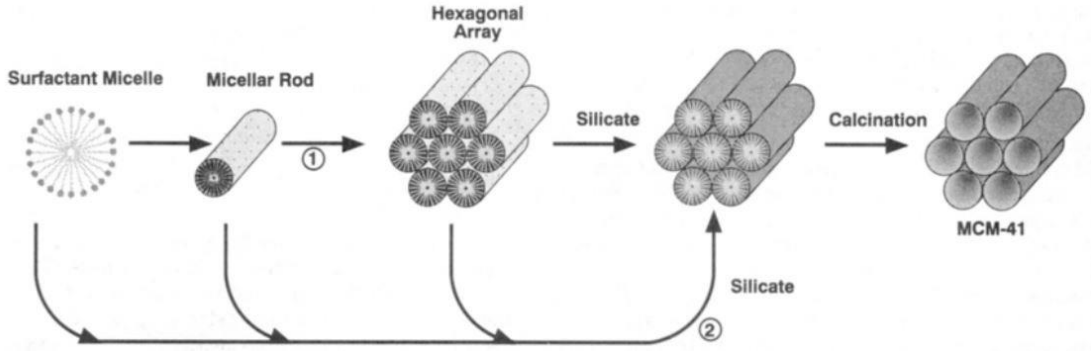

Figure 1.18. Two formation mechanisms proposed by the authors of the first periodic mesoporous silicates: 1) Surfactants organize into a liquid crystal before the addition of the silica precursor and 2) The liquid crystal forms upon the addition of the silica precursor molecules [160]

the nanostructure of the porous films will be discussed next but the ultimate result is that the surfactants form a liquid crystal surrounded by the (organo)silica polymer(s). As a result, the surfactants (more precisely, the liquid crystal formed by the surfactants) are referred to as a template or a structure-directing agent (SDA). The subsequent removal of the surfactants results in a porous film which largely inherits the nanostructure of the liquid crystal (Figure 1.18). The surfactant removal is usually accomplished via solvent extraction, burn-out or a thermal decomposition. The solvent extraction consists in washing the material with a suitable solvent which would dissolve the surfactants without affecting the organo(silica) polymers. The surfactant burn-out can be achieved in various temperatures, usually higher than 300-400°C, at ambient conditions but it is suitable only for matrix polymers which are not decomposed at these conditions, i.e. while suitable to obtain porous silica materials, this approach is not suitable for materials containing organic constituents. Finally, the thermal decomposition is similar to the burn-out but by performing the anneal in an inert atmosphere, the oxidation of the organics in the matrix is avoided.

1.6.1. Mechanism of formation: self-assembly

The tendency of surfactants to self-assemble arises from their amphiphilic character, i.e. from the fact that within the same molecule, there are (at least) two regions which respond differently to polar or nonpolar molecules with which they interact. Surfactant is an abbreviation for surface active molecule which refers to their tendency to adsorb on interfaces. The driving force for a surfactant to adsorb at an interface is to lower the free energy of that phase boundary. The interfacial free energy per unit area represents the amount of work required to expand the interface.[167] The term interfacial tension is often used instead of interfacial free energy per unit area. Thus, the surface tension of water, for instance, is the interfacial free energy per unit area of the boundary between water and the air above it. Adsorption of surfactants at that boundary reduces the surface tension. Beyond certain concentration, called critical micelle concentration (CMC), the surfactants aggregate into micelles. Micelle formation, can be viewed as an alternative mechanism for removing the lipophobic part of the surfactant from contact with the solvent,

thereby reducing the free energy of the system. Based on the mass action law model and the general relationship between the free energy change and the equilibrium constant,

$$\Delta G^0 = -RT \ln K$$

we can derive the approximate relation for micelle formation:

$$\Delta G^0 = RT \ln CMC$$

In the thermodynamic analysis of Israelachvili et al.[168] linking the molecular characteristics of the surfactant molecules to their self-assembly and in particular the critical micelle concentration, a geometric consideration establishes a link between the micelle shape and the molecular characteristics. These molecular characteristics are referred to as a surfactant packing parameter *g* and include the volume of the lipophobic tail *V*, the area of the lipophilic head a_0 which minimizes the free energy of the aggregate and the critical length l_c which the micelle radius cannot surpass where the l_c is directly dependent on the lipophobic tail length which for a hydrocarbon chain can be estimated by Tanford's formula[169] $l_c = (1.5+1.265n_c)$Å where n_c is the number of carbon atoms. The *g* parameter sets an expectation for a surfactant shape as given in Table 1.2.

Micelle shape	Surfactant packing parameter, *g*
Sphere	$\frac{V}{a_0 l_c} \simeq \frac{1}{3}$
Cylinder	$\frac{V}{a_0 l_c} \simeq \frac{1}{2}$
Planar bilayer	$\frac{V}{a_0 l_c} \simeq 1$

Table 1.2. Relationship between molecular characteristics and micelle shape

The surfactant packing into micelles can also be considered in terms of the micelle curvature which provides the possible micelle shapes and describes the transitions from one shape to another.[168] For instance, spheroids cannot accommodate amphiphiles in their regions of greatest curvature once these amphiphiles can no longer pack into spheres, i.e., once $\frac{V}{a_0 l_c}$ exceeds 1/3 excluding oblate and prolate spheres from the tenable micelle shapes. Importantly, the progression of spherical shapes observed with the increase of the surfactant concentration can be described in terms of a decreasing surface curvature of the micelles, i.e. the surface curvature decreases in the order from the spherical through the rod-like to the planar bilayer or lamellar structures.

1.6.1.1. True liquid-crystal templating

In the true liquid-crystal templating route, the concentration of the surfactant is so high that a lyotropic liquid-crystalline phase is formed. Next, the liquid crystal is infiltrated with the inorganic precursors which condense around the surfactant micelles without modifying the liquid crystal.[170,171]

1.6.1.2. Cooperative self-assembly

In the cooperative self-assembly route, surfactant concentrations may be below those necessary for obtaining liquid crystalline assemblies or even micelles. For instance, it has been shown that under the synthesis conditions reported in the pioneering work of the Mobil team, the hexagonal liquid crystal phase is not formed during the synthesis of MCM-41 and it was proposed that the formation of MCM-41 begins with the deposition of a silicate layer on the surface of isolated rodlike micelles.[172] These rods are eventually surrounded by a hexagonal silica mesostructured while heating and aging of this material complete silicate condensation. Alternatively, it was proposed that the surfactants self-assemble in a hexagonal liquid crystal upon silicate addition. Silicate species are initially organized in layers and a subsequent aging induces folding and rearrangement of the sheets around rodlike micelles leading to the MCM-41 mesostructures.[173,174] The charged silicates behave as polyelectrolytes which shift the phase boundaries of micellar systems resulting at liquid crystal phases at much lower surfactant concentrations than in pure surfactant-water systems. A third proposed mechanism, referred to as charge density matching mechanism, suggests that the MCM-41 phase might be derived from a lamellar phase which is favored by the electrostatic matching between the anionic silicate species and the cationic surfactants.[175,176] However, once the silica condensation is initiated, the negative charge density is reduced, leading to an increase of the optimal surface per polar group. This new situation leads in turn to a charge rearrangement in order to keep the electroneutrality. As a consequence, the interface begins to develop a more marked curvature, causing the lamellar to hexagonal transition. Thus, the creation of a well-defined and compatible hybrid interface between the inorganic walls and the organic templates is central to the generation of a well-ordered hybrid structure. From a kinetic perspective, the formation of an organized hybrid mesostructure is the result of the balance of two competitive processes: phase separation/organization of the template and inorganic polymerization. Two aspects are essential to fine-tune the self-assembly and the construction of the inorganic framework: the reactivity of the inorganic precursors and the interactions to generate a well-defined hybrid interface.[177]
Therefore, both surfactant and inorganic soluble species direct the synthesis of mesostructured materials. The hybrid solids thus formed are strongly dependent on the interaction between surfactants and the inorganic precursors. In the case of ionic surfactants, the formation of the mesostructured material is mainly governed by electrostatic interactions. In the simplest case, the charges of the surfactant (S) and the mineral species (I) are opposite, in the synthesis conditions. Two main direct synthesis routes have been identified: S^+I^- and S^-I^+.[178] Two other synthesis paths, considered to be indirect, also yield hybrid mesophases from the self-assembly of inorganic and surfactant species bearing the same charge: counterions get involved as charge compensating species. The $S^+X^-I^+$ path takes place under acidic conditions, in the presence of

halogenide anions (X); the $S^{-}M^{+}I^{-}$ route is characteristic of basic media, in the presence of alkaline cations (M). In the case of nonionic surfactants (N), the main interactions between the template and the inorganic species are H-bonding or dipolar, giving birth to the neutral path: $S^{0}I^{0}$,[179] $N^{0}I^{0}$,[180] and $N^{0}F\text{-}I^{+}$.[181]

As-synthesized mesostructured hybrids are often weakly condensed, which permits substantial structural evolution upon processing. Depending on the hydrothermal treatment imposed to mesostructured hybrids (temperature, pH), hexagonal (p6mm) to cubic (Ia3d),[182] hexagonal (p6mm) to lamellar,[183] or lamellar to hexagonal (p6mm)[183] transformations were observed. The transformation is mainly driven by the surfactant; as-synthesized silicate walls are still flexible enough to undergo rearrangement and follow the phase transformation. By an evaluation of the activation parameters for different paths, the effects of precondensation from the post-condensation that occurs during hydrothermal treatment have been separated. Both processes influence the characteristics of the final material and its ability to transform.

1.6.1.3. Evaporation-induced self-assembly

The true liquid-crystal templating and the cooperative self-assembly are not suitable for the deposition of highly uniform thin films. Therefore, the evaporation-induced self-assembly (EISA) has been developed by Brinker's group (Figure 1.19).[184,185] In the EISA approach, an excess of a volatile solvent is used to ensure that the surfactant concentration in the solution remains below the CMC. Additionally, the solution must consist of solvents and reactants which are volatile. Since less condensed entities (small and mobile) are preferred during self-assembly, conditions which favor hydrolysis but hinder condensation of the inorganic species are essential.

Through variation of the initial alcohol/water/surfactant/matrix precursor mole ratio it is possible to follow different trajectories in composition space and to arrive at different final mesostructures.[185] Upon addition of the solution to the substrate, the preferential evaporation of the volatile solvent during dip- or spin-coating concentrates the depositing film in nonvolatile

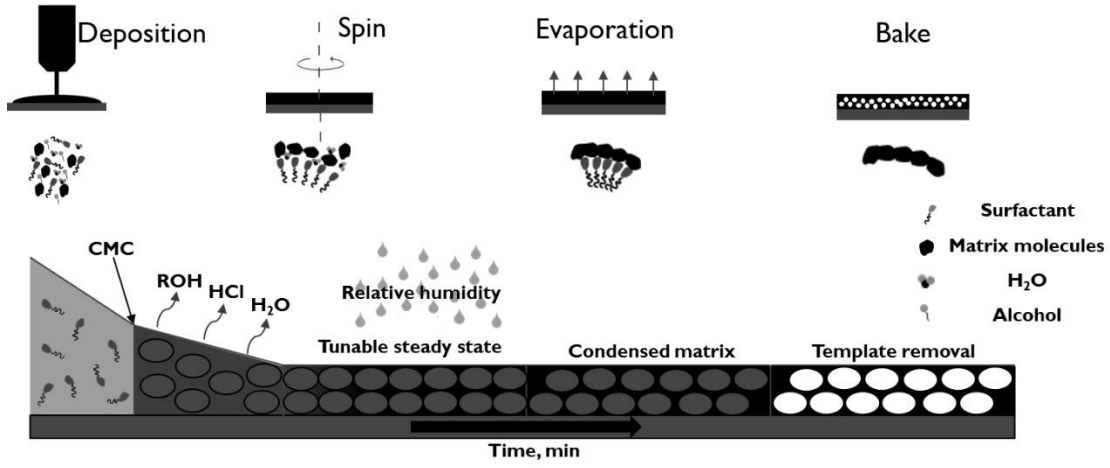

Figure 1.19. Formation of periodic mesoporous films via evaporation-induced self-assembly (EISA)

surfactant and silica species. The evaporation of the volatile species is one of the main parameters that governs the entire film-formation process. When the surfactant concentration reaches the equivalent of the CMC for the system, micelles start to form. Eventually, an organized mesostructure film is obtained. The main challenge of the EISA compared to the previously described precipitation methods is that it is a mainly kinetically governed mechanism that requires a high control on the processing conditions, and it can lead to metastable hybrid materials that require additional steps to be stabilized. The quality of the final mesostructure is thus highly dependent on the processing conditions and more especially on the atmosphere composition (water and solvent relative pressures) since the latter defines the evaporation rate and the system content in water and solvent at equilibrium. This latter stage of pseudo equilibrium, where the inorganic framework is poorly condensed, is referred to as a Tunable Steady State (TSS).[186,187] It can last from a few seconds to a few hours for fast or slow condensing inorganic phases respectively.[187] It is during the TSS that a change in the atmosphere composition results in a modification of the film composition involving potentially a modification of the mesostructure.

1.6.2. Periodic mesoporous silica films for low-k

Employing nonionic surfactants such as poly(alkyleneoxide) triblock copolymers and long-chain alkane oligo(ethylene oxide) materials, highly ordered silica films with k values of 2.1 and lower have been described.[188] The films varied in porosity and pore diameter from 51 to 75% and 3.4 to 9.0 nm, respectively, depending on the type of surfactant. Nevertheless, the stability of the reported dielectric constant with exposure to the ambient conditions and in particular water adsorption was not investigated. Clearly, a hydrophobization step is crucial before the periodic mesoporous silica films can be considered for a low-k application. Films calcined at 600 °C in air and then treated with HMDS at 160°C to render the pore surface more hydrophobic exhibited porosities ranging from 50 to 90% and dielectric constants of 2.6 or less.[189] A dielectric constant as low as 1.42 at 1 MHz was reported using Pluronic P123 as a templating agent following an in-situ hydrophobization with TMCS.[190] The Si-CH_3 groups in the silylated PMS films has been shown to be stable up to 400-450°C which is acceptable for a microelectronics application.[191] Unfortunately, the reported pore sizes are much too large for a low-k application. When Brij-76 is employed as a templating agent, films with a pore size of ca. 3 nm are usually obtained.[192] A Brij-76-templated PMS film has been reported which after a calcination at 500°C had a porosity of 39% with an elastic modulus of 14.4, a dielectric constant of 2.55 and a leakage current density less than 2×10^{-6} A/cm^2 up to 1.6MV/cm.[193] Changing the Brij-76 to TEOS molar ratio, and as a result the pore volume of the PMS, affects the pore ordering while an aging period of 20 days before spin coating destroys the pore ordering.[194]

In order to reduce the shrinkage characteristic of sol-gel films, a vapor infiltration treatment at 150°C for 1h has been developed. In this method, an ordered mesoporous silica film is first prepared by spin-coating a solution containing TEOS and a nonionic surfactant. Then, a vapor infiltration treatment is performed using TEOS or trimethylethoxysilane (TMES). The vapor infiltration treatments effectively improve mechanical strength and hydrothermal stability. While the non-treated film contracts by 34%, the densified silica wall as a result of the penetration of TEOS or TMES molecules has a high structural stability and hardly contracts under a calcination process, <5%. The TMES-treated films have better hydrothermal stability as compared to those treated with TEOS vapors due to the higher hydrophobicity imparted by the trimethylsilyl groups incorporated in the silica walls. The dielectric constant of the TMES-treated mesoporous silica film was 1.8. The pore size of 3 nm seems more suitable for a low-k application.[195] Similarly, a vapor phase method using TEOS for the preparation of mesostructured silica films and TMES in a post-synthesis treatment has been developed. In this approach, the surfactant is spin-coated and consequently exposed to the silicate precursors from a vapor-phase at 90°C for 90 min. The dielectric constant of the TMES-treated mesoporous silica film has been reported to be 1.5–1.7.[196] Unfortunately, elastic modulus was not reported in these studies.

Another approach to ensure the hydrophobicity of the PMS films includes the use of an additional matrix precursor which contains a Si-CH_3 group(s) such as the methyltrialkoxysilanes. For films derived from MTMS/TEOS > 1, no significant presence of residual silanol groups can be seen in FTIR spectra.[134] Nevertheless, it has been shown that the co-condensation of TEOS and MTES results in a reduced pore order when the molar amount of the MTES is increased with respect to TEOS. For instance, while PMS can be obtained when only TEOS is employed, when the MTES/TEOS ratio is 0.1, no pore organization is observed.[197] In different synthesis conditions, the pore order is lost when the MTMS/TEOS ratio increases beyond 0.33.[133] This effect has been explained with the significantly faster polycondensation of MTES which results in oligomers not suitable to obtain a PMS film. However, well ordered PMS films can still be obtained using the MTES if the solution aging is optimized, i.e. the solution needs to be deposited sooner than if only TEOS was employed. Following the latter approach, it was shown that ordered PMS films can be obtained even at a MTES/TEOS ratio of 0.25.[197] As a result, a film with a cubic pore organization, a dielectric constant of 2.32 and a Young's modulus higher than 15 GPa has been demonstrated.[198] In spite of an the crystallinity of the silica walls, much lower mechanical properties were reported when cetyltrimethylammonium bromide (CTAB) was employed as an SDA with YM of 1.5 GPa at a dielectric constant of 2.0.[134]

1.6.3. Periodic mesoporous organosilica films for low-k

Periodic mesoporous organosilica (PMO) materials were discovered in 1999 by three different groups.[199–201] PMOs are a class of organic–inorganic nanocomposites based on silsesquioxane precursors containing an organic bridge between two Si atoms, $(EtO)_3Si–R–Si(OEt)_3$. From a low-k application perspective, an important feature of PMO materials is their ability to undergo self-hydrophobization - a silanol-consuming transformation of bridging methylene to terminal methyl groups.[202] The reaction, shown schematically in Figure 1.20, has been observed at a temperature higher than 300°C and involves the transfer of a proton from a silanol to a bridging group, to break a Si-R-Si bridge and simultaneously create a new Si-O-Si bridge. Ozin et al. elaborately described the preparation of thin films consisting of methane-, ethane-, or ring-PMOs, the latter of which is a multi-organic bridged organosilica made out of interconnected $[Si(CH_2)]_3$ rings.[203,204] They showed that the dielectric constant of the films decreases while the Young's modulus and hardness increase with substitution of the bridged silsesquioxane for silica in the framework.[204] Furthermore, the measured dielectric constants, after removal of the surfactant at 300°C are 2.9, 2.9 and 2.5 for porous methylene, ethylene and the ring PMO, respectively, while the corresponding elastic moduli are 12.7, 13.3 and 11.8 GPa. Interestingly, methylene and ring PMO films treated at 400°C exhibit a lower k compared with the ones treated at 300°C, suggesting that the self-hydrophobization is beneficial to the dielectric properties of the films. The effect of the thermal treatment on the hydrophilicity of methylene PMO samples was also studied.[205] Water adsorption isotherms and water contact angles of methane-, ethane-, ethene- and ring-PMO films post-treated at different temperatures, from 300°C to 500°C were reported. Following anneals at temperatures above 400°C, the ring- and methane-PMOs are the most hydrophobic due to the self-hydrophobization process. Another type of interesting PMO material for low-k was obtained by employing a polyhedral oligomeric silsesquioxane (POSS) precursor. The resulting PMO possesses air pockets in the pore walls which resulted in a k-value of 1.7.[206] A PMO film templated by a non-ionic surfactant, Brij-76, has also been reported. The non-ionic surfactant is believed to be more compatible with chip manufacturing. The ring PMO was shown to have a high chemical stability at pH=14.[207] In

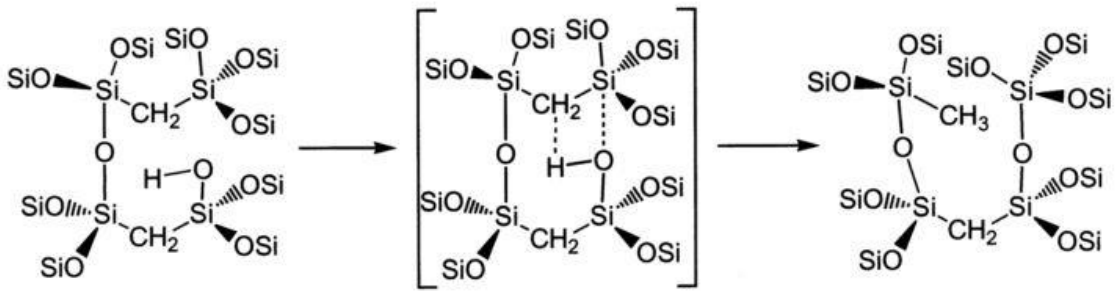

Figure 1.20. Self-hydrophobization reaction consists of a transformation of a bridging methylene into a terminal methyl in the presence of silanol groups[202]

another study where a non-ionic surfactant, BrijL4, was employed, extremely low k value of 1.58 with a very good YM of 5.5 GPa was reported.[208] Furthermore, the viability of a vapor-phase PMO deposition has been demonstrated by a vacuum-assisted aerosol deposition in which the aerosol is generated by atomizing a solution of PMO precursors, surfactant, and water in a chosen organic solvent. Evaporation of the solvent induces self-assembly inside the aerosol droplets. Then, the aerosol is deposited through a converging nozzle on a spinning substrate forming a thin film.[209] Ethane-PMO films with ultra-low k values and high mechanical stabilities were synthesized by this deposition technique.

1.7. Goal of the PhD research

The main goal of this research has been the development and evaluation of self-assembly-based mesoporous organosilicate films for low-k dielectrics application. More specifically, the focus has been on quantifying in a reliable way the most popular approaches for improving the mechanical properties of the low-k films, in particular, the Young's modulus (YM). The popular approaches for improving the YM are the introduction of bridging alkylene groups in the silica matrix, the UV cure, and the control of the pore arrangement. The alkylene-bridged organosilicates have gained the interest of the low-k community because they enable the incorporation of carbon in the film's matrix without compromising the matrix connectivity. The high carbon content in silica-based low-k materials is important for a good chemical stability required during the chip manufacturing. However, the impact of the replacement of siloxane (Si-O-Si) bonds by bridging alkylene (Si-$(CH_2)_n$-Si) groups on the YM had not been established experimentally in a reliable way. In terms of additional improvement of the YM, one established approach is the UV cure but its impact on the bridging alkylene groups was not known. A newer approach is a laser anneal treatment whose impact on the organic part of the low-k had been the biggest concern. On the other hand, theoretical work has shown that control over the pore structure of the porous films could enable optimization of the mechanical properties. Therefore, this work has aimed at establishing experimentally the benefits of employing PMO films as low-k dielectrics. However, there has been very limited number of PMO films reported in literature. Additionally, all of the reported PMO films possess the same pore organization, the 2D hexagonal, which results in films with anisotropic properties and, according to the theoretical work, suboptimal Young's modulus. Therefore, there was a need to expand the portfolio of PMO films and in particular, to obtain films with a pore organization different than the 2D hexagonal. The mesostructures identified to be the most promising are the body-centred cubical and the 3D hexagonal. Two strategies which could lead to new PMOs were identified. In the first strategy, a new PMO could be synthesized by choosing a surfactant with a suitable packing parameter. In the second, the surfactant self-assembly could be influenced by controlling the ambient conditions during the

PMO deposition. An additional issue which was recognized in the majority of the reported PMO films was that they were templated by ionic surfactants which, however, have been asserted to be unsuitable for low-k application. Still, the PMO films templated by ionic surfactants have the smallest pore size of about 2 nm which is considered to be the higher limit for the pore size of a low-k film suitable for future generation chips. Therefore, it was important to obtain empirical evidence for the effect of the ionic surfactants on the electrical low-k properties, in particular, the leakage current density and the dielectric breakdown field.

1.8. References

[1] S. J. Smith, https://newsroom.intel.com/newsroom/wp-content/uploads/sites/11/2017/03/Stacy-Smith-2017-Manufacturing.pdf **2017**.

[2] M. Kaku, *PHYSICS OF THE FUTURE*; 2012; Vol. 53.

[3] Lars Blackmore, *Front. Eng.* **2016**, *4*, 15.

[4] Understanding Bioinformatics and Sequencing - National Human Genome Research Institute, https://www.genome.gov/25019999/understanding-bioinformatics-and-sequencing/.

[5] C. C. M. Mody, *The long arm of Moore's law : Microelectronics and American science*; MIT Press, 2017.

[6] G. E. Moore, *Electronics* **1965**, *38*.

[7] Gordon E. Moore, *IEDM Tech. Dig.* **1975**, 11.

[8] Inside Volta: The World's Most Advanced Data Center GPU, https://devblogs.nvidia.com/parallelforall/inside-volta/.

[9] Samsung 10 nm LPE Process, http://www.techinsights.com/technology-intelligence/overview/latest-reports/samsung-10-nm-LPE-process/.

[10] 10nm Rollout Marching Right Along, http://www.techinsights.com/about-techinsights/overview/blog/10nm-rollout-marching-right-along/.

[11] Leading at the Edge: Intel Technology and Manufacturing, https://newsroom.intel.com/press-kits/leading-edge-intel-technology-manufacturing/#leading-at-the-edge-intel-technology-and-manufacturing.

[12] D. Hisamoto, W. C. Lee, J. Kedzierski, H. Takeuchi, K. Asano, C. Kuo, E. Anderson, T. J. King, J. Jeffrey, C. Hu, *IEEE Trans. Electron Devices* **2000**, *47*, 2320.

[13] M. Baklanov, K. Maex, M. Green, *Dielectric Films for Advanced Microelectronics*; Baklanov, M. R.; Green, M. L.; Maex, K., Eds.; John Wiley & Sons, Ltd: Chichester, UK, 2007.

[14] D. Edelstein, J. Heidenreich, R. Goldblatt, W. Cote, C. Uzoh, N. Lustig, P. Roper, T.

McDevitt, W. Motsiff, A. Simon, J. Dukovic, R. Wachnik, H. Rathore, R. Schulz, L. Su, S. Luce, J. Slattery, *Electron Devices Meet. 1997. IEDM '97. Tech. Dig. Int.* **1997**, *4*, 773.

[15] W. Volksen, R. D. Miller, G. Dubois, *Chem. Rev.* **2010**, *110*, 56.

[16] G. Dubois, W. Volksen, In *Advanced Interconnects for ULSI Technology*; John Wiley & Sons, Ltd: Chichester, UK, 2012; pp. 1–33.

[17] B. El-Kareh, *Fundamentals of semiconductor processing technologies*; Kluwer Academic Publishers, 1995.

[18] *National Technology Roadmap for Semiconductors, Semiconductor Industry Association*; 1994.

[19] K. Fischer, M. Agostinelli, C. Allen, D. Bahr, M. Bost, P. Charvat, V. Chikarmane, Q. Fu, C. Ganpule, M. Haran, M. Heckscher, H. Hiramatsu, E. Hwang, P. Jain, I. Jin, R. Kasim, S. Kosaraju, K. S. Lee, H. Liu, R. McFadden, S. Nigam, R. Patel, C. Pelto, P. Plekhanov, M. Prince, C. Puls, S. Rajamani, D. Rao, P. Reese, A. Rosenbaum, S. Sivakumar, B. Song, M. Uncuer, S. Williams, M. Yang, P. Yashar, S. Natarajan, In *2015 IEEE International Interconnect Technology Conference and 2015 IEEE Materials for Advanced Metallization Conference, IITC/MAM 2015*; IEEE, 2015; pp. 5–7.

[20] K. Maex, M. R. Baklanov, D. Shamiryan, F. Iacopi, S. H. Brongersma, Z. S. Yanovitskaya, *J. Appl. Phys.* **2003**, *93*, 8793.

[21] P. S. Ho, J. Leu, W. W. Lee, *Low Dielectric Constant Materials for IC Applications*; Ho, P. S.; Leu, J.; Lee, W. W., Eds.; Springer-Verlag Berlin Heidelberg 2003, 2003.

[22] H. Yang, G. Lucovsky, *J. Non. Cryst. Solids* **1999**, *254*, 128.

[23] M. J. Loboda, *Microelectron. Eng.* **2000**, *50*, 15.

[24] D. G. Shamiryan, M. R. Baklanov, S. Vanhaelemeersch, K. Maex, *Electrochem. Solid-State Lett.* **2001**, *4*, F3.

[25] D. D. Burkey, K. K. Gleason, *J. Appl. Phys.* **2003**, *93*, 5143.

[26] J. Lubguban, T. Rajagopalan, N. Mehta, B. Lahlouh, S. L. Simon, S. Gangopadhyay, *J. Appl. Phys.* **2002**, *92*, 1033.

[27] J. Rouquerolt, D. Avnir, C. W. Fairbridge, D. H. Everett, J. H. Haynes, N. Pernicone, J. D. F. Ramsay, K. S. W. Sing, K. K. Unger, *Pure Appl. Chem.* **1994**, *66*, 1739.

[28] V. Jousseaume, A. Zenasni, O. Gourhant, L. Favennec, M. R. Baklanov, *Adv. Interconnects ULSI Technol.* **2012**, 35.

[29] M. R. Baklanov, L. Zhao, E. Van Besien, M. Pantouvaki, *Microelectron. Eng.* **2011**, *88*, 990.

[30] A. Grill, S. M. Gates, T. E. Ryan, S. V. Nguyen, D. Priyadarshini, *Appl. Phys. Rev.* **2014**, *1*, 11306.

[31] S. M. Gates, G. Dubois, E. T. Ryan, A. Grill, M. Liu, D. Gidley, *J. Electrochem. Soc.* **2009**, *156*, G156.

[32] S. Balakrishnan, R. Brain, L. Zhao, In *Advanced Interconnects for ULSI Technology*; John Wiley & Sons, Ltd: Chichester, UK, 2012; pp. 235–265.

[33] H. Zahedmanesh, M. Gonzalez, I. Ciofi, K. Croes, J. Bömmels, Z. Tokei, *Microelectron. Eng.* **2015**, *156*, 70.

[34] H. Zahedmanesh, P. R. Besser, C. J. Wilson, K. Croes, *J. Appl. Phys.* **2016**, *120*.

[35] D. Priyadarshini, S. Nguyen, H. Shobha, S. Cohen, T. Shaw, E. Liniger, C. K. Hu, C. Parks, E. Adams, J. Burnham, A. H. Simon, G. Bonilla, A. Grill, D. Canaperi, D. Edelstein, D. Collins, M. Balseanu, M. Stolfi, J. Ren, K. Shah, In *2014 IEEE International Interconnect Technology Conference / Advanced Metallization Conference, IITC/AMC 2014*; IEEE, 2014; pp. 185–188.

[36] A. Castex, L. Favennec, V. Jousseaume, J. Bruat, J. Deval, B. Remiat, G. Passemard, M. Pons, *Microelectron. Eng.* **2005**, *82*, 416.

[37] M. O'Neill, M. K. Haas, B. K. Peterson, R. N. Vrtis, S. J. Weigel, D. Wu, M. D. Bitner, E. J. Karwacki, *MRS Proc.* **2011**, *914*, 914.

[38] A. Grill, *Annu. Rev Mater. Res.* **2009**, *39*, 49.

[39] W. Lee, T. H. Kim, Y. Choa, *Korean J. Mater. Res.* **2016**, *26*, 427.

[40] W. Lee, A. Fukazawa, Y. Choa, *Korean J. Mater. Res.* **2016**, *26*, 455.

[41] D. J. Michalak, J. M. Blackwell, J. M. Torres, A. Sengupta, L. E. Kreno, J. S. Clarke, D. Pantuso, *J. Mater. Res.* **2015**, *30*, 3363.

[42] J. El Sabahy, G. Castellan, F. Ricoul, V. Jousseaume, *J. Phys. Chem. C* **2016**, acs. jpcc.6b00204.

[43] N. Sahu, B. Parija, S. Panigrahi, *Indian J. Phys.* **2009**, *83*, 493.

[44] C. J. Brinker, G. W. Scherer, In *Sol-Gel Science*; 1990; pp. 786–837.

[45] D. E. Bornside, C. W. Macosko, L. E. Scriven, *J. Appl. Phys.* **1989**, *66*, 5185.

[46] D. Meyerhofer, *J. Appl. Phys.* **1978**, *49*, 3993.

[47] D. B. Hall, P. Underhill, J. M. Torkelson, *Polym. Eng. Sci.* **1998**, *38*, 2039.

[48] C. J. Brinker, A. J. Hurd, P. R. Schunk, G. C. Frye, C. S. Ashley, *J. Non. Cryst. Solids* **1992**, *147–148*, 424.

[49] C. Brinker, G. Scherer, *Sol-gel science: the physics and chemistry of sol-gel processing*; 1990.

[50] D. E. Haas, J. N. Quijada, S. J. Picone, D. P. Birnie III, *Proc. SPIE - Int. Soc. Opt. Eng.* **2003**, *3943*, 280.

[51] X. Min, X. Orignac, R. M. Almeida, *J. Am. Ceram. Soc.* **1995**, *78*, 2254.

[52] B. K. Daniels, C. R. Szmanda, M. K. Templeton, P. Trefonas III, In *1986 Microlithography Conferences*; Willson, C. G., Ed.; 1986; pp. 192–201.

[53] M. H. Eres, D. E. Weidner, L. W. Schwartz, *Langmuir* **1999**, *15*, 1859.

[54] N. Zhang, D. F. Chao, *Int. Commun. Heat Mass Transf.* **1999**, *26*, 1069.

[55] L. E. SCRIVEN, C. V. STERNLING, *Nature* **1960**, *187*, 186.

[56] H. Kozuka, Y. Ishikawa, N. Ashibe, *J. Sol-Gel Sci. Technol.* **2004**, *31*, 245.

[57] S. B. Jung, T. J. Ha, H. H. Park, *J. Appl. Phys.* **2007**, *101*, 24109.

[58] M. R. Baklanov, K. Maex, *Philos. Trans. A. Math. Phys. Eng. Sci.* **2006**, *364*, 201.

[59] Y. Toivola, J. Thurn, R. F. Cook, *J. Electrochem. Soc.* **2002**, *149*, F9.

[60] R. A. Donaton, F. Iacopi, R. Baklanov, D. Shamiryan, B. Coenegrachts, H. Struyf, M. Lepage, M. Meuris, M. Van Hove, W. D. Gray, H. Meynen, D. De Roest, S. Vanhaelemeersch, K. Maex, *Proc. IEEE 2000 Int. Interconnect Technol. Conf. (Cat. No.00EX407)* **2000**, 93.

[61] F. Iacopi, M. R. Baklanov, E. Sleeckx, T. Conard, H. Bender, H. Meynen, K. Maex, *J. Vac. Sci. Technol. B Microelectron. Nanom. Struct.* **2002**, *20*, 109.

[62] M. G. Albrecht, *J. Electrochem. Soc.* **1998**, *145*, 4019.

[63] Y. K. Siew, G. Sarkar, X. Hu, J. Hui, A. See, C. T. Chua, *J. Electrochem. Soc.* **2000**, *147*, 335.

[64] S. Choi, M. J. Word, V. Kumar, I. Adesida, *J. Vac. Sci. Technol. B Microelectron. Nanom. Struct.* **2008**, *26*, 1654.

[65] R. F. Cook, E. G. Liniger, *J. Electrochem. Soc.* **1999**, *146*, 4439.

[66] L. W. Hrubesh, L. E. Keene, V. R. Latorre, *J. Mater. Res.* **1993**, *8*, 1736.

[67] M.-H. Jo, J.-K. Hong, H.-H. Park, J.-J. Kim, S.-H. Hyun, S.-Y. Choi, *Thin Solid Films* **1997**, *308–309*, 490.

[68] M.-H. Jo, H.-H. Park, D.-J. Kim, S.-H. Hyun, S.-Y. Choi, J.-T. Paik, *J. Appl. Phys.* **1997**, *82*, 1299.

[69] S.-B. Jung, H.-H. Park, *Thin Solid Films* **2002**, *420–421*, 503.

[70] C. J. Brinker, G. W. Scherer, In *Sol-Gel Science*; 1990; pp. 514–615.

[71] C. Jin, S. List, S. Yamanaka, W. W. Lee, K. Taylor, W.-Y. Hsu, L. Olsen, J. D. Luttmer, R. Havemann, D. Smith, T. Ramos, A. Maskara, *MRS Proc.* **1996**, *443*, 99.

[72] C. C. Cho, D. M. Smith, J. Anderson, *Mater. Chem. Phys.* **1995**, *42*, 91.

[73] A. Jain, S. Rogojevic, S. V. Nitta, V. Pisupatti, W. N. Gill, P. C. Wayner, J. L. Plawsky, T. E. F. M. Standaert, G. S. Oehrlein, *MRS Proc.* **1999**, *565*, 29.

[74] A. Jain, S. Rogojevic, F. Wang, W. N. Gill, P. C. Wayner, J. L. Plawsky, A. Haberl, W. Lanford,

MRS Proc. **2000**, *612*, D5.25.1.

[75] S. Yu, T. K. S. Wong, K. Pita, X. Hu, V. Ligatchev, *J. Appl. Phys.* **2002**, *92*, 3338.

[76] R. Saxena, O. Rodriguez, W. Cho, W. N. Gill, J. L. Plawsky, M. R. Baklanov, K. P. Mogilnikov, *J. Non. Cryst. Solids* **2004**, *349*, 189.

[77] A. Jain, S. Rogojevic, W. N. Gill, J. L. Plawsky, I. Matthew, M. Tomozawa, E. Simonyi, *J. Appl. Phys.* **2001**, *90*, 5832.

[78] D. M. Smith, J. Anderson, C. C. Cho, G. P. Johnston, S. P. Jeng, *MRS Proc.* **1995**, *381*, 261.

[79] Z. W. He, C. M. Zhen, X. Q. Liu, W. Lan, D. Y. Xu, Y. Y. Wang, *Thin Solid Films* **2004**, *462–463*, 168.

[80] C. Murray, C. Flannery, I. Streiter, S. E. Schulz, M. R. Baklanov, K. P. Mogilnikov, C. Himcinschi, M. Friedrich, D. R. T. Zahn, T. Gessner, *Microelectron. Eng.* **2002**, *60*, 133.

[81] S. Lin, L. Lui, M. Daniels, A. Gonzalez, J. T. Wetzel, K. A. Monnig, P. A. Winebarger, S. Jang, D. Yu, M. S. Liang, In *Proceedings of the IEEE 2001 International Interconnect Technology Conference (Cat. No.01EX461)*; IEEE, 2001; pp. 146–148.

[82] B. R. Murthy, C. K. Chang, Ahilakrishnamoorthy, Y. W. Chen, A. Naman, *MRS Proc.* **2004**, *812*, F6.6.

[83] M. E. Davis, R. F. Lobo, *Chem. Mater.* **1992**, *4*, 756.

[84] E. M. Flanigen, J. M. Bennett, R. W. Grose, J. P. Cohen, R. L. Patton, R. M. Kirchner, J. V. Smith, *Nature* **1978**, *271*, 512.

[85] D. M. BIBBY, N. B. MILESTONE, L. P. ALDRIDGE, *Nature* **1979**, *280*, 664.

[86] Z. Li, M. C. Johnson, M. Sun, E. T. Ryan, D. J. Earl, W. Maichen, J. I. Martin, S. Li, C. M. Lew, J. Wang, M. W. Deem, M. E. Davis, Y. Yan, *Angew. Chemie* **2006**, *118*, 6477.

[87] Z. Wang, H. Wang, A. Mitra, L. Huang, Y. Yan, *Adv. Mater.* **2001**, *13*, 746.

[88] R. Tiriolo, N. Rangnekar, H. Zhang, M. Shete, P. Bai, J. Nelson, E. Karapetrova, C. W. Macosko, J. I. Siepmann, E. Lamanna, A. Lavano, M. Tsapatsis, *Adv. Funct. Mater.* **2017**, *1700864*, 1.

[89] T. Seo, T. Yoshino, Y. Cho, N. Hata, T. Kikkawa, *Japanese J. Appl. Physics, Part 1 Regul. Pap. Short Notes Rev. Pap.* **2007**, *46*, 5742.

[90] S. Eslava, M. R. Baklanov, C. E. a Kirschhock, F. Iacopi, S. Aldea, K. Maex, J. a. Martens, *Langmuir* **2007**, *23*, 12811.

[91] S. Eslava, C. E. A. Kirschhock, S. Aldea, M. R. Baklanov, F. Iacopi, K. Maex, J. A. Martens, *Microporous Mesoporous Mater.* **2009**, *118*, 458.

[92] L. Hu, J. Wang, Z. Li, S. Li, Y. Yan, *J. Mater. Res.* **2006**, *21*, 505.

[93] S. Eslava, M. R. Baklanov, A. V. Neimark, F. Iacopi, C. E. a Kirschhock, K. Maex, J. a.

Martens, *Adv. Mater.* **2008**, *20*, 3110.

[94] Z. B. Wang, A. Mitra, H. T. Wang, L. M. Huang, Y. Yan, *Adv. Mater.* **2001**, *13*, 1463.

[95] T. Seo, T. Yoshino, N. Ohnuki, Y. Seino, Y. Cho, N. Hata, T. Kikkawa, *J. Electrochem. Soc.* **2011**, *158*, H659.

[96] S. Eslava, S. Delahaye, M. R. Baklanov, F. Iacopi, C. E. A. Kirschhock, K. Maex, J. A. Martens, *Langmuir* **2008**, *24*, 4894.

[97] T. Yoshino, N. Ohnuki, N. Hata, Y. Seino, *Jpn. J. Appl. Phys.* **2009**, *48*, 50210.

[98] T. Sato, T. Yamamoto, Y. Hata, Y. Seino, Y. Kayaba, S.-I. Kuroki, T. Kikkawa, *ECS J. Solid State Sci. Technol.* **2013**, *2*, N89.

[99] S. Eslava, F. Iacopi, M. R. Baklanov, C. E. a Kirschhock, K. Maex, J. a. Martens, *J. Am. Chem. Soc.* **2007**, *129*, 9288.

[100] S. Li, Z. Li, Y. Yan, *Adv. Mater.* **2003**, *15*, 1528.

[101] T.-Y. Li, C.-Y. Chang, B.-Z. Wan, *Thin Solid Films* **2014**, *562*, 513.

[102] Y. Zhu, T. E. Müller, J. A. Lercher, *Adv. Funct. Mater.* **2008**, *18*, 3427.

[103] K. Yamamoto, Y. Sakata, Y. Nohara, Y. Takahashi, T. Tatsumi, *Science* **2003**, *300*, 470.

[104] R. Poloni, J. Kim, *J. Mater. Chem. C* **2014**, *2*, 2298.

[105] R. Farrell, T. Goshal, U. Cvelbar, N. Petkov, M. A. Morris, *Interface Mag.* **2011**, *20*, 39.

[106] S. J. Martin, J. P. Godschalx, M. E. Mills, E. O. Shaffer II, P. H. Townsend, *Adv. Mater.* **2000**, *12*, 1769.

[107] Q. J. Niu, S. J. Martin, J. P. Godschalx, P. H. Townsend, In *ACS Symp. Ser.*; 2004; pp. 199–208.

[108] M. S. Silverstein, B. J. Bauer, R. C. Hedden, H. Lee, B. G. Landes, *Macromolecules* **2006**, *39*, 2998.

[109] M. S. Silverstein, M. Shach-Caplan, B. J. Bauer, R. C. Hedden, H. Lee, B. G. Landes, *Macromolecules* **2005**, *38*, 4301.

[110] Y. Chen, L. Chen, X. Wang, X. He, *Macromol. Chem. Phys.* **2005**, *206*, 2483.

[111] S.-G. Park, S.-W. Rhee, *J. Vac. Sci. Technol. A Vacuum, Surfaces, Film.* **2006**, *24*, 291.

[112] V. Jousseaume, A. Zenasni, L. Favennec, G. Gerbaud, M. Bardet, J. P. Simon, A. Humbert, *J. Electrochem. Soc.* **2007**, *154*, G103.

[113] A. Zenasni, V. Jousseaume, P. Holliger, L. Favennec, O. Gourhant, P. Maury, G. Gerbaud, *J. Appl. Phys.* **2007**, *102*, 94107.

[114] A. Zenasni, V. Jousseaume, O. Gourhant, L. Favennec, P. Maury, *Microelectron. Eng.* **2008**, *85*, 2102.

[115] J. A. Lubguban, J. Sun, T. Rajagopalan, B. Lahlouh, S. L. Simon, S. Gangopadhyay, *Appl.*

Phys. Lett. **2002**, *81*, 4407.

[116] A. Grill, V. Patel, *Appl. Phys. Lett.* **2001**, *79*, 803.

[117] A. Grill, *J. Appl. Phys.* **2003**, *93*, 1785.

[118] C. Guedj, G. Imbert, E. Martinez, C. Licitra, N. Rochat, V. Arnal, *Microelectron. Reliab.* **2007**, *47*, 764.

[119] a. M. Urbanowicz, B. Meshman, D. Schneider, M. R. Baklanov, *Phys. Status Solidi* **2008**, *205*, 829.

[120] L. Prager, P. Marsik, L. Wennrich, M. R. Baklanov, S. Naumov, L. Pistol, D. Schneider, J. W. Gerlach, P. Verdonck, M. R. Buchmeiser, *Microelectron. Eng.* **2008**, *85*, 2094.

[121] D. D. Burkey, K. K. Gleason, *J. Electrochem. Soc.* **2004**, *151*, F105.

[122] M. S. . K. Y.-H. . K. H. J. . L. Y. . Kim J.Y.a Hwang, *J. Appl. Phys.* **2001**, *90*, 2469.

[123] P. T. Hurley, L.-S. Du, P. L. McDaniel, B. K. Peterson, S. J. Weigel, M. K. Haas, R. N. Vrtis, D. Sinatore, M. D. Bitner, K. E. Theodorou, M. L. O'Neill, *Mater. Res. Soc. Symp. Proc.* **2007**, *990*, 3.

[124] a. Grill, V. Patel, K. P. Rodbell, E. Huang, M. R. Baklanov, K. P. Mogilnikov, M. Toney, H.-C. Kim, *J. Appl. Phys.* **2003**, *94*, 3427.

[125] V. Jousseaume, L. Favennec, A. Zenasni, O. Gourhant, *Surf. Coatings Technol.* **2007**, *201*, 9248.

[126] A. Grill, V. Patel, *J. Appl. Phys.* **2008**, *104*, 24113.

[127] A. Grill, *J. Vac. Sci. Technol. B* **2016**, *34*, 20801.

[128] S. M. Gates, D. a. Neumayer, M. H. Sherwood, A. Grill, X. Wang, M. Sankarapandian, *J. Appl. Phys.* **2007**, *101*, 94103.

[129] C. Wu, Y. Li, M. R. Baklanov, K. Croes, *ECS J. Solid State Sci. Technol.* **2014**, *4*, N3065.

[130] G. Gerbaud, S. Hediger, M. Bardet, L. Favennec, A. Zenasni, J. Beynet, O. Gourhant, V. Jousseaume, *Phys. Chem. Chem. Phys.* **2009**, *11*, 9729.

[131] A. M. Urbanowicz, K. Vanstreels, P. Verdonck, D. Shamiryan, S. De Gendt, M. R. Baklanov, *J. Appl. Phys.* **2010**, *107*, 104122.

[132] G. Carlotti, P. Colpani, D. Piccolo, S. Santucci, V. Senez, G. Socino, L. Verdini, **2002**, *414*, 99.

[133] A. Balkenende, F. K. de Theije, J. C. K. Kriege, *Adv. Mater.* **2003**, *15*, 139.

[134] F. K. de Theije, A. R. Balkenende, M. A. Verheijen, M. R. Baklanov, K. P. Mogilnikov, Y. Furukawa, *J. Phys. Chem. B* **2003**, *107*, 4280.

[135] S. Eslava, M. R. Baklanov, J. Urrutia, C. E. A. Kirschhock, K. Maex, J. A. Martens, *Adv. Funct. Mater.* **2008**, *18*, 3332.

[136] C. J. Brinker, G. W. Scherer, *Sol-Gel Sci.* **1990**, 96.

[137] W. Stöber, A. Fink, E. Bohn, *J. Colloid Interface Sci.* **1968**, *26*, 62.

[138] D. a Loy, K. J. Shea, *Chem. Rev.* **1995**, *95*, 1431.

[139] G. Dubois, W. Volksen, T. Magbitang, R. D. Miller, D. M. Gage, R. H. Dauskardt, *Adv. Mater.* **2007**, *19*, 3989.

[140] G. Dubois, W. Volksen, T. Magbitang, M. H. Sherwood, R. D. Miller, D. M. Gage, R. H. Dauskardt, *J. Sol-Gel Sci. Technol.* **2008**, *48*, 187.

[141] J. S. Rathore, L. V. Interrante, G. Dubois, *Adv. Funct. Mater.* **2008**, *18*, 4022.

[142] N. Tajima, T. Ohno, T. Hamada, K. Yoneda, N. Kobayashi, S. Hasaka, M. Inoue, *Appl. Phys. Lett.* **2006**, *89*, 61907.

[143] N. Tajima, T. Ohno, T. Hamada, K. Yoneda, S. Kondo, N. Kobayashi, M. Shinriki, Y. Inaishi, K. Miyazawa, K. Sakota, S. Hasaka, M. Inoue, *Japanese J. Appl. Physics, Part 1 Regul. Pap. Short Notes Rev. Pap.* **2007**, *46*, 5970.

[144] H. W. Ro, K. Char, E. C. Jeon, H. J. Kim, D. Kwon, H. J. Lee, J. K. Lee, H. W. Rhee, C. L. Soles, D. Y. Yoon, *Adv. Mater.* **2007**, *19*, 705.

[145] S. Kim, Y. Toivola, R. F. Cook, K. Char, S.-H. Chu, J.-K. Lee, D. Y. Yoon, H.-W. Rhee, *J. Electrochem. Soc.* **2004**, *151*, F37.

[146] B. R. Kim, J. W. Kang, K. Y. Lee, J. M. Son, M. J. Ko, *J. Mater. Sci.* **2007**, *42*, 4591.

[147] B. R. Kim, J. M. Son, M. J. Ko, *J. Mater. Sci.* **2007**, *42*, 5381.

[148] M. S. Oliver, G. Dubois, M. Sherwood, D. M. Gage, R. H. Dauskardt, *Adv. Funct. Mater.* **2010**, *20*, 2884.

[149] P.-I. Wang, Z. Wu, T.-M. Lu, L. V. Interrante, *J. Electrochem. Soc.* **2006**, *153*, G267.

[150] B. Wang, Y. R. Shang, Z. Ma, L. Pan, Y. S. Li, *Polym. (United Kingdom)* **2017**, *116*, 105.

[151] Y. Matsuda, J. S. Rathore, L. V Interrante, R. H. Dauskardt, G. Dubois, *ACS Appl. Mater. Interfaces* **2012**, *4*, 2659.

[152] S. Mendiratta, C.-H. Lee, M. Usman, K.-L. Lu, *Sci. Technol. Adv. Mater.* **2015**, *16*, 54204.

[153] I. Stassen, N. Burtch, A. Talin, P. Falcaro, M. Allendorf, R. Ameloot, *Chem. Soc. Rev.* **2017**, *46*, 3185.

[154] K. Zagorodniy, G. Seifert, H. Hermann, *Appl. Phys. Lett.* **2010**, *97*, 10.

[155] S. Eslava, L. Zhang, S. Esconjauregui, J. Yang, K. Vanstreels, M. R. Baklanov, E. Saiz, *Chem. Mater.* **2013**, *25*, 27.

[156] M. Usman, C.-H. Lee, D.-S. Hung, S.-F. Lee, C.-C. Wang, T.-T. Luo, L. Zhao, M.-K. Wu, K.-L. Lu, *J. Mater. Chem. C* **2014**, *2*, 3762.

[157] H. Guo, M. Wang, J. Liu, S. Zhu, C. Liu, *Microporous Mesoporous Mater.* **2016**, *221*, 40.

[158] I. Stassen, M. Styles, G. Grenci, H. V. Gorp, W. Vanderlinden, S. D. Feyter, P. Falcaro, D. De Vos, P. Vereecken, R. Ameloot, *Nat. Mater.* **2015**, *15*, 304.

[159] P. J. Waller, F. Gándara, O. M. Yaghi, *Acc. Chem. Res.* **2015**, *48*, 3053.

[160] B. J. Nordell, T. D. Nguyen, C. L. Keck, S. Dhungana, A. N. Caruso, W. A. Lanford, J. T. Gaskins, P. E. Hopkins, D. R. Merrill, D. C. Johnson, L. L. Ross, P. Henry, S. W. King, M. M. Paquette, *Adv. Electron. Mater.* **2016**, *2*, 1600073.

[161] K. S. W. SING, D. H. EVERETT, R. A. W. HAUL, L. MOSCOU, R. A. PIEROTTI, J. ROUQUEROL, T. SIEMIENIEWSKA, *Pure Appl. Chem.* **1984**, *57*, 603.

[162] C. T. Kresge, M. E. Leonowicz, W. J. Roth, J. C. Vartuli, J. S. Beck, *Nature* **1992**, *359*, 710.

[163] J. S. Beck, J. C. Vartuli, W. J. Roth, M. E. Leonowicz, C. T. Kresge, K. D. Schmitt, C. T. W. Chu, D. H. Olson, E. W. Sheppard, S. B. McCullen, J. B. Higgins, J. L. Schlenker, *J. Am. Chem. Soc.* **1992**, *114*, 10834.

[164] K. Holmberg, J. Bo, B. Kronberg, *Surfactants and Polymers in Aqueous Solution*; 2002.

[165] J. N. Israelachvili, D. J. Mitchell, B. W. Ninham, *J. Chem. Soc. Faraday Trans. 2* **1976**, *72*, 1525.

[166] C. Tanford, *J. Phys. Chem.* **1972**, *76*, 3020.

[167] G. S. Attard, J. C. Glyde, C. G. Göltner, *Nature* **1995**, *378*, 366.

[168] C. G. Goltner, M. Antonietti, *Adv. Mater.* **1997**, *9*, 431.

[169] C.-Y. Chen, S. L. Burkett, H.-X. Li, M. E. Davis, *Microporous Mater.* **1993**, *2*, 27.

[170] A. Steel, S. W. Carr, M. W. Anderson, *J. Chem. Soc. Chem. Commun.* **1994**, 1571.

[171] A. Firouzi, D. Kumar, L. Bull, T. Besier, P. Sieger, Q. Huo, S. Walker, J. Zasadzinski, C. Glinka, J. Nicol, A. Et, *Science (80-.).* **1995**, *267*, 1138.

[172] G. D. Stucky, A. Monnier, F. Schüth, Q. Huo, D. Margolese, D. Kumar, M. Krishnamurty, P. Petroff, A. Firouzi, M. Janicke, B. F. Chmelka, *Mol. Cryst. Liq. Cryst. Sci. Technol. Sect. A. Mol. Cryst. Liq. Cryst.* **1994**, *240*, 187.

[173] A. Monnier, F. Schüth, Q. Huo, D. Kumar, D. Margolese, R. S. Maxwell, G. D. Stucky, M. Krishnamurty, P. Petroff, A. Firouzi, M. Janicke, B. F. Chmelka, Cooperative formation of inorganic-organic interfaces in the synthesis of silicate mesostructures. *Science* **1993**, *261*, 1299–303.

[174] G. J. D. a a Soler-Illia, C. Sanchez, B. Lebeau, J. Patarin, *Chem. Rev.* **2002**, *102*, 4093.

[175] Q. Huo, D. I. Margolese, U. Ciesla, P. Feng, T. E. Gier, P. Sieger, R. Leon, P. M. Petroff, F. Schüth, G. D. Stucky, *Nature* **1994**, *368*, 317.

[176] P. T. Tanev, T. J. Pinnavaia, *Science (80-.).* **1995**, *267*, 865.

[177] S. A. Bagshaw, E. Prouzet, T. J. Pinnavaia, *Science (80-.).* **1995**, *269*, 1242.

[178] A. C. Voegtlin, F. Ruch, J. L. Guth, J. Patarin, L. Huve, *Microporous Mater.* **1997**, *9*, 95.

[179] C. C. Landry, S. H. Tolbert, K. W. Gallis, A. Monnier, G. D. Stucky, P. Norby, J. C. Hanson, *Chem. Mater.* **2001**, *13*, 1600.

[180] S. H. Tolbert, C. C. Landry, G. D. Stucky, B. F. Chmelka, P. Norby, J. C. Hanson, A. Monnier, *Chem. Mater.* **2001**, *13*, 2247.

[181] Y. Lu, R. Ganguli, C. Drewien, M. Anderson, *Nature* **1997**, *389*, 651.

[182] C. J. Brinker, Y. Lu, A. Sellinger, H. Fan, *Adv. Mater.* **1999**, *11*, 579.

[183] D. Grosso, F. Cagnol, G. J. de A. A. Soler-Illia, E. L. Crepaldi, H. Amenitsch, A. Brunet-Bruneau, A. Bourgeois, C. Sanchez, *Adv. Funct. Mater.* **2004**, *14*, 309.

[184] D. Grosso, F. Ribot, C. Boissiere, C. Sanchez, *Chem. Soc. Rev.* **2011**, *40*, 829.

[185] D. Zhao, P. Yang, N. Melosh, J. Feng, B. F. Chmelka, G. D. Stucky, *Adv. Mater.* **1998**, *10*, 1380.

[186] H. Fan, H. R. Bentley, K. R. Kathan, P. Clem, Y. Lu, C. J. Brinker, *J. Non. Cryst. Solids* **2001**, *285*, 79.

[187] C. M. Yang, A. T. Cho, F. M. Pan, T. G. Tsai, K. J. Chao, *Adv. Mater.* **2001**, *13*, 1099.

[188] J. Y. Chen, F. M. Pan, L. Chang, A. T. Cho, K. J. Chao, *J. Vac. Sci. Technol. B* **2005**, *23*, 2034.

[189] S. Jung, T. Ha, J. Seon, H. Park, Phase behavior of ordered mesoporous silica film prepared by Brij-76 block copolymer. *Microporous Mesoporous Mater.* **2008**, *111*, 188–193.

[190] S.-B. Jung, C.-K. Han, H.-H. Park, *Appl. Surf. Sci.* **2005**, *244*, 47.

[191] S. B. Jung, H. H. Park, *Thin Solid Films* **2006**, *494*, 320.

[192] S. Tanaka, H. Tada, T. Maruo, N. Nishiyama, Y. Egashira, K. Ueyama, *Thin Solid Films* **2006**, *495*, 186.

[193] T. Maruo, S. Tanaka, H. W. Hillhouse, N. Nishiyama, Y. Egashira, K. Ueyama, *Thin Solid Films* **2008**, *516*, 4771.

[194] S. Jung, T. Ha, H. Park, *J. Colloid Interface Sci.* **2008**, *320*, 527.

[195] T. J. Ha, S. G. Choi, S. B. Jung, B. G. Yu, H. H. Park, *Ceram. Int.* **2008**, *34*, 947.

[196] T. Asefa, M. MacLachlan, N. Coombs, G. Ozin, *Nature* **1999**, *402*, 867.

[197] S. Inagaki, S. Guan, Y. Fukushima, T. Ohsuna, O. Terasaki, *J. Am. Chem. Soc.* **1999**, *121*, 9611.

[198] B. J. Melde, B. T. Holland, C. F. Blanford, A. Stein, *Chem. Mater.* **1999**, *11*, 3302.

[199] T. Asefa, M. J. MacLachlan, H. Grondey, N. Coombs, G. A. Ozin, *Angew. Chemie Int. Ed.* **2000**, *39*, 1808.

[200] K. Landskron, B. D. Hatton, D. D. Perovic, G. A. Ozin, *Science* **2003**, *302*, 266.

[201] B. D. Hatton, K. Landskron, W. Whitnall, D. D. Perovic, G. A. Ozin, *Adv. Funct. Mater.* **2005**,

15, 823.

[202] W. Wang, D. Grozea, S. Kohli, D. D. Perovic, G. A. Ozin, *ACS Nano* **2011**, *5*, 1267.

[203] M. Seino, W. Wang, J. E. Lofgreen, D. P. Puzzo, T. Manabe, G. A. Ozin, *J. Am. Chem. Soc.* **2011**, *133*, 18082.

[204] F. Goethals, I. Ciofi, O. Madia, K. Vanstreels, M. R. Baklanov, C. Detavernier, P. Van Der Voort, I. Van Driessche, *J. Mater. Chem.* **2012**, *22*, 8281.

[205] J. Zhang, G. Zhang, Y. Gao, R. Sun, C. P. Wong, *J. Mater. Sci.* **2016**, *51*, 7966.

[206] W. Wang, D. Grozea, A. Kim, D. D. Perovic, G. a Ozin, *Adv. Mater.* **2010**, *22*, 99.

[207] M. R. Baklanov, C. Adelmann, L. Zhao, S. De Gendt, *ECS J. Solid State Sci. Technol.* **2014**, *4*, Y1.

[208] Y. Yan, C. M. Lew, Y. Liu, B. Day, G. M. Kloster, H. Tiznado, M. Sun, F. Zaera, J. Wang, *Langmuir* **2009**, *25*, 5039.

[209] S. Eslava, J. Urrutia, A. N. Busaworv, M. R. Baklanov, F. Iacopi, S. Aldea, K. Maex, J. A. Martens, C. E. A. Kirschhock, *J. Am. Chem. Soc.* **2008**, *130*, 17528.

[210] Y. Liu, M. Sun, C. M. Lew, J. Wang, Y. Yan, *Adv. Funct. Mater.* **2008**, *18*, 1732.

[211] H. K. Hunt, C. M. Lew, M. Sun, Y. Yan, M. E. Davis, *Microporous Mesoporous Mater.* **2010**, *128*, 12.

[212] Y. Liu, C. Lew, M. Sun, R. Cai, J. Wang, G. Kloster, B. Boyanov, Y. Yan, *Angew. Chemie Int. Ed.* **2009**, *48*, 4777.

[213] Y. Chen, G. Zhu, Y. Peng, H. Bi, J. Feng, S. Qiu, *Microporous Mesoporous Mater.* **2009**, *123*, 45.

[214] C. M. Lew, Z. Li, S. Li, S. J. Hwang, Y. Liu, D. I. Medina, M. Sun, J. Wang, M. E. Davis, Y. Yan, *Adv. Funct. Mater.* **2008**, *18*, 3454.

CHAPTER 2. EFFECT OF UV CURE ON OXYCARBOSILANE LOW-K PROPERTIES

In this chapter, we first compare the ultra-violet (UV) and vacuum ultra-violet (VUV) resistance of the methylene and ethylene bridging groups in oxycarbosilanes films. We find that similar to the Si-CH_3 bonds, the Si-CH_2-Si bonds are not affected by a 5.6 eV irradiation. On the other hand, the concentration of the Si-CH_2-CH_2-Si groups decreases during such UV exposure. We observe more significant difference in alkylene reduction when the films are exposed to VUV (7.2 eV). The ethylene groups are depleted by more than 75% while the methylene and methyl groups are diminished by only about 40%. The experimental results are qualitatively supported by ab-initio quantum-chemical calculations.

***M. Redzheb**, L. Prager, S. Naumov, M. Krishtab, S. Armini, P. Van Der Voort, M. R. Baklanov, Effect of the C-bridge length on the ultraviolet-resistance of oxycarbosilane low-k films, Applied Physics Letters, 108(1), 012902 (2016)*

Next, we discuss, in more detail, the effect of the UV cure on the low-k properties of methylene-bridged oxycarbosilane films. The as-deposited films were exposed to UV light with λ=172 nm, 222 nm, 254 nm or 185/254 nm at 400°C for durations spanning from 1 to 20 min. While light with wavelength of about 172 nm is detrimental to the electrical and chemical properties of the low-k films, it notably improves the mechanical properties. The induced damage is reduced by shortening the UV treatment but at the expense of the template removal efficiency. Furthermore, when compared to the template removal efficiency of a 2 h thermal cure, an exposure to 222 nm light as short as 3 min is more efficient in removing the template. When the films are UV cured for 20 min with λ=222 nm, the best combination of k and Young's modulus is obtained. UV-cure using 254 nm or dual band 254/185 nm photons seems to have a negligible contribution to the template removal efficiency within the investigated doses. Finally, the HF etching mechanism is discussed and the role of the interfacial layer between the low-k film and the Si substrate is highlighted.

***M. Redzheb**, L. Prager, M. Krishtab, S. Armini, K. Vanstreels, A. Franquet, P. Van Der Voort, M.R. Baklanov, Impact of UV wavelength and curing time on the properties of spin-coated low-k films, 2015 IEEE International Interconnect Technology Conference and 2015 IEEE Materials for Advanced Metallization Conference (IITC/MAM), 99-102 (2015)*

***M. Redzheb**, L. Prager, M. Krishtab, S. Armini, K. Vanstreels, A. Franquet, P. Van Der Voort, M.R. Baklanov, UV cure of oxycarbosilane low-k films, Microelectronic Engineering, 156, 103-107 (2016)*

2.1. Introduction

Porous low-k materials are considered in pursuit of reducing the resistance × capacitance (RC) delay, dynamic power consumption and cross-talk noise with downscaling the metal interconnect dimension in ultra-large-scale integration (ULSI) devices.[1,2] In recent years there has been growing interest in low-k materials containing backbone carbon such as oxycarbosilanes and periodic mesoporous organosilicas (PMOs).[3–5] The Si-$(CH_2)_x$-Si have been shown to lead to better adhesive and cohesive fracture energies as compared to silica.[6] It has also been suggested that higher YM and lower density than *a*-silica could be obtained if many Si-O-Si were replaced by Si-CH_2-Si.[7,8] Additionally, the control over the pore organization leads to further improvement of E.[8–10] All these advantages make oxycarbosilane based materials very promising for sub 10-nm technology nodes because further scaling of the dielectric constant of PECVD deposited materials meets fundamental problems.[11]

Besides the mechanical properties of the low-k films, the common challenge of silica based low-k materials hindering their integration is the plasma induced damage (PID). However, the presence of bridging alkylene groups has been shown to lead to reduction in the PID[4,12] as compared to low-k films containing carbon only in the form of methyl groups. Additionally, quantum chemical calculations have revealed improved oxidation resistance for alkylene compared to methyl groups.[13] Furthermore, it has been reported that the length of the bridging group influences the cohesive fracture energy,[6] the YM and the hardness.[8] The control over the pore structure is also limited by the length and the rigidity of the bridging organic group.[14] Notably, while PECVD is the established deposition approach throughout the IC industry, the sol-gel route can provide better compositional and structural control over the film properties.[15]

The effect of UV light on the low-k film is of major interest in two main contexts: i) UV-assisted thermal porogen removal (UV-cure) and ii) plasma processing. For porogen removal the energy of the radiation can independently be controlled in order to optimize the polymer decomposition and the enhancement of the low-k properties.[16–18] On the other hand, in plasma processing, the energy and intensity of the photons are determined by the required chemistry and plasma conditions. For example, the typical fluorocarbon-based plasmas used for low-k etching emit photons in the wavelength range 100-350 nm[19] and the extent of their impact correlates with the penetration depth.[20] Therefore, it is of paramount importance to quantify the contribution of the UV light to the PID.[21–23] There are numerous studies reporting the effect of the UV on carbon-doped oxide films[16,17,20] but it has not been investigated in detail for alkylene-bridged films.[24,25]

UV-cure study of spin-coated methylsilsesquioxane[18] films has been previously reported. Our group reported the UV-cure investigation of nanoclustered silica[26] and spin-on films.[27,28] Nevertheless, these films did not contain backbone carbon. Finally, IBM reported[24] the use of

UV-cure with a broad band lamp during integration of an oxycarbosilane film but no systematic study was presented. The present work focuses on the stability of the backbone carbon and the damage mechanisms during UV irradiation.

2.2. Experimental Section

Two matrix compositions were investigated in this work - the first porous film obtained through the acid-catalyzed polycondensation of 1,2-bis(triethoxysilyl)ethane contains ethylene bridging groups (EtLK) while the second film which was obtained from 1,2-bis(triethoxysilyl)methane and triethoxymethylsilane contains methylene and methyl groups (MeLK). Nonionic PEO-hydrocarbon (($C_{2n}H_{4n+2}O_{n+1}$)-(C_mH_{2m+1})) block copolymers were employed as templates where the EtLK was templated by BrijS10 while the MeLK was templated by BrijL4. The sols for the MeLK films were provided by SBA Materials Inc[2] and the films obtained after a thermal decomposition of the template were commercially known as uLK222. Therefore, since the formulation of SBA Materials was proprietary, no further information is available on the synthesis conditions of the uLK222 sol. Nevertheless, this is not of great importance for the conclusions of the studies to be presented. SBA Materials provided one more sol with a higher surfactant to precursor ratio in attempt to obtain low-k films with a dielectric constant of 2.0. The latter films are referred to as MeLK2.0. The synthesis procedure of the EtLK films included the dissolution of 0.4 g BrijS10 in 9 ml 1-methoxy-2-propanol and 0.5 ml 1M HCl by stirring for 30 min at room temperature (RT). Next, 1 ml BTESE was added to the solution and further stirred for 30 min at RT. The solution was spun at 5000 rpm for 60 s on a Si substrate with a native SiO_2 surface. Following the deposition, the samples were annealed at 140°C for 5 min at ambient atmosphere. The UV cure was performed in a custom-built chamber (Figure 2.1). In order to exclude the effect of atmospheric gasses on the low-k films properties, the chamber was evacuated down to 5 mbar. Next, the chamber was flushed with high purity N_2 to maintain a pressure of 20 mbar. Afterwards, the temperature was increased from room temperature to 400°C by a heater

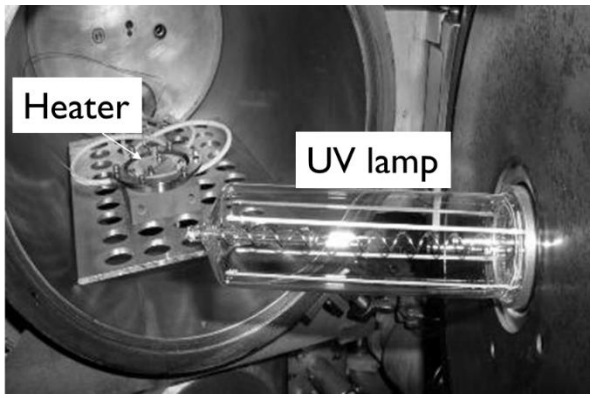

Figure 2.1. A photo of the curing chamber

[2] In March 2017, the company SBA Materials stopped all research and commercial activity.

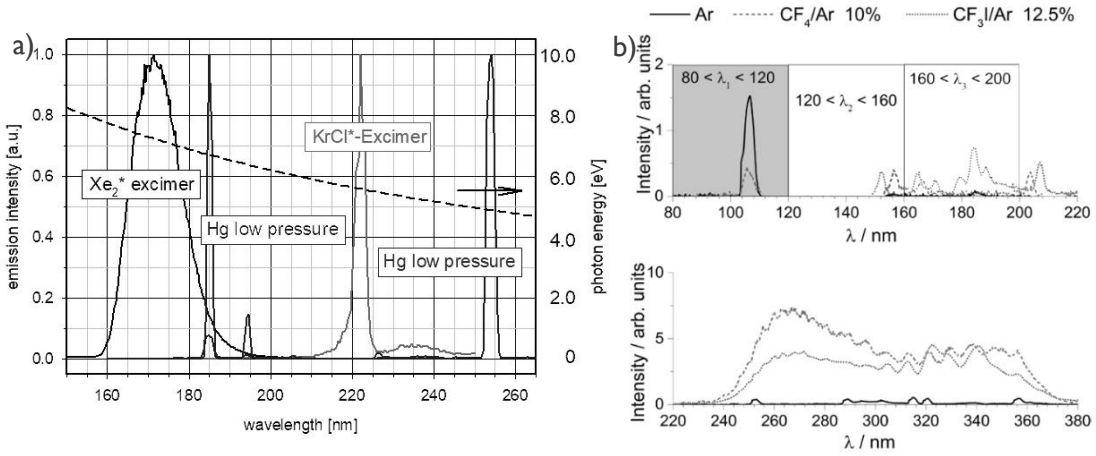

Figure 2.2. Emission spectra of a) the UV sources employed in this work; b) typical low-k etch chemistries

element in about 2 min. Finally, the samples were exposed to UV for variable time. The UV irradiation was generated by Xe_2^* excimer, 172 ± 12 nm; I=15 W/m², $KrCl^*$ excimer, 222 ± 1.2 nm; I=130 W/m², or low pressure (LP) Hg lamps — one allowing the 185 nm line to pass through and the other one absorbing the higher energy photons. Figure 2.2 depicts the emission spectra of the UV sources employed in this study compared to the emission spectra of typical low-k etch chemistries. Table 2.1 presents the emission peaks and the measured intensities. The intensities were measured at the height of the samples by a UV radiometer (Epigap, Berlin) calibrated according to the UV spectrum of the LP Hg emission. Samples annealed at 400 °C for 3, 5, 10, and 120 min were used as references.

UV source	Wavelength [nm]	Intensity [W/m²]
Xe_2^*	172 ± 12	15
KrCl	222 ± 1.2	130
LP Hg	185/254	40
LP Hg	254	80

Table 2.1. Emission peaks and intensities of the employed UV sources

2.3. Results and Discussion

2.3.1. Effect of the C-bridge length on the UV resistance of oxycarbosilanes films

The FTIR spectra in the 500-4000 cm^{-1} range associated with the thermally treated reference samples EtLK and MeLK films are shown in Figure 2.3. The band at 1250-950 cm^{-1} is usually attributed to the absorption from three different oxide structures – network, cage and suboxide.[29] However, overlapping in this region is the signal from the alkylene bridges: Si-CH_2-Si[30,31] at ≈1080-1040 cm^{-1} and Si-CH_2-CH_2-Si[32] at 1160 cm^{-1}. While the band below 900 cm^{-1} is often ascribed to Si$(CH_3)_x$ groups,[29] for EtLK it has been explained in terms of tilting vibrations and translational oscillations of the ethylene unit against the rest of the molecule.[33]

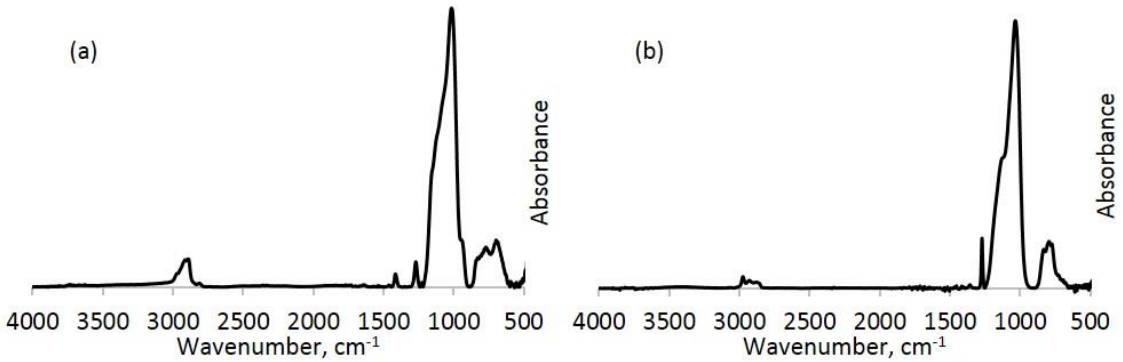

Figure 2.3. FTIR spectra of the reference (thermally treated) (a) EtLK and (b) MeLK

Nevertheless, contribution from $Si(CH_3)_x$ is not excluded due to conversion of the alkylene groups into alkyl.[34,35] Furthermore, the region below 3000 cm^{-1} contains the signals associated with the C-H stretch vibrations in -CH_3 (2975 and 2905 cm^{-1}) and -CH_2 (2930 and 2880 cm^{-1}) units. The CH_3 groups in MeLK are bonded to the matrix as Si-CH_3 while the CH_2 signal is mainly attributed to the remaining template. On the other hand, due to the ethylene groups in the matrix, the spectrum of EtLK is characterized by intense CH_2 bands even when the surfactant is virtually removed. Next, the peak at 1275 cm^{-1} in MeLK is attributed to Si-CH_3. However, in EtLK we attribute the peak at 1270 cm^{-1} mainly to C-H bending in Si-CH_2-CH_2-Si although the formation of Si-CH_3 is not excluded due to the thermal instability of organic species but so far it has not been demonstrated in the literature. We estimate the concentration of the ethylene bridges by the absorption at ~1415 cm^{-1} which has been attributed to out-of-plane rocking of Si-C and deformational vibrations of C-H bonds.[13,31,36] The latter band is a suitable indicator since it does not overlap with band(s) produced by the organic template. However, the cleaving of the Si-CH_2-CH_2-Si chain which is expected to result into Si-alkyl groups, leads to absorption at the same frequency.[35,37] On the other hand, the Si-CH_2-Si are monitored by the signal at about 1360 cm^{-1} which has been attributed to C-H bending mode.[29,31,38] The latter overlaps with a broad peak centered at ≈1350 cm^{-1} originating from the hydrocarbon chain of the template.[39] Consequently, the concentration of methylene bridges before the UV cure cannot be unambiguously estimated by FTIR. Nevertheless, the absorption due to the template can be shown to be negligible between the 3 and 10 min UV cure for both of the photon energies of 222 and 172 nm.[25]

Figure 2.5 depicts the peaks assigned to the alkylene groups. Exposure of EtLK to 222 nm photons leads to about 10% decrease of the ethylene peak intensity when comparing 3 min to 10 min cure. On the other hand, 172 nm cure results in ≈75% intensity reduction between 1 and 10 min cure which decreases the associated signal down to noise level.

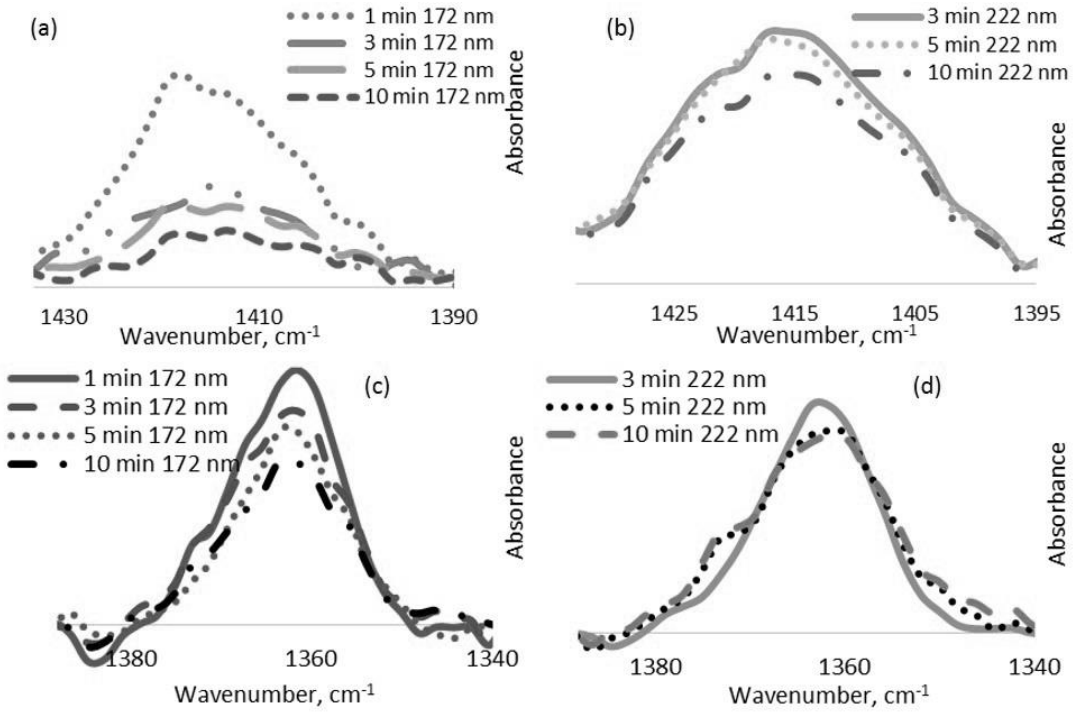

Figure 2.5. FTIR spectra zoomed in the region attributed to Si-CH_2-CH_2-Si in EtLK after (a) 172nm (b) 222nm and to Si-CH_2-Si in MeLK after (c) 172nm (d) 222nm UV cure

In comparison, the methylene peak in MeLK is also diminished by about 10% by the exposure to the 222 nm light. However, only 40% intensity loss of the methylene peak is observed after exposure to 172 nm photons.In general, the Si-C bonds are less affected by photons with λ=222 nm as compared to λ=172 nm.[40] However, there is a significant difference in how the irradiation affects the MeLK and the EtLK films. While for the MeLK, the decrease of the methylene peak can be attributed to a self-hydrophobization process[35] which is also supported by the increased intensity of the bands assigned to Si-O-Si and Si-CH_3, the decrease of the ethylene peak in EtLK cannot. The latter assertion stems from the fact that when the EtLK film is annealed, compared to the not-annealed spectrum, the intensity of the peak at 1415 cm^{-1} increases by about 10%. The increase is attributed to the higher concentration of the absorbing species such as C-H bonds caused by the thermally-induced bond rearrangement as a result of which the –CH_2–

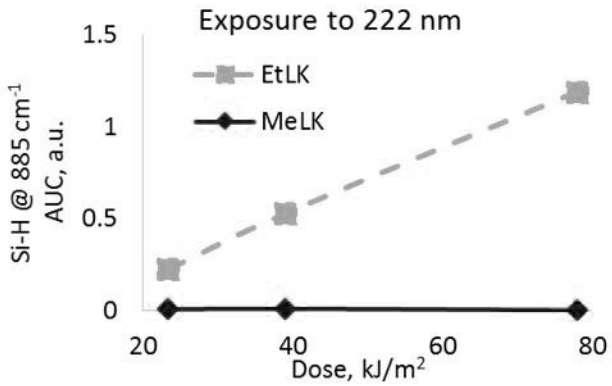

Figure 2.4. Area under the curve (AUC) observed for the peak at 885cm^{-1} attributed to Si-H after 222nm UV cure.

groups are transformed into $–CH_3$. Since we do not expect a detrimental effect on the Si-alkyl groups,[29] we attribute the 222 nm UV-induced decrease of the 1415 cm^{-1} peak to fragmentation of the $Si-CH_2-CH_2-Si$ chain. Additionally, Si-H bonds formation is evident from the bands at 885 cm^{-1} and 2250 cm^{-1}, whose intensities and calculated areas under the curves (AUC) increase with exposure time. Figure 2.4 depicts the evolution of the absorption at 885 cm^{-1}. Furthermore, Si-H are not present in the reference EtLK films indicating that they are generated during the exposure to UV light. The observed Si-H bond signals hint at a formation of Si dangling bonds passivated by H atoms or radicals. The latter are present as a result of the UV-assisted template decomposition which involves C-H bonds breaking.[41] Figure 2.4 further emphasizes the different effects of the 222 nm light on EtLK and MeLK by showing no Si-H bond formation for the MeLK film.

The damaging effect of the VUV light (λ <200 nm) on the organic component of the hybrid low-k and specifically on the methyl groups is well-known.[20,29] While our results conform to the previous reports, we observe about twice more significant effect on the ethylene as compared to the methylene groups (Figure 2.5 a and c). Additionally, after 10 min VUV exposure the intensity of the peak attributed to $Si-CH_3$ (not shown) in MeLK decreases to ≈70% compared to its intensity after 1 min cure similar to the $Si-CH_2-Si$ peak which decreases to ≈60% compared to its intensity after 1 min cure (Figure 2.5 c).

Rakhimova et al.[20] reported an increase of the quantum yield for breaking $Si-CH_3$ bonds by VUV photons for films with ≈50% porosity compared to films with ≤45% porosity. The latter suggests that the differences we have discussed so far might be due to the porosity difference between a 55% porous EtLK with respect to 45% porous MeLK. This hypothesis was tested by depositing EtLK (38-40%) and MeLK (33-38%) with the same target porosity and exposing them at 400°C to 172 nm light for 2, 5 and 10 min. This experiment was performed with a different source whose intensity is not available. Figure 2.6 shows the intensity changes of the peaks attributed to the alkylene groups relative to the first measured point. The intensity of the methylene peak decreases by about 10% increasing the exposure time from 2 to 10 min but the

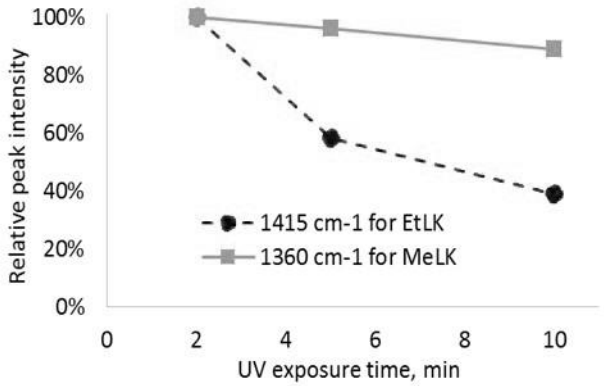

Figure 2.6. Evolution of the peak intensity attributed to the bridging alkylene groups after 172nm cure

ethylene peak is reduced by 60% in the same time range. The effects observed in this additional experiment seem to be less pronounced than those discussed above which is probably related to the different intensity of the Xe_2^* excimer source or to the fact that the shortest VUV irradiation was 2 min instead of 1 min. The latter seems especially relevant when we consider the large difference in peak intensity after 1 and 3 min exposure in Figure 2.5a. Nevertheless, this result confirms our observation that the ethylene bridging groups are depleted faster than the methylene groups and porosity does not play a determining role under the investigated experimental conditions.

Quantum chemical calculations were performed using the Density Functional Theory (DFT) B3LYP method[42,43] (Jaguar version 8.3 program) to study VUV spectra and energetics of reactivity of various polymer compositions. The structures of model polymers were optimized at B3LYP/6-31(d,p) level. The frequency analysis was made at the same level of theory to obtain thermodynamic parameters such as total enthalpy (H) and Gibbs free energy (G) at 298 K. The reaction enthalpies (Δ H) and Gibbs free energies of reaction (Δ G) were calculated as the difference of the calculated total enthalpies and Gibbs free energies between the reactants and products, respectively. The energies of excited states and electronic transition spectra were calculated using the Time Dependent[44] (TD) DFT method at B3LYP/6-31+G(d,p) level of theory.

The results of the calculations are shown in Figure 2.7. The energy schema shows the formation of reactive triplet state T_1 after absorption of a high energy photon (e.g. 172 nm). The

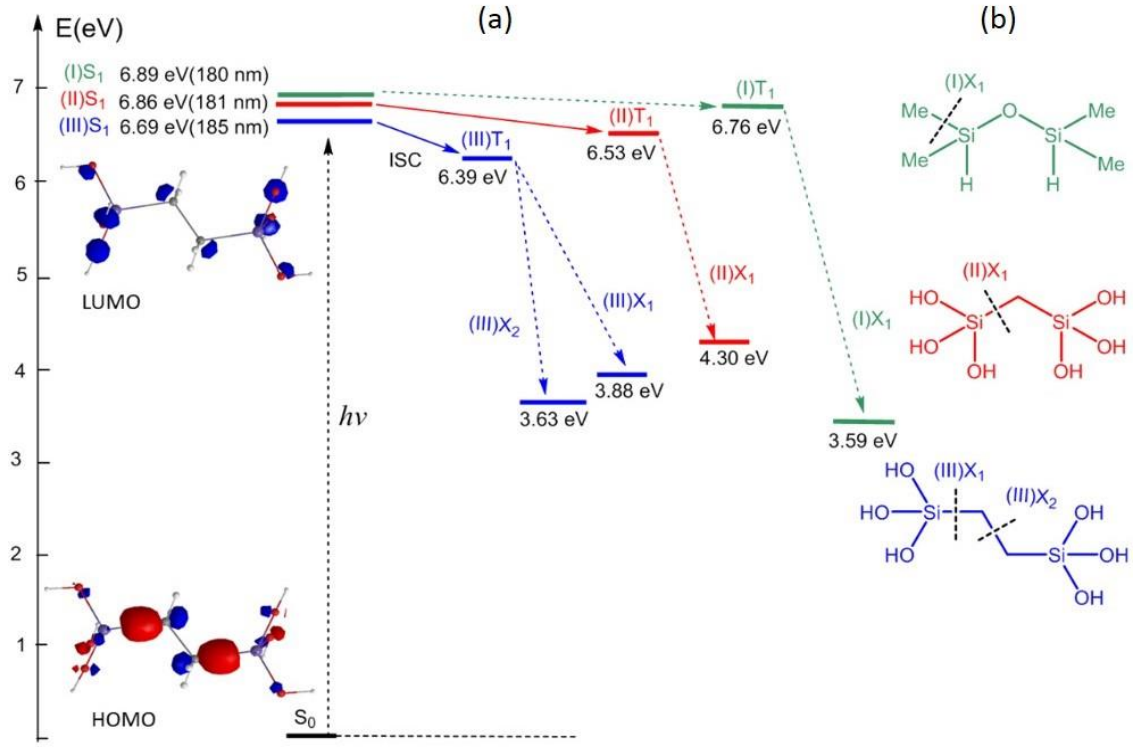

Figure 2.7. Results of DFT quantum chemical calculations: (a) energy scheme of the radicals formation after excitation; (b) model structures used for calculations; molecular orbitals are given for the case of structure (III)

dissociation reactions X_1 and X_2 lead to formation of two radicals through Si-C bond and C-C bond scission, respectively (Figure 2.7b). The C-C bond scission is energetically more favorable than Si-C bond ones. However, it should be noted, that the σ -electron from the highest occupied molecular orbital, which has bonding character, is strongly localized on Si-C bond (as shown for the structure (III)). After excitation into the lowest unoccupied molecular orbital, which has σ -character, this Si-C bond will be weakened, facilitating dissociation reaction X_1. From the comparison of the possible dissociation reactions it can be seen, that decomposition of model polymer (II) with only one CH_2 group is energetically less favorable than that of (III).

2.3.2. UV cure of methylene-bridged oxycarbosilanes low-k films with a target k=2.2

The template removal as a function of treatment time was deduced from the changes in the RI (Figure 2.8). Ten minutes anneal at 400°C leads to a ΔRI≈0.176 which is 90% of the largest ΔRI observed in this study. The thermal treatment alone, however, is not able to remove the remaining organic species with the same efficiency, and after 2 h thermal anneal an RI of 1.275 is reached while lower RIs are observed for some of the UV-cured samples. Similarly, the LP Hg lamps do not lead to an efficient template removal which seems to be due to insufficient photon doses reached within the investigated treatment times. The latter is attributed to two factors: i) 254 nm photons do not possess enough energy to cleave C-C bonds; ii) the intensity of the 185 nm line, which is one tenth of the overall source intensity, is too low to contribute significantly to the template removal. Nevertheless, when compared to the thermally treated samples, the additional exposure to the emission from the LP Hg lamps results in films with lower RIs indicating that higher intensity sources are required in order to study better their impact on the low-k properties. In contrast, the anneal at 400°C combined with an exposure to 222 nm and 172 nm photons leads to nearly complete template removal for curing times as short as 3 and 1 min, respectively.

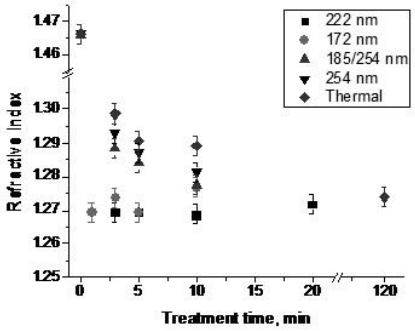

Figure 2.8. Refractive index as a function of treatment time. The error bars represent the 3σ variation of the RI.

The chemical modifications of the films have been investigated by FTIR analysis. The main bands of interest for the composite films include the C–H_x stretching (3000–2850 cm^{-1}); CH_3 bending in Si–CH_3 (≈1275 cm^{-1}); C-H_2 scissoring in Si-CH_2-Si overlapping with the absorption of the

unhydrolyzed ethoxy groups[45] (≈1360 cm^{-1}) and due to C-H rocking in the hydrocarbon chain[39] of the template (1351cm^{-1}); Si–O–Si asymmetric stretches (1250–970 cm^{-1}); isolated SiO-H stretches (3745 cm^{-1}); H bound –OH stretches (3400-3700 cm^{-1}); Si-H deformation (895 cm^{-1}) and stretching (≈2250 cm^{-1}).[37] The region between 2850 and 2950 cm^{-1} reflects mainly the presence of CH_2 allowing estimation of the amount of remaining template. A comparison of the integrated absorption from this region, excluding the peak at 2980 cm^{-1} which is mainly from $Si-CH_3$ groups, supports our conclusion that the amount of template after thermal treatment and exposure to LP Hg lamps decreases but not as much as after irradiation with 222 and 172 nm (Figure 2.9). For the latter two, following the initial decrease, the AUC hardly changes up until 10 min of treatment. The slight decrease in the case of 222 nm might be due to small amounts of template still being removed but after 10 min the same area under the curve is observed for both sources.

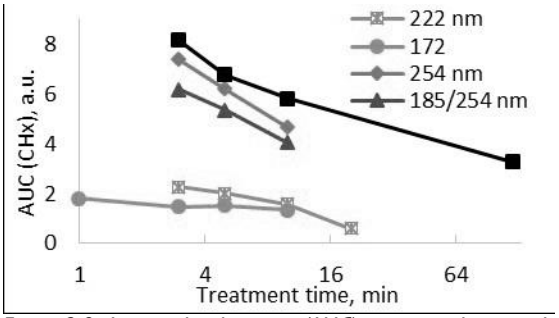

Figure 2.9. Area under the curve (AUC) corresponding mainly to CH_2 vibrations below 2950 cm^{-1}

Thermally induced C-loss is expected *not* to occur in N_2 atmosphere up until a temperature of 650°C.[34,46] Nevertheless, the methylene groups have been shown to be converted into methyl groups through a self-hydrophobization process which occurs in the presence of proximal silanol groups around 400°C.[34] This process is responsible for both hydrophobization of the film and enhancement of the Si-O network seen in FTIR as increase in intensity of the 1270 and 1060 cm^{-1} bands. The intensity of the Si-O peak increases also due to polycondensation. In order to establish the effect of the UV photons on the methylene groups, we first consider the spectra

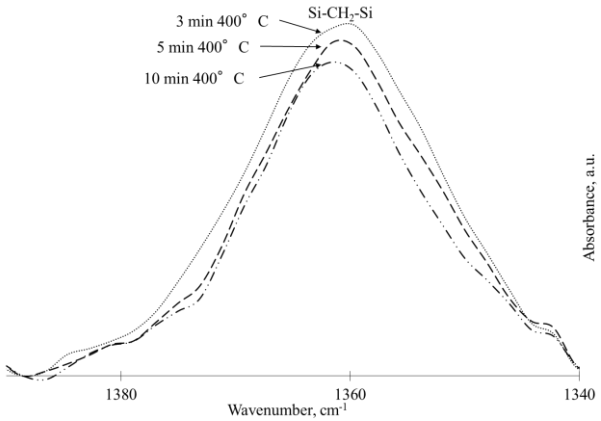

Figure 2.10. FTIR region of C-H deformation attributed to the Si-CH_2-Si for thermally treated oxycarbosilane film

of the thermally treated films. The band at ≈1360 cm^{-1} decreases with ≈10% (Figure 2.10) between the 3 and 10 min exposures. This decrease is partially attributed to template removal.[39,47] To support our interpretation, we synthesized model films without methylene groups targeting the same thickness and porosity. Next, we annealed them for up to 20 min. After 10 min anneal the model films were 50 nm thicker and their RI was similar, within the experimental variation, to the oxycarbosilane films annealed for the same time. In the FTIR spectra of the as-deposited model films, (Figure 2.11) there is a broad band at ≈1351 cm^{-1} with FWHM > 30 cm^{-1} which after 10 min anneal decreases down to 16% from its initial intensity and changes ≈20% between the 3 and 10 min treatments. Therefore, the template contributes to the absorption observed at 1360 cm^{-1} and while the present data does not allow us to quantify the exact contribution we note that after 3 min anneal the absorption observed from the model films was 14% of that from the oxycarbosilane film. These observations raise the question whether we can draw reliable conclusions about the backbone carbon and its stability during irradiation. Regarding the 222 and 172 nm cures, the answer is affirmative because of two reasons: first, the intensity of the peak at 2930 cm^{-1} for the shortest UV cure is more than thrice lower as compared to 10 min anneal; and second, the absorption of the deformational mode is about 10 times lower than that of the stretching mode. Based on these observations we conclude that a potential contribution from the template to the deformational band in the spectra of the 222 and 172 nm irradiated films would be on the order of the experimental error.

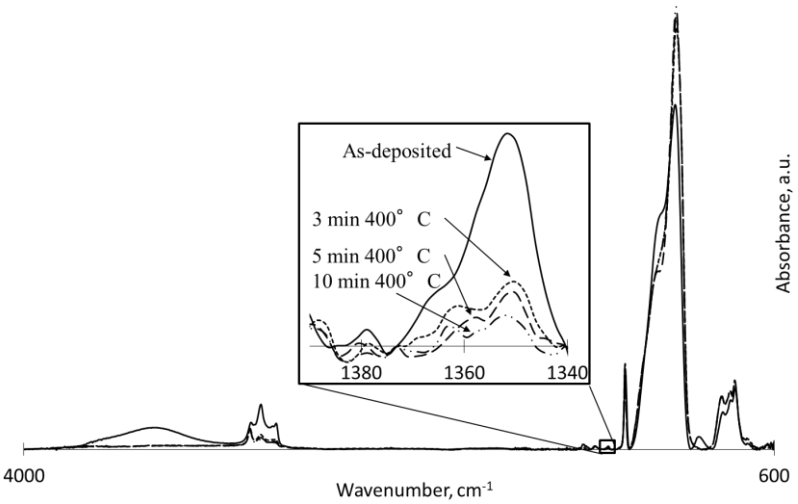

Figure 2.11. FTIR of model low-k films not containing Si-CH_2-Si bonds

Taking into account the latter discussion we consider the spectra of the 222 nm irradiated films (Figure 2.12). The increase in the intensity of the Si-O-Si peak is accompanied by a blue shift which might be understood in terms of the formation of Si-CH_3 bonds and cage-like structures[37] and reduction of the suboxide-like SiO_x ($x<2$) structures.[48] As expected, the organic part of the matrix was not affected adversely by the UV radiation and even the self-hydrophobization process can be hardly identified between the 3 and 10 min exposures. Nevertheless, the latter

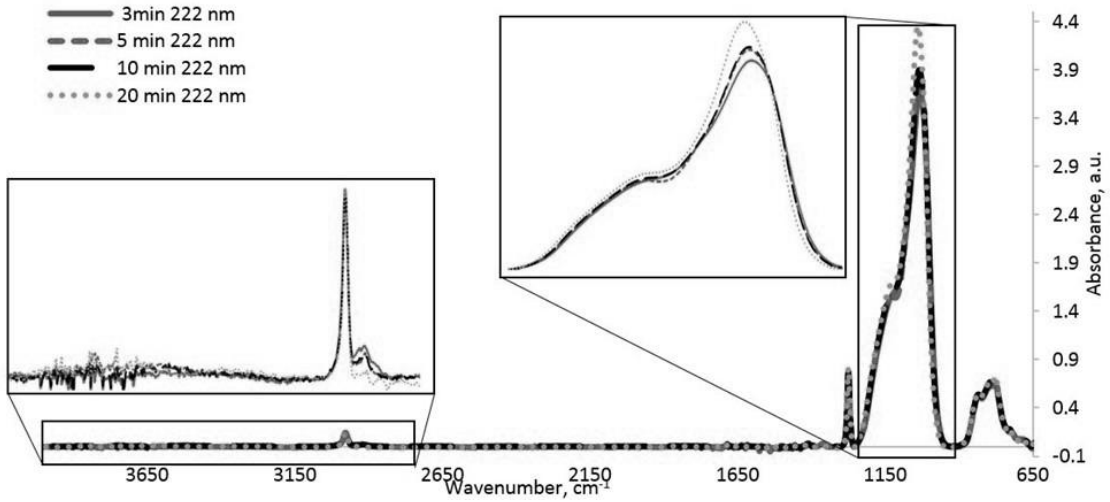

Figure 2.12. FTIR spectra of 222 nm irradiated films

explains the significant difference in the CH_2 content observed between the samples exposed to 222 nm for 10 min and for 20 min (Figure 2.9). Additionally, the AUC (Figure 2.13a) of the peak at ≈1360 cm^{-1} decreases by about 50% for the sample irradiated for 20 min. The weak intensity of the band complicates its analysis because of interference fringes which are characteristic for transmission spectra of thin films on thick substrates beyond certain resolution.[49] Finally, the fact that we did not observe Si-H bonds formation further suggests that no Si dangling bonds were formed during the exposure to the UV photons and therefore they are not detrimental to the bridging methylene groups.

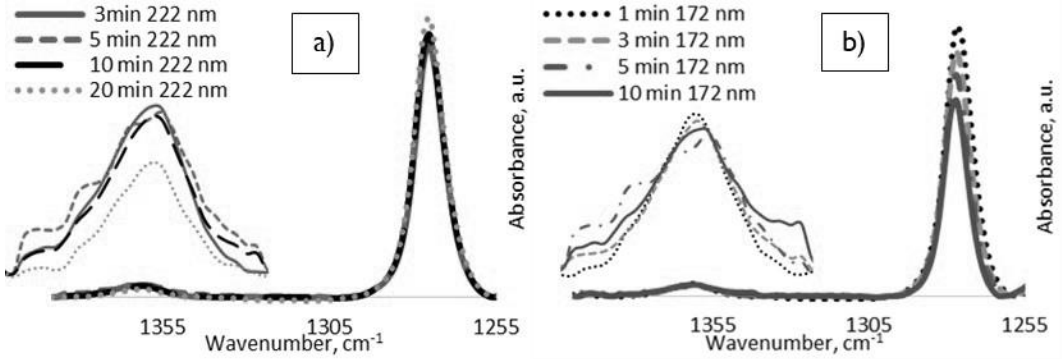

Figure 2.13. FTIR spectral region reflecting the evolution of the C-H deformation in Si-CH_3 (~1275 cm^{-1}) and Si-CH_2-Si (1360 cm^{-1}) of a) 222 nm irradiated films and b) 172 nm irradiated films

The VUV photons with λ=172 nm break the Si-CH_3 bonds observed by the decrease of 2975, 1275 cm^{-1} bands (Figure 2.14) and the Si-C stretching vibration at 775 cm^{-1}. Additionally, peaks at 2255 and 885 cm^{-1} indicate Si-H bond formation. The carbon loss is accompanied by a blue shift of the peak assigned to Si-O asymmetric stretch[50] as well as increase of its intensity indicating possible densification. Additionally, hydrophilization occurs when the methyl groups are replaced by OH groups which further absorb moisture evident by a sharp peak at 3745 cm^{-1} and by a progressively broadening band between 3200 and 3700 cm^{-1}, respectively. The surface hydrophilization is also manifested by water contact angle (WCA)<45° while it is ≥90° following

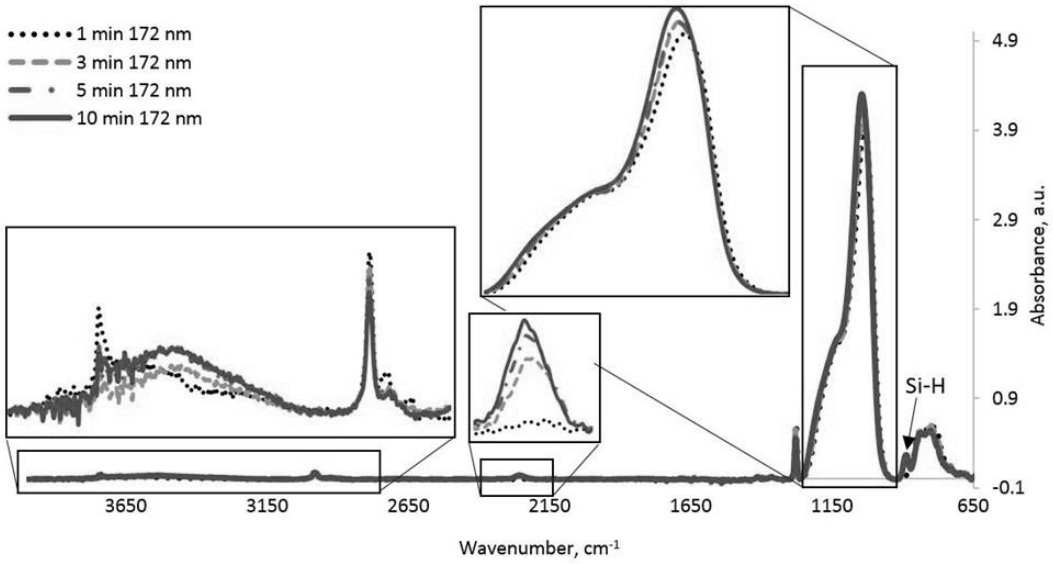

Figure 2.14. FTIR of 172 nm irradiated films

the rest of the investigated treatments. Further analysis reveals that even though the integrated area of the C-H stretch is systematically lower for the 172 nm cured films than that of the 222 nm cured films, it stays relatively constant with exposure time and the 2930 cm^{-1} band from C-H_2 stretch is clearly observed. The latter implies that the methylene groups are not significantly affected by the high energy photons. Further support for this conclusion is found by examining the band at 1360 cm^{-1} (Figure 2.13b). It has ≈20% lower intensity than that of a 3 min 222 nm cured film but it does not decrease further. The 172 nm light has sufficient energy to cause dissociation of the methylene groups as shown in Figure 2.7. However, when comparing the dissociation of methyl groups with that of methylene groups, the former seems more likely. This explains why the FTIR peak attributed to the Si-CH_3 groups in Figure 2.13b is seen to decrease monotonically with UV cure duration. As a result, the Si-CH3 groups seem to protect the Si-CH_2-Si groups.

The films were also characterized by EP. All of the films produce type IV isotherms with narrow H2 hysteresis. Knowing the open pore volume and the RI, we calculated the refractive index of the skeleton $RI_{skeleton}$.[51] The open porosity of the 222 nm treated films (Figure 2.15a) decreases with the longer UV cure, most significantly after 20 min – by about 3 %. The $RI_{skeleton}$ is reduced

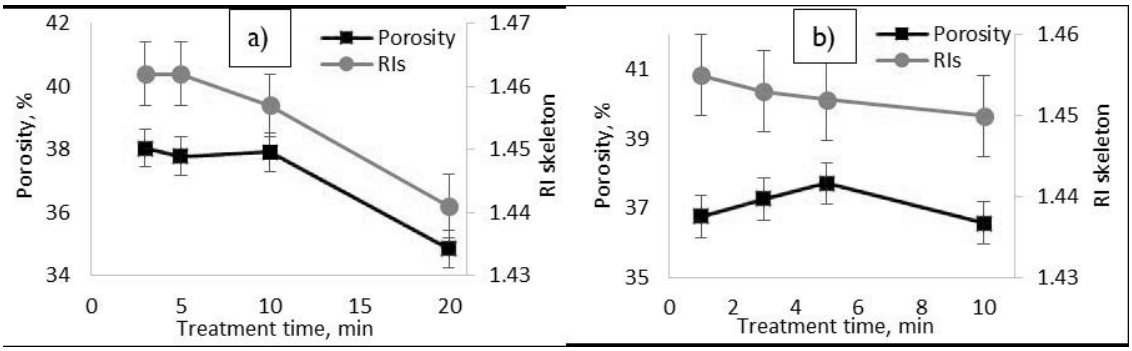

Figure 2.15. The effect of a) 222 nm and b) 172 nm cure on open porosity and $RI_{skeleton}$

with treatment time. This can be understood in terms of the self-hydrophobization process where the number of Si-C bonds is reduced while at the same time bulky Si-CH_3 groups are formed leading to the formation of micropores smaller than the kinetic size of the toluene molecule (≈0.65 nm) making them inaccessible and consequently being part of the matrix. Additionally, the $RI_{skeleton}$ seems to drop even within 10 min cure which was hinted by the evolution of the C-H stretch peaks but was not obvious from the C-H deformation band. Since the UV cures are performed at 400°C, the self-hydrophobization is expected to take place throughout the treatment. On the other hand, the more apparent trend in the $RI_{skeleton}$ might be a result of the thickness variation within a sample since it is within the experimental error.

The porosity of the 172 nm treated films increases for the initial 5 min by about 1% and decreases after 10 min back to the value measured after 1 min. The initial rise is attributed to template removal which is supported by 23% decrease of the IR signal from C-H_2 stretch (Figure 2.9). The films exposed for 3 and 5 min have overlapping bands for CH_2 stretch which is reflected in apparent increase of about 5% in the calculated AUC. The consequent porosity decrease is attributed to densification caused by the scission of methyl groups and matrix cross-linking. Furthermore, the calculated $RI_{skeleton}$ does not change beyond the experimental error (determined based on the variation of the measured RI within a sample and assuming constant porosity) when we compare 1 min through 10 min exposures. The replacement of Si-C with Si-O bonds would reduce the RI but, the loss of the CH_3 groups is expected to lead to densification. On the other hand, the volume of the mesopores decreases while that of the micropores increases (Figure 2.16) which suggests that some pores might have become so small that they are not accessible for toluene anymore which would effectively reduce the calculated $RI_{skeleton}$. The PSD calculated for 222 nm cured films does not change up to 10 min supporting the conclusion that the template is almost completely removed even for the shortest exposure of 3 min. Nevertheless, 20 min cure led to narrowing of the PSD suggesting pore collapse.

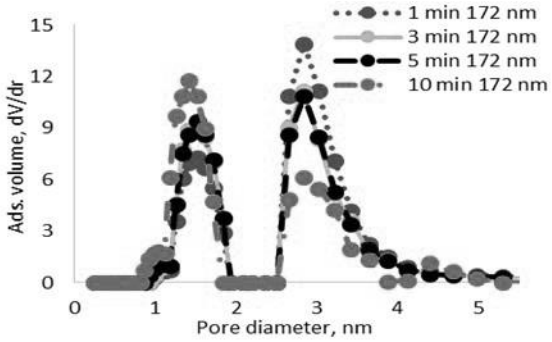

Figure 2.16. Pore size distribution calculated for 172 nm cured films

The YM and the k for the films cured with 222 and 172 nm are summarized in Figure 2.17. The damaging effect of light with λ <200 nm has been well documented[28,40] and we observed increase in YM as well as k with the increased dose. The latter has been rationalized by a

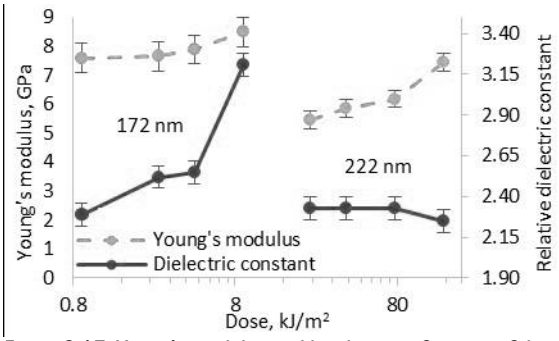

Figure 2.17. Young's modulus and k value as a function of dose (Intensity × treatment time)

densification caused by the removal of C-species and condensation of the formed radicals. It is remarkable, however, that we observed k≈2.3 with improved YM of 7.6 GPa as compared to 5.7 GPa for the 2h thermally treated film. On the other hand, in order to avoid damaging the low-k, light with λ >200 nm is usually preferred. As expected, the cure with λ =222 nm does not have a detrimental effect on the k in the investigated range. Additionally, a beneficial effect on the elastic modulus is observed – it increases steadily with treatment time from 5.5 GPa after 3 min up to 7.5 GPa after 20 min curing. We obtained similar k and YM for 1 min 172 nm and 20 min 222 nm treatment but the latter treatment is more suitable due to the lower remaining template and the absence of silanol groups.

The inability of the light produced by the LP Hg sources to remove the template is reflected in the calculated k for the films irradiated for 10 min – 2.36 and 2.34 for 254 and 185/254 nm photons, respectively. These values are ≈0.1 lower than the film which was only thermally treated for 10 min. This finding confirms the potency of the light to assist the template removal if higher intensity source is employed.

The chemical stability of the films in 0.5wt% HF has been investigated. The films irradiated between 3 and 10 min with 172 nm light are completely etched within less than one minute as a result of the replaced $SiCH_3$ with SiOH groups. The film cured for 1 min is etched for longer than 3 min, indicating lower damage by the VUV photons. On the other hand, 4 min HF dip leads to internal etching deduced by a decrease of the RI from 1.27 to 1.23 accompanied also by a thickness loss of ≈25%. The films exposed to LP Hg lamps and the thermally treated reference samples, are removed in about 6-7 min. The samples irradiated with 222 nm photons for up to 10 min show decreased chemical stability being completely etched in less than 4 min. Twenty minutes cure, on the other hand, improved the chemical stability up to 5 min.

SE modelling was performed on films dipped in HF for a duration 1 min shorter than needed for a complete dissolution. Using isotropic one-layer Cauchy function, the model becomes less adequate as compared to the films before dipping in HF resulting in an increase of the associated mean square error. The observed dispersion is better modelled by a two-layer Cauchy model. For the top layer a thickness of ≈200 nm corresponding to a RI=1.27 is calculated, while a

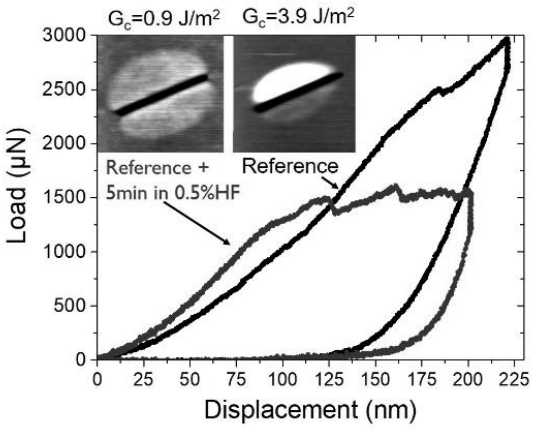

Figure 2.18. Load-displacement curves from wedge indentation tests; Inset: SPM images of (left) reference low-k after HF dip and (right) reference (2 h thermal anneal) low-k film

thickness less than 5 nm associated to a RI≈1 is reported for the bottom layer. These findings suggest that the Si-low-k interface play an important role in the explanation of the apparent difference in the chemical stability. In order to investigate if there are changes in the interfacial energy during HF dip, a tape-pull test was performed. The 2 h annealed film is easily removed by the tape after 5 min HF dip, unlike the non-dipped film which remains on the Si substrate. Quantification of the interface energies with and without 5 min dip in 0.5 wt% HF was performed by nanoindention tests using wedge indenter. For the HF-treated sample a pop-in, early indication for the formation of interface cracks, is observed (Figure 2.18) at a lower load than for the pristine one. By using the semi-empirical solution introduced by Yeap et al.,[52] the interfacial adhesion (G_c) for pristine and HF-dipped films are calculated to be 3.9 and 0.9 J/m^2, respectively. The G_c values are understood in the context of a preferential etching of the layer close to the interface. Therefore, the faster HF etch of the film irradiated with 222 nm photons compared to the reference thermally treated films seems to be due to difference in chemical composition of the bottom layer. The difference might be related to remaining template in the bottom of the thermally treated films which would be the most difficult to remove unlike the UV-treated-films where the template removal is uniform.[40] However, a film annealed for 2 h and consequently UV-treated with a broad band UV source (λ >200 nm), removing the remaining template, did not result in a shorter chemical stability. This observation might be explained by the more extended hydrophobization which would have occurred for 2h anneal. The latter is supported by the observation that the HF stability improves by about 1 min after a 20 min as compared to a 10 min 222 nm UV-cure.

In order to elucidate the mechanism of the HF etch, ToF-SIMS analysis was performed on 222 nm cured and 2h annealed films before and after HF dip. There are no differences in the profiles of Si^-, C^- and O^-. Following the HF dip, the concentration of F^- increases (Figure 2.19) throughout the thickness of the film. Furthermore, we observe more significant F^- accumulation close to the

Si interface. Additionally, three times higher increase of F^- is detected after HF-dip for the film cured with 222 nm photons compared to the HF-dipped reference film. The latter observation correlates with the almost twice faster dissolution of the 222 nm irradiated films. Considering the faster F^- accumulation at the low-k-Si interface in light of the observed decrease of the interfacial energy with HF dip we deduce the existence of a driving force for the interfacial F^- build-up. The driving force might be due to a hydrophilic layer containing OH^- groups which have been reported[53] to be eliminated and replaced by F^- as a major reaction route for SiO_2 dissolution in HF solution with pH>1.5.

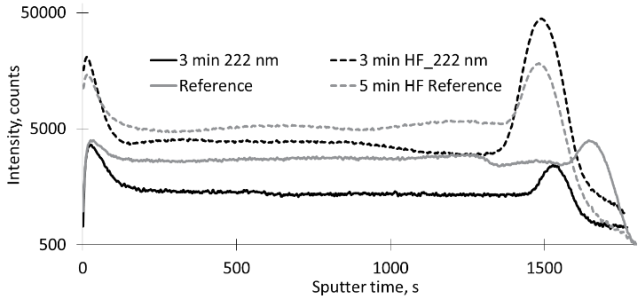

Figure 2.19. ToF-SIMS F^- profiles of reference (2 h anneal) and 3 min 222 nm cured films before and after HF dip

2.3.3. UV cure of methylene-bridged oxycarbosilanes low-k films with a target k=2.0

Upon UV cure, the same trends in the electrical and mechanical properties are observed for the more porous film of SBA Materials with a target dielectric constant of 2.0. Considering the postulated by Rakhimova et al.[20] porosity dependence of the quantum efficiency of the photo-induced C-depletion, we compare the effect of the 222 nm and 172 nm photons on the concentration of the $Si-CH_3$ bonds as deduced by the intensity of the absorption at 1275 cm^{-1} (Figure 2.20). Notably, the comparison is performed on FTIR spectra normalized to the intensity of the peak corresponding to the Si-O-Si stretching at ≈1035 cm^{-1}. The latter is a suitable normalization when the films being compared have different densities. When the change of the methyl concentration is compared between the two MeLK films, no evidence is observed for an increased quantum efficiency in the removal of the methyl groups. The 2.0 and 2.2 versions of the MeLK films maintain a similar methyl concentration as a function of the exposure time to

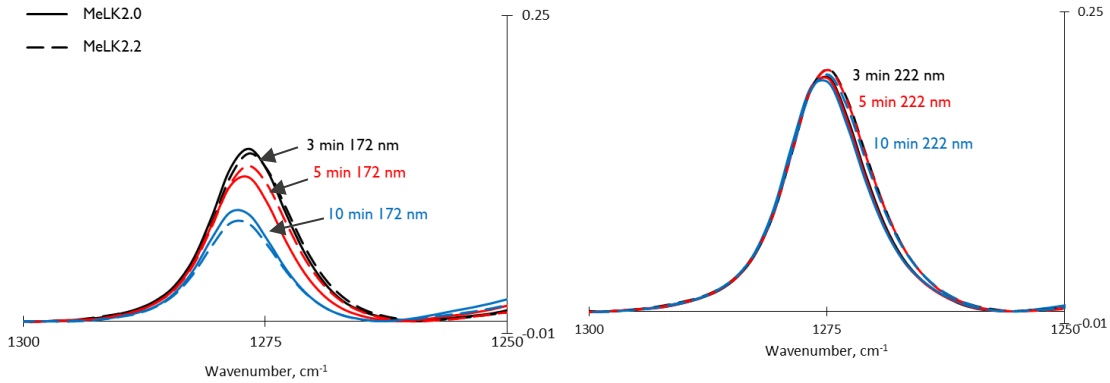

Figure 2.20. Effect of the a) 172 nm and b) 222 nm UV cure on the $Si-CH_3$ bond concentration deduced by FTIR spectra

the source with λ =172 nm (Figure 2.20 a). Additionally, the Si-CH_3 concentration seems to be similar in the MeLK2.2 and MeLK2.0 films given that the 222 nm photons were shown not to affect the Si-CH_3 groups (Figure 2.20 b). The only consistent difference between the FTIR spectra of the two films is the stronger contribution from the cage structure in the MeLK2.0 films (not shown) which is known to correlate with the low-k porosity.[37] Since generally the same chemical modifications were observed for the MeLK2.2 and MeLK2.0 films, the discussion will not be repeated here.

Similar to the MeLK2.2, both the 172 nm and the 222 nm cures lead to an increase of the Young's modulus of the MeLK2.0 with the increase in UV dose (Figure 2.21 a). Also, the improvement of the mechanical properties is more significant for the higher energy photons. Nevertheless, the damaging effect of the 172 nm light to the carbon content in the low-k results in hydrophilization and lower stability against the moisture absorption and as a result the dielectric constant increases in parallel with the YM. In contrast, the dielectric constant decreases with increasing the UV dose of the 222 nm light. Interestingly, for the 222 nm UV cure, no saturation is observed of both the YM increase and the k-value decrease and after a 20 min UV cure the YM becomes 5.55 GPa and the k reaches 2.07. These properties are comparable to the oxycarbosilane films reported by IBM[6,54] which is remarkable since the MeLK2.0 film is not synthesized by a pure bridged precursor (e.g. BTESM or BTESE) and as a result, it is expected to have a lower matrix connectivity as compared to IBM's reports. Interestingly, the decrease in dielectric constant upon UV cure with 222 nm is observed in spite of the decrease in porosity (Figure 2.21 b). Since the calculated porosity reflects only the volume accessible to toluene, the decreased porosity might be the result of the creation of micropores smaller than 0.6 nm, the kinetic size of toluene, rather than an overall increase in film density. The micropores, on the other hand, might be created as a result of the self-hydrophobization process. Importantly, since the same trends are observed in the MeLK2.2 films, we conclude that the beneficial effect of the 222 nm UV cure reproducibly results in films with promising low-k properties. Furthermore, it would be interesting to increase the UV dose further in order to find out when the beneficial effects saturate or reverse.

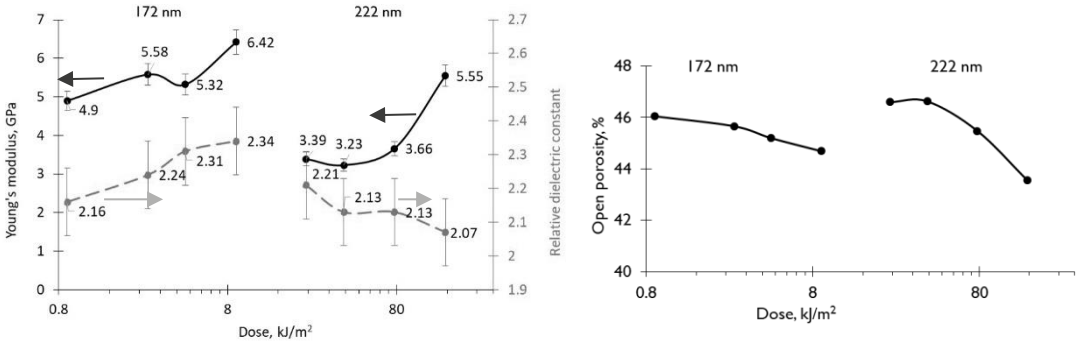

Figure 2.21. a) Young's modulus and dielectric constant, and b) porosity as a function of UV dose. The lower dose corresponds to the 172 nm UV cure while the higher dose - to the 222 nm UV cure

2.4. Conclusions

In conclusion, the UV and VUV irradiation has a more detrimental effect on ethylene-bridged oxycarbosilane films as compared to those containing methylene groups. While it is known that photons with energy lower than 6.2 eV (e.g. λ =222 nm) do not have any detrimental effect on the Si-CH_3 content, we showed that this also applies for the bridging methylene groups. On the other hand, the concentration of the bridging ethylene groups is reduced even by the 222 nm light. The difference in the stability of these two alkylene groups is more apparent when the films are exposed to 172 nm light. The ethylene groups are depleted by more than 75% while methylene loss is limited to only 40%. The experimental results were qualitatively supported by DFT quantum chemical calculations.

We noted that the methylene groups (Si-CH_2-Si) were affected little by the employed photon energies between 4.9 and 7.2 eV. The UV doses achieved by the LP Hg sources were insufficient to remove the template. Comparable k and Young's modulus values ($k \leq 2.3$, YM $\geq$ 7.5 GPa) were shown after 1 min 172 nm and 20 min 222 nm irradiations, but the latter produced superior low-k films because of a better template removal and hydrophilization discernible from the FTIR spectra. Based on the analysis of the EP data, we showed that the longer UV cure causes densification of the film, while the matrix becomes less dense. The latter was rationalized in terms of the expected reorganizations within the oxycarbosilane films, the self-hydrophobizaiton reaction. The effects of the UV cure were reproduced on higher porosity films for which the best low-k properties were obtained following a 20 min of 222 nm UV cure. In particular, a YM of 5.5 GPa was calculated for a film with a dielectric constant of 2.07. Finally, we postulated a role of the low-k-to-substrate interface in determining the stability of the films in an aqueous HF solution.

2.5. References

[1] M. R. Baklanov, K. Maex, *Philos. Trans. A. Math. Phys. Eng. Sci.* **2006**, *364*, 201.

[2] W. Volksen, R. D. Miller, G. Dubois, *Chem. Rev.* **2010**, *110*, 56.

[3] E. T. Ryan, D. Priyadarshini, S. M. Gates, H. Shobha, J. Chen, K. Virwani, A. Madan, E. Adams, E. Huang, E. Liniger, D. Collins, M. Stolfi, K. S. Yim, A. Demos, A. Grill, *2015 IEEE Int. Interconnect Technol. Conf. 2015 IEEE Mater. Adv. Met. Conf. IITC/MAM 2015* **2015**, 349.

[4] A. Grill, S. M. Gates, T. E. Ryan, S. V. Nguyen, D. Priyadarshini, *Appl. Phys. Rev.* **2014**, *1*, 11306.

[5] E. Todd Ryan, S. M. Gates, S. A. Cohen, Y. Ostrovski, E. Adams, K. Virwani, A. Grill, *J. Appl. Phys.* **2014**, *115*, 144107.

[6] G. Dubois, W. Volksen, T. Magbitang, R. D. Miller, D. M. Gage, R. H. Dauskardt, *Adv. Mater.* **2007**, *19*, 3989.

[7] H. Li, J. M. Knaup, E. Kaxiras, J. J. Vlassak, *Acta Mater.* **2011**, *59*, 44.

[8] B. D. Hatton, K. Landskron, W. Whitnall, D. D. Perovic, G. A. Ozin, *Adv. Funct. Mater.* **2005**, *15*, 823.

[9] D. Jauffrès, R. Dendievel, M. Verdier, *Thin Solid Films* **2011**, *520*, 430.

[10] H. Fan, C. Hartshorn, T. Buchheit, D. Tallant, R. Assink, R. Simpson, D. J. Kissel, D. J. Lacks, S. Torquato, C. J. Brinker, *Nat. Mater.* **2007**, *6*, 418.

[11] D. J. Michalak, J. M. Blackwell, J. M. Torres, A. Sengupta, L. E. Kreno, J. S. Clarke, D. Pantuso, *J. Mater. Res.* **2015**, *30*, 3363.

[12] H. Kazi, R. James, S. Gaddam, U. Chiluwal, J. Rimsza, J. Du, J. Kelber, In *Interconnect Technology Conference / Advanced Metallization Conference (IITC/AMC)*; 2014; pp. 237–240.

[13] S. Sugahara, K. I. Usami, M. Matsumura, *Japanese J. Appl. Physics, Part 1 Regul. Pap. Short Notes Rev. Pap.* **1999**, *38*, 1428.

[14] B. Hatton, K. Landskron, W. Whitnall, D. Perovic, G. A. Ozin, *Acc. Chem. Res.* **2005**, *38*, 305.

[15] M. R. Baklanov, C. Adelmann, L. Zhao, S. De Gendt, *ECS J. Solid State Sci. Technol.* **2014**, *4*, Y1.

[16] P. Marsik, A. M. Urbanowicz, P. Verdonck, D. De Roest, H. Sprey, M. R. Baklanov, *Thin Solid Films* **2011**, *519*, 3619.

[17] A. M. Urbanowicz, K. Vanstreels, P. Verdonck, D. Shamiryan, S. De Gendt, M. R. Baklanov, *J. Appl. Phys.* **2010**, *107*, 104122.

[18] A. Zenasni, F. Ciaramella, V. Jousseaume, C. Le Cornec, G. Passemard, *J. Electrochem. Soc.* **2007**, *154*, G6.

[19] H. Shi, D. Shamiryan, J. F. de Marneffe, H. Huang, P. S. Ho, M. R. Baklanov, In *Advanced Interconnects for ULSI Technology*; John Wiley & Sons, Ltd: Chichester, UK, 2012; pp. 79–128.

[20] T. V. Rakhimova, A. T. Rakhimov, Y. A. Mankelevich, D. V. Lopaev, A. S. Kovalev, A. N. Vasil'eva, S. M. Zyryanov, K. Kurchikov, O. V Proshina, D. G. Voloshin, N. N. Novikova, M. B. Krishtab, M. R. Baklanov, *J. Phys. D. Appl. Phys.* **2014**, *47*, 25102.

[21] B. Jinnai, S. Fukuda, H. Ohtake, S. Samukawa, *J. Appl. Phys.* **2010**, *107*, 43302.

[22] N. Matsunaga, H. Okumura, B. Jinnai, S. Samukawa, *Jpn. J. Appl. Phys.* **2010**, *49*, 04DB06.

[23] S. Uchida, S. Takashima, M. Hori, M. Fukasawa, K. Ohshima, K. Nagahata, T. Tatsumi, *J.*

Appl. Phys. **2008**, *103*, 73303.

[24] W. Volksen, S. Purushothaman, M. Darnon, M. F. Lofaro, S. a. Cohen, J. P. Doyle, N. Fuller, T. P. Magbitang, P. M. Rice, L. E. Krupp, H. Nakagawa, Y. Nobe, T. Kokubo, G. J. M. Dubois, *ECS J. Solid State Sci. Technol.* **2012**, *1*, N85.

[25] M. Redzheb, L. Prager, M. Krishtab, S. Armini, K. Vanstreels, A. Franquet, P. Van Der Voort, M. R. Baklanov, *Microelectron. Eng.* **2016**, *156*, 103.

[26] S. Eslava, F. Iacopi, A. M. Urbanowicz, C. E. a. Kirschhock, K. Maex, J. a. Martens, M. R. Baklanov, *J. Electrochem. Soc.* **2008**, *155*, G231.

[27] a. M. Urbanowicz, B. Meshman, D. Schneider, M. R. Baklanov, *Phys. Status Solidi* **2008**, *205*, 829.

[28] E. a. Smirnov, K. Vanstreels, P. Verdonck, I. Ciofi, D. Shamiryan, M. R. Baklanov, M. Phillips, *Jpn. J. Appl. Phys.* **2011**, *50*, 05EB03.

[29] S. M. Gates, D. a. Neumayer, M. H. Sherwood, A. Grill, X. Wang, M. Sankarapandian, *J. Appl. Phys.* **2007**, *101*, 94103.

[30] J. Heo, H. J. Kim, J. Han, J.-W. Shon, *Thin Solid Films* **2007**, *515*, 5035.

[31] C. Rau, W. Kulisch, *Thin Solid Films* **1994**, *249*, 28.

[32] V. Rebbin, M. Jakubowski, S. Pötz, M. Fröba, *Microporous Mesoporous Mater.* **2004**, *72*, 99.

[33] F. Hoffmann, M. Güngerich, P. J. Klar, M. Fröba, *J. Phys. Chem. C* **2007**, *111*, 5648.

[34] T. Asefa, M. J. MacLachlan, H. Grondey, N. Coombs, G. A. Ozin, *Angew. Chemie Int. Ed.* **2000**, *39*, 1808.

[35] C. Vercaemst, J. T. a Jones, Y. Z. Khimyak, J. C. Martins, F. Verpoort, P. Van Der Voort, *Phys. Chem. Chem. Phys.* **2008**, *10*, 5349.

[36] Y. Kayaba, F. Nishiyama, Y. Seino, T. Kikkawa, *J. Phys. Chem. C* **2011**, *115*, 12981.

[37] A. Grill, D. A. Neumayer, *J. Appl. Phys.* **2003**, *94*, 6697.

[38] S. Sugahara, T. Kadoya, K. Usami, T. Hattori, M. Matsumura, *J. Electrochem. Soc.* **2001**, *148*, F120.

[39] A. M. Dattelbaum, M. L. Amweg, J. D. Ruiz, L. E. Ecke, A. P. Shreve, A. N. Parikh, *J. Phys. Chem. B* **2005**, *109*, 14551.

[40] L. Prager, P. Marsik, L. Wennrich, M. R. Baklanov, S. Naumov, L. Pistol, D. Schneider, J. W. Gerlach, P. Verdonck, M. R. Buchmeiser, *Microelectron. Eng.* **2008**, *85*, 2094.

[41] V. Jousseaume, A. Zenasni, O. Gourhant, L. Favennec, M. R. Baklanov, *Adv. Interconnects ULSI Technol.* **2012**, 35.

[42] A. D. Becke, *J. Chem. Phys.* **1996**, *104*, 1040.

[43] C. Lee, W. Yang, R. G. Parr, *Phys. Rev. B* **1988**, *37*, 785.

[44] R. Bauernschmitt, R. Ahlrichs, *Chem. Phys. Lett.* **1996**, *256*, 454.

[45] P. Innocenzi, *J. Non. Cryst. Solids* **2003**, *316*, 309.

[46] M. Kanezashi, M. Kawano, T. Yoshioka, T. Tsuru, *Ind. Eng. Chem. Res.* **2012**, *51*, 944.

[47] R. Van Grieken, G. Calleja, G. D. Stucky, J. a. Melero, R. a. García, J. Iglesias, *Langmuir* **2003**, *19*, 3966.

[48] P. G. Pai, *J. Vac. Sci. Technol. A Vacuum, Surfaces, Film.* **1986**, *4*, 689.

[49] M. Milosevic, S. W. King, *ECS J. Solid State Sci. Technol.* **2015**, *1*, N3146.

[50] Y.-H. Kim, M. S. Hwang, H. J. Kim, J. Y. Kim, Y. Lee, *J. Appl. Phys.* **2001**, *90*, 3367.

[51] M. Baklanov, K. Maex, M. Green, *Dielectric Films for Advanced Microelectronics*; Baklanov, M. R.; Green, M. L.; Maex, K., Eds.; John Wiley & Sons, Ltd: Chichester, UK, 2007.

[52] K. B. Yeap, K. Zeng, H. Jiang, L. Shen, D. Chi, *J. Appl. Phys.* **2007**, *101*, 123531.

[53] Q. T. Le, G. Vereecke, H. Struyf, E. Kesters, M. R. Baklanov, In *Advanced Interconnects for ULSI Technology*; John Wiley & Sons, Ltd: Chichester, UK, 2012; pp. 129–171.

[54] G. Dubois, W. Volksen, T. Magbitang, M. H. Sherwood, R. D. Miller, D. M. Gage, R. H. Dauskardt, *J. Sol-Gel Sci. Technol.* **2008**, *48*, 187.

CHAPTER 3. EFFECT OF LASER ANNEAL ON OXYCARBOSILANE LOW-K PROPERTIES

This chapter describes the investigation of the laser anneal's ability to remove the template from and to improve the Young's modulus of oxycarbosilane low-k films. The work was performed in a collaboration with Ultratech who performed the laser anneals in their facility in San Jose, California, USA. As a result, this work was performed in two stages. The first stage included laser anneal of as-deposited films in *ambient* lab atmosphere by two different laser sources – a visible wavelength nanosecond laser with λ =532 nm and an infrared CO_2 laser with λ =10.6 μ m. Nevertheless, only the results from the anneal with the IR laser are included here since no template removal was observed following the anneal with the visible laser. In the second stage, the laser anneals were performed in a controlled N_2 atmosphere with the same IR laser source. The IR laser anneal affects mostly the organic content of the organosilicate matrix leading to depletion and reorganization. Nevertheless, when compared to a reference film annealed in a furnace at 400°C for 2 h, the tested conditions reveal a processing window which allows for a 13% improvement of the Young's modulus while not impacting the dielectric constant of 2.25.

***M. Redzheb**, S. Armini, K. Vanstreels, J. Meersschaut, M. R. Baklanov, Y. Wang, S. Chen, V. Le, M. Awdshiew, P. Van Der Voort, Laser anneal of oxycarbosilane low-k film, 2016 IEEE International Interconnect Technology Conference / Advanced Metallization Conference (IITC/AMC), 156-158 (2016)*

3.1. Introduction

Reliable ultra-low-k materials are needed in order to reduce the resistance-capacitance signal delay in future generation ultra-large scale integrated interconnects.[1,2] In order to reduce the dielectric constant below 2.5, porosity needs to be introduced in the organosilicate films. However, due to the detrimental effect of this approach on the mechanical reliability, treatments for improvement of the mechanical stability are under investigation. The most popular approach for the enhancement of the Young's modulus has been the application of ultra-violet (UV) irradiation with a wavelength longer than 200 nm. The UV cure (UV irradiation at temperature ≈ 400°C) is used for both template removal and to promote crosslinking in the porous film. Alternatively, a short pulse laser anneal has been investigated for improving the mechanical properties of low-k films. Volksen and co-authors[3] investigated the laser anneal of dense and porous organosilicate films and noted the ability of this approach to improve the Young's modulus with a limited negative impact on the dielectric constant. On the other hand, Raymunt et al.[4] reported theoretical and experimental investigation of the effect of a laser anneal on the bonding structure of an organosilicate low-k film. Nevertheless, these studies did not consider the laser anneal for a porogen removal or investigate its effects on oxycarbosilane films which contain backbone carbon as bridging alkylene (Si-$(CH_2)_x$-Si) groups. The latter have been shown[5,6] to be more promising low-k candidates than the conventional carbon-doped oxides where carbon is present solely as $–CH_3$ groups.

3.2. Experimental Section

The investigated films were prepared by using the sol-gel method where a stabilized sol is spin-deposited onto a Si substrate. The coating sol was prepared by mixing a matrix and a template solution. The former was obtained by stirring 1.1 ml 1,2-bis(triethoxysilyl)ethane (BTESE), 0.56 ml 0.02 molar hydrochloric acid, and 0.64 ml methyltriethoxysilane (MTES) in 2 ml ethanol at 60°C for 1 hour. The BTESE is the source of the bridging ethylene groups (Si-CH_2-CH_2-Si) while the MTES is the source of methyl groups making the film hydrophobic. In parallel, the template solution was prepared by dissolving 0.3763 g polyoxyethylene (18) tridecyl ether in 16 ml 1-methoxy-2-propanol after stirring for ca. 45 min at room temperature (RT). Next, the template solution was added to the cooled down to RT matrix solution and further stirred for 15 min at RT. Finally, the mixture was transferred to a 50 ml polyethylene bottle and aged for 24 hours at RT. In the first experiment, the solution was spin-coated on 3.5x3.5 cm square Si coupons while in the second, on a 300 millimetre diameter Si wafer at 1500 rpm for 60 s. Following the deposition, the film was soft baked at 150°C for 2 min in an ambient atmosphere in order to promote polycondensation and solvent evaporation. The resulting thickness was ca. 216 nm. A control sample was annealed in N_2 atmosphere at 400°C for 2h.

The laser anneals from the first experiment were performed on a lab tool in a non-controlled ambient atmosphere. Two laser sources were investigated – a green laser with λ =532 nm and an infrared CO_2 laser with an output peak around 943 cm^{-1} out of the resonance frequency of the organosilicate matrix. The absorption of the CO_2 radiation is facilitated by the free carriers in the n-type Si substrate.[4] Temperatures between 725 and 1180°C were detected by a pyrometer calibrated to the melting temperature of an undoped Si. Two laser exposure durations (dwell time), 400 and 800 μs, were investigated. The samples were additionally heated by a hot plate at 150°C.

At stage two, the soft-baked wafer was laser-annealed in an Ultratech LSA201 system equipped with a CO_2 infrared laser. Eight power densities with a dwell time of 800 μ s were used to generate eight test patterns with width of 30 mm on the wafer. The scanning step size was 25% meaning that each spot was annealed four times. These annealing conditions allow for a wafer 300 mm in diameter to be annealed within 3 min. The wafer was additionally heated by a hot plate at 150°C. Temperatures between 900 and 1145°C were detected by the pyrometer. The treatments were performed in an inert N_2 atmosphere.

3.3. Results and Discussion

3.3.1. Screening for laser anneal conditions for oxycarbosilanes low-k films

The temperature values observed during the laser anneal (LA) cannot be directly compared to the furnace anneal temperature. One reason is the fact that the temperature deduced during LA is that of the silicon substrate and the thermal profile normal to the substrate is not available. In other words, it is not entirely clear the actual temperature to which the low-k is exposed. Furthermore, unlike a furnace anneal where the low-k films are exposed to the set temperature for hours, the LA is less than a millisecond. For instance, it has been demonstrated that resist films can be annealed at a ~3 times higher temperature than their glass transition temperature when employing sub-millisecond laser anneal.[7]

Increasing the laser power, which corresponds to an increase in substrate temperature, results in a decrease of the refractive index indicating the removal of the template (Figure 3.1). The

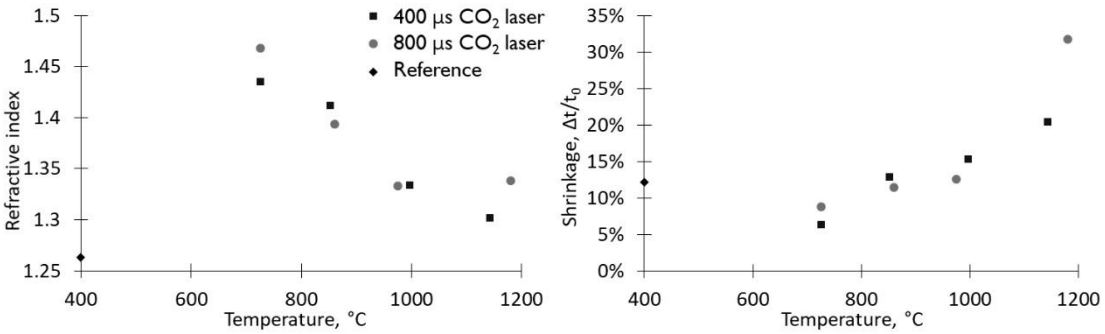

Figure 3.1. Refractive index (a) and Δ thickness (b) as a function of laser anneal temperature compared to a reference annealed at 400°C for 2h in N_2

lowest RI is reached for the highest temperature of 1142°C which is close to the melting temperature of the silicon substrate. Still, the lowest RI of 1.3 achieved by the laser anneal is higher than the RI of the reference film, 1.26 (Figure 3.1). The latter is probably due to a densification or a pore collapse of the low-k matrix caused by the high annealing temperatures. This explanation is supported by the higher than the 12% reference thickness change observed for the films annealed at a temperature higher than 1000°C (Figure 3.1). Furthermore, the porosity of the film laser annealed at 1142°C is 32.8% as compared to the 38% porosity of the reference film.

Based on the FTIR spectra, the template seems not completely removed at temperatures around and below 1000°C. The presence of the template can be deduced by considering both the strong C-H_2 stretch-related absorptions at 2885 cm^{-1} and 2910 cm^{-1} and the broad –OH-related absorption between 3100 cm^{-1} and 3700 cm^{-1}. The evolution of the template removal can also be monitored from a peak at 1730 cm^{-1} which is not present in the as-deposited films and appears following the laser anneal. The peak is attributed to the formation of C=O bonds as part of a formic acid termination identified during the thermal decomposition of poly(ethylene oxide)-containing molecules in an ambient oxygen-containing atmosphere.[8]

Remarkably, according to the FTIR analysis, the laser anneal does not seem to affect the carbon covalently bonded to the matrix, i.e. the ethylene and the methyl groups, below a temperature of 1000°C. The intensity of the peaks attributed to the methyl and ethylene absorptions at 1275 cm^{-1} and 1412 cm^{-1}, respectively, does not change below a temperature of 1000°C (Figure 3.2). Nevertheless, the temperature required for a complete template removal, as inferred from the lowest value of RI, which is higher than 1000°C cause a significant carbon depletion from the low-k matrix. Unfortunately, FTIR does not allow for a definite analysis of which among the

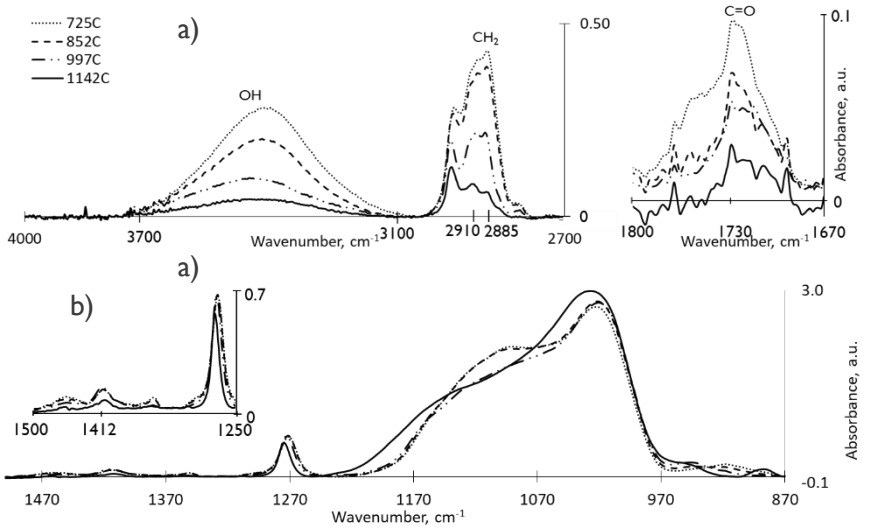

Figure 3.2. FTIR spectra showing a) the template removal efficiency of the laser anneal and b) its effect on the low-k matrix

methyl and the ethylene groups are more strongly affected by the laser anneal since the two peaks mentioned, 1275 cm^{-1} and 1412 cm^{-1}, have been attributed to both the Si-CH_3[9] and Si-CH_2-CH_2-Si[10] groups since they are the result of the deformational modes of the C-H bonds. On the other hand, the C-H_x stretching modes at wavenumbers just below 3000 cm^{-1} overlap with absorptions from the template for which it is difficult to deduce whether it is completely removed. It seems more likely that effectively the ethylene groups would be depleted preferentially since they might be transformed into methyl groups by a scission of the C-C bonds. More importantly, an evidence of the preferential ethylene groups' depletion can be obtained from a more detailed analysis of the 1275 cm^{-1} peak. When the peak is observed in a low-k film containing carbon only as Si-CH_3 groups, it is narrower than when there is an additional contribution from the ethylene groups. Compared to the laser anneal at 1000°C, the anneal at 1150°C results in a lower intensity but also a narrower peak at 1275 cm^{-1} showing the significant depletion of the ethylene groups whose concentration seems to be so low that they do not contribute to the 1275 cm^{-1} peak. Finally, the damaging effect of the 1150°C laser anneal is manifested by the appearance of an absorption at 883 cm^{-1} which is attributed to the presence of Si-H bonds which are most likely the result of the formation of dangling bonds which are consequently passivated by H radicals formed from the decomposition of the organics.

3.3.2. IR laser anneal in a controlled inert atmosphere

Given the results from the first evaluation stage of the effect of the laser anneal on the low-k films, in the second stage we focused on the laser anneal temperatures around 1000°C, in particular between 900°C and 1145°C. Within this temperature range, the lowest RI is observed at ≈1040°C while at lower and higher temperatures slightly higher RIs are measured (Figure 3.3) but these differences in the temperature range above 980°C are not statistically significant. Additionally, toluene ellipsometric porosimetry (EP) measurements reveal that there is no difference in the open porosity, calculated to be 38 %, for the annealing conditions above 940°C. The only condition which can definitely be claimed to result in an incomplete template removal is the annealing at 900°C in which case 3% lower open porosity is calculated. The calculated pore size distribution (PSD) further supports this interpretation by indicating narrower PSD for

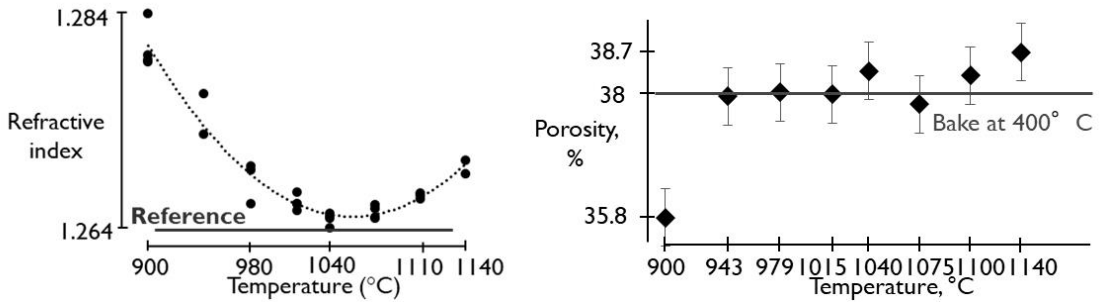

Figure 3.3. Refractive index and open porosity results show that the laser anneal between 940°C and 1140°C leads to films with similar optical properties

the film cured at 900°C which is explained by the remaining template on the pore walls effectively making the pores smaller. No differences in the PSD are observed for the films annealed at a temperature higher than 900°C. The EP data additionally indicates a lack of pore collapse or significant densification which might have been expected[4] given the high temperatures achieved. Furthermore, it is important to limit the shrinkage of the film since it contributes to the compressive stress during integration. The shrinkage observed for the reference films, furnace annealed at 400°C in N_2 ambient for 2 h, is ca. 11 % while for the laser annealed films we observe that increasing the laser power results in a steady increase of the shrinkage up to 19.4 % for the highest laser power utilized in this study. The anneals at a temperature up to 1040°C allow to achieve shrinkage comparable to the one observed in the reference film.

Nevertheless, the FTIR spectra (Figure 3.4) reveal removal of the organics from the film even for the lowest laser power applied. This is further observed in the ERD spectra where C content decreases from ca. 22% to 15% when the anneal temperature exceeds 1000°C. Furthermore, FTIR analysis indicates faster reduction of the bridging ethylene groups as compared to the methyl groups and virtually complete depletion at the highest laser power. ERD and FTIR further

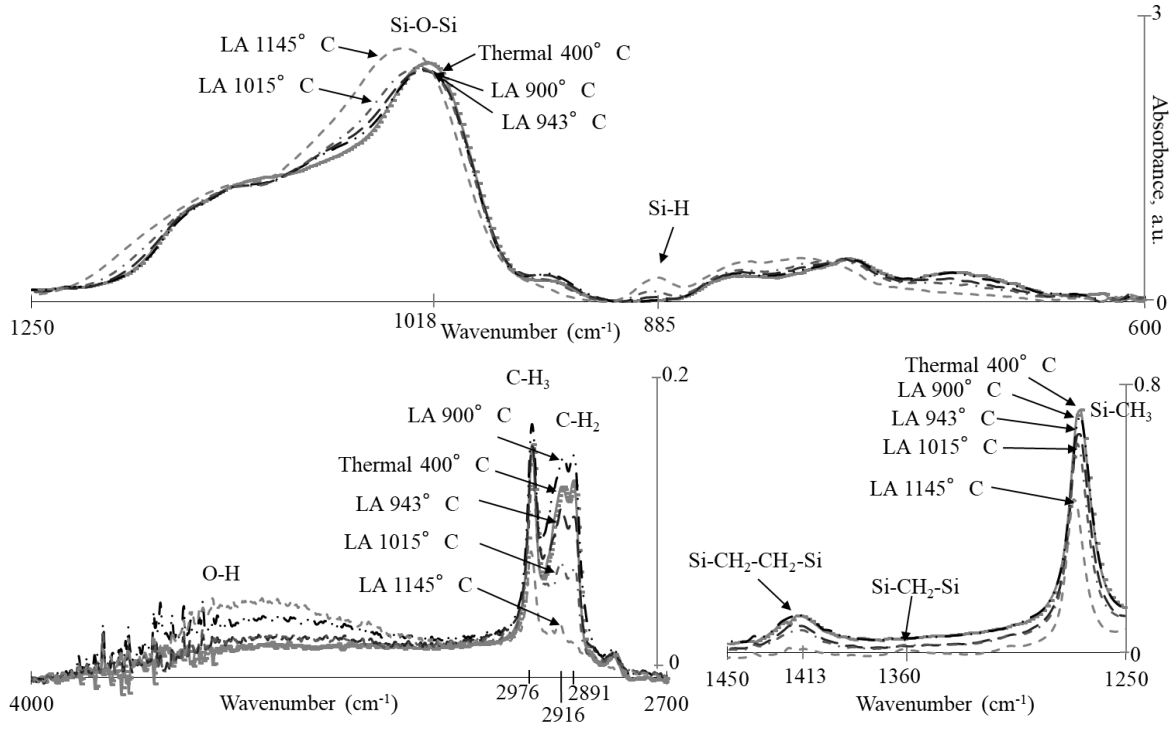

Figure 3.4. FTIR spectra of the laser annealed films compared to the reference film annealed at 400°C for 2h

agree on the Si-O bond formation which is seen in the FTIR spectra as a blue shift as well as intensity increase of the region attributed mainly to Si-O-Si absorption and as an increase in the relative content of Si and O in the ERD spectra. Nevertheless, while based on the FTIR spectra, a further removal of organics with higher temperature is apparent, the C-content deduced from the ERD spectra stays constant. The latter might point to a bond redistribution which was

discussed in a previous study.[3] One manifestation of the bond rearrangements seems to be the formation of Si-CH_2-Si groups evident by a weak peak at 1360 cm^{-1}. The latter can be explained by the cleavage of the C-C bonds in ≡ Si-CH_2-CH_2-Si≡ groups in combination with the presence of ≡ Si• radical due to ≡ Si-CH_3 bond dissociation. Another modification of the films evident by peaks at 885 and 2245 cm^{-1} is the appearance of ≡ Si-H bonds. These compositional changes evident from the FTIR spectra reveal the numerous passivation processes occurring with the ≡ Si• radicals formed due to the breaking of the ≡ Si-C bonds. Additionally, the C-extraction leads to surface hydrophilization for the highest temperatures achieved. The surface water contact angle (WCA) was measured to be around 90° for temperatures below 1100°C while at a T≥1100°C, a statistically significant decrease of the WCA occurs leading to a value of 80° after applying the highest laser power.

The modifications of the films were further monitored by spectroscopic ellipsometry in the range from 1.4 to 8 eV. The ellipsometric dispersion observed for the samples annealed at a temperature higher than 1000°C can be modelled by the sum of two Lorentz oscillators while only one is sufficient for the film annealed at 900°C. The absorption common for all of the samples is centered at ca. 8.5 eV and is attributed to the optical bandgap of the low-k.[11,12] On the other hand, the second absorption is centered at 6.7 eV (Figure 3.5). The latter may be attributed to the formation of O_3≡ SiSiSi≡ O_3 structures[13] which once again indicate the extensive modifications of the low-k matrix.

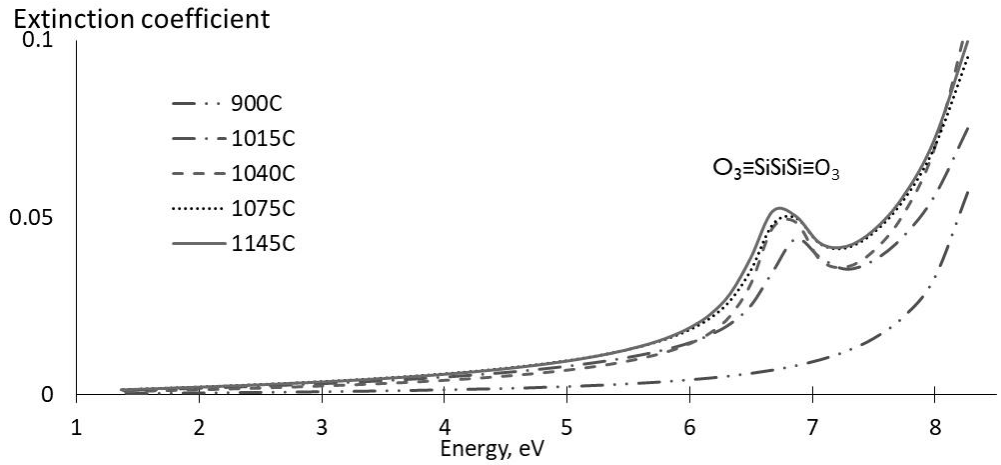

Figure 3.5. Modelled spectroscopic ellipsometric dispersion of the extinction coefficient showing the appearance of an absorption at 6.7 eV when the film is annealed at a temperature higher than 1000°C

The Young's modulus and the dielectric constant values increase with higher laser power (Figure 3.6) which is consistent with the deduced bond rearrangements. The higher k observed for the film cured at 900°C also supports the hypothesis for an incomplete template removal. In spite of the relatively damaging effect of the laser anneal to the chemical structure of the low-k film, we find a window of processing conditions around 1000°C which results in virtually the same dielectric constant as for the reference film and a higher elastic modulus. In particular, the laser anneal at 1015°C leads to about a 13% higher YM value of 4.59 GPa as compared to the

reference film with YM=4.07 GPa and the dielectric constant calculated for both of the films is 2.25.

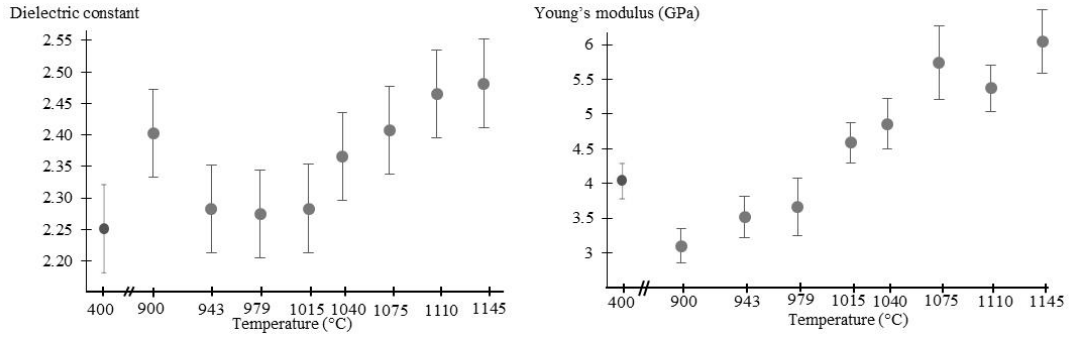

Figure 3.6. Dielectric constant and Young's modulus as a function of the laser annealing temperature

3.4. Conclusions

Laser anneal was investigated for porogen removal and its ability to improve the mechanical strength of oxycarbosilane ultra low-k films. The increase in the Young's modulus is the result of the high activation energy achieved as a result of the high temperatures around and in excess of 1000°C which ensures the condensation of the silanol groups and the densification of the matrix. High laser power corresponding to a surface temperature of ca. 1000°C is required in order to achieve complete template removal. To obtain a -OH-free low-k film, the laser anneal needs to be performed in an inert atmosphere. Extensive bond rearrangements mostly related to the replacement or reorganization of the organic content of the organosilicate matrix are shown. Around 1000°C, there exists a processing window which allows for a 13% higher Young's modulus value as compared to the reference films annealed in a furnace at 400°C, with no impact on the dielectric constant calculated to be 2.25. Remarkably, no significant film densification is deduced within the processing window.

3.5. References

[1] M. R. Baklanov, C. Adelmann, L. Zhao, S. De Gendt, *ECS J. Solid State Sci. Technol.* **2014**, *4*, Y1.

[2] G. Dubois, W. Volksen, In *Advanced Interconnects for ULSI Technology*; John Wiley & Sons, Ltd: Chichester, UK, 2012; pp. 1–33.

[3] W. Volksen, G. Dubois, A. Kellock, T. P. Magbitang, R. D. Miller, D. Miller, S. Cohen, E. E. Simonyi, L. Ramirez, D. Markle, S. Chen, S. Zhou, X. Wang, Y. Wang, *J. Electrochem. Soc.* **2008**, *155*, G224.

[4] A. M. Raymunt, R. T. Bell, M. O. Thompson, P. Clancy, *J. Phys. Chem. C* **2015**, *119*, 12616.

[5] G. Dubois, W. Volksen, T. Magbitang, R. D. Miller, D. M. Gage, R. H. Dauskardt, *Adv. Mater.* **2007**, *19*, 3989.

[6] D. J. Michalak, J. M. Blackwell, J. M. Torres, A. Sengupta, L. E. Kreno, J. S. Clarke, D.

Pantuso, *J. Mater. Res.* **2015**, *30*, 3363.

[7] F. Bérubé, S. Kaliaguine, *Microporous Mesoporous Mater.* **2008**, *115*, 469.

[8] A. Grill, D. A. Neumayer, *J. Appl. Phys.* **2003**, *94*, 6697.

[9] S. Sugahara, K. I. Usami, M. Matsumura, *Japanese J. Appl. Physics, Part 1 Regul. Pap. Short Notes Rev. Pap.* **1999**, *38*, 1428.

[10] S. W. King, B. French, E. Mays, *J. Appl. Phys.* **2013**, *113*, 44109.

[11] X. Guo, H. Zheng, S. W. King, V. V. Afanas'ev, M. R. Baklanov, J.-F. de Marneffe, Y. Nishi, J. L. Shohet, *Appl. Phys. Lett.* **2015**, *107*, 82903.

[12] K. Awazu, H. Kawazoe, K. I. Muta, *J. Appl. Phys.* **1991**, *70*, 69.

CHAPTER 4. PROPERTIES OF SELF-ASSEMBLY-BASED LOW-K FILMS: EFFECT OF THE REPLACEMENT OF SI-O-SI BY SI-CH_2-SI

This chapter reports the effect of the replacement of Si-O-Si by Si-CH_2-Si groups on the mechanical and electrical properties of silica-based hybrid sol-gel thin films. For a reliable inference, two sets of organosilica films were synthesized – one consisting of a silica matrix decorated with methyl groups (Si-CH_3) while the other further incorporating bridging methylene (Si-CH_2-Si) functionalities. As a result, at the film density of 0.87 g cm^{-3}, a higher Young's modulus of 6.6 GPa was deduced for the film containing Si-CH_2-Si groups compared to 5.3 GPa for the one with Si-O-Si functionalities. Concurrently, the introduction of the methylene bridging groups leads to a dielectric constant increase from 2.12 to 2.27. Furthermore, the type of surfactant, ionic or nonionic, employed as a templating agent has a negligible effect on the electrical properties and the reliability performance of the porous organosilica films. When dipped in 0.5 wt% HF, internal etching is observed for the films containing the methylene groups while the films without the organic bridges are internally etched only if an organic solvent is added to the aqueous HF solution.

***M. Redzheb**, S. Armini, T. Berger, M. Jacobs, M. Krishtab, K. Vanstreels, S. Bernstorff and P. Van Der Voort, On the mechanical and electrical properties of self-assembly-based organosilicate porous films, Journal of Materials Chemistry C, (2017)*

4.1. Introduction

Silica-based porous materials are utilized as an antireflective, antifogging and superhydrophobic coating on solar cells[1,2], interlayer and intermetal dielectrics in integrated circuits, chromatographic supports, selective adsorbents[3], bone grafts for bone tissue regeneration[4], sensors for environmentally responsive materials, photonic devices and others[5]. For many of these applications, the mechanical stability of the porous silica-based material has a limiting role on the overall device performance. As a result, the superior Young's modulus (YM) values reported for porous oxycarbosilane (OCS) and periodic mesoporous organosilica (PMOs) films as compared to other silica-based films have attracted the attention of the semiconductor industry[6–8]. The higher YM values have been attributed to the presence of the Si-$(CH_2)_n$-Si units[6,9] which has been generally supported by the modelling work[10]. Nevertheless, deducing the contribution of the organic bridging groups to the YM seems to be a difficult experimental task when the films being compared are obtained via two different deposition techniques, e.g. spin-on vs plasma-enhanced chemical vapour deposition (PECVD), or when the films are expected to have a different matrix connectivity, like in methylsilsesquioxanes (MSSQ) vs OCS.[11,12] Moreover, the matrix elastic moduli of OCS films reported[6,11–13] so far are lower than those observed for silica. Additionally, the mechanical properties of polycarbosilane films[14,15] have been shown to be similar to those of oxycarbosilanes. On the other hand, a direct comparison between the YM of porous silica and porous OCS or PMO films is challenging due to an overestimation of the YM in hydrophilic SiO_2 films caused by the presence of absorbed moisture.[16,17] Therefore, an appropriate comparison of the mechanical properties requires films which are hydrophobic, possess similar pore volume and/or dielectric constant, as well as matrix connectivity, and differ only in the presence of the organic bridging groups. In order to meet these requirements, we synthesized two sets of films - one with a molar ratio of tetraethylorthosilicate (TEOS) : methyltriethoxysilane (MTES) = 1:1 and the second with a molar ratio of bis(triethoxysilyl)methane (BTESM) : methyltriethoxysilane (MTES) = 1:1. The TEOS and BTESM precursors are the source of the Si-O-Si and Si-CH_2-Si groups. The MTES precursor is employed in order to obtain hydrophobic films[18–21]. Furthermore, the incorporation of the precursors in the final films is expected to be similar between the two sets since the bridged precursor bis(triethoxysilyl)ethane has been shown to have polycondensation kinetics similar to TEOS.[20] As a result of the comparable precursor incorporation, a similar degree of matrix connectivity is expected to be achieved. Finally, the pore volume can be controlled by optimizing the surfactant to precursor ratio.

The use of surfactants in the synthesis solution enables the control of the films' pore arrangement (mesophase).[22] The films' mesophase depends on the synthesis parameters such as the surfactant to precursor ratio, the pH, the solution aging conditions such as the aging

temperature and time as well as the organosilica precursor.[5] All of these parameters, ultimately, determine the degree of polycondensation and the size distribution of the organosilica oligomers. Consequently, the interaction of the organosilica oligomers with the surfactant molecules is one of the main determinants of the film's final mesophase. On the other hand, the mesophase can also be controlled by the deposition conditions such as the presence of an electric field, the surface energy of the substrate, the vapour pressure of the solvents, the ambient relative humidity, the atmospheric ethanol content, the deposition temperature and the substrate's spin speed.[5,23] Therefore, obtaining a desired mesophase using different surfactants would require a specific and, probably, different organosilica oligomer distribution as well as different surfactant to precursor ratios for each surfactant. Such an experimental design, in an attempt to deduce the effect of the replacement of the Si-O-Si by the Si-CH_2-Si groups, would introduce the confounding variable of the significant differences in the films' matrices and would, most likely, result in large differences in the films' pore volumes. Furthermore, if the pore order is achieved in some of the films but not in the others or if the pore order is different in the different films, the interpretation of the results would be further complicated. Instead, in this study, the (organo)silica precursors are pre-condensed at 60°C for 1 h before the template is introduced and the resulting solution is further aged at room temperature for 24 h before deposition. These synthesis conditions combined with the use of 50% MTES make it unlikely that an ordered porosity film will be achieved. The MTES disrupts the ordered porosity when it is polycondensed together with the TEOS and the (organo)silica precursor mixture contains more than 33% MTES.[24–26] The higher than 33% MTES content can be incorporated without disrupting the mesophase by a two-step synthesis procedure where the MTES is introduced into the solution just before the deposition.[27–29]

There are numerous studies which considered spin-coated organosilica dielectrics for low-k application but none of them provides a systematic study of all the parameters on which the YM depends. Ideally, in order to engineer the optimal YM for a low-k film one needs to consider pore volume, film and skeleton densities, chemical composition, relative content of the different siloxane ring sizes, average connectivity number of the skeleton, pore shape and organization, as well as, pore size distribution. We compare the YM of the films as a function of Si-CH_2-Si vs. Si-O-Si functionalities incorporated into the matrix, while keeping constant the matrix connectivity of the layers. In addition, the impact of the nature of the templating surfactant on the electrical reliability of the low-k film is discussed.

4.2. Experimental Section

Tetraethylorthosilicate (TEOS), methyltriethoxysilane (MTES), 1-methoxy-2-propanol, polyoxyethylene (10) stearyl ether (Brij-76), Polyoxyethylene (4) lauryl ether (BrijL4), Pluronic F127 and cetyltrimethylammonium chloride (25 wt%, CTAC) were purchased from Sigma

Aldrich, bis(triethoxysilyl)methane (BTESM) was obtained from Fluorochem, hydrochloric acid (HCl, 37%) was acquired from KMG Chemicals, and absolute ethanol (99.9%) was purchased from Merck. All materials were used as received.

TEOS	MTES	BTESM	surfactant	Label[1]
1	1	0	0.126	MSQC
1	1	0	0.210	MSQL4
1	1	0	0.077	MSQS10
1	1	0	0.004	MSQF127
0	1	1	0.240	OCSC
0	1	1	0.320	OCSL4
0	1	1	0.124	OCSS10
0	1	1	0.004	OCSF127

Table 4.1. Molar ratio of the reagents employed in the synthesis of the films. [1]The labels reflect the matrix composition, MSQ for methylsilsesquioxane-like films and OCS for oxycarbosilane-like films, and the associated templating surfactant where C=CTAC, L4=BrijL4, S10=BrijS10 and F127=PluronicF127

Two types of organosilica thin films were prepared using a sol-gel method: one with silica matrix and containing Si-CH_3 groups (MSQ), and another with hybrid matrix containing both Si-CH_2-Si and Si-O-Si bonds as well as Si-CH_3 groups (OCS). Furthermore, each matrix type was templated by four different surfactants – one ionic, CTAC, and three non-ionic, Brij L4, Brij S10 and Pluronic F127. The synthesis conditions were optimized in order to obtain films with similar pore volume and details about the reagents' molar ratios can be found in Table 4.1. A typical synthesis included the preparation of two solutions, a matrix and a template solution, in parallel. The matrix solution was obtained by mixing 2 ml ethanol, 0.58 ml 0.02 molar HCl, 1.048 ml BTESM and 0.6 ml MTES by stirring and refluxing for 1 h at 60°C. When a film morphology is desired, the acidic (organo)silica synthesis is more suitable than the neutral or basic pH since it results in more polymer-chain-like (organo)silica oligomers.[30] In the meantime, the template solution was prepared by mixing 0.34 ml BrijL4 with 12 ml 1-methoxy-2-propanol. Next, the two solutions were mixed at room temperature and stirred for 15 min. Before deposition the solutions were aged in a PE bottle at room temperature for 24 h. The solutions were spin-coated at 1500 rpm on 300 mm Si wafers on which native oxide had been grown. Next, the films were soft-baked at 150°C in ambient atmosphere for 2 min and hard-baked at 400°C in N_2 for 2 h. Finally, in order to simulate a common practice in the IC industry, the films were UV-cured at 400°C in N_2 for 2 min with a broadband UV source with λ >200 nm.[6]

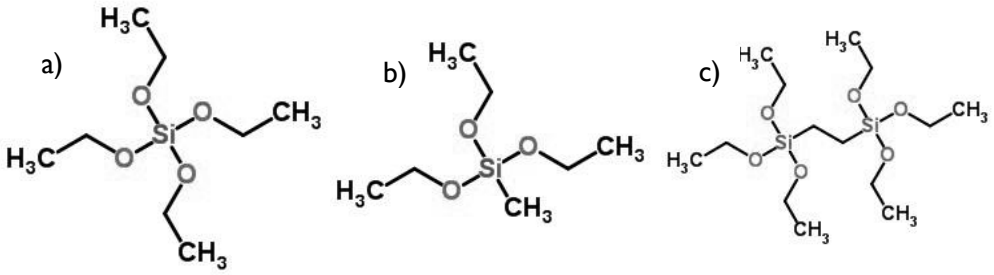

Figure 4.1. Structure of the employed (organo)silica precursors: a) TEOS; b) MTES; c) BTESM

4.3. Results and Discussion

4.3.1. Chemical composition of OCS and MSQ films

As a result of the employed synthesis strategy, if the precursors contributed to the final matrix compositions in proportions dictated by their molar ratios in the synthesis solutions, two times larger carbon content would be expected in the OCS as compared to the MSQ films. Consistently, a depth-resolved x-ray photoemission spectroscopy (XPS) study revealed that the elemental composition of MSQ was Si:C:O = 35:8:57 as compared to 34:15:51 in OCS films (Figure 4.2). Clearly, all of the carbon in the MSQ matrices is incorporated as methyl (-CH_3) groups. Nevertheless, the attribution of the additional carbon in the OCS films to methylene (-CH_2-) groups is not straightforward due to the self-hydrophobization[31] process which leads to transformation of the methylene groups to methyl groups at elevated temperatures in the presence of Si-OH. The higher carbon content in the OCS films is at the expense of the Si-O-Si groups which is why the binding energy of the Si (2p) peak is lower in the OCS than in the MSQ (Figure 4.2). Nevertheless, the binding energy of the Si 2p peak cannot provide a definitive proof of the incorporation of the carbon in the OCS as a bridging Si-CH_2-Si since in both $(R_3SiO)_3$-Si-CH_3 and $(RO)_3$-Si-CH_2-Si-(RO_3), the silicon atom is in a T group, i.e. connected to three -O-SiR_3 functionalities and one heterofunctionality such as the methyl and methylene groups. On the other hand, in the OCS films, the chemical bonding environment of the carbon is expected to consist of not only one silicon and three hydrogen atoms but also of two silicon atoms and two hydrogen atoms. Therefore, the binding energy of the C (1s) peak in the OCS films indicates the presence of the Si-CH_2-Si groups.[32]

The chemical compositions of the films were further deduced from the FTIR spectra which were normalized to the thickness of the films (Figure 4.3). In MSQ-like films, the band from 1000 to 1250 cm^{-1} is often peak-fitted with three peaks, linear (≈1037 cm^{-1}), network (≈1071 cm^{-1}) and cage (≈1134cm^{-1}) (Figure 4.4), which reflect, among other things, the distribution of the siloxane

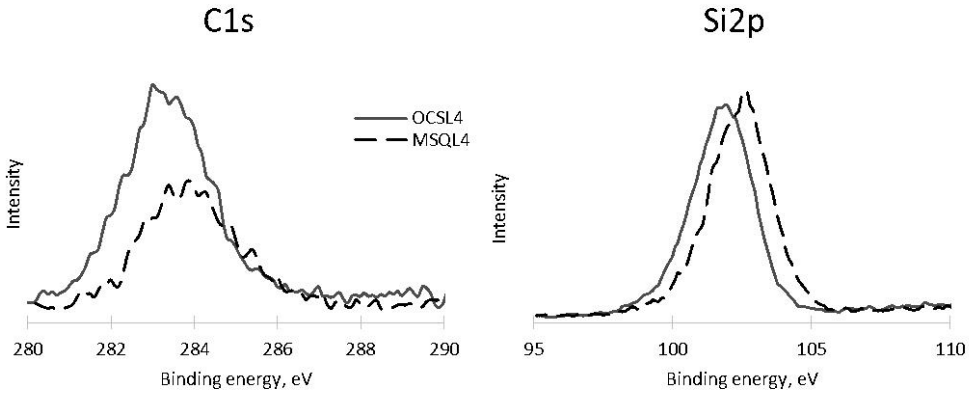

Figure 4.2. Carbon 1s and silicon 2p XPS spectra of the OCS and MSQ films. The shown results were obtained after half of the thickness of the films was etched away by Ar^+ ions.

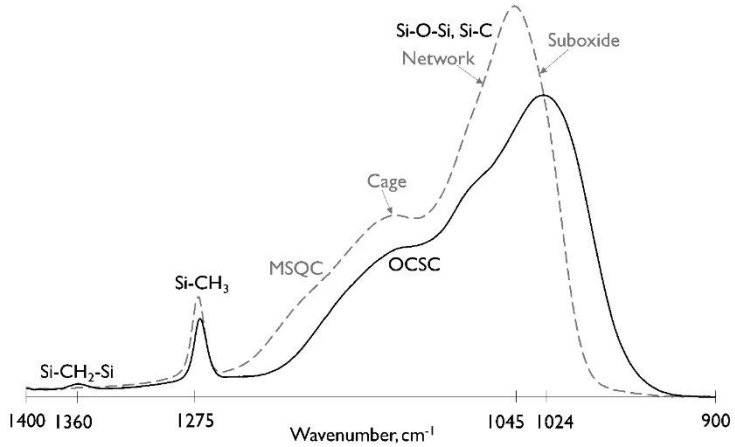

Figure 4.3. The incorporation of bridging methylene units into the silica matrix leads to a decrease of the intensity as well as a red shift of the main FTIR peak in the region 900-1200 cm^{-1}. The represented films have similar pore volume of ≈35%.

bonding angles below 144°, around 144° and above 150°, respectively.[33,34] While a similar analysis can be applied to the OCS films, we are not aware of studies which justify it given that, in this region, additional absorptions related to the methylene groups are expected which will be discussed below. For both the OCS and the MSQ films, the presence of the Si-CH_3 groups can be seen from the peak at 1275 cm^{-1}. The Si-CH_3 content in our MSQ films is lower than the typical methylsilsesquioxanes since the films were obtained from 1 to 1 ratio between MTES and TEOS while typical MSSQs[35–37] are synthesized by employing only MTES. However, MTES contains three network-forming groups while TEOS has four which means that our MSQ films have higher matrix connectivity as compared to the typical MSSQ films. As a result, the MSQ films contain a smaller contribution from cage structures than observed for a typical MSSQ[38,39] which can be seen from the intensity of the shoulder at 1130 cm^{-1} relative to the main peak at

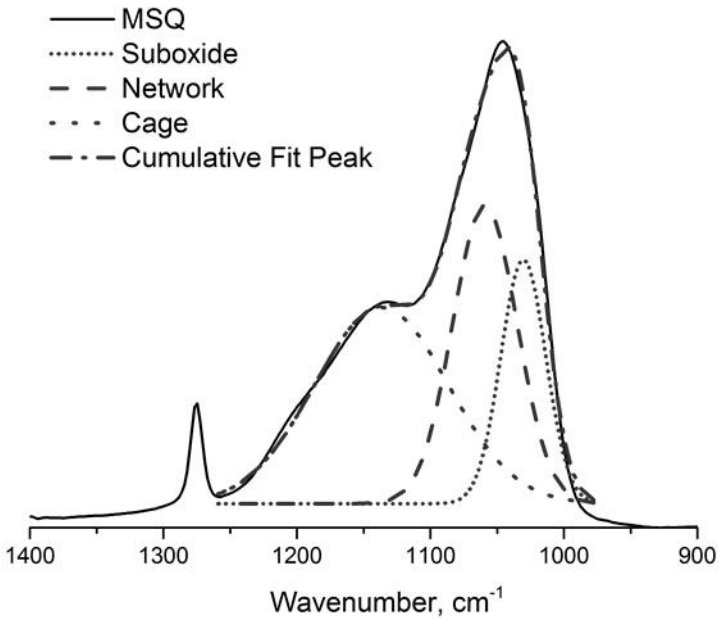

Figure 4.4. The 950-1250 cm^{-1} FTIR region of MSQ-like films is often peak-fitted by three siloxane peaks: suboxide, network and cage

1045 cm^{-1}. Additionally, the template removal temperature of 400°C further decreases the relative content of the siloxane cages due to their low thermal stability.[37,38] On the other hand, the higher carbon content in OCS as compared to MSQ films is confirmed from the red shift of the main peak, from 1045 to 1024 cm^{-1}. Furthermore, the significant number of methylene groups in the OCS films is proved by the presence of the peak at 1360 cm^{-1} as well as the shoulder at 1080-1040 cm^{-1}.[40,41] Additionally, the carbon incorporated in the network of the matrix, as opposed to being in $-CH_3$ groups, results in decreased intensity of the main Si-O-Si peak further supporting the interpretation for the significant incorporation of methylene bridging functionalities.

The different pore sizes and pore size distributions (Figure 4.5), resulting from the different templating molecules, do not affect the low-k matrix bonding configuration as deduced from the 950-1400 cm^{-1} region of the FTIR spectra which are normalized to the intensity of the main peak (Figure 4.6). In spite of the different pore structures, the spectra of the MSQ films with similar pore volume (within 2 percentage points) overlap almost perfectly. Only the spectrum of the MSQL4 film displays lower intensity of the high wavenumber shoulder around 1150 cm^{-1}, attributed to the cage siloxane structure[34], together with a red shift, from 1047 to 1042 cm^{-1}, of the main siloxane peak indicating an average Si-O-Si angle lower than 144°. Both observations can be explained with the lower pore volume[34,42–46] calculated for the MSQL4 as compared to the other MSQ films, 30 vs ≥37%. We observed a similar correlation for the OCS films (Figure 4.6) where larger pore volume differences than those for the MSQ films were calculated (Table 4.2). Nevertheless, the OCSL4 film seems to be an outlier since it has an open pore volume of 38%, similar to that of OCSC, but the high-wavenumber shoulder at ≈1140 cm^{-1} is as low as that of OCSF127 which has open pore volume of 32.5%. Additionally, the main siloxane peak of the OCSL4 film is red-shifted even in comparison to the lowest pore volume OCSF127 film, 1026

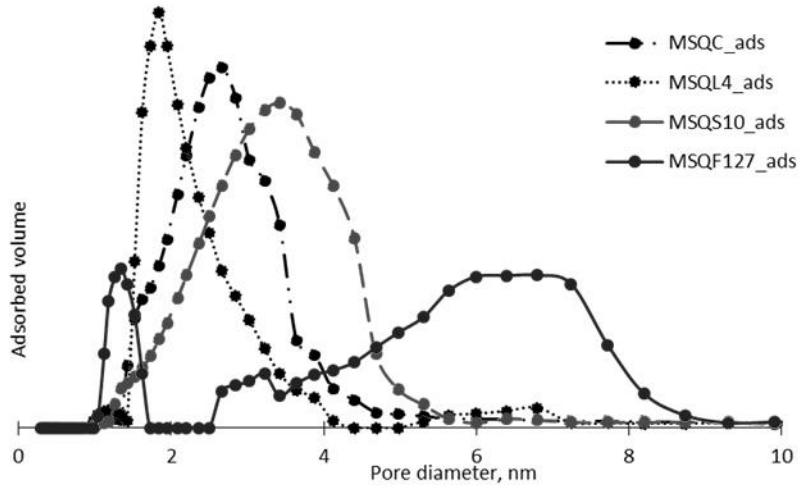

Figure 4.5. Pore size distributions (PSD) calculated from the adsorption branch of the toluene EP isotherms for MSQ films. Similar PSDs were obtained for the OCS films

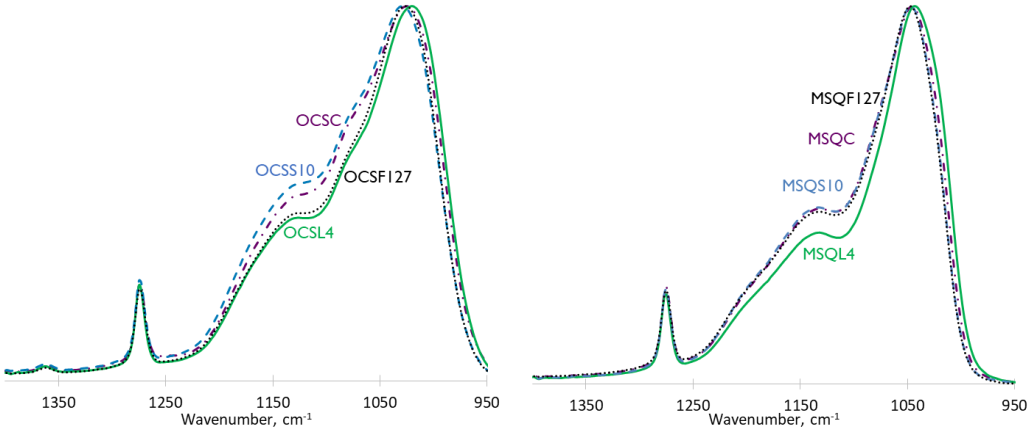

Figure 4.6. FTIR spectra of the region corresponding to the low-k matrices as a function of the templating agent

vs 1020 cm^{-1}. The latter might be due to the fact that films with uniform nanoscale confinement of the silica framework, deduced from the presence of a Debye-Scherrer ring in the GISAXS pattern (Figure 4.7), lead to a silica framework with a smaller portion of larger than 4-membered siloxane rings than found in amorphous silica films with wide pore size distribution.[47] This will be discussed more in detail in the next paragraph dedicated to the GISAXS results.

	Thermal cure					Thermal + UV				
	RI	YM [GPa]	k	Porosity [%]	Density [g/cm^3]	RI	YM [GPa]	k	Porosity [%]	Density [g/cm^3]
MSQC	1.271	5.0	2.35	34.9	0.95	1.260	6.0	2.21	37.1	0.94
OCSC	1.285	5.2	2.35	35.9	0.93	1.270	6.7	2.28	38.7	0.88
MSQL4	1.285	6.9	2.36	30.5	1.02	1.282	7.7	2.34	30.2	1.02
OCSL4	1.284	6.6	2.30	37.5	0.92	1.276	7.3	2.27	38.3	0.91
MSQS10	1.257	4.6	2.26	38.1	0.90	1.247	5.3	2.13	39.3	0.86
OCSS10	1.264	4.0	2.23	38.4	0.85	1.254	5.1	2.14	43.8	0.83
MSQF127	1.273	6.0	2.32	33.9	0.98	1.261	6.3	2.20	39.6	0.93
OCSF127	1.312	8.1	2.48	30.9	1.03	1.303	8.8	2.42	32.5	1.01

Table 4.2. Properties of MSQ and OCS observed before and after UV cure. Pore volume was calculated from EP measurements

4.3.2. Pore structure of OCS and MSQ films

From the well-defined Debye-Scherrer ring observed in the GISAXS patterns of the BrijL4 and Pluronic F-127-templated films (Figure 4.7), a narrow pore size distribution characteristic of wormlike pores is deduced. Employing FitGISAXS[48], the Debye-Scherrer ring can be reproduced assuming a monodisperse scatterer (i.e. pore) size distribution and using the Percus-

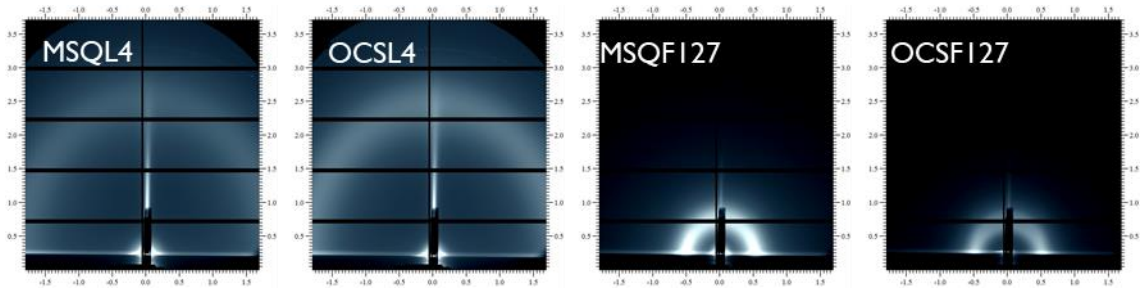

Figure 4.7. GISAXS patterns of BrijL4 and Pluronic F127-templated MSQ and OCS films

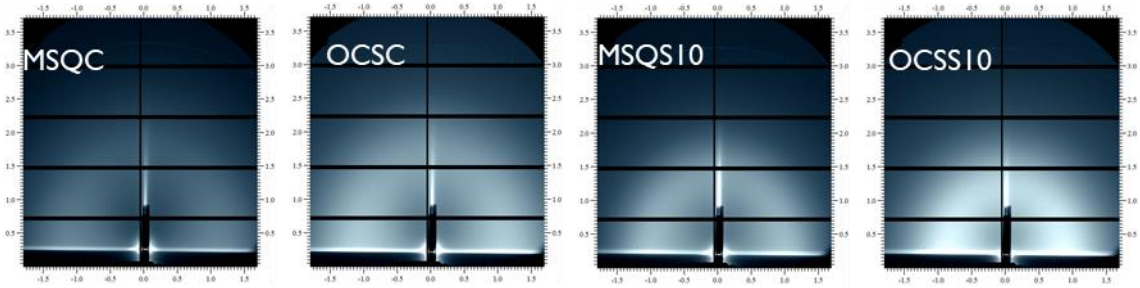

Figure 4.8. GISAXS patterns of the CTAC and BrijS10-templated MSQ and OCS films

Yevick model[49] of hard spheres with three-dimensional short-range order for the structure factor. In contrast, a wider pore size distribution is deduced for the CTAC and BrijS10-templated films which produce more diffuse GISAXS patterns (Figure 4.8).

Next, we discuss in more detail the GISAXS results observed for the films templated by BrijL4 and CTAC since they possess the smallest pore diameter which is the most suitable for low-k application. The patterns can be modelled employing a form factor describing randomly oriented spheroid pores. The pore shape is a result of the film's unidirectional shrinkage along the axis normal to the surface during the thermally induced template removal.[50] The film shrinkage is unidirectional since the in-plane shrinkage is limited by the adhesion of the film to the substrate. Therefore, the pores have a larger average diameter parallel to the substrate than the diameter normal to the surface. The pore diameters calculated for the BrijL4-templated films are 2.3 and 1.7 nm, along the parallel and the normal direction to the surface, respectively. Furthermore, the pore volume of the OCSL4 film which was calculated to be 37.6% is close to the pore volume calculated from the EP measurements, 38.1%. Unlike the EP, the pore volume calculated from the GISAXS includes not only the open pores accessible to an adsorbate but also the closed pores. Therefore, since the pore volumes deduced from an analysis of the EP and the GISAXS results are very close, the presence of closed pores is ruled out. On the other hand, while in the OCSL4 film there is no preferential orientation of the pores, deduced from the lack of diffraction spots, there is a short-range pore order evident from the presence of the Debye-Scherrer ring[51]. The short-range pore order implies that both the pore size and the pore wall thickness have a narrow size distribution similar to films with oriented pores. The pore walls with uniform thickness below 2 nm have been shown[47] to contain a higher percentage of small and stiff 3- and 4-membered siloxane rings. Therefore, the uniform wall thickness in the BrijL4-templated films might explain the red shift of the main FTIR peak at ca. 1000 cm^{-1} which is an indication of an increased contribution from small siloxane rings. Nevertheless, in spite of the clear correlation between the pore wall thickness and the content of small siloxane rings, wall thicknesses larger than 2 nm were not reported[47] while, based on the GISAXS analysis, the OCSL4 and MSQL4 were calculated to have a wall thickness of ≈4.5 nm.

Unlike the OCSL4, the scattering resulting from the OCSC film (Figure 4.8) was modelled using a local monodisperse approximation[52] size distribution and a Gaussian distribution function.

The pore size distribution parallel and perpendicular to the surface were centred at 3.5 and 2.5 nm, respectively. In this case, the pore volume calculated from the GISAXS analysis was 40% which is 5% larger than the 35% porosity calculated from EP for the same film. This difference provides an indication of the presence of micropores inaccessible for toluene in the OCSC film. Finally, the differences in the pore shape and the size distribution have little or no effect on the conclusions related to the effect of the replacement of the siloxane bonds by the methylene groups which will be presented in the next section. We can make this conclusion because the GISAXS patterns associated with a particular surfactant were independent of the matrix composition (Figure 4.7 and Figure 4.8), for instance the GISAXS patterns of the OCSC and the MSQC were very similar reflecting the similarity in the pore structure of the two films.

4.3.3. Mechanical and dielectric properties of OCS and MSQ films

The effect of the UV cure on low-k films, including MSQ and OCS-like films, has been the focus of a number of previous reports[37,53–55] and is therefore not going to be discussed in depth here. Typically, a UV cure with $\lambda \geq 200$ nm leads to removal of the remaining template increasing the pore volume and therefore decreasing the dielectric constant (Figure 4.9). Simultaneously, the YM might increase due to the conversion of the cage-like structure into a network structure and, generally, due to an increase of the matrix connectivity (Figure 4.9).

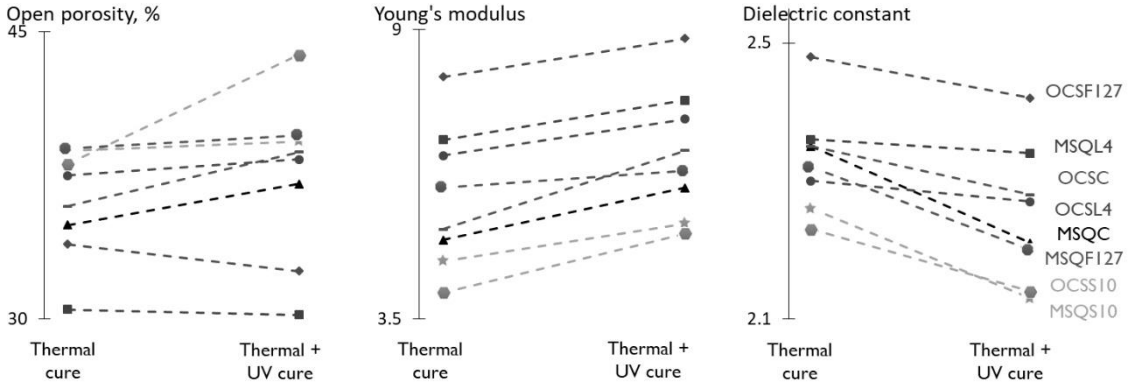

Figure 4.9. UV cure leads, generally, to increase of open porosity and Young's modulus and decrease of dielectric constant.

For the same density, the OCS films possess both a higher elastic modulus[11,12] and a higher dielectric constant than the MSQ films (Figure 4.10). The higher dielectric constant in films obtained from a bridged organosilica precursor as compared to MSQ-like films was previously observed[56] but it was considered to be an experimental artefact and attributed to an environmental effect increasing the experimental error. On the other hand, Dubois et al.[11] recognized it to be an intrinsic property of the low-k films based on alkylene-bridged precursors. The authors reached this conclusion by comparing a film obtained by the exclusive use of a bridged precursor with a film obtained from TEOS and MTES in which case the difference might have been due to a lower matrix density of the film containing the MTES as a result of the

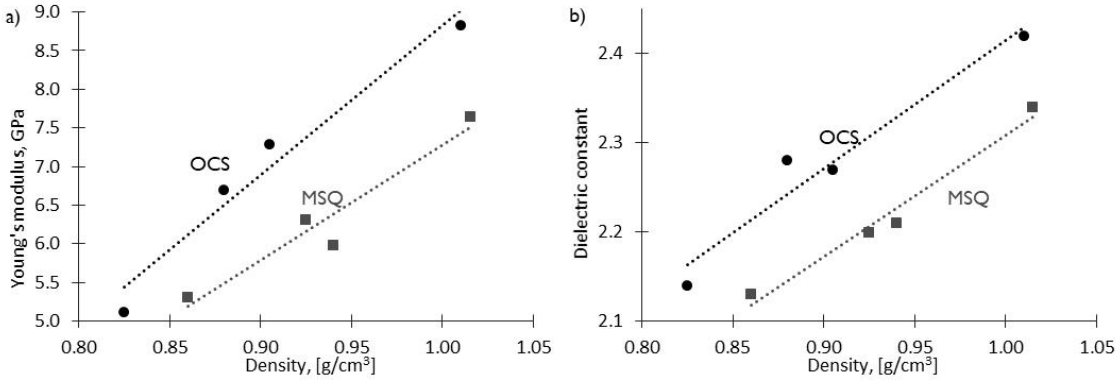

Figure 4.10. After UV cure, OCS films result in a) higher Young's modulus as compared to MSQ but the OCS films possess b) higher dielectric constant than MSQ films at an equivalent density

incorporation of the bulky Si-CH_3 groups[57]. On the other hand, we conclude that the MSQ films have lower matrix density as compared to the OCS due to a difference in the Si-O-Si and Si-CH_2-Si functionalities which is in line with a previous theoretical work[10] where it was shown that by replacing the siloxane bonds with organic bridges so that the CH_2/Si ratio is around 0.25 the mass density increases. The conclusion for the lower density in MSQ films is further supported by the refractive indices of the matrix (calculated from EP measurements[58]) which were observed to be systematically lower by ~0.04 for the MSQ films as compared to the OCS films. Therefore, larger pore volume is needed for the OCS films as compared to the MSQ films in order to achieve the same dielectric constant.

The UV-cured OCS films possess very similar properties to the previously reported[11] equally dense oxycarbosilane films. This is remarkable since Dubois and co-authors restricted their synthesis to the sole use of bridged precursors limiting in this way the reduction in matrix connectivity associated with the use of a methyl-containing precursor such as MTES. The reduced matrix connectivity is expected to result in films with lower YM. Notably, the difference in YM between the MSQ and OCS films is significantly smaller than previously reported.[11] A case in point is our observation of an MSQ film with an YM of 5.3 GPa having 44% open pore volume and a density of 0.86 g cm^{-3} which is in line with the YM expected for an equivalent density oxycarbosilane film obtained using only a bridged precursor.[6,11,12] Furthermore, the dielectric constant of the MSQ film is 2.1 which reinforces the applicability and the competitiveness as low-k dielectrics of the MSQ and OCS films reported in this work. Nevertheless, there are at least two factors which make a direct comparison with the literature impossible. Firstly, we are comparing UV-cured films with films reported in literature which only received a thermal cure at 450°C.[11,12] An anneal temperature of 450°C leads to a larger increase in connectivity as compared to a 400°C anneal[38,55] but it is not clear how it compares to a UV cure at 400°C. Secondly, the Young's moduli we report were obtained by nanoindentation (NI) measurements of ca. 200 nm thick films which may have resulted in overestimated values due

to a substrate effect.[59] In order to minimize the substrate effect, we performed the NI measurements at an indentation depth of <10% of film thickness. However, due to the similar film thicknesses, the contribution from a substrate effect is expected to be comparable among the films reported here and therefore the comparison between the OCS and MSQ moduli is reliable. The elastic moduli of the MSQ and the OCS films differ by 1.7 GPa which is significantly smaller difference than in previous reports. We hypothesize that the previously reported substantial improvement of the mechanical properties of the oxycarbosilane films as compared to the methylsilsequioxane films was associated with the increased average connectivity number in the matrix of the oxycarbosilanes which was not monitored. This hypothesis is supported by a later work[60] by Volksen et al. where they reported a UV-cured oxycarbosilane film with a dielectric constant of 2.0 and a YM of 7.5 GPa demonstrating improvement over the originally reported properties obtained following an anneal. Moreover, the synthesis of the methylsilsesquioxane reported by Dubois et al. takes place in alkaline conditions in contrast to the acidic catalysis which we utilized. It is well known[61] that the alkaline catalysis of the TEOS and MTES polycondensation reaction leads to more branched oligomers while the acidic catalysis results in linear molecules. As a consequence, a stronger contribution from the cage structure is evident from the FTIR spectra when the synthesis is performed in a basic solution[62] as compared to the MSQ we report. A stronger contribution from the cage structure is an indication of enhanced incorporation of MTES as compared to TEOS in the final organosilica matrix which is a prerequisite for a reduced matrix connectivity lowering in this way the film elastic modulus. On the other hand, it is known[63] that the alkali-catalysed polycondensation of TEOS and MTES leads to ≈20% non-hydrolysed alkoxy groups which might not contribute to the matrix connectivity, unlike the equivalent acid-catalysed polycondensation where the hydrolysis is very fast. Therefore, we conclude that the substantial improvement of the mechanical properties of the oxycarbosailne films over the methylsilsesquioxane films reported in literature is partially due to a significant difference in the matrix connectivity. By controlling for the matrix connectivity, we demonstrate that at a film density of 0.86 g cm^{-3} the improvement of the YM is about 1.7 GPa when some of the Si-O-Si are replaced by Si-CH_2-Si.

Low-k films with pore volume higher than 60-70% are exceedingly difficult to achieve.[6] Therefore, the conclusion that the OCS films require larger pore volume than the MSQ films in order to achieve the same dielectric constant appears to be a drawback for the former. This drawback is counter-balanced by the potential to increase the carbon content of the low-k film without decreasing its matrix connectivity. The increased C-content is desired in order to allow for a damage-free material integration in the IC manufacturing. For instance, the ratio of open pore volume to a relative carbon content (porosity/%C) has been shown to correlate with the plasma-induced damage[64] (PID) meaning that the lower the pore volume and the higher the C-

content, the lower the PID. However, in OCS-like films, the gains in the porosity/%C ratio associated with the increased carbon content are partly offset by the required porosity increase for a particular dielectric constant. On the other hand, if an alternative integration approach to the conventional patterning and metallization flow is considered, such as a template replacement scheme[65] where the processing-related damage to the low-k films is largely avoided, low C-content dielectrics might be more appealing than high C-content dielectrics since it would be easier to achieve a lower dielectric constant with lower pore volume in low-C materials.

4.3.4. HF stability of the MSQ and OCS films

The MSQ films are, generally, removed faster than the OCS films in a 0.5 weight % HF aqueous solution as deduced from thickness measurements (Figure 4.11). This is expected since the MSQ films have lower carbon content which has been shown to be responsible for the improved chemical stability of PMO low-k films.[66] Notably, the refractive indices of the MSQ films remain constant until the films are completely removed from the Si substrate. The modifications in the MSQ films are similar to that observed in PECVD films,[67] i.e. little to no chemical changes are deduced from the FTIR measurements before the films are completely removed. This behaviour has been attributed to the presence of an "inhibitor"[67], the removal of which leads to a very fast film removal, apparently, independent of film thickness. Two scenarios seem likely for such a behaviour, one in which a kinetic barrier, corresponding to the aforementioned "inhibitor", exists and it prevents a very fast reaction from occurring while the second scenario includes etching of a layer at the film-substrate interface resulting in a delamination of the films. We can confidently assign the source of the kinetic barrier to the inability of the aqueous solution of HF to wet the hydrophobic organosilica films because it has been demonstrated that the diffusion of H_2O in the low-k happens at the Si-low-k interface rather than through its bulk.[68] An additional evidence for the negligible wetting in the bulk of the MSQ films is the surface hydrophilization we observed after as short as 30 s of dipping in HF (Figure 4.12) which does not lead to an increased H_2O adsorption during water EP experiments (Figure 4.13) indicating that the bulk of the films is hydrophobic and inaccessible to the H_2O molecules. At the same

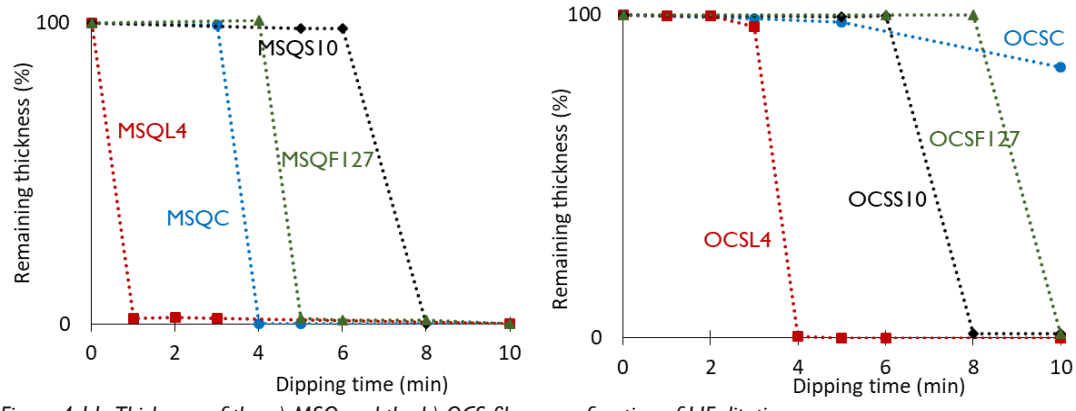

Figure 4.11. Thickness of the a) MSQ and the b) OCS films as a function of HF dip time

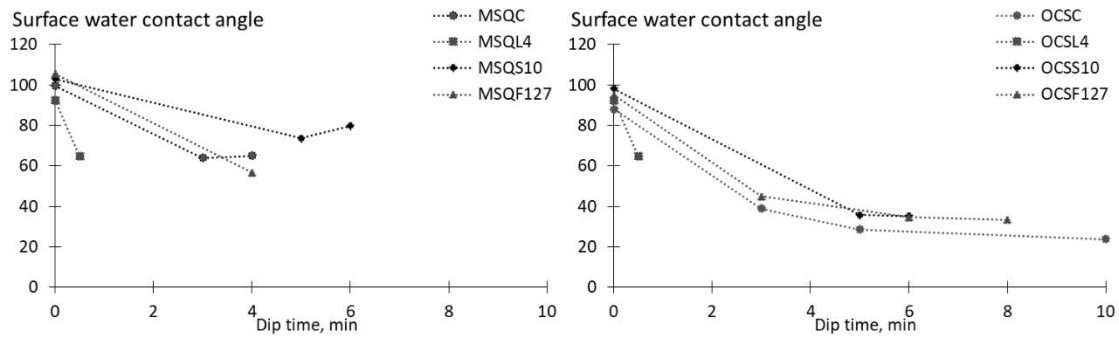

Figure 4.12. Water contact angle values measured following an HF dip

time, it is well-known that the presence of H_2O molecules enhances the HF etch rate of the SiO_2.[69] On the other hand, the reaction with fast kinetics is clearly the HF etching of Si-O bonds leading to the water-soluble H_2SiF_6 and H_2O[70] as reaction by-products. For example, we observed that the porous SiO_2 films, obtained using the same surfactants as for MSQ and OCS, are completely etched away within 5 s. Thermally grown SiO_2 has been reported to be etched with a rate of 100 nm/min in an aqueous HF solution.[67] The second scenario is supported by a demonstration of a preferential diffusion of aqueous species at the interface between the Si substrate and the low-k. As previously reported,[54] we also observed evidence for a preferential etching at the bottom interface based on ellipsometric results. Similarly, in the MSQ films, the mean square error (MSE), which is the measure used to quantify the goodness-of-fit, between the experimental dispersion and the one-layer Cauchy model increases from about 0.5 to up to 2 as a function of a dip time. Modelling the experimental dispersion for the MSQ films with a two layer Cauchy model results in a decrease of the MSE down to the expected value of ca. 0.5. The modelling converges to a bottom layer with a thickness close to the pore size of the film and a RI of ≈1 and a top layer with thickness and RI close to the pristine values. It was shown[54] that this observation correlated with decreased adhesion and therefore it was inferred to be a strong evidence for interfacial HF etching. The decreased adhesion, therefore, can lead to a delamination of the film from the substrate resulting in a conclusion for a fast and complete film removal. Additionally, the fact that the chemical changes are limited to the vicinity of the substrate would explain why no changes are observed in a transmission FTIR which is not sensitive enough for modifications confined to several nanometres. Nevertheless, it is often

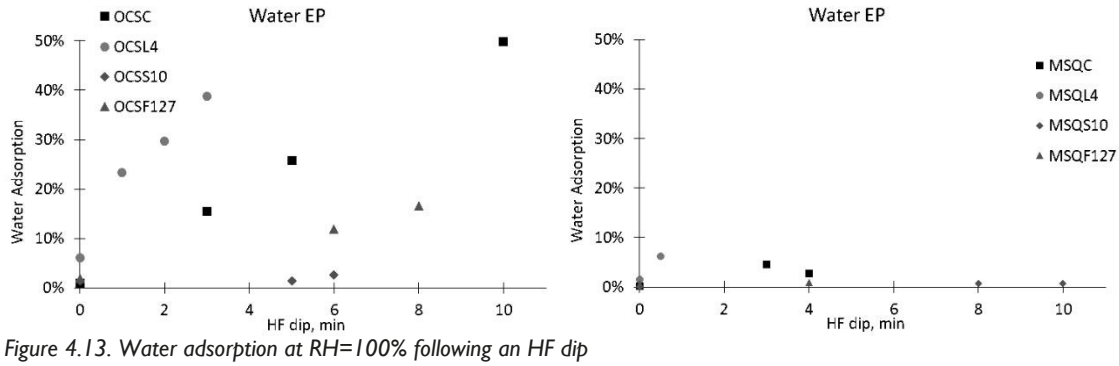

Figure 4.13. Water adsorption at RH=100% following an HF dip

possible to spot visually the film in the HF solution if the film has indeed delaminated but has not been completely dissolved by the HF. In some experiments, we observed the presence of the film on the Si substrate when it was withdrawn from the solution but no film remained upon rinsing with H_2O. In order to determine the influence of the interfacial etching on the deduced chemical stability, we performed additional experiments where the MSQ films were deposited on a 50 nm SiCN layer and then dipped in 0.5% HF in order to compare their stability with the films deposited on a native SiO_2. The SiCN layer is not etched by the HF and therefore if the deduced chemical stability of the MSQ films was determined by the etching of the interfacial SiO_2 then a higher chemical stability would be deduced for the MSQ films deposited on a SiCN film.

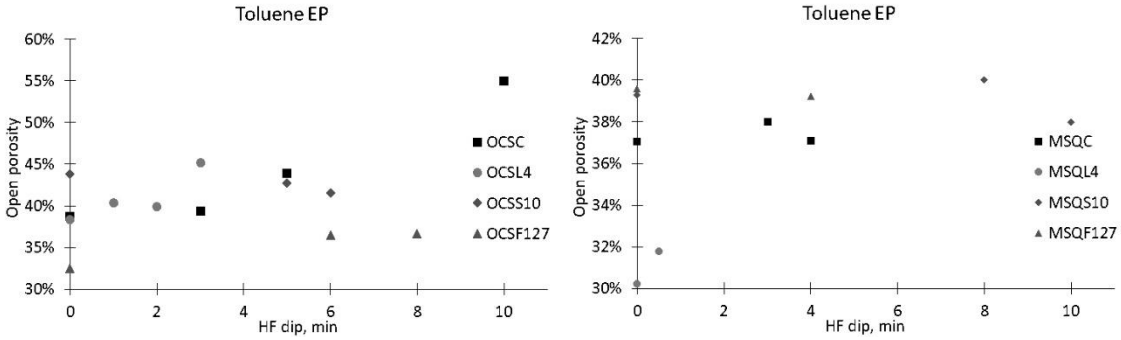

Figure 4.14. Open porosity as a function of HF dip time

The MSQ films deposited on a SiCN layer were etched away by the 0.5% HF for the same time as the films deposited on a native SiO_2 layer. Therefore, the etching of the interfacial SiO_2 and as a consequence the decreased adhesion between the Si substrate and the low-k film do znot seem to have a determining role on the deduced chemical stability.

As a result of the HF dip, the bulk of the OCS films is gradually etched away. This is evidenced by the increase in open porosity of the OCS films by up to 11 percentage points (Figure 4.14). In contrast, the porosity change in the MSQ films is limited to ca. 1.5 percentage points. Additionally, the FTIR spectra reveal a modification of the organosilica matrix of the OCS films as a function of the dipping time (Figure 4.15). The blue shift of the main peak might be interpreted to be due to a C-depletion[45] but the insignificant changes of the peaks at 1275 and 1360 cm^{-1}, attributed to C-H deformational modes in Si-CH_3 and Si-CH_2-Si, respectively, do not support such an interpretation. Therefore, the blue shift is probably due to the increased porosity.[46] The increased relative contribution of the high-wavenumber shoulder further supports this conclusion since it has been correlated to a decreased density in organosilica low-k films.[34,42–46] The correlation between the discussed changes in the FTIR spectra and porosity is strengthened by the less prominent modifications observed for OCSF127 and OCSS10. For both of these films, a moderate porosity increase of up to 4 percentage points correlates with less significant changes in the FTIR spectra even if the blue shift of the main peak and the increased contribution of the high-wavenumber shoulder are still clearly observed. The internal

etching of the OCS films is accompanied by a hydrophilization of the bulk of the films. The amount of adsorbed water increases with longer HF treatment (Figure 4.13). This observation also correlates well with the changes in the FTIR spectra and the porosity values. Unlike the MSQ films where the water adsorption is limited to the hydrophilic surface with the highest adsorption of 6%, the pores of the OCSC, which survives the longest in the HF solution, are completely filled by H_2O during a water EP experiment indicating that the entire bulk has become hydrophilic. This is also reflected in the region beyond 3000 cm^{-1} in the FTIR spectra where the hydrophilization is evident by the presence of a peak at 3700 cm^{-1} together with a broad peak between 3400 and 3700 cm^{-1} attributed to isolated silanol and H-bonded –OH groups, respectively. Interestingly, the investigation of the surface hydrophilicity by water contact angle (WCA) measurements revealed surface hydrophilization for all of the organosilica matrices. The WCA in the MSQ becomes between 60 and 75° and remains relatively constant with dipping time. On the other hand, the surface WCA of the OCS films decreases progressively with dipping time down to as low as 20° for the OCSC film (Figure 4.12).

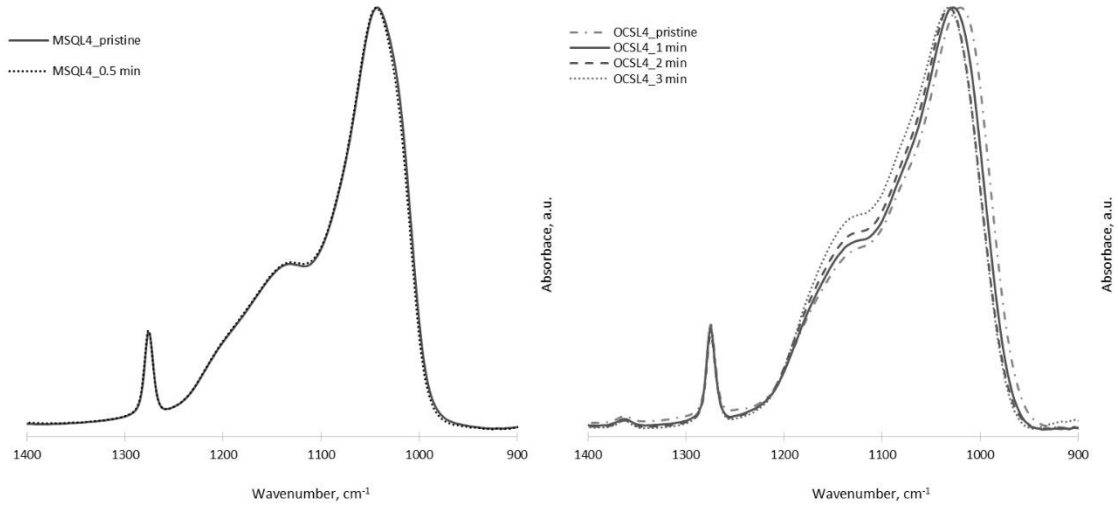

Figure 4.15. FTIR spectra of the MSQL4 and OCSL4 films following HF dips

To clarify the mechanism of the MSQ film removal, we investigated the effect of the improved wetting by adding 10% ethanol to the 0.5% HF solution. We investigated only MSQS10 and MSQC but since we observed the same trends we believe we can extend the conclusions to all of the MSQ films. The results presented in Figure 4.16 reveal virtually the same trends as those observed for the OCS films when dipped in 0.5% HF. In particular, the RI decreases with dipping time and the intensity of the high wavenumber shoulder at 1135 cm^{-1} increases relative to the main peak at 1035 cm^{-1}. Furthermore, a blue shift is observed for the Si-O-Si peak as well as a relative increase of the Si-CH_3 peak. These observations are evidence for an internal and preferential etch of the Si-O bonds. Surprisingly, the lowest RI is observed when the film is dipped for 3 min which is the same duration required to completely remove the film by a 0.5% HF aqueous solution. Therefore, the total time required to completely etch away the MSQ films

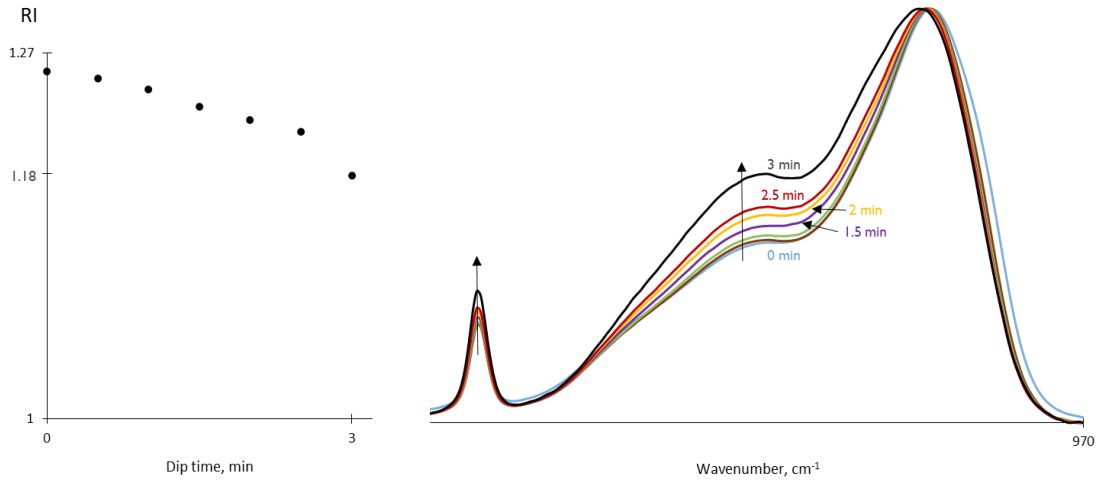

Figure 4.16. HF etching of MSQC upon addition of 10% ethanol: a) RI decreases due to internal etching; b) the preferential etching of Si-O bonds leads to increase in the relative C content

is the same with and without the addition of ethanol even if it clearly improves the wetting of the solution. These results indicate that the apparently different etch of the MSQ and OCS films by the HF solution is mainly due to a better wetting of the OCS films by the aqueous HF solution while the mechanism, as expected based on the similar film compositions, is the same.

4.3.5. Template dependence of electrical reliability

Ionic surfactants used as a template in self-assembly-based low-k films have been reported to result in films with electrical reliability unsuitable for low-k application due to an excess of remaining ions after the template removal resulting in extremely high leakage current.[71] For instance, a ToF-SIMS investigation of the films described herein revealed about three times larger amount of Cl^- ions in the CTAC-templated films as compared to those templated with non-ionic surfactants where the source of Cl^- is the HCl acid used as a catalyst. Nevertheless, employing the ionic surfactant CTAC we obtained films with electrical properties comparable to those templated with the non-ionic surfactants. In particular, we compared the flatband voltage (V_{FB}) of the MSQ and the OCS films after anneal and after an additional UV cure. The flatband voltage is a function of the concentration of the interface states between the low-k and the Si substrate and is therefore employed as a predictor of electrical reliability. We calculated the V_{FB} based on the flatband capacitance method.[72] The flatband voltage values observed for the CTAC-templated films follow the trends observed for the non-ionic surfactants, i.e. a negative V_{FB} observed after an anneal becomes close to zero after an additional UV cure. Since the pore volume increases during the UV cure indicating a template removal, the V_{FB} values seem to be dependent on the template residues remaining after anneal at 400°C. Furthermore, the stress-induced leakage current was measured and no significant difference between the films templated with the ionic and the non-ionic surfactants was observed. Similarly to the films templated with

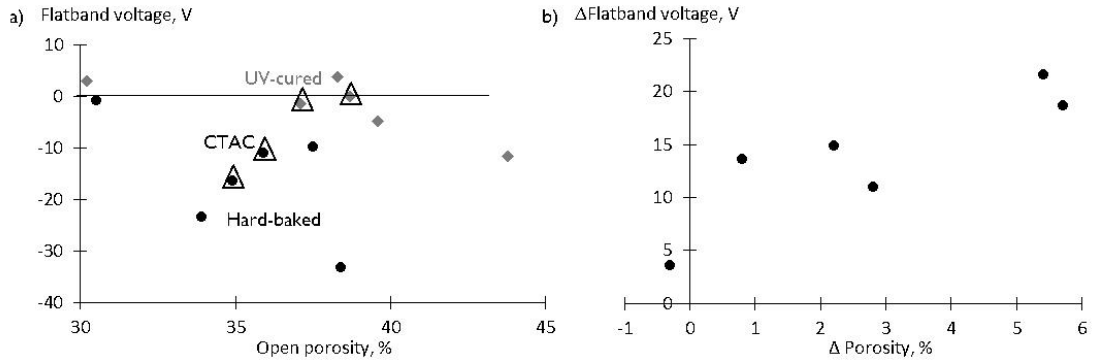

Figure 4.17. a) Flatband voltage approaches zero with the reduction of the remaining template due to a UV cure; b) clear correlation between the removed template and the change in V_{FB}. The triangles indicate the data points observed for the films templated with the ionic surfactant which do not stand out of the observed trends.

the non-ionic surfactants, the leakage current density for the CTAC-templated films at 1 MV cm^{-1} was calculated to be below 10^{-9} A cm^{-2}.

On the other hand, in accordance with a previous report, the flatband voltage correlates inversely with the open pore volume (Figure 4.17a). Ting and co-authors suggested[71] that the progressive negative shift is the result of a higher Si-OH content with the higher pore volume. This suggestion would explain why the V_{FB} becomes closer to zero following a UV-cure (Figure 4.17a) since the UV-cure induces additional condensation as evident from the FTIR spectra (Figure 4.18). Nevertheless, there is no evidence of Si-OH groups in the FTIR spectra for any of the films reported here. An alternative explanation for the inverse correlation between the V_{FB} and the pore volume might be that there is a correlation between the pore volume and the amount of template residues remaining at the interface with the Si substrate following the template removal, resulting in a higher number of interfacial charges for higher pore volume films. This explanation is supported by the clear positive correlation between the evolution of the pore volume and the flatband voltage (Figure 4.17b) with UV cure, i.e. the more template is

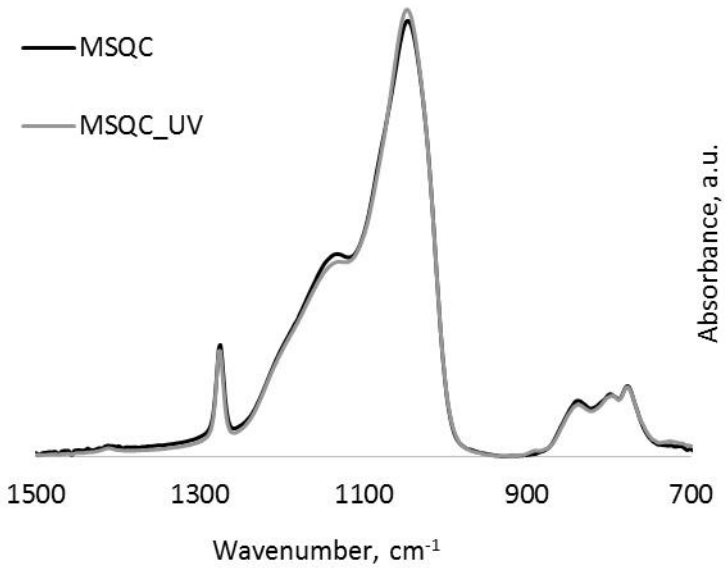

Figure 4.18. UV cure leads to small increase in network and decrease of cage

removed, corresponding to the increase in the pore volume, the closer to zero is the V_{FB}. Finally, the trend towards a less negative flatband voltage with UV cure has been previously observed but rather than to a template removal it was attributed to defect states being populated by electrons photo-injected from the Si substrate.[73] We do not exclude such a mechanism and acknowledge its potential contribution. Indeed, the increase of the V_{FB} of the MSQL4 film, in spite of the lack of pore volume change, points to the latter mechanism being most likely the dominant one.

4.4. Conclusions

The effect of the replacement of Si-O-Si by Si-CH_2-Si functionalities on the electrical and mechanical properties of hybrid organosilica films was investigated. Relatively small differences between the Young's moduli of the two types of matrices, e.g. 6.6 GPa with and 5.3 GPa without the methylene bridging groups for films with density of ~0.87 g cm^{-3} was established. This effect is counteracted by a higher dielectric constant for the films containing methylene groups – 2.27 with and 2.12 without the Si-CH_2-Si groups at the same density. This observation was attributed to an increased matrix density when Si-O-Si are replaced by Si-CH_2-Si groups. In contrast to the MSQ films, bulk etching by 0.5 wt% HF solution is observed for the methylene-containing films. The latter is due to the lower hydrophobicity of the OCS films when compared to the MSQ films. Furthermore, in contrast to a previous report, ionic and non-ionic surfactants were shown to result in a comparable amount of interface charges, deduced from a flatband voltage shift observed in the C-V characteristic. The latter finding expands the choice of suitable templating agents in the context of low-k application. The reported results allow for a more rational design of organosilica films in which insulating and/or mechanical properties are of critical importance.

4.5. References

[1] M. Faustini, L. Nicole, C. Boissière, P. Innocenzi, C. Sanchez, D. Grosso, *Chem. Mater.* **2010**, *22*, 4406.

[2] L. Ye, S. Zhang, Q. Wang, L. Yan, H. Lv, B. Jiang, *RSC Adv.* **2014**, *4*, 35818.

[3] P. Van der Voort, D. Esquivel, E. De Canck, F. Goethals, I. Van Driessche, F. J. Romero-Salguero, *Chem. Soc. Rev.* **2013**, *42*, 3913.

[4] D. Arcos, M. Vallet-Regí, *Acta Biomater.* **2010**, *6*, 2874.

[5] C. Sanchez, C. Boissière, D. Grosso, C. Laberty, L. Nicole, *Chem. Mater.* **2008**, *20*, 682.

[6] D. J. Michalak, J. M. Blackwell, J. M. Torres, A. Sengupta, L. E. Kreno, J. S. Clarke, D. Pantuso, *J. Mater. Res.* **2015**, *30*, 3363.

[7] E. Todd Ryan, S. M. Gates, S. A. Cohen, Y. Ostrovski, E. Adams, K. Virwani, A. Grill, *J. Appl. Phys.* **2014**, *115*, 144107.

[8] A. Grill, S. M. Gates, T. E. Ryan, S. V. Nguyen, D. Priyadarshini, *Appl. Phys. Rev.* **2014**, *1*, 11306.

[9] M. S. Oliver, G. Dubois, M. Sherwood, D. M. Gage, R. H. Dauskardt, *Adv. Funct. Mater.* **2010**, *20*, 2884.

[10] H. Li, J. M. Knaup, E. Kaxiras, J. J. Vlassak, *Acta Mater.* **2011**, *59*, 44.

[11] G. Dubois, W. Volksen, T. Magbitang, R. D. Miller, D. M. Gage, R. H. Dauskardt, *Adv. Mater.* **2007**, *19*, 3989.

[12] G. Dubois, W. Volksen, T. Magbitang, M. H. Sherwood, R. D. Miller, D. M. Gage, R. H. Dauskardt, *J. Sol-Gel Sci. Technol.* **2008**, *48*, 187.

[13] Y. Kayaba, F. Nishiyama, Y. Seino, T. Kikkawa, *J. Phys. Chem. C* **2011**, *115*, 12981.

[14] Y. Matsuda, J. S. Rathore, L. V Interrante, R. H. Dauskardt, G. Dubois, *ACS Appl. Mater. Interfaces* **2012**, *4*, 2659.

[15] J. S. Rathore, L. V. Interrante, G. Dubois, *Adv. Funct. Mater.* **2008**, *18*, 4022.

[16] X. Guo, J. E. Jakes, S. Banna, Y. Nishi, J. Leon Shohet, *J. Vac. Sci. Technol. A Vacuum, Surfaces, Film.* **2014**, *32*, 31512.

[17] X. Guo, J. E. Jakes, M. T. Nichols, S. Banna, Y. Nishi, J. L. Shohet, *J. Appl. Phys.* **2013**, *114*, 84103.

[18] R. M. De Vos, W. F. Maier, H. Verweij, *J. Memb. Sci.* **1999**, *158*, 277.

[19] S. Kim, Y. Toivola, R. F. Cook, K. Char, S.-H. Chu, J.-K. Lee, D. Y. Yoon, H.-W. Rhee, *J. Electrochem. Soc.* **2004**, *151*, F37.

[20] H. L. Castricum, A. Sah, J. A. J. Geenevasen, R. Kreiter, D. H. A. Blank, J. F. Vente, J. E. ten Elshof, *J. Sol-Gel Sci. Technol.* **2008**, *48*, 11.

[21] M. Kanezashi, M. Kawano, T. Yoshioka, T. Tsuru, *Ind. Eng. Chem. Res.* **2012**, *51*, 944.

[22] M. Aliofkhazraei, *Comprehensive guide for mesoporous materials, Volume 4: Application and Commercialization*; Aliofkhazraei, M., Ed.; Nova Science Publishers, Inc.: New York, 2015.

[23] M. P. Tate, V. N. Urade, S. J. Gaik, C. P. Muzzillo, H. W. Hillhouse, *Langmuir* **2010**, *26*, 4357.

[24] S. Jung, T. Ha, H. Park, *J. Colloid Interface Sci.* **2008**, *320*, 527.

[25] T. J. Ha, S. G. Choi, S. B. Jung, B. G. Yu, H. H. Park, *Ceram. Int.* **2008**, *34*, 947.

[26] L. Malfatti, T. Kidchob, P. Falcaro, S. Costacurta, M. Piccinini, M. C. Guidi, A. Marcelli, A. Corrias, M. F. Casula, H. Amenitsch, P. Innocenzi, *Microporous Mesoporous Mater.* **2007**, *103*, 113.

[27] M. Matheron, A. Bourgeois, T. Gacoin, A. Brunet-Bruneau, P.-A. Albouy, J.-P. Boilot, J.

Biteau, P. Lacan, *Thin Solid Films* **2006**, *495*, 175.

[28] M. Matheron, T. Gacoin, J.-P. Boilot, *Soft Matter* **2007**, *3*, 223.

[29] M. Matheron, A. Bourgeois, A. Brunet-Bruneau, P.-A. Albouy, J. Biteau, T. Gacoin, J.-P. Boilot, *J. Mater. Chem.* **2005**, *15*, 4741.

[30] C. J. Brinker, *J. Non. Cryst. Solids* **1988**, *100*, 31.

[31] T. Asefa, M. J. MacLachlan, H. Grondey, N. Coombs, G. A. Ozin, *Angew. Chemie Int. Ed.* **2000**, *39*, 1808.

[32] L. M. Han, J.-S. Pan, S.-M. Chen, N. Balasubramanian, J. Shi, L. S. Wong, P. D. Foo, *J. Electrochem. Soc.* **2001**, *148*, F148.

[33] S. Yasuhara, T. Sasaki, T. Shimayama, K. Tajima, H. Yano, S. Kadomura, M. Yoshimaru, N. Matsunaga, S. Samukawa, *J. Phys. D. Appl. Phys.* **2010**, *43*, 65203.

[34] A. Grill, D. A. Neumayer, *J. Appl. Phys.* **2003**, *94*, 6697.

[35] Y. H. Chen, H. E. Tu, J. Leu, *Microporous Mesoporous Mater.* **2012**, *162*, 181.

[36] Y.-Y. Lyu, J.-H. Yim, Y. Byun, S.-Y. Lee, I.-S. Jung, L. S. Pu, *Eur. Polym. J.* **2004**, *40*, 2505.

[37] A. Zenasni, F. Ciaramella, V. Jousseaume, C. Le Cornec, G. Passemard, *J. Electrochem. Soc.* **2007**, *154*, G6.

[38] H. W. Ro, E. S. Park, C. L. Soles, D. Y. Yoon, *Chem. Mater.* **2010**, *22*, 1330.

[39] Y. Abe, H. Hatano, T. Gunji, *J. Polym. Sci. Part A Polym. Chem.* **1995**, *33*, 751.

[40] J. Heo, H. J. Kim, J. Han, J.-W. Shon, *Thin Solid Films* **2007**, *515*, 5035.

[41] C. Rau, W. Kulisch, *Thin Solid Films* **1994**, *249*, 28.

[42] K. Vanstreels, C. Wu, M. Gonzalez, D. Schneider, D. Gidley, P. Verdonck, M. R. Baklanov, *Langmuir* **2013**, *29*, 12025.

[43] A. Grill, V. Patel, *J. Appl. Phys.* **2008**, *104*, 24113.

[44] M. Darnon, N. Casiez, T. Chevolleau, G. Dubois, W. Volksen, T. J. Frot, R. Hurand, T. L. David, N. Posseme, N. Rochat, C. Licitra, *J. Vac. Sci. Technol. B Microelectron. Nanom. Struct.* **2013**, *31*, 11207.

[45] Y.-H. Kim, M. S. Hwang, H. J. Kim, J. Y. Kim, Y. Lee, *J. Appl. Phys.* **2001**, *90*, 3367.

[46] G. Lucovsky, *J. Vac. Sci. Technol. B Microelectron. Nanom. Struct.* **1987**, *5*, 530.

[47] H. Fan, C. Hartshorn, T. Buchheit, D. Tallant, R. Assink, R. Simpson, D. J. Kissel, D. J. Lacks, S. Torquato, C. J. Brinker, *Nat. Mater.* **2007**, *6*, 418.

[48] D. Babonneau, *J. Appl. Crystallogr.* **2010**, *43*, 929.

[49] J. K. Percus, G. J. Yevick, *Phys. Rev.* **1958**, *110*, 1.

[50] P. Chatterjee, S. Hazra, H. Amenitsch, *Soft Matter* **2012**, *8*, 2956.

[51] S. Förster, S. Fischer, K. Zielske, C. Schellbach, M. Sztucki, P. Lindner, J. Perlich, *Adv.*

Colloid Interface Sci. **2011**, *163*, 53.

[52] J. S. Pedersen, *J. Appl. Crystallogr.* **1994**, *27*, 595.

[53] A. Zenasni, V. Jousseaume, P. Holliger, L. Favennec, O. Gourhant, P. Maury, G. Gerbaud, *J. Appl. Phys.* **2007**, *102*, 94107.

[54] M. Redzheb, L. Prager, M. Krishtab, S. Armini, K. Vanstreels, A. Franquet, P. Van Der Voort, M. R. Baklanov, *Microelectron. Eng.* **2016**, *156*, 103.

[55] A. Zenasni, B. Remiat, C. Waldfried, C. Le Cornec, V. Jousseaume, G. Passemard, *Thin Solid Films* **2008**, *516*, 1097.

[56] B. R. Kim, J. M. Son, M. J. Ko, *J. Mater. Sci.* **2007**, *42*, 5381.

[57] H. W. Ro, K. Char, E. C. Jeon, H. J. Kim, D. Kwon, H. J. Lee, J. K. Lee, H. W. Rhee, C. L. Soles, D. Y. Yoon, *Adv. Mater.* **2007**, *19*, 705.

[58] M. Baklanov, K. Maex, M. Green, *Dielectric Films for Advanced Microelectronics*; Baklanov, M. R.; Green, M. L.; Maex, K., Eds.; John Wiley & Sons, Ltd: Chichester, UK, 2007.

[59] O. O. Okudur, K. Vanstreels, I. De Wolf, U. Hangen, *J. Appl. Phys.* **2016**, *119*, 25302.

[60] W. Volksen, S. Purushothaman, M. Darnon, M. F. Lofaro, S. a. Cohen, J. P. Doyle, N. Fuller, T. P. Magbitang, P. M. Rice, L. E. Krupp, H. Nakagawa, Y. Nobe, T. Kokubo, G. J. M. Dubois, *ECS J. Solid State Sci. Technol.* **2012**, *1*, N85.

[61] C. Brinker, G. Scherer, *Sol-gel science: the physics and chemistry of sol-gel processing*; 1990.

[62] S. Yu, T. K. S. Wong, X. Hu, K. Pita, *J. Electrochem. Soc.* **2003**, *150*, F116.

[63] R. A. Assink, B. D. Kay, *Annu. Rev. Mater. Sci.* **1991**, *21*, 491.

[64] A. Grill, *J. Vac. Sci. Technol. B* **2016**, *34*, 20801.

[65] L. Zhang, J.-F. de Marneffe, N. Heylen, G. Murdoch, Z. Tokei, J. Boemmels, S. De Gendt, M. R. Baklanov, *Appl. Phys. Lett.* **2015**, *107*, 92901.

[66] F. Goethals, I. Ciofi, O. Madia, K. Vanstreels, M. R. Baklanov, C. Detavernier, P. Van Der Voort, I. Van Driessche, *J. Mater. Chem.* **2012**, *22*, 8281.

[67] P. Verdonck, Q. T. Le, J. Devonport, D. R. Huanca, S. G. dos Santos Filho, T. Conard, J. Meersschaut, M. R. Baklanov, S. Van Elshocht, *ECS J. Solid State Sci. Technol.* **2014**, *4*, N3140.

[68] X. Zhang, J. N. Myers, J. D. Bielefeld, Q. Lin, Z. Chen, *ACS Appl. Mater. Interfaces* **2014**, *6*, 18951.

[69] J. K. Kang, C. B. Musgrave, *J. Chem. Phys.* **2002**, *116*, 275.

[70] Q. T. Le, G. Vereecke, H. Struyf, E. Kesters, M. R. Baklanov, In *Advanced Interconnects for*

ULSI Technology; John Wiley & Sons, Ltd: Chichester, UK, 2012; pp. 129–171.

[71] C.-Y. Ting, H.-S. Sheu, W.-F. Wu, B.-Z. Wan, *J. Electrochem. Soc.* **2007**, *154*, G1.

[72] E. Nicollian, J. Brews, E. Nicollian, *MOS (metal oxide semiconductor) physics and technology*; Wiley: New York, 1982.

[73] H. Sinha, J. L. Lauer, M. T. Nichols, G. A. Antonelli, Y. Nishi, J. L. Shohet, *Appl. Phys. Lett.* **2010**, *96*, 10.

CHAPTER 5. TEMPLATE-DEPENDENT HYDROPHOBICITY IN MESOPOROUS ORGANOSILICA FILMS

A template dependence of the degree of self-hydrophobization of methylene-bridged periodic mesoporous organosilica (PMO) films is reported. The film with the smallest pore size of 1.7 nm, templated by CTAC, results in higher hydrophilicity when compared to films with a pore size of 4.1 or 5.3 nm, templated by BrijL4 and BrijS10, respectively. Both the surface and the bulk hydrophilicity were evaluated by water contact angle measurements and water ellipsometric porosimetry and the same trends were observed. Additionally, we provide the first evidence for a steric hindrance of the self-hydrophobization process. We show that a partial template removal results in the methylene-to-methyl transformation being observed at a temperature as low as 200°C, significantly lower than previously demonstrated. These results should be taken into account when PMO materials are considered for applications such as low-k dielectrics, membranes, catalyst and chromatographic supports, and drug carriers.

***M. Redzheb**, P. Van Der Voort, S. Armini, Template dependent hydrophobicity in mesoporous organosilica films, Microporous and Mesoporous Materials, In press, Available online 7 October 2017*

5.1. Introduction

Periodic mesoporous organosilica (PMO) materials possess organic groups as bridges between Si atoms, $(R'O)_3$-Si-R-Si-$(OR')_3$ where R is the organic bridging group.[1–3] These organic bridges allow for the tuning of the surface properties such as the hydrophobicity, the alteration of the surface reactivity and the protection from chemical attack.[1,2,4,5] Notably, the uniform distribution of the bridging organic groups in the bulk of the material means that their benefits extend beyond impacting only the surface properties. The uniform bulk distribution of functionalities is especially important in porous materials which are attractive due to their high surface-to-volume ratio. In this case, ideally all of the accessible surface possesses the desired functional groups. For instance, employing alkylene bridged organosilicates, the internal hydrophobicity of the PMO can be fine-tuned depending on the choice of the alkylene bridge, e.g. methylene or ethylene, and the annealing temperature.[5] The fine-tuning of the hydrophobicity enables the engineering of the host-guest interactions and benefits applications such as drug delivery, catalysis, protein refolding, and separation.[1] Furthermore, hydrophobic PMOs are stable in high humidity environment, giving them an advantage for applications in solar cells, nanoelectronics, and displays.[3]

The hydrophobicity of the PMOs can be controlled by the annealing temperature due to a self-hydrophobization process, which has been shown to occur at a temperature of at least 350°C.[6] The mechanism of the self-hydrophobization of methylene-bridged PMO materials is reported in literature and involves the transformation of a methylene (Si-CH_2-Si) into a methyl group (Si-CH_3) in the presence of a silanol functionality (Si-OH) which is transformed into a siloxane (Si-O-Si) bridge.[7] The self-hydrophobization has also been observed in ethylene-bridged PMOs[5] but the mechanism has been asserted to be different than in the methylene-bridged PMO.[7] As a result, the hydrophobicity has been established to depend on the type of the alkylene bridge and the annealing temperature.[5] Nevertheless, in this work, we show that the PMOs' hydrophobicity depends also on the type of the templating molecules. The impact of the template on the hydrophobicity is discussed in light of its effect on the degree of polycondensation in as-deposited films[8] and on the pore size of the PMO materials.

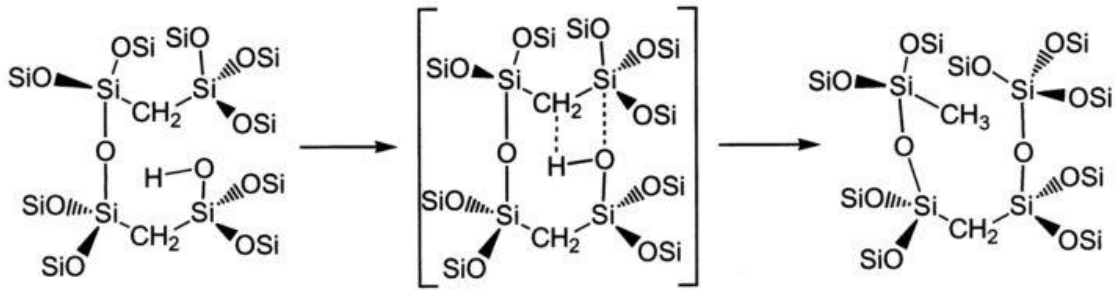

Figure 5.1. Mechanism of the self-hydrophobization reaction

5.2. Experimental Section

Three methylene-bridged mesoporous organosilica films were prepared using the sol-gel method based on the evaporation-induced self-assembly mechanism. The films were templated by the cetyltrimethylamino chloride (CTAC), BrijL4 and BrijS10 and were labelled MPMOC, MPMOL4 and MPMOS10, respectively. The molar ratios of the reagents are given in Table 5.1. In a typical synthesis, 11.1 ml 1-methoxy-2-propanol were mixed with 0.81 ml 25% aqueous solution of CTAC and 1.05 ml 0.02 M HCl. After stirring for 10 min for homogenization, 1.29 ml bis(triethoxysilyl)methane (BTESM) were added and further stirred for 15 min. After aging at ambient conditions for ≈24 h, the solutions were dispensed on a H_2O_2 cleaned Si substrate and spun at 1500 rpm for 60 s. Next, the films were annealed in an oven at 150°C for 10 min in ambient atmosphere. Finally, the films were annealed at various temperatures between 200 and 500°C in inert N_2 atmosphere for 2 h with a heating rate higher than 50°/min.

Label	BTESM	1-methoxy-2-propanol	H_2O	Surfactant	$[H^+]$
MPMOC	1	31	25	0.17 CTAC	0.0057
MPMOS10	1	31	16	0.1 BrijS10	0.0057
MPMOL4	1	31	16	0.27 BrijL4	0.0057

Table 5.1. Molar ratio of the reagents employed in the synthesis of the PMO films. MPMOC – CTAC; MPMOS10 – BrijS10; MPMOL4 – BrijL4

5.3. Results and Discussion

The thermal self-hydrophobization process characteristic of PMO materials can occur at a temperature as low as 200°C which is much lower than previously reported.[6] The self-hydrophobization was ascertained by difference FTIR spectra (Figure 5.2) showing the appearance of a Si-CH_3 peak at 1275 cm^{-1}. The Si-CH_3 group is not present in the organosilica precursor and no IR absorption associated with its presence is observed in the as-deposited films (Figure 5.2a). Nevertheless, upon a two hour anneal at 200°C in N_2, a peak at 1275 cm^{-1} can be seen for the CTAC-templated film. The appearance of the peak is demonstrated by

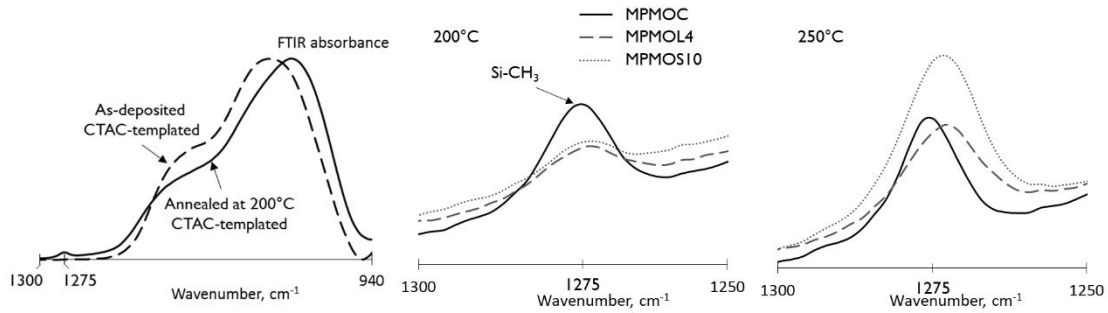

Figure 5.2. Self-hydrophobization is evident from the difference FTIR spectra. a) FTIR spectra of as-deposited and annealed at 200°C PMO. b) Difference spectra of the three PMO films after anneal at 200°C. c) Difference spectra of the three PMO films after an anneal at 250°C.

difference FTIR spectra (Figure 5.2b) where the spectrum obtained before the anneal is subtracted from the spectrum after the anneal, as a result of which, the positive peaks (peaks above the baseline) are an indication of the formation of functionalities in the film. Notably, after the anneal at 200°C, the Si-CH_3 peak is clearly present in the CTAC-templated film. Nevertheless, in the BrijL4 and BrijS10-templated films, the peak is much less pronounced and close to noise level. The 1275 cm^{-1} peak becomes more prominent in the spectra associated with the films templated with the non-ionic surfactants after a two hours anneal at 250°C (Figure 5.2c). These observations seem to indicate that depending on the templating molecule, different activation energies are required in order to initiate the self-hydrophobization. However, this explanation seems unlikely given that the same organosilica precursor was employed for the synthesis of all of the films. Rather, the self-hydrophobization process is sterically hindered as long as the template is present in the films, i.e. when part of the template is decomposed and some pore volume is introduced, the Si-CH_2-Si to Si-CH_3 transformation occurs. The evidence for this explanation comes from SE measurements in which as a result of the anneal at 200°C the RI of the MPMOC dropped by 0.12, from 1.49 down to 1.37, while the RI change of the MPMOL4 and MPMOS10 films were limited to 0.03 and 0.02, respectively. These changes in the RI values can be explained by a decrease in density associated to the thermal decomposition of the surfactant molecules of which CTAC seems to be the one with the lowest stability. On the other hand, the anneal at 250°C results in a Δ RI of 0.05 in the films templated with non-ionic surfactants, which seems to reflect the presence of sufficient pore volume in order to initiate the self-hydrophobization, as evident from Figure 5.2c. In order to test our hypothesis about the effect of the surfactant on the self-hydrophobizaiton, we deposited a BrijS10-templated film, annealed it at 150°C for 10 min to crosslink the matrix, performed an hour long solvent extraction in acetone at room temperature and then annealed the film at 200°C for 2 h in N_2. As a result of the solvent extraction of the template, the RI of the film dropped from 1.49 to 1.29 indicating that about 80% of the template was removed. The anneal at 200°C caused further RI decrease of 0.01 which is smaller than the Δ RI of 0.02 observed when the film was annealed without the solvent extraction step which seems reasonable given that a majority of the template

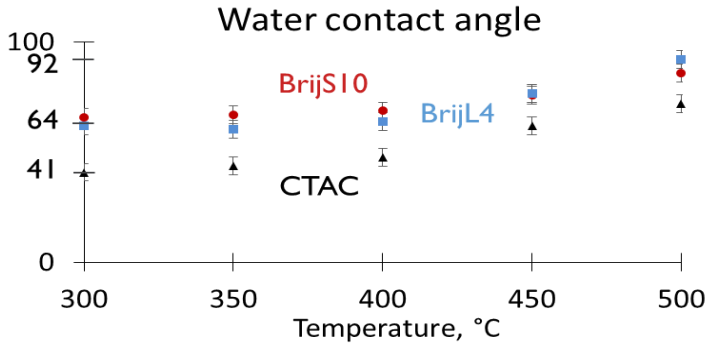

Figure 5.3. Surface water contact angle as a function of the annealing temperature.

had been removed. Compared to the film on which no solvent extraction was performed, the film which was treated by both solvent extraction and anneal at 200°C has a two times larger concentration of Si-CH_3 groups, as inferred from the two times larger area associated with the FTIR peak located at 1275 cm^{-1} (Figure 5.4). Therefore, the presence of a template in the pores has a strong contribution in deterring the self-hydrophobization reaction. Finally, no evidence of a self-hydrophobization was observed after a 2 h anneal at 150°C.

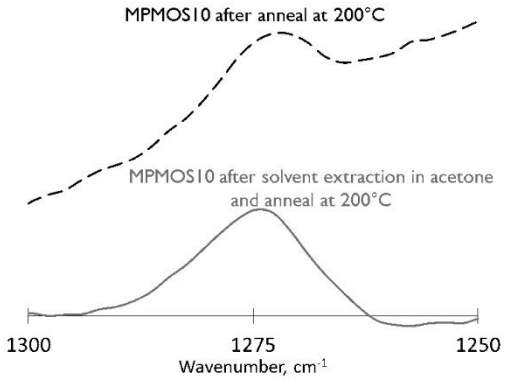

Figure 5.4. Difference FTIR spectra showing the two times higher intensity of the Si-CH_3 peak when the anneal at 200°C is preceded by a solvent extraction step

As a result of the self-hydrophobization process, for all the investigated films, the temperature increase from 300 to 500°C leads to an increase of the surface WCA by up to 30° (Figure 5.3). Systematically lower contact angles are observed for the CTAC-templated films. In an attempt of explaining this systematic difference, we consider the effect of the roughness, measured by AFM, on the WCA values. The lowest RMS roughness value of 0.3 nm was observed for the MPMOC films, while for MPMOL4 and MPMOS10 the RMS roughness was found to be 3.0 and 0.8 nm, respectively. Therefore, we can conclude that the trend observed in the measured roughness values do not help explaining the differences in the surface wetting. Given the hydrophilicity of the layers, in a Wenzel regime, the higher roughness of the films templated with non-ionic surfactants would result in lower effective contact angle,[9] which does not explain why systematically lower contact angles are observed for MPMOC. However, the Wenzel description is probably unsuitable for the surface of a porous film since the pores under the droplet will be flooded by water which is better described by the Cassie equation.[9] In this scenario, for films obtained from the same matrix molecule, the effective WCA of films with higher porosity is expected to be lower than that of films with lower porosity. This expectation is not met by the results shown in Figure 5.3 since, excluding the anneal at 300°C, MPMOS10 is the film with the highest porosity, followed by MPMOL4, and the film with the lowest porosity is MPMOC (Figure 5.5). Therefore, geometrical consideration cannot explain the observed differences in wetting. Notably, the WCAs observed for all of the films are systematically lower than those reported in literature. This discrepancy might be due to the low heating rate, e.g. 1°/min, which is usually reported[4,5] for the anneal of PMO films, in contrast to the anneal

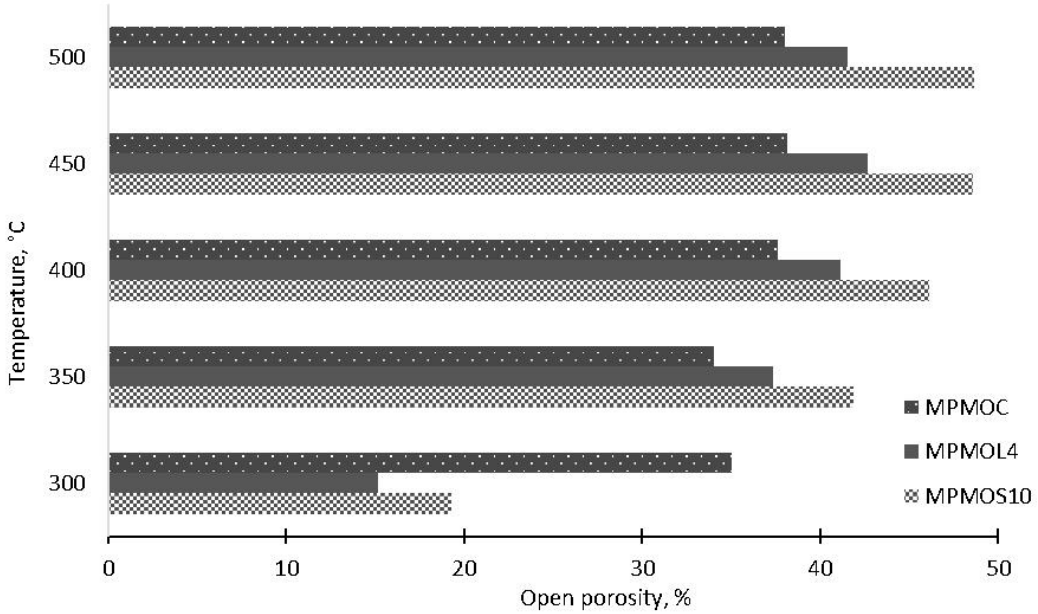

Figure 5.5. Open porosity calculated from ellipsometric porosimetry measurements using toluene as an adsorbate following anneals at a temperature between 300 and 500°C

conditions applied in our work, where the heating rate was higher than 50°/min. Therefore, the effective anneal durations reported in literature are significantly longer than ours, leading to more effective self-hydrophobization reactions.

To investigate whether the observed difference in hydrophilicity is due to a difference in the chemical composition of the films we compare their FTIR spectra (Figure 5.6). An analysis of the region between the 3300 and 4000 cm^{-1}, where the absorption from O-H stretching vibrations is expected, reveals the bulk hydrophilicity of the films. The wide absorption centered at around 3515 cm^{-1} is indicative of H-bonded -OH often attributed to the presence of moisture. On the other hand, the sharp peak at 3732 cm^{-1} is due to absorption from isolated, non-H-bonded, R_3Si-OH groups. As it can be seen in Figure 5.6, in agreement with the reported WCA values, the CTAC-templated films result in a stronger -OH absorption of both isolated R_3Si-OH and H-bonded -OH groups. Given the high temperatures to which these films were subjected, the H-bonded -OH groups might be due to subsequently adsorbed moisture, as a consequence of the presence of R_3Si-OH groups. These results make clear that the hydrophilicity of the films is not

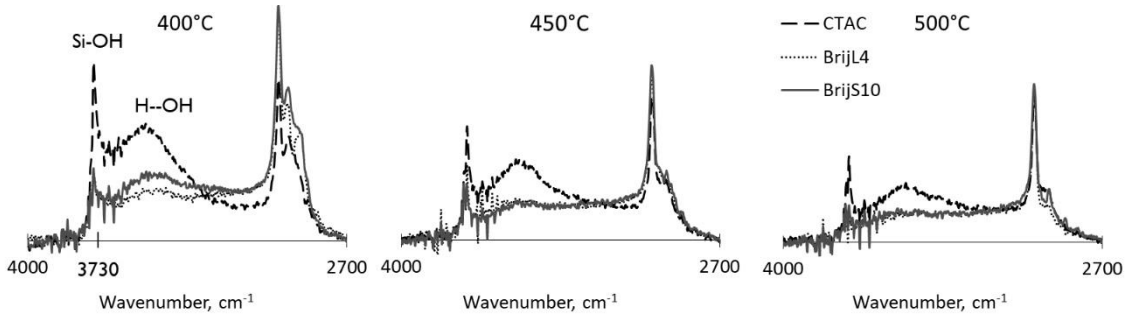

Figure 5.6. FTIR absorbance spectra of the 2700-4000 cm^{-1} region where absorption from C-H and O-H stretch can be observed. The annealing temperature after which the FTIR was measured is indicated

limited to their surface but extends to the bulk. The hydrophilicity is observed in spite of the clear indication that the self-hydrophobization takes place. Therefore, the observed differences in the hydrophobicity seem to be due to a different extent to which the self-hydrophobization occurs in each film. Notably, in the temperature range between 350 and 500°C, the CTAC-templated films result in the lowest $SiCH_3$-to-SiOSi ratio when compared with the films templated by the non-ioinic surfactants. The notation "SiOSi" refers to the peak centered at 1030 cm^{-1} which is the result of matrix-related absorptions such as the vibration of Si-O-Si and Si-C-Si groups (Figure 5.7). The $SiCH_3$-to-SiOSi ratios are compared, rather than the absolute $SiCH_3$ intensities in order to take into account the differences in density, which are nevertheless small and therefore do not affect the trends. As expected, the R_3SiOH and R_3SiCH_3 absorptions are inversely correlated, explaining the observed differences in hydrophilicity.

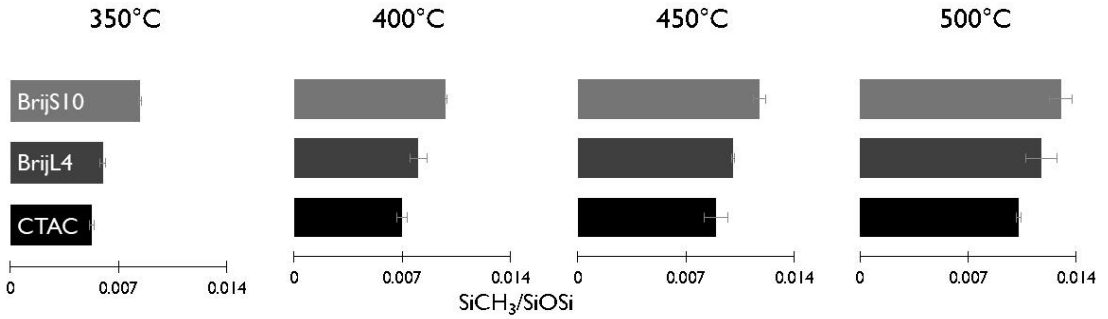

Figure 5.7. Extent of self-hydrophobization as revealed by the intensity ratio of the FTIR peaks at 1275 and 1030 cm^{-1} attributed to $SiCH_3$ and SiOSi, respectively

Nevertheless, deducing the hydrophilicity from the FTIR spectra does not seem completely reliable given the difference in the nature of the interactions between the organosilica oligomers and the ionic versus the non-ionic surfactants. The ionic surfactants interact with the organosilica oligomers and the organosilica walls through Coulomb forces, while the non-ionic surfactants interact through H-bonding. Therefore, the R_3Si-OH groups present in the films templated by the non-ionic surfactants might be "disguised" due to the H-bonding with the remaining non-ionic surfactants and as a result lowering and broadening the intensity of the –OH stretching absorption. Furthermore, as shown earlier, the BrijL4 and the BrijS10 molecules are dissociated at a higher temperature than the CTAC molecules. Thus, compared to the film templated with the ionic surfactant, the larger amount of remaining template in the films templated with the non-ionic surfactants further reduces the reliability of the FTIR analysis.

An additional evidence for the template-dependent hydrophobicity comes from water EP measurements. Following an anneal at 400°C, the MPMOC film adsorbs water at a relative pressure of 0.75 (Figure 5.8a). In comparison, the MPMOL4 film starts adsorbing moisture at a relative humidity of 90%. The most hydrophobic film appears to be the MPMOS10 since no water adsorption is evident indicating a WCA higher than 90°. When the pore size is taken into account (Figure 5.9) and the internal WCA is calculated using the Kelvin equation, the MPMOL4

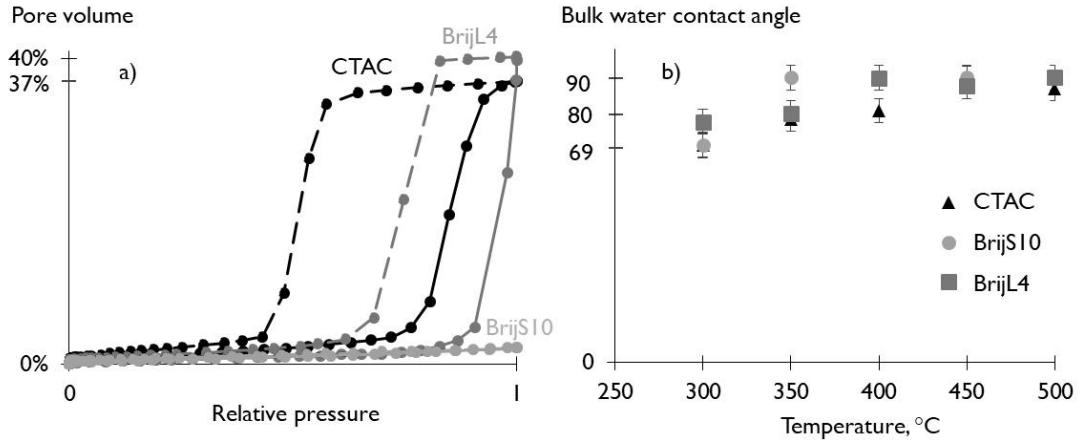

Figure 5.8. Water EP results: a) Water adsorption isotherms after annealing the films at 400°C; b) Internal (bulk) water contact angle calculated employing the Kelvin equation

and MPMOS10 seem to have a contact angle close to or above 90° while the MPMOC film has a contact angle close to 80° (Figure 5.8b).

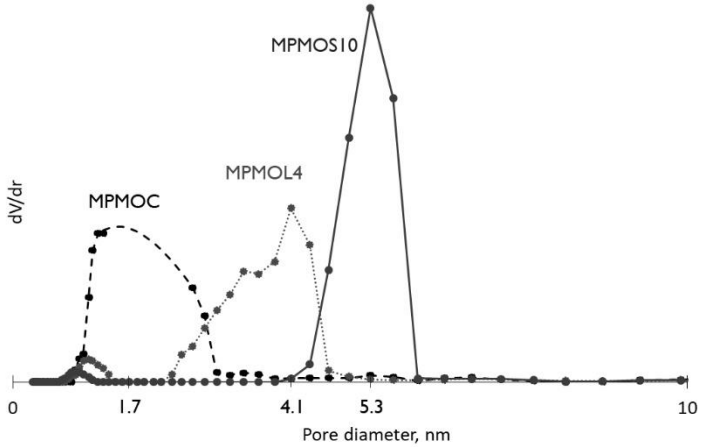

Figure 5.9. Pore size distribution calculated based on the toluene EP isotherms. The shown PSDs were obtained for the films annealed at 400°C after which almost all of the template is removed

On the other hand, considering all of the annealing temperatures, among the films being compared, the MPMOS10 seems to require the lowest activation energy in order to achieve a hydrophobic film since an annealing temperature of 350°C is sufficient to result in a film which does not adsorb moisture, even at 100% relative humidity. The MPMOL4 becomes hydrophobic only at 400°C while the MPMOC must be annealed at a temperature higher than 450°C before its internal WCA becomes 90°. These results support the conclusions based on the FTIR spectra. Nevertheless, the values of the internal WCA calculated using the Kelvin equation might be questionable, since the Kelvin equation has been shown not to be physically justified when approaching pore dimensions of ~2 nm or smaller.

The most convincing evidence for the template-dependent hydrophobicity in PMOs comes from a grafting treatment, where the films were exposed to the silylation agent dimethylamino trimethylsilane (DMATMS) from a vapour phase at 250°C and the RI changes were observed.

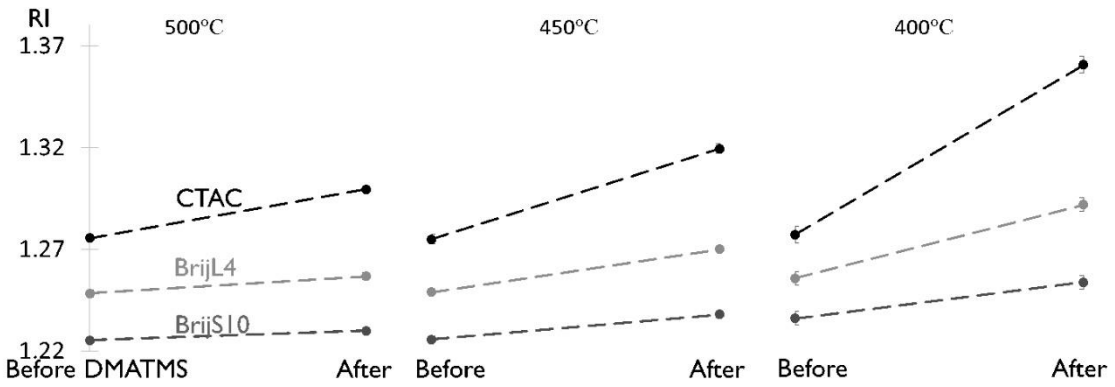

Figure 5.10.Change of the refractive index (RI) as a result of a silylation with dimethylamino trimethylsilane (DMATMS) of films annealed at a) 500°C; b) 450°C and c) 400°C

The ΔRI of the films follows similar trends independent of the annealing temperature (Figure 5.10). Essentially, the ΔRI decreases in the order MPMOS10 > MPMOL4 > MPMOC. The RI of the films increases due to a decrease in the pore volume as a result of the grafting of the Si-OH groups with $–Si(CH_3)_3$ groups (Figure 5.11). These results confirm that the largest concentration of Si-OH groups are associated with the MPMOC, while the smallest with the MPMOS10 film.

To understand the observed template-dependence of the PMO hydrophobicity, we consider two main effects – the capillary condensation and the competition between the self-hydrophobization and the silanol condensation reactions. First, we consider the capillary condensation because of the clear trend observed between the pore size and the hydrophobicity, i.e. the smaller the pore size the more hydrophilic the film. This trend is similar to the higher hydrophilicity reported in silica films with smaller pore size as compared to films with larger pore size.[10,11] Nevertheless, compared to the PMO films, the porous silica films are hydrophilic and they readily adsorb ambient moisture. Therefore, the larger amount of water observed in the silica films with smaller pore size by Anedda et al. can be explained considering the Kelvin equation, which indicates that at a particular relative humidity the surface with a higher curvature, i.e. smaller pores, will adsorb more water. Additionally, in films with a small pore size, Anedda et al. report H-bonding interaction which ultimately "masks" the Raman signal

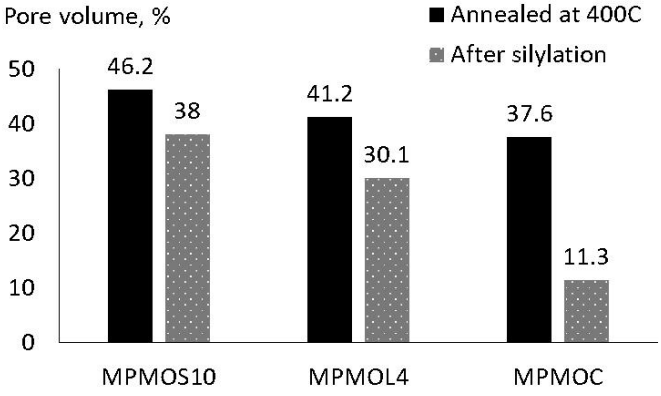

Figure 5.11. Pore volume change as a result of the silylation with DMATMS. Only the results for the films annealed at 400°C are shown.

from isolated Si-OH groups indicating that either H_2O molecules have adsorbed on these sites or due to their proximity the silanols have formed H-bonds. Therefore, in their study, the signal from isolated silanols increases with pore size. Similarly, Eslava et al.,[12] who investigated hydrophobic porous organosilica films, have suggested that in contrast to large pores, the silanols in small pores form H-bonds due to their proximity as a result of the high surface curvature of the small pores. This is contrary to what we observe (Figure 5.6). The isolated silanols are present in the CTAC-templated films, while their presence is significantly reduced in the films with larger pore sizes. Therefore, simply considering the capillary effect and the curvature of the pores seem insufficient to explain our observations.

Second, a silanol group can be consumed either by a condensation reaction or by a self-hydrophobization reaction. In contrast to the silanol condensation which occurs even at room temperature, the self-hydrophobization occurs only when a temperature of ca. 200°C is reached. Therefore, any differences among the films in the Si-OH content upon reaching the temperature of 200°C or higher will translate in varying potential number of self-hydrophobization reactions. Such differences are expected since a template-dependent polycondensation kinetics has been demonstrated in silica films,[8] where the polycondensation in films templated by non-ionic surfactants was slowed down as compared to a film templated by ionic surfactants. The effect of the template on the polycondensation has been attributed to the tendency of the hydrophilic poly(ethylene oxide) (PEO) chains of the non-ionic surfactants to penetrate into the silica walls which does not happen with the ionic surfactants. However, this effect influences the Si-OH condensation, not only during the drying of the film, but as long as the hydrophilic chains of the non-ionic template are present. Because of the small changes in RI at a temperature of ca. 200°C for the films templated by non-ionic surfactants, the PEO chains seem to be unaffected up until at least 200°C. As a result, we conclude that the silanol condensation during annealing is impeded in films templated by the non-ionic surfactants and therefore the Si-OH groups are available for self-hydrophobization reactions. At the same time, in the films templated by ionic surfactants, where no blocking of the silanol condensation occurs, the silanols are consumed in condensation reactions and therefore become unavailable for self-hydrophobization reactions. This hypothesis also explains the difference between the BrijL4 and BrijS10-templated films since BrijL4 has a shorter PEO chain than BrijS10.

5.4. Conclusions

The self-hydrophobization reaction characteristic of PMO materials can occur at a temperature as low as 200°C, significantly lower than previously reported. Also, the self-hydrophobization is affected by the presence of a template requiring a higher activation energy in low density materials. We have provided extensive experimental evidence for a template dependence of the degree of self-hydrophobization in methylene-bridged PMOs. The CTAC-templated film with a

pore size of 1.7 nm results in a higher hydrophilicity when compared to films templated by BrijL4 and BrijS10 with a pore size of 4.1 or 5.3 nm, respectively. The template-dependent hydrophobicity has been tentatively attributed to the blocking of the silanol condensation by the poly(ethylene oxide) chains in the Brij-type surfactants leading to a higher concentration of Si-OH groups available for self-hydrophobization reactions. Our findings are important when PMO materials are expected to have both a small pore size and high hydrophobicity, such as for low-k dielectrics application. Similarly, the hydrophilic to hydrophobic balance is important for the diffusion of molecules in membranes, chromatographic supports and drug carriers.

5.5. References

[1] P. Van der Voort, D. Esquivel, E. De Canck, F. Goethals, I. Van Driessche, F. J. Romero-Salguero, *Chem. Soc. Rev.* **2013**, *42*, 3913.

[2] W. Wang, J. E. Lofgreen, G. A. Ozin, *Small* **2010**, *6*, 2634.

[3] S. S. Park, M. Santha Moorthy, C.-S. Ha, *NPG Asia Mater.* **2014**, *6*, e96.

[4] F. Goethals, I. Ciofi, O. Madia, K. Vanstreels, M. R. Baklanov, C. Detavernier, P. Van Der Voort, I. Van Driessche, *J. Mater. Chem.* **2012**, *22*, 8281.

[5] W. Wang, D. Grozea, S. Kohli, D. D. Perovic, G. A. Ozin, *ACS Nano* **2011**, *5*, 1267.

[6] T. Asefa, M. J. MacLachlan, H. Grondey, N. Coombs, G. A. Ozin, *Angew. Chemie Int. Ed.* **2000**, *39*, 1808.

[7] B. D. Hatton, K. Landskron, W. Whitnall, D. D. Perovic, G. A. Ozin, *Adv. Funct. Mater.* **2005**, *15*, 823.

[8] V. R. Koganti, S. Das, S. E. Rankin, *J. Phys. Chem. C* **2014**, *118*, 19450.

[9] D. Quéré, *Phys. A Stat. Mech. its Appl.* **2002**, *313*, 32.

[10] A. Anedda, C. M. Carbonaro, F. Clemente, R. Corpino, P. C. Ricci, D. Fisica, U. Cagliari, *J. Phys. Chem. B* **2003**, *107*, 13661.

[11] C. M. Carbonaro, F. Clemente, R. Corpino, P. C. Ricci, A. Anedda, *J. Phys. Chem. B* **2005**, *109*, 14441.

[12] S. Eslava, M. R. Baklanov, J. Urrutia, C. E. A. Kirschhock, K. Maex, J. A. Martens, *Adv. Funct. Mater.* **2008**, *18*, 3332.

CHAPTER 6. GEMINI-TEMPLATED PMO FILMS

Periodic mesoporous organosilica thin films were synthesized by evaporation-induced self-assembly of 1,2-bis(triethoxysilyl)ethane and an ionic Gemini 16-12-16 surfactant under acidic conditions. The synthesis of Gemini-templated PMO film is investigated in an attempt to control the film's pore organization. Control over the pore organization is required in order to investigate the impact of the pore arrangement on the mechanical properties. The Gemini 16-12-16 has been selected as the most promising candidate due to its large head size which favours the formation of spherical micelles and therefore, the formation of cubic pore arrangement. The films were characterized by FTIR spectroscopy, GISAXS, ellipsometric porosimetry, impedance measurements and nanoindentation. The ease of control of the packing parameter in Gemini surfactants makes the PMO film templated by a Gemini an exciting first step towards small pore size PMO films with engineered mesophases.

6.1. Introduction

Periodic mesoporous organosilica (PMO) materials have been predominantly reported as powders.[1] Nevertheless, the PMO's most promising functional morphology seems to be as thin films due to their potential application as smart coatings, for sensing, membrane separation, displays, and due to their ability to be integrated into electronic or electromechanical devices[2–4]. For example, PMO films are considered to be promising candidates as interlayer dielectric materials in micro-electronic devices (low-k materials).[5] The first PMO films evaluated for a potential low-k application were reported more than 10 years ago.[4] While Ozin's group has been the most productive in this area, recently, our group expanded the choice of PMOs suitable for low-k application.[6] In spite of these achievements, the semiconductor industry has found it challenging to take advantage of the available materials calling for further material innovation which also allows for a rational mesophase control.[5] In powders, the PMO mesophase has been shown to be systematically controlled by the use of Gemini surfactants ($C_{m\text{-}s\text{-}m}$).[7] These surfactants possess a structure resembling a pair of conventional single chain surfactants covalently connected by a spacer. The spacer can be varied in length granting control over the surfactant packing parameter[8,9] which is crucial for engineering the PMO mesophase.

6.2. Experimental Section

In this work, we demonstrate the possibility of obtaining small pore size spin-coated PMO films via the evaporation-induced self-assembly mechanism. The templating agent, Gemini 16-12-16 ($[C_{16}H_{33}N(CH_3)_2(CH_2)_{12}N(CH_3)_2C_{16}H_{33}]Br_2$), was synthesized based on a previously reported procedure[10] in which stoichiometric amounts of 1,12-dibromododecane and N,N-dimethyl hexadecylamine were refluxed for 24h in acetone. The dried surfactant was used for the subsequent synthesis of the PMO solution. The molar ratios of the reagents in the solution was 1,2-bis(triethoxysilyl)ethane (BTESE) : Gemini 16-12-16 : 1-methoxy-2-propanol : H_2O : HCl = 1:0.21:34:20:0.037. After stirring for 300 min at room temperature, the solution was spin-coated on a UV/O_3 cleaned 4x4 cm^2 Si substrate at 5000 rpm for 60 s. The template was removed from the condensed film by thermal decomposition at 400°C for 2h in inert N_2 ambient. The film was consequently silylated at 250°C by an exposure to N,N-dimethylamino trimethylsilane (DMATMS) vapours at a pressure of 2 Torr following a pre-bake at 250°C for 10 min.

An ethane-bridged mesoporous organosilica film templated by the non-ionic surfactant poly(ethylene glycol) (18) tridecyl ether was also synthesized in order to ascertain the template-dependent hydrophilicity described in the previous chapter. The film was obtained from a solution containing 1,2-bis(triethoxysilyl)ethane (BTESE), Poly(ethylene glycol) (18) tridecyl ether, 1-methoxy-2-propanol, H_2O, and HCl in molar ratio of 1:0.06:26:20:0.037. After stirring for 300 min at room temperature, the solution was spin-coated on a UV/O_3 cleaned 4x4 cm^2 Si

substrate at 1500 rpm for 60 s. The template removal was the same as for the Gemini-templated PMO. No silylation was performed on this film.

6.3. Results and Discussion

The chemical structure of the films following the template removal at 400°C was investigated by transmission FTIR measurements. Figure 6.1 shows the characteristic absorptions of the ethylene-bridged PMO[11–13] in the ranges 500-1500 and 2700-4000 cm^{-1} providing evidence for the presence of intact Si-CH_2-CH_2-Si groups. The absorptions centred at 1273 and 1417 cm^{-1} are attributed to C-H deformation in the bridging ethylene groups. Notably, isolated, non-hydrogen-bonded, Si-OH groups are present as deduced from the sharp peak at 3734 cm^{-1}. Additionally, a small amount of physisorbed water, H-bonded - OH groups, is deduced from the wide peak centred at ca. 3530 cm^{-1}. It has been previously demonstrated that an ethane PMO does not become completely hydrophobic even after annealing at a temperature as high as 500°C.[14] Nevertheless, in contrast to that report, our group has shown[6] that a complete hydrophobization can be achieved for a methylene-bridged precursor at 400°C. Therefore, we hypothesize that the observed signal attributed to Si-OH functionalities is a result of the use of the ionic Gemini 16-12-16 surfactant. This hypothesis found support from the results of an additional experiment in which a non-ionic templating agent, namely $C_{13}H_{27}(CH_2CH_2O)_{18}$, was employed in the PMO synthesis instead of the Gemini surfactant. No Si-OH peak was observed in the FTIR spectrum of the film templated with the non-ionic surfactant (Figure 6.2). Nevertheless, we demonstrate that the hydrophobicity of the Gemini-templated PMO film can be ensured upon exposure to DMATMS vapours at 250°C for 5 min. The Si-OH signal as well as the signal attributed to adsorbed H_2O disappears completely, providing evidence to the assignment to physisorbed water molecules.

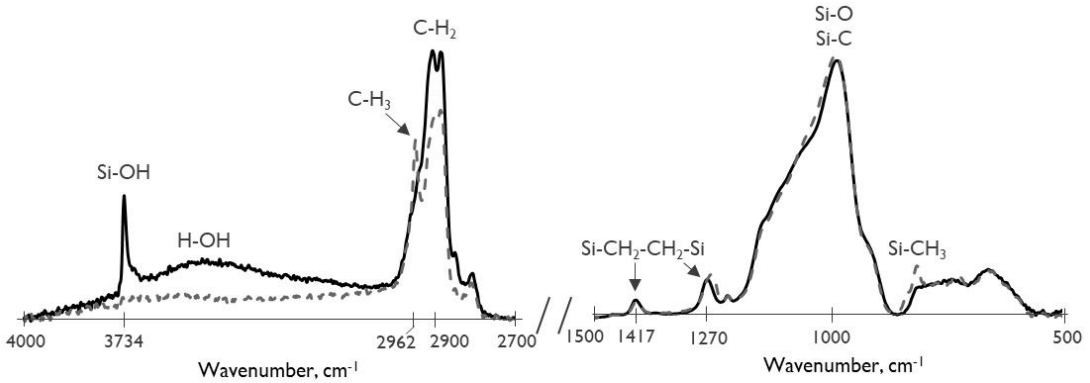

Figure 6.1. FTIR spectra of the Gemini-templated PMO after template removal at 400°C (solid line) and after further silylation with DMATMS (dashed line)

The pore volume of the PMO was investigated by ellipsometric porosimetry (EP) measurements employing toluene as an adsorbate. Figure 6.3 presents the isotherms observed following the template decomposition as well as after the silylation with DMATMS. Both of the isotherms are type IVb[15] indicating the small pore size calculated to be ca. 2 nm. Notably, the silylation results

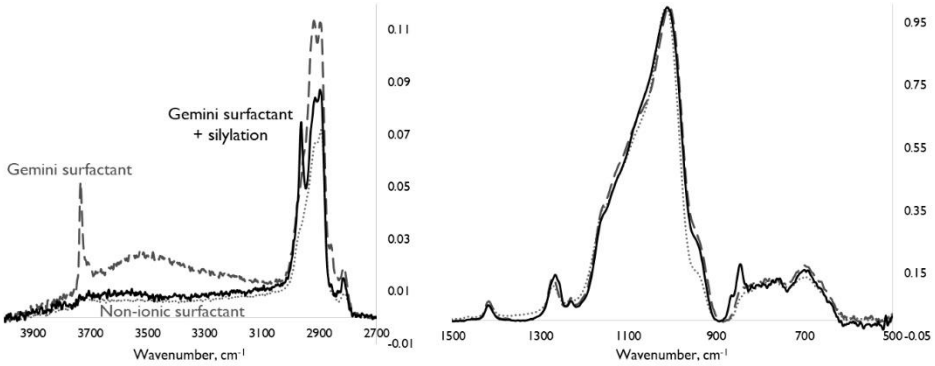

Figure 6.2. Comparison of the FTIR spectra of ethane PMO templated with Gemini vs non-ionnic surfactant. Unlike the Gemini-templated PMO, no Si-OH groups are apparent in the films templated by a non-ionic surfactant.

in a not negligible 8% decrease in pore volume. The latter observation is an additional evidence for the significant amount of Si-OH groups in the film which open the possibility for grafting desired functional groups. Additionally, the pore size distribution was not affected by the functionalization as can be seen from the inset in Figure 6.3. The uniformity of the silylation reaction was deduced from a combination of the transmission FTIR results and the mean square error (MSE) which is used as a figure of merit for the goodness-of-fit of the modelled spectroscopic ellipsometric dispersion. Following the silylation step, the MSE increased from 0.2 to 0.4 which is within the range of MSE values observed for ~160 nm thick films. Therefore, we acknowledge a potential non-uniformity of the silylation probably due to pore blocking. Nevertheless, the small increase of the MSE combined with the disappearance of the IR Si-OH peak indicate that the silylation has been largely uniform throughout the thickness of the film.

The pore organization was investigated by grazing-incidence small-angle x-ray scattering (GISAXS) at the Austrian SAXS beamline in ELETTRA, Italy. Figure 6.4 shows the scattering pattern observed for the Gemini-templated PMO. The deduced pore organization is a distorted p6m which has been shown to correspond better to a c2mm space group.[16] The distortion is the result of a uniaxial shrinkage normal to the stiff Si substrate. The analysis of the semi-elliptical ring, seen in the scattering pattern, provides information about the anisotropy of the pore

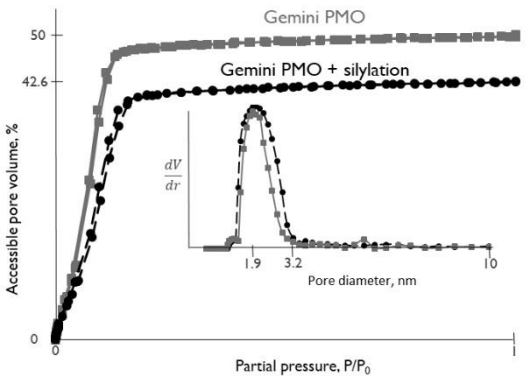

Figure 6.3. Toluene EP isotherms of a Gemini PMO film and the same film after silylation. The inset shows the pore size distribution

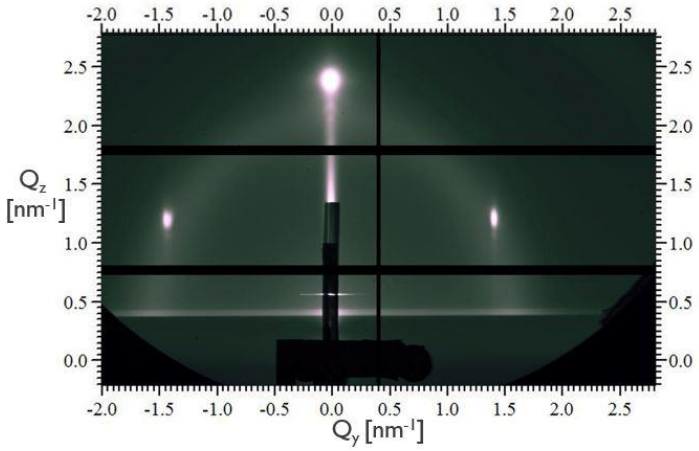

Figure 6.4. GISAXS pattern indicative of a distorted p6m pore organization.

dimensions normal (r_s) and parallel (r_l) to the surface. The r_l/r_s ratio was calculated to be 1.53 which is similar to previously observed deviations[16] from the ideal case in which the ratio is expected to be 1.

Additionally, we investigated the dependence of the pore organization on the ambient relative humidity at which the as-spun film is aged. An as-deposited film aged at lab humidity, which was typically ca. 40-45%, results in a wormlike mesophase (Figure 6.5). On the other hand, a film aged at 67% humidity for 6 h leads to a clear diffraction peak indicating the formation of a 2D hexagonal phase. Regarding the mesophase formation, these results demonstrate the importance of the humidity conditions at which the as-deposited film is aged.

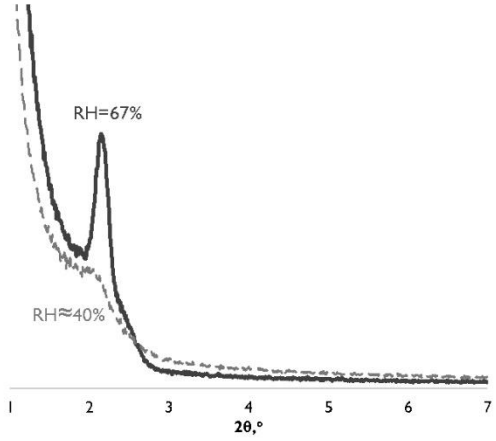

Figure 6.5. XRD spectra showing the effect of the relative humidity (RH) at which the as-spun film is aged. The high humidity of 67% results in an oriented pore structure unlike the aging at RH=40%

Following the silylation, the film was evaluated for a low dielectric constant (low-k) insulator application. The capacitance of a metal-insulator-semiconductor structure, obtained by a Pt evaporation through a shadow mask on the PMO film, was measured as a function of frequency. It has been pointed out[6] that the dielectric constant of low-k films should be reported at a frequency of 100 kHz due to a potential rapid increase in the dissipation factor at higher frequencies. Nevertheless, in literature, the dielectric constant is often reported at a frequency

of 1 MHz. Therefore, for a better comparison with the available literature we report the results from both frequencies. At 100 kHz, we calculated a dielectric constant of 2.16 and we observed a dielectric loss of 4.6×10^{-3}. On the other hand, the relative permittivity at 1 MHz was calculated

Organosilica precursor	Template	Pore volume, %	$\bar{d}$, nm	YM, GPa	k
POSS[17]	CTAC	39.0	1.56	3.3[s]	1.73[m]
3-ring[6]	BrijS10	55.0	3.0	-	1.8[k]
HFPDB[18]	BrijL4	-	6.0	5.54[n]	1.58[m]
3-ring[14,19]	CTAC	49.0	2.0	14.4[s]	1.63[m]
BTESE[4,14]	CTAC	45.0	2.0	10.2[s]	2.2[m]
BTESM[4,14]	CTAC	53.0	2.0	10.1[s]	2.3[m]
BTESE[20]	CTAC	47.0	2.18	29[s]	1.7[m]
BTESE[tw]	Gemini	42.6	1.9	4.7[n]	2.1[k]

Table 6.1. Comparison of the low-k relevant properties of PMO films reported in literature with the film demonstrated in this work. All of the films are reported to have 2D hexagonal pore organization. The Young's modulus (YM) was measured by s – SAWS or n – NI. The dielectric constant was reported at k – 100 kHz or m – 1MHz. tw – this work. POSS - polyhedral oligomeric silsesquioxane; 3-ring - 1,1,3,3,5,5-hexaethoxytrisilacylohexane; BTESM – 1,2-bis(triethoxysilyl)methane; HFPDB - [hexfluoropropane-2,2-diyl)dibenzyl-bridged organosilane; CTAC - cetyltrimethylammonium chloride.

to be 2.10 while the dielectric loss remained below 0.1 at 2.27×10^{-2}. Furthermore, the Young's modulus, investigated by nanoindentation, was calculated to be 4.7 GPa which is higher than the ≈4 GPa requirement established to ensure a compatibility with the chemical mechanical polishing step.[21] Based on these results, combined with the calculated small pore size of 2 nm at the pore volume of 40 to 50%, we demonstrate that the Gemini-templated PMO film is a suitable low-k dielectric candidate. A comparison of our results with those reported in literature (Table 6.1) is not straightforward due to differences in the characterization methodology. While the possible effects of the capacitive reactance resulting in a higher dissipation factor and therefore in a lower dielectric constant were already mentioned, similar difficulties exist in the determination of the Young's modulus which is most often reported based on nanoindentation (NI) or surface acoustic wave spectroscopy (SAWS) measurements. In both techniques, the characterized films are assumed to possess isotropic properties[22] which clearly does not apply for a film with a 2D hexagonal pore organization, which is the most often reported mesophase. These films possess significantly different stiffness coefficients in the longitudinal and transverse axes, hence the extracted results would strongly depend on the direction from which the response is measured. Thereby, not only the characterization methodology but also the measurement conditions could affect the extracted results. For instance, employing the SAWS results in an YM value, which is more representative of the in-plane YM component, because acoustic waves propagate parallel to the substrate.[20,23] On the other hand, an NI measurement using a Berkovich tip provides mainly the out-of-plane YM component.[24] Compared to the in-plane components, the YM component normal to the substrate is the weakest in PMO films with a 2D hexagonal pore organization and pores parallel to the substrate.[5] At a pore volume of 50%, the in-plane YM is expected to be about two times larger than the out-of-plane YM.[5,25] The difference between the YM components becomes larger when the uniaxial film shrinkage, characteristic of the sol-

gel deposition, is taken into account.[26] Therefore, we expect the differences in the film properties to be less significant if they are characterized by the same methodology. In light of these considerations, our demonstration of a Gemini-templated PMO film hints at the possibility of obtaining PMO films with engineered mesophases by taking advantage of the configurability of the surfactant packing parameter of the Gemini surfactants.

6.4. Conclusions

In conclusion, for the first time, we have shown the results of the synthesis and the characterization of an ethane-PMO film templated with the ionic Gemini 16-12-16 surfactant molecules. A distorted 2D hexagonal pore organization with a pore size distribution centred at 2 nm was deduced. The Gemini-templated PMO films were shown to meet the material specifications as low-k dielectric layers. The demonstration of a PMO film templated with a Gemini surfactant, a class of surfactants whose packing parameter can relatively easily be controlled, opens the possibility for a systematic engineering of the mesophase of PMO films with a small pore size.

6.5. References

[1] P. Van der Voort, D. Esquivel, E. De Canck, F. Goethals, I. Van Driessche, F. J. Romero-Salguero, *Chem. Soc. Rev.* **2013**, *42*, 3913.

[2] P. Innocenzi, L. Malfatti, *Chem. Soc. Rev.* **2013**, *42*, 4198.

[3] N. Mizoshita, T. Tani, S. Inagaki, *Chem. Soc. Rev.* **2011**, *40*, 789.

[4] B. D. Hatton, K. Landskron, W. Whitnall, D. D. Perovic, G. A. Ozin, *Adv. Funct. Mater.* **2005**, *15*, 823.

[5] D. J. Michalak, J. M. Blackwell, J. M. Torres, A. Sengupta, L. E. Kreno, J. S. Clarke, D. Pantuso, *J. Mater. Res.* **2015**, *30*, 3363.

[6] F. Goethals, I. Ciofi, O. Madia, K. Vanstreels, M. R. Baklanov, C. Detavernier, P. Van Der Voort, I. Van Driessche, *J. Mater. Chem.* **2012**, *22*, 8281.

[7] H. I. Lee, C. Pak, S. H. Yi, J. K. Shon, S. S. Kim, B. G. So, H. Chang, J. E. Yie, Y.-U. Kwon, J. M. Kim, *J. Mater. Chem.* **2005**, *15*, 4711.

[8] T. Lu, Y. Lan, C. Liu, J. Huang, Y. Wang, *J. Colloid Interface Sci.* **2012**, *377*, 222.

[9] S. D. Wettig, R. E. Verrall, *J. Colloid Interface Sci.* **2001**, *235*, 310.

[10] P. Van der Voort, M. Mathieu, F. Mees, E. F. Vansant, *J. Phys. Chem. B* **1998**, *102*, 8847.

[11] F. Hoffmann, M. Güngerich, P. J. Klar, M. Fröba, *J. Phys. Chem. C* **2007**, *111*, 5648.

[12] V. Rebbin, M. Jakubowski, S. Pötz, M. Fröba, *Microporous Mesoporous Mater.* **2004**, *72*, 99.

[13] M. Redzheb, L. Prager, S. Naumov, M. Krishtab, S. Armini, P. Van Der Voort, M. R. Baklanov, *Appl. Phys. Lett.* **2016**, *108*, 12902.

[14] W. Wang, D. Grozea, S. Kohli, D. D. Perovic, G. A. Ozin, *ACS Nano* **2011**, *5*, 1267.

[15] M. Thommes, K. Kaneko, A. V. Neimark, J. P. Olivier, F. Rodriguez-Reinoso, J. Rouquerol, K. S. W. Sing, *Pure Appl. Chem.* **2015**, *87*, 1051.

[16] P. Chatterjee, S. Hazra, H. Amenitsch, *Soft Matter* **2012**, *8*, 2956.

[17] M. Seino, W. Wang, J. E. Lofgreen, D. P. Puzzo, T. Manabe, G. A. Ozin, *J. Am. Chem. Soc.* **2011**, *133*, 18082.

[18] J. Zhang, G. Zhang, Y. Gao, R. Sun, C. P. Wong, *J. Mater. Sci.* **2016**, *51*, 7966.

[19] K. Landskron, B. D. Hatton, D. D. Perovic, G. A. Ozin, *Science* **2003**, *302*, 266.

[20] W. Wang, D. Grozea, A. Kim, D. D. Perovic, G. a Ozin, *Adv. Mater.* **2010**, *22*, 99.

[21] S. Lin, L. Lui, M. Daniels, A. Gonzalez, J. T. Wetzel, K. A. Monnig, P. A. Winebarger, S. Jang, D. Yu, M. S. Liang, In *Proceedings of the IEEE 2001 International Interconnect Technology Conference (Cat. No.01EX461)*; IEEE, 2001; pp. 146–148.

[22] K. Vanstreels, C. Wu, M. Gonzalez, D. Schneider, D. Gidley, P. Verdonck, M. R. Baklanov, *Langmuir* **2013**, *29*, 12025.

[23] M. Leonhardt, D. Schneider, J. Kaspar, S. Schenk, *Surf. Coatings Technol.* **2004**, *185*, 292.

[24] A. Delafargue, F. J. Ulm, *Int. J. Solids Struct.* **2004**, *41*, 7351.

[25] Y. H. Zhao, G. P. Tandon, G. J. Weng, *Acta Mech.* **1989**, *76*, 105.

[26] H. Miyoshi, H. Matsuo, H. Tanaka, K. Yamada, Y. Oku, S. Takada, N. Hata, T. Kikkawa, *Japanese J. Appl. Physics, Part 1 Regul. Pap. Short Notes Rev. Pap.* **2005**, *44*, 1161.

CHAPTER 7. TIME-RESOLVED GISAXS INVESTIGATION OF THE SELF-ASSEMBLY OF SPIN-COATED PMO FILMS

The mesophase formation in spin-coated periodic mesoporous organosilica (PMO) films aged at a controlled ambient humidity is investigated by time-resolved grazing-incidence small-angle x-ray scattering (GISAXS). The investigation demonstrates, for the first time, the existence of a tunable steady state in PMO spin-coated films. Thus, a film deposited at a relative humidity of 20% results in a lamellar mesophase, while a subsequent increase to 70% leads to a phase transformation resulting in a $P6_3/mmc$ space group, observed for the first time in a PMO film. On the other hand, an increase of the surfactant to organosilica precursor molar ratio, between 0.26 and 0.31, results in films which when placed at 70% humidity form a mix of a 2D and a 3D hexagonal phases. A further increase of the surfactant amount leads to films with a 2D hexagonal phase. On the other hand, if the H_2O to organosilica precursor ratio is reduced from 30 to 15, instead of a 3D hexagonal phase, a cubic mesophase is observed. Finally, the importance of the polycondensation degree of the organosilica oligomers is emphasized by demonstrating different mesophases as a function of the solution aging.

***M. Redzheb**, S. Bernstorff, B. Sartori, P. Van Der Voort, S. Armini, Periodic Mesoporous Organosilica Films with a Tunable Steady-State Mesophase, ChemPhysChem (2017)*

7.1. Introduction

Controlling the pore organization of mesoporous (organo)silica films is of crucial importance in many applications. A mix of hexagonally close-packed and body-centered cubical mesophases allow an improved regulation of the diffusion speed through a membrane used for DNA translocation.[1] Similarly, the nanoporous structure has been shown to have a great influence on the permeability to solution-phase redox probes.[2–4] Plane space groups, of which p6mm is the most often reported, allow to obtain films with birefringent properties.[5,6] The importance of the pore architecture has also been demonstrated for a selective capturing of proteins where 3D porous structures have shown a better performance in selectively enriching low molecular weight peptides with respect to 2D hexagonal mesophase.[7] Additionally, the pore texture has been shown to be important in loading and releasing of organic molecules using a fluorescent labeling molecule.[8] A cubic mesophase is expected to result in a material which can sustain high porosities and therefore can lead to an ultra-low dielectric constant[9] PMO film which is considered a promising intermetal insulating (low-k) candidate for future generation microchips. Furthermore, a cubic mesophase is expected to result in a film with an optimal Young's modulus[10] for a given density.

The synthesis parameters and deposition conditions which determine the mesophase in periodic mesoporous silica (PMS) films have been extensively researched.[11–13] On the other hand, periodic mesoporous organosilica (PMO) films are similar to PMS in terms of chemistry and templating mechanism, namely during a deposition they rely on the Si-OH polycondensation during an evaporation-induced self-assembly of surfactant molecules. Therefore, the parameters recognized to be determining the pore organization in the PMS are expected to be equally important in the determination of the mesophase in PMOs. Nevertheless, considering the available literature, two of these factors seem to be neglected in the synthesis and deposition of PMO films. The first one is the degree of organosilica polycondensation. It has been demonstrated[13] that the formation of different mesophases for silicas can be triggered by varying the degree of silica polycondensation, which might simply translate into varying the aging of the solution. The second factor, shown to influence the surfactant organization in PMS, is the relative humidity at which the film is deposited and subsequently aged.[14–18] Nevertheless, the ambient relative humidity has still not been established as a relevant parameter to be controlled in the deposition of PMO thin films. The humidity conditions at which the films were deposited and aged before the template extraction is specified in few[19] but not in the majority of the reports on PMO thin films.[20–23] In addition, the effect of the ambient humidity on ordered mesoporous silica films has been studied on dip-coated films, but there is only one study[18] which considers the effect of humidity on the mesophase in spin-coated films. As a result, all the recent reviews[24–29] which consider PMOs, and in particular PMO films, for various applications

do not mention the effect of humidity. We consider this to be a deficiency in the literature which can potentially hinder progress in material understanding and nanoscale engineering. We present results which demonstrate the importance of the humidity conditions at which an as-deposited PMO film is aged before a template extraction.

In addition, since none of the above-mentioned studies has shown time-resolved measurements of the mesophase formation in spin-coated PMO films, we present our results from a time-resolved grazing-incidence small angle x-ray scattering (GISAXS) investigation of the effect of the relative humidity on spin-coated PMO films. In this way, we demonstrate, for the first time, the existence of a tunable steady state in a spin-coated PMO film.

7.2. Experimental Section

The coating solution was synthesized using a modified synthesis procedure of Landskron et al.[30] In a typical synthesis ethanol (1.44 ml), HCl (0.71 ml 10^{-3}M), cetyltrimethylamonium chloride (0.85 ml 25% aqueous solution), and 1,1,3,3,5,5-hexaethoxy-1,3,5-trisilacyclohexane, also referred to as ring precursor, (0.93 ml) were mixed and stirred for 20 min at room temperature. The range of the investigated synthesis conditions are provided in Table 7.1. Following the stirring, the solution was spin-coated at 2500 rpm for 45 s on a 100 Si substrate on which a native oxide had been grown. The deposition was performed at RH=20%. The as-deposited films were transferred within 5 min into a humidity-controlled cell, specifically designed for GISAXS measurements. The humidity level could be maintained within ±2 percentage points from the set value. Following the aging at a controlled humidity, the films were dried by reducing the humidity to 20% and observing the changes in the GISAXS pattern until no further modifications were apparent. Radiation damage could be observed visually on the surface of the sample. In order to clarify its impact on the observed GISAXS patterns, the sample was translated perpendicular to the specular plane by 1 cm. The same pattern was observed indicating that the x-ray did not have a determining impact on the mesophase formation. Next, the films were annealed at 150°C for 10 min on a hot plate in a non-controlled ambient atmosphere. Finally, the template was thermally decomposed at 400°C in inert N_2 atmosphere for 2 h.

Ring precursor	CTAC	H_2O	HCl, x10^{-4}	C_2H_5OH	Mesophase at RH=70%
1	0.26	30.0	2.9	10.0	3D hex
1	0.28-0.31	30.8-32.5	2.9	10.0	2D + 3D hex
1	>0.31	>32.5	2.9	10.0	2D hex
1	0.15	8.4	2.9	10.0	No scattering
1	0.25	13.3	2.9	10.0	Cubic*
1	0.29-0.31	15.4-16.6	2.9	10.0	Cubic**
1	>0.31	>16.6	2.9	10.0	2D hex

Table 7.1. Molar ratios of the investigated syntheses conditions

7.3. Results and Discussion

The mesophase of an as-deposited film with a cetyltrimethylammonium chloride (CTAC) to 1,1,3,3,5,5-hexaethoxy-1,3,5-trisilacyclohexane (ring precursor), i.e. a surfactant to organosilica precursor ratio of 0.26 transforms from a lamellar to a 3D hexagonal phase when the ambient humidity is increased from 20 to 70% (Figure 7.1). The lamellar mesophase observed at RH=20% is deduced by the diffraction spots situated only in the specular plane (Figure 7.1a). The lamellar phase is characterized by alternating sheets of surfactant and organosilica oligomers parallel to the substrate. No phase transformations are observed when the relative humidity is maintained at 20%. On the other hand, mesophase transformations occur when the RH is increased to 70 % with an average rate of 5 percentage points per minute. The increased humidity results in a moisture adsorption by the film which is evident from the shift of the GISAXS diffraction spots towards smaller scattering vector values (not shown). As a result of the adsorbed water, the surfactant molecules organize into micelles evident by the clearly defined Debye-Scherrer ring which can be seen at an intermediate stage (Figure 7.1b) when the film has still not reached an equilibrium with the ambient humidity of 70%. The continued water adsorption leads to an increase in the spacing between the micelles apparent by the "shrinking" Debye ring (not shown). Finally, the mesophase transforms into a well-defined $P6_3/mmc$ space group and stabilizes which is established by the unchanging scattering pattern (Figure 7.1c). A simulation of the observed scattering pattern with NANOCELL[31] allowed us to deduce the unit cell parameters of a=7.5 nm and c=11.5 nm.

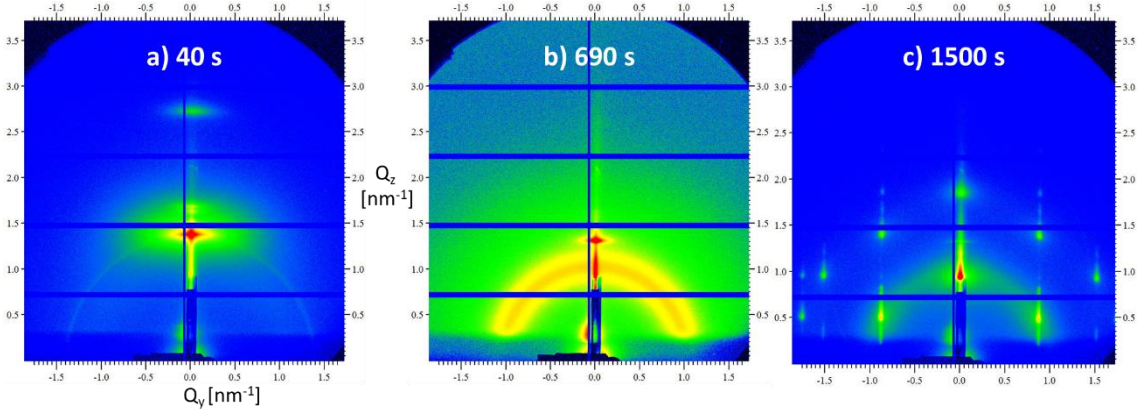

Figure 7.1. GISAXS patterns of a PMO film placed at a controlled humidity environment: a) As-deposited film at RH=20%; b) Debye ring formed upon increase of RH to 70%; c) 3D hexagonal phase stabilized at RH=70%; Sample to detector distance (SDD) = 1.99 m

To obtain a 3D hexagonal phase, the surfactant to organosilica precursor ratio needs to be 0.26 or lower. The lowest ratio we investigated was 0.15 which resulted in a diffuse scattering indicating the lack of an ordered organization as well as no formation of micelles due to the low surfactant concentration. On the other hand, the ratios in the range between 0.27 and 0.31 lead to films with a mixed 2D (p6mm) and 3D hexagonal mesophase at RH=70% (Figure 7.2a), while the ratios higher than 0.31 and up to 0.6 result in films with a 2D hexagonal mesophase (not

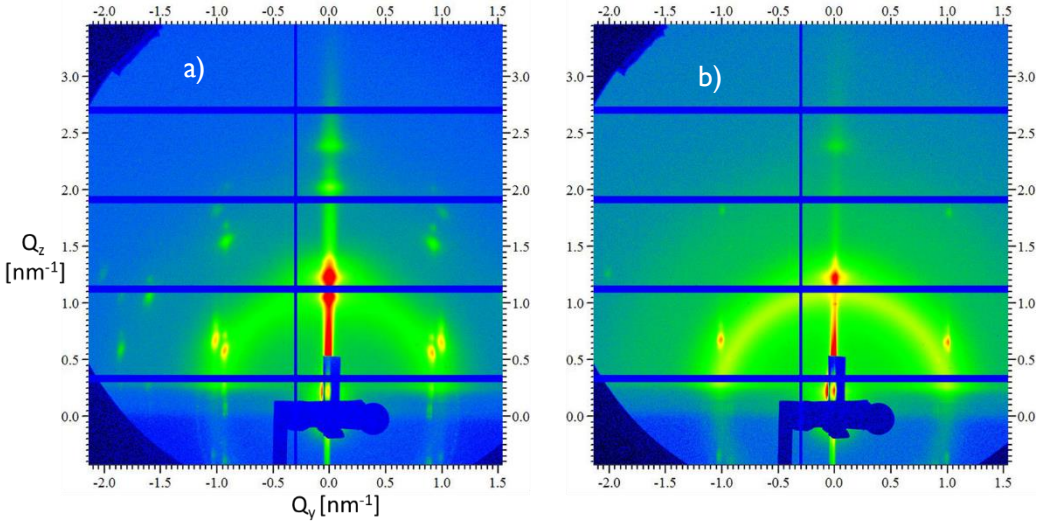

Figure 7.2. a) A mix of 2D and 3D hexagonal phases obtained at a surfactant:organosilica ratio of 0.31 at RH=70% while a further increase of humidity to 85% leads to b) disappearance of the 3D hexagonal phase and only the 2D phase remains. SDD=1.87 m

shown). The thickness of the films as seen in TEM micrographs is more than 900 nm. According to ellipsometric measurements, the thickness of the films is up to ~1200 nm. Generally, the thickness of the films increases with the surfactant to organosilica precursor ratio.

The high ambient humidity of 70% has competing effects on the self-assembly of the surfactant-organosilica system. On the one side, the increased humidity provides the driving force to the CTAC molecules to organize into micelles with increased surface curvature[16] while, on the other hand, it causes the depolymerization[32] of the organosilica oligomers which drives a decrease of the micelle surface curvature. Both of these effects were deduced when a film with a surfactant to organosilica precursor ratio of 0.31 was placed in a controlled humidity cell. When the relative humidity is increased from 20 to 70%, the initially observed lamellar phase evolves into an intermediate 2D hexagonal phase. Consequently, at 70% humidity, the 2D hexagonal phase transforms into a 3D hexagonal phase. This transformation can be understood in terms of increasing surface curvature of the micelles induced by the H_2O molecules adsorbed at the palisade of the micelles.[16] On the other hand, we observed for the first time, a 3D to 2D hexagonal phase transformation when keeping the humidity at 70%. We interpret this unexpected behavior in light of the charge density matching mechanism[33–35] proposed as an explanation for the interaction between ionic surfactants, such as CTAC, and charged matrix molecules, which determines the formation of a specific mesophase. The proposed mechanism takes into account the surface charge density characteristic of each lyotropic liquid crystal formed by the surfactant molecules. The charge density decreases going from a lamellar structure through the bicontinuous phases, followed by the phases formed by tubular micelles, such as the 2D hexagonal phase, while the lowest charge density is associated with phases consisting of spherical micelles,[36] including the 3D hexagonal phase. Therefore, the transformation from a 2D hexagonal to a 3D hexagonal phase, observed during the humidity

increase, results in a decrease in charge density. However, in order to maintain the formed mesophase the organosilica oligomers also must decrease their charge density which occurs as a result of the condensation reactions. In a condensation reaction the charged Si-OH_2^+ or Si-O^- groups, depending on the pH, are consumed to form neutral Si-O-Si units. Thus, a hindered polycondensation reaction or a competing hydrolysis reaction would counteract the decrease in charge density associated with the 2D to 3D phase transformation. The fact that first a 2D to 3D hexagonal phase transformation occurs indicates that it was allowed by the combination of the charge density of the organosilica matrix and the effect of the adsorbed H_2O. However, the reverse transformation from a 3D to a 2D phase observed without changing the humidity conditions hints at an increase of the charge density of the organosilica matrix, possibly due to hydrolysis of Si-O-R bonds. The Si-O-R bonds can be either Si-O-C_2H_5 or Si-O-Si. The ethoxy groups are expected to be completely hydrolyzed before the deposition since the H_2O to organosilica precursor molar ratio in the initial solution is ca. 30:1 which translates into a H_2O to Si-O-C_2H_5 ratio of 5:1 and the pH is close to 3.8. Thus, a hydrolysis of Si-O-C_2H_5 groups can be ruled out as the source of the additional charge. Therefore, a hydrolytic depolymerization,[32,37] transforming Si-O-Si bonds into Si-OH, seems to be caused by the excess of water in the solution combined with the water adsorbed at 70% humidity. Additional support for the given explanation was observed when the relative humidity was increased to 85% following the stabilization of the mixed phase for more than 10 min at 70%, established by the unchanging scattering pattern (Figure 7.2b). As a result of the additional water adsorption, the diffraction spots attributed to the 3D hexagonal phase disappeared and only those indicative of the 2D hexagonal phase remained.

The ordered mesophase is maintained when the humidity is decreased down to 20%, following a ~30 min exposure to 70% humidity (Figure 7.3a). The decreasing humidity leads to evaporation

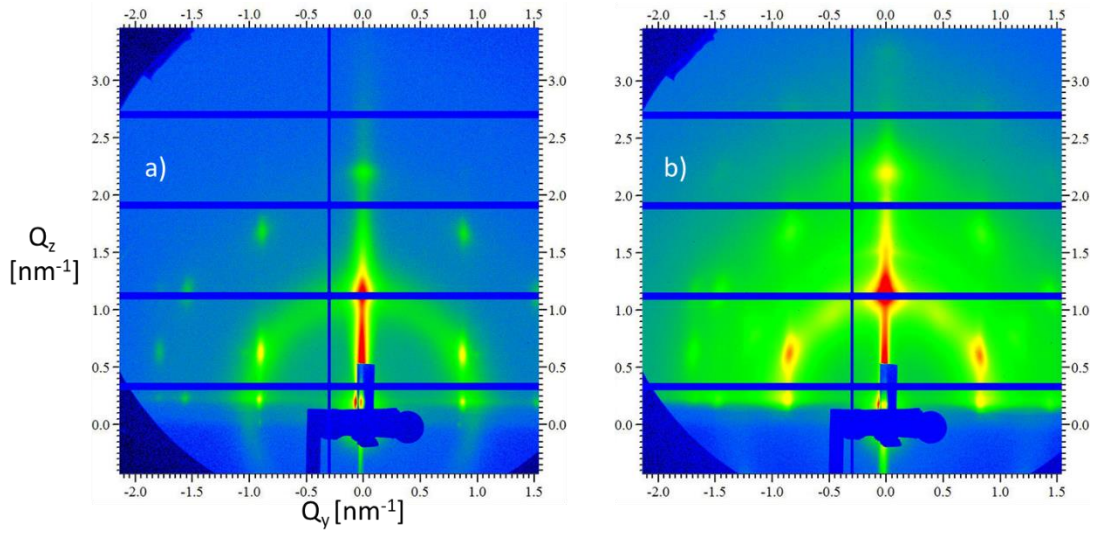

Figure 7.3. Effect of a) drying at RH=20% following an aging at RH=70% and b) template burn-out at 400°C on the PMO mesophase stability. SDD=1.87 m

of the water from the film causing contraction of the unit cell normal to the substrate which can be concluded from a comparison of the GISAXS pattern at 70% (Figure 7.1c) with that at 20% humidity (Figure 7.3a). The reduced amount of water in the film allows for a limited surfactant reorganization decreasing the size of the ordered domains apparent from the less sharp and more diffuse diffraction spots. Nevertheless, the scattering pattern associated with the 3D hexagonal phase is maintained following the thermal decomposition of the template performed at 400°C in N_2 atmosphere for 2h (Figure 7.3b). Still, it indicates further disorganization of the mesophase resulting in the small domains observed in the TEM micrographs (Figure 7.4).

Notably, since the surfactant employed in this work is an aqueous solution, the increase in surfactant to organosilica ratio translates into an increase in the H_2O to organosilica ratio. For instance, at a surfactant to organosilica ratio of 0.26, the H_2O to organosilica ratio is 30 (i.e. H_2O:-OC_2H_5=5:1) while at a surfactant to organosilica ratio higher than 0.31, the water to organosilica ratio is higher than 32.5.

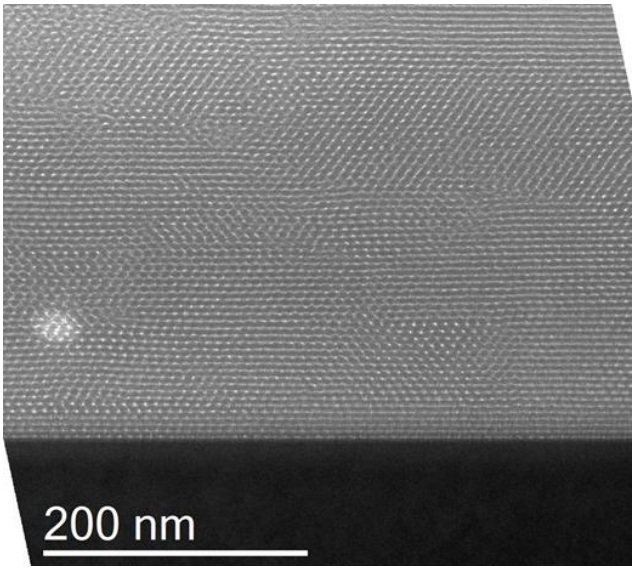

Figure 7.4. TEM micrograph showing the 3D hexagonal phase obtained at a molar ratio CTAC:ring precursor = 0.26

Therefore, in order to test the effect of the water to organosilica ratio, we decreased the amount of water by decreasing the volume of acid from 710 to 7.1 μl and increased the acid concentration from 10^{-3} to 10^{-1} M in order to maintain the solution pH. As a result, at a CTAC to organosilica ratio of 0.26, the water to organosilica ratio became 14 (i.e. H_2O:Si-OC_2H_5≈2.33). When the latter solution is spun and consequently placed in the controlled humidity cell at RH=20%, a diffuse scattering is observed with a weak diffraction spot in the specular plane indicating the presence of a lamellar structure. When the humidity is consequently increased up to 70%, the formation of micelles occurs which can be deduced by the appearance of a Debye ring. Once again, the spacing between the micelles increases as the water adsorption continues which becomes apparent from the "shrinking" Debye ring. After more than 25 min at RH=70%, diffraction spots appear indicating the formation of an ordered mesophase (Figure 7.5

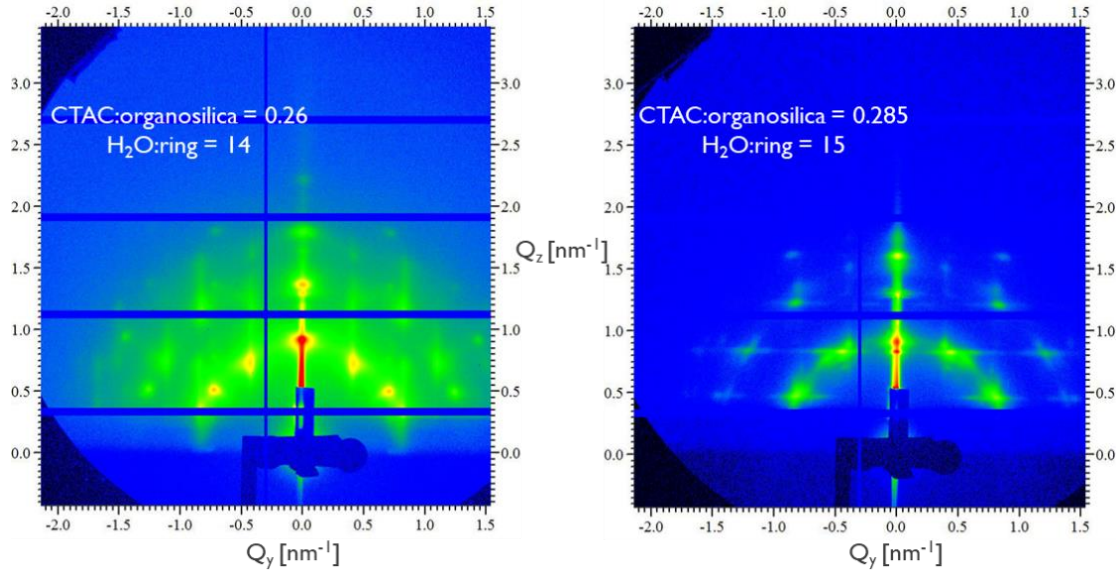

Figure 7.5. GISAXS patterns showing the differing mesophase as a result of the reduced water to organosilica ratio

a). If instead of exposing the film to a high humidity ambient, it is kept at 20% humidity following the deposition then a lamellar mesophase is deduced. On the other hand, increasing the surfactant to organosilica ratio to 0.285 which leads to an increase of the H_2O to organosilica ratio to 15.4 results in a still different mesophase (Figure 7.5 b). Similar to when the ratio is 0.26, the diffraction spots appear only after the film has been exposed to 70% humidity for at least 25 min. The latter pattern is observed for films obtained from a solution containing a surfactant to organosilica ratio of up to 0.305. Increasing the ratio further results in a 2D hexagonal mesophase. The scattering patterns are largely maintained when the humidity is decreased back to 20%, the ambient humidity at the synchrotron building. It was not possible to examine the SAXS patterns of the films following a template removal but an XRD and a TEM investigation showed that ordered PMO films were obtained (Figure 7.6). Unfortunately, the indexing of the SAXS patterns from Figure 7.5 has been unsuccessful probably because they do not correspond to one space group or even if the ordered domains belong to the same space group, their orientation might be different giving rise to additional diffraction spots. Based on the simulations performed with NANOCELL, the scattering patterns are tentatively attributed to the existence of a cubic mesophase(s) but the patterns could not be reproduced in their entirety. These films were thicker than the films obtained from a higher H_2O to organosilica ratio. The thickness values observed in TEM micrographs are between 1.1 and 1.32 μm. The striations can be clearly observed in the TEM images. According to ellipsometric measurements, the thickness of some of the films is as high as 2.3 μm. Nevertheless, the one-layer Cauchy function cannot model adequately the experimental dispersion of the films thicker than 1 μm and therefore values as high as 2 μm do not seem reliable. On the other hand, the thickness observed in the TEM images is expected to be representative.

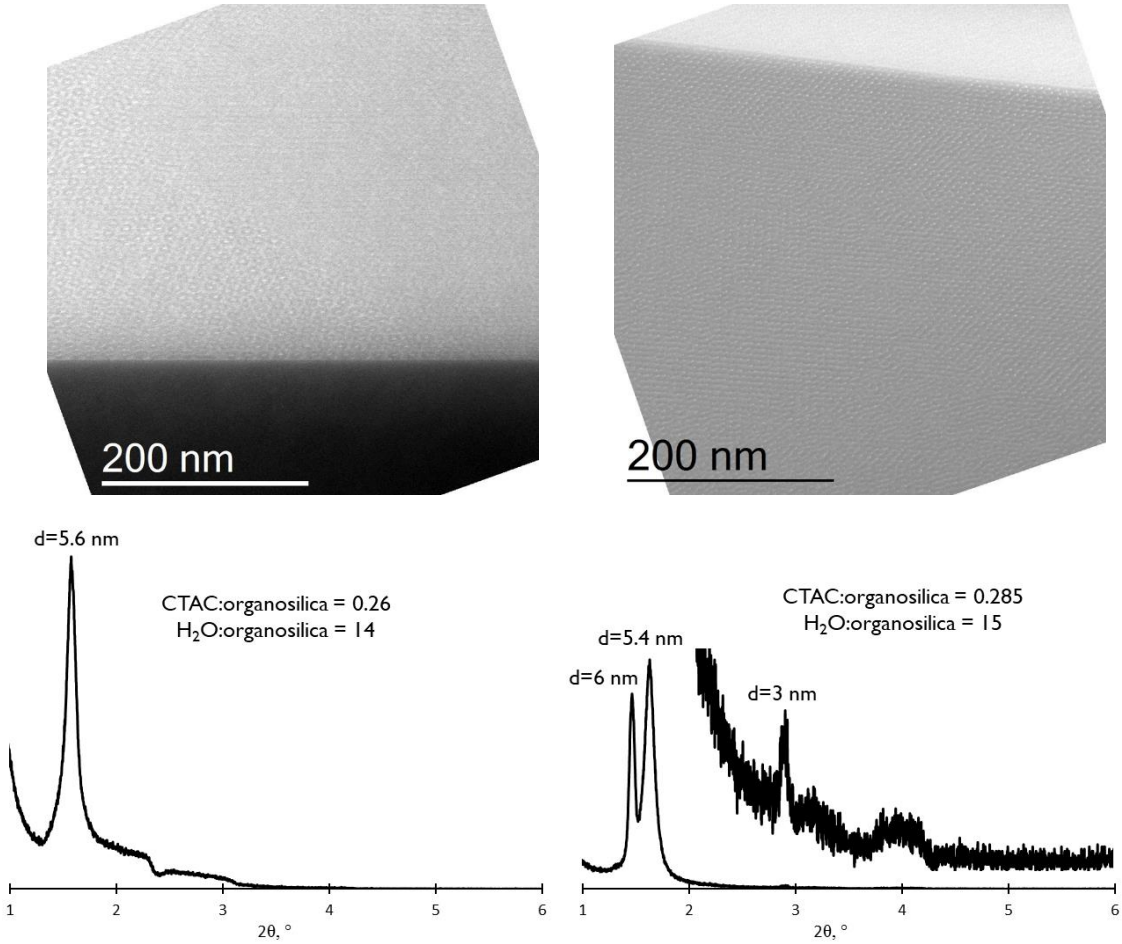

Figure 7.6. TEM micrographs and X-ray diffractograms obtained following a template removal from the films shown in Figure 7.5

The mesophase is further determined by the degree of polycondensation of the organosilica molecules at the moment of deposition, i.e. by the solution aging time. A well-defined 2D hexagonal phase unaffected by the humidity conditions is deduced for a film deposited from a solution with a surfactant to organosilica precursor ratio of 0.29 and aged for 40 min at room temperature which corresponds closely to the original report of Landskron et al.[30] The unit cell enlarges when the humidity is increased to 70% due to water adsorption but it does not lead to a phase transformation (Figure 7.7a).

On the other hand, corroborating a previous report,[22] a disordered wormlike mesophase coexisting with a small domain of 2D hexagonal phase is observed when the deposited solution contains a surfactant to organosilica precursor ratio of 0.29 and is aged at RT for 70 min. Nevertheless, the small domain size of the 2D hexagonal mesophase is completely disrupted when the film is placed at RH=70% (Figure 7.7b).

The narrow window of solution aging within which the deposition needs to occur in order to obtain an ordered mesoporous film is a drawback when an industrial application is targeted. Therefore, given that the thickness of the films described so far is more than 800 nm and that for a low-k application, a thickness below 200 nm would be the most suitable, we investigated

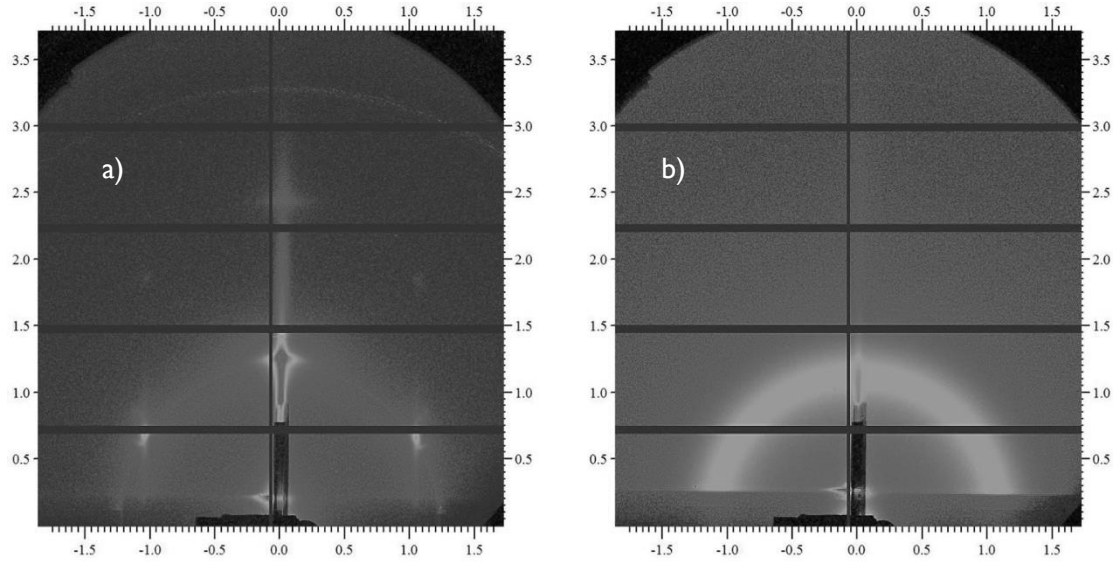

Figure 7.7. Effect of solution aging on the film mesophase: a) 2D hexagonal phase from a 40 min aged solution; b) no pore order from a solution aged for 70 min

the effect of the dilution of the solution in order to slow down the polycondensation and therefore, extend the shelf-life of the solution as well as the deposition window within which an ordered mesoporous film can be obtained. For this strategy to work, the solvent employed for dilution needs not to influence the hydrolysis and condensation other than by changing the concentration of the reagents. Therefore, ideally, an aprotic solvent such as acetone should be employed. Nevertheless, in order to ensure a good film uniformity with low roughness, we performed the dilution using a high boiling point solvent,[38] 1-methoxy-2-propanol, which is also expected not to interfere in a direct way with the hydrolysis and condensation. Additionally, in order to ensure that the degree of organosilica polycondensation is close to the optimal, the dilution was performed after stirring the original solution for 40 min. As a result, ordered

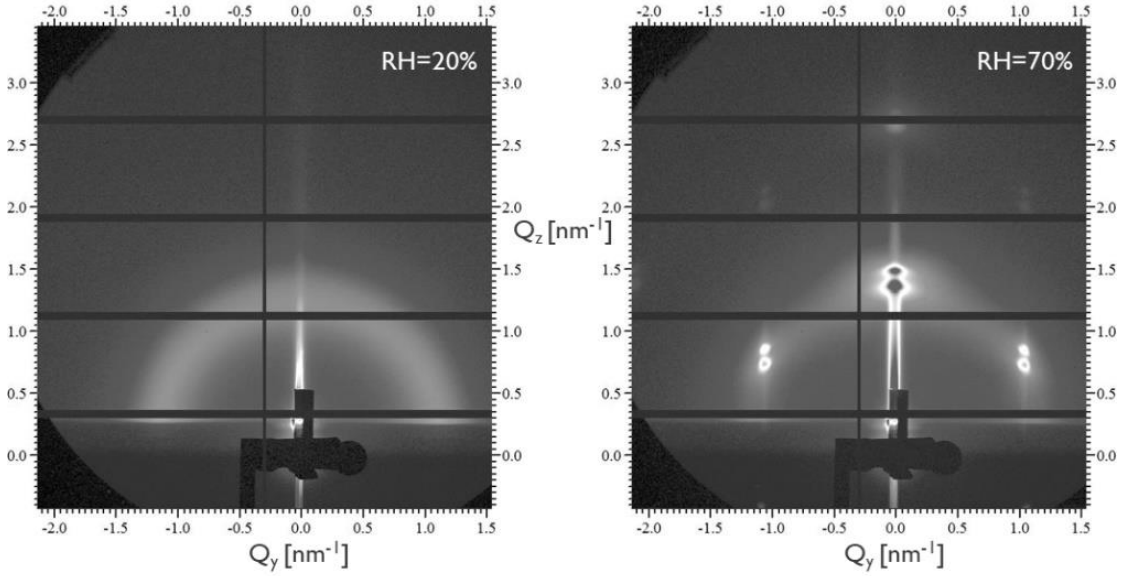

Figure 7.8. The tunable stead state is observed even in a film as thin as 150 nm resulting in phase transformation from a) wormlike mesophase into b) 2D hexagonal phase

mesophase was observed for films as thin as 150 nm. Importantly, the tunable steady state (TSS) exists in films as thin as 150 nm. The thinner the films the faster they are expected to dry during spin-coating and therefore their matrices are expected to condense faster and probably shorten the window of the TSS. Nevertheless, the phase transformation (Figure 7.8) observed for the 150 nm film shows that the polycondensation is not complete more than 5 min after the spinning which is when the first GISAXS patterns are obtained. Also, the phase transformation shown at Figure 7.8 occurred after about 120 min solution aging showing that the deposition window which allows obtaining ordered PMO has been extended. Another deposition following 200 min of solution aging also resulted in a GISAXS pattern indicative of a 2D hexagonal mesophase (not shown). The dilution experiments were also performed on a 20 min aged solution but the lamellar-to-3D-hexagonal phase transformation was not observed after the dilution. However, the latter was not due to the dilution but rather due to an aged (probably, hydrolyzed) precursor which is discussed next.

The organosilica precursor is sensitive to the ambient atmosphere. A freshly open bottle of organosilica precursor was used to obtain the results reported here. However, the use of a precursor from a bottle which was opened two months earlier did not allow us to reproduce the reported results. At RH=70%, it resulted in a Debye ring indicating a disordered wormlike phase rather than the 3D hexagonal phase demonstrated earlier. This observation implies a precursor aging effect due to the precursor sensitivity to moisture which can cause hydrolysis, as previously described for other alkoxysilicates.[18] No evidence of a hydrolysis was observed for the organosilica precursor in the bottles opened within the three days' timeframe of the GISAXS experiments at ELETTRA.

Due to the use of CTAC in these syntheses, the films are not completely hydrophobic. The hydrophilicity of the films is evident from the FTIR spectrum shown in Figure 7.9. The spectrum contains a sharp peak at 3735 cm^{-1} indicating the presence of isolated silanol groups which need to be silylated in order to obtain a hydrophobic film. Furthermore, a peak at 1360 cm^{-1} reveals

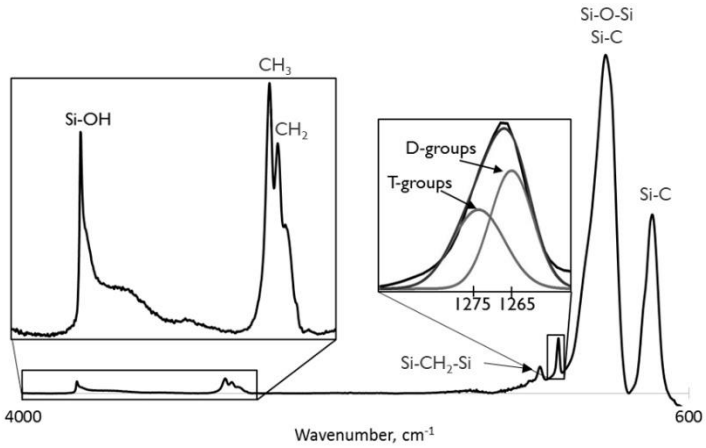

Figure 7.9. FTIR spectrum containing the characteristic bands observed for all of the PMO films described in this chapter

the presence of intact methylene groups. Importantly, the peak around 1260 cm^{-1} is broader than a typical Si-CH_3 peak. Therefore, it can be peak-fitted by two Gaussian peaks centered at 1275 and 1265 cm^{-1}. The peak at 1275 cm^{-1} corresponds to the C-H vibration in $(R_3SiO)_3SiCH_3$ T groups while the one at 1265 cm^{-1} to a $(R_3SiO)_2Si(CH_3)_2$ D groups. Figure 7.10 shows the sequence of self-hydrophobization reactions which result in the formation of D groups from silicon atom bonded to two methylene groups as is the case in the ring precursor. The presence of D groups reduces significantly the average connectivity number, which is the number of network forming bonds per networked atom, of the organosilicate matrix.[39] A connectivity number lower than 2.4 is below the percolation of rigidity which means that the mechanical stability is compromised. It has been shown that if each Si atom had three network-forming bonds and one bond to a methyl group, i.e. T groups, then a connectivity number of 2.4 would be reached.[39] Therefore, in order to achieve optimal mechanical properties, the formation of D groups should be avoided. Nevertheless, the peak-fitting of the band at ca. 1270 cm^{-1} reveals that the concentration of the D groups is higher than the concentration of T groups. Therefore, the ring precursor seems not to be a suitable precursor when an optimization of the low-k mechanical properties is needed. However, a complication of this analysis is that since each silicon atom is bonded to two methylene groups, upon a self-hydrophobization reaction, the formed functionality is also a D group but one where the silicon is bonded to two siloxane, one methylene and one methyl functionalities. Such D groups are equivalent to a T group in terms of a contribution to the average connectivity number. Unfortunately, it is not clear whether the two types of D groups can be distinguished by an FTIR analysis.

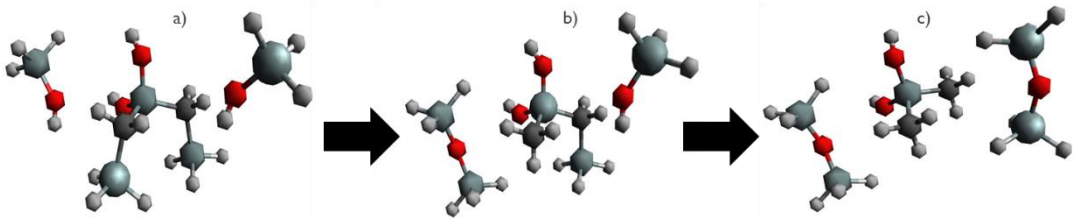

Figure 7.10. The self-hydrophobization sequence which results in the formation of D, $(R_3SiO)_2Si(CH_3)_2$, groups: a) Si atom bonded to two methylene groups with two silanols in proximity; b) one self-hydrophobizatoin results in a D group where the Si is bonded to methylene and methyl group; c) second self-hydrophobization leads to a D group where the Si is bonded to two methyl groups

An evaluation of the Young's moduli of the films described in this chapter (points in Figure 7.11) reveals that the films possess inferior mechanical properties when compared to oxycarbosilane films from literature in which no pore order was present (line in Figure 7.11).[40] These oxycarbosilane films have been obtained from a methylene-bridged precursor but one that does not allow the formation of D groups, i.e. the BTESM. Therefore, the lower YM observed for our films might be due to a lower matrix connectivity as compared to those in literature. Another factor which is very likely to contribute to the observed difference is the fact that Dubois et al. annealed their films at 450°C while we annealed the PMOs at the more compatible with the

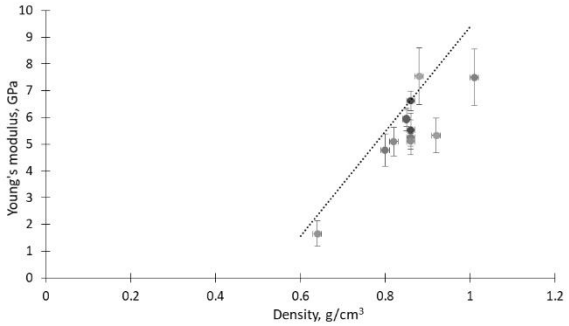

Figure 7.11. Comparison of the YM of the obtained PMO films (points) to oxycarbosilane films[40](line) in which no pore order has been observed

BEOL processing temperature of 400°C. The higher anneal temperature of 450°C certainly results in higher silanol condensation and consequently, potentially higher matrix connectivity. However, the PMO films are expected to achieve higher YM values due to their ordered pores.[10] While it is difficult to make a conclusion on the effect of the pore order on the YM when comparing with results in literature due to experimental differences, when we compare to films with disordered porosity obtained in our laboratory (to be presented in the next chapter), we do not see a clear benefit to the YM from the ordered porosity. Nevertheless, the latter is probably due to the limited pore order observed in our PMO films (Figure 7.4 and Figure 7.6). Therefore, further efforts to increase the size of the domains with ordered pores and ultimately obtain a monocrystal-like PMO are necessary in order to be able to draw a more reliable conclusion about the effect of the pore organization on the YM.

7.4. Conclusions

In summary, we have demonstrated, for the first time, the existence of a tunable steady state in PMO spin-coated films. Therefore, we stressed the importance of the ambient relative humidity at which an as-deposited film is aged. Controlling the aging conditions, we were able to obtain films with 3D or 2D hexagonal phases depending on the surfactant to organosilica molar ratio. Additionally, in the context of the charge density matching mechanism, we demonstrated the competing effects of the adsorbed H_2O molecules on the mesophase determination. The interaction between the H_2O and CTAC molecules leads to an increase of the micelle surface curvature; in the meantime, the H_2O molecules can cause depolymerization of the siloxane bonds creating conditions which favor the decrease of the micelle surface curvature. Furthermore, we emphasized the importance of the polycondensation degree of the organosilica oligomers by demonstrating different mesophases as a function of the solution aging, i.e. 3D hexagonal after 20 min, 2D hexagonal after 40 min aging and no ordered mesophase if the solution is aged for longer than 70 min. Additionally, GISAXS patterns tentatively attributed to cubic mesophases were observed when the water to organosilica molar ratio was reduced from 30 to 14. Notably, the TSS exists in spin-coated films as thin as 150 nm more than 5 min after

the deposition. Finally, the deposition window which makes possible obtaining films with an ordered mesophase can be extended by at least 160 min by diluting the solution with a suitable solvent.

7.5. References

[1] Z. Chen, Y. Jiang, D. R. Dunphy, D. P. Adams, C. Hodges, N. Liu, N. Zhang, G. Xomeritakis, X. Jin, N. R. Aluru, S. J. Gaik, H. W. Hillhouse, C. J. Brinker, *Nat. Mater.* **2010**, *9*, 667.

[2] M. Etienne, A. Quach, D. Grosso, L. Nicole, C. Sanchez, A. Walcarius, *Chem. Mater.* **2007**, *19*, 844.

[3] A. Walcarius, E. Sibottier, M. Etienne, J. Ghanbaja, *Nat. Mater.* **2007**, *6*, 602.

[4] T. C. Wei, H. W. Hillhouse, *Langmuir* **2007**, *23*, 5689.

[5] C. H. Ko, J. M. Kim, R. Ryoo, *Microporous Mesoporous Mater.* **1998**, *21*, 235.

[6] R. Ryoo, C. H. Ko, S. J. Cho, J. M. Kim, *J. Phys. Chem. B* **1997**, *101*, 10610.

[7] Y. Hu, A. Bouamrani, E. Tasciotti, L. Li, X. Liu, M. Ferrari, *ACS Nano* **2010**, *4*, 439.

[8] H. Lian, Y. Liang, Y. Yamauchi, K. C. Wu, *J. Phys. Chem.* **2011**, *115*, 6581.

[9] D. J. Michalak, J. M. Blackwell, J. M. Torres, A. Sengupta, L. E. Kreno, J. S. Clarke, D. Pantuso, *J. Mater. Res.* **2015**, *30*, 3363.

[10] D. Jauffrès, R. Dendievel, M. Verdier, *Thin Solid Films* **2011**, *520*, 430.

[11] D. Grosso, F. Ribot, C. Boissiere, C. Sanchez, *Chem. Soc. Rev.* **2011**, *40*, 829.

[12] L. Nicole, C. Boissière, D. Grosso, A. Quach, C. Sanchez, *J. Mater. Chem.* **2005**, *15*, 3598.

[13] D. Grosso, F. Babonneau, P. Albouy, H. Amenitsch, A. R. Balkenende, A. Brunet-Bruneau, J. Rivory, *Chem. Mater.* **2002**, *14*, 931.

[14] A. Gibaud, D. Grosso, B. Smarsly, A. Baptiste, J. F. Bardeau, F. Babonneau, D. A. Doshi, Z. Chen, C. J. Brinker, C. Sanchez, *J. Phys. Chem. B* **2003**, *107*, 6114.

[15] F. Cagnol, D. Grosso, G. J. de A. A. Soler-Illia, E. L. Crepaldi, F. Babonneau, H. Amenitsch, C. Sanchez, *J. Mater. Chem.* **2003**, *13*, 61.

[16] D. Grosso, F. Cagnol, G. J. de A. A. Soler-Illia, E. L. Crepaldi, H. Amenitsch, A. Brunet-Bruneau, A. Bourgeois, C. Sanchez, *Adv. Funct. Mater.* **2004**, *14*, 309.

[17] D. Grosso, F. Babonneau, C. Sanchez, G. J. de A. A. Soler-Illia, E. L. Crepaldi, P. A. Albouy, H. Amenitsch, A. R. Balkenende, A. Brunet-Bruneau, *J. Sol-Gel Sci. Technol.* **2003**, *26*, 561.

[18] M. P. Tate, V. N. Urade, S. J. Gaik, C. P. Muzzillo, H. W. Hillhouse, *Langmuir* **2010**, *26*, 4357.

[19] A. Grunenwald, A. Ayral, P.-A. Albouy, C. Licitra, P. Gergaud, D. Quemener, A. Deratani, V. Rouessac, A. Zenasni, V. Jousseaume, *Microporous Mesoporous Mater.* **2012**, *150*, 64.

[20] J. Zhang, G. Zhang, Y. Gao, R. Sun, C. P. Wong, *J. Mater. Sci.* **2016**, *51*, 7966.

[21] T. Jiang, S. J. Ding, Z. Y. Fan, W. Zhang, *Adv. Mater. Res.* **2014**, *887–888*, 757.

[22] W. Wang, D. Grozea, S. Kohli, D. D. Perovic, G. A. Ozin, *ACS Nano* **2011**, *5*, 1267.

[23] M. Seino, W. Wang, J. E. Lofgreen, D. P. Puzzo, T. Manabe, G. A. Ozin, *J. Am. Chem. Soc.* **2011**, *133*, 18082.

[24] S. S. Park, M. Santha Moorthy, C.-S. Ha, *NPG Asia Mater.* **2014**, *6*, e96.

[25] P. Van der Voort, D. Esquivel, E. De Canck, F. Goethals, I. Van Driessche, F. J. Romero-Salguero, *Chem. Soc. Rev.* **2013**, *42*, 3913.

[26] M. A. Wahab, J. N. Beltramini, *RSC Adv.* **2015**, *5*, 79129.

[27] M. Aliofkhazraei, *Comprehensive guide for mesoporous materials, Volume 4: Application and Commercialization*; Aliofkhazraei, M., Ed.; Nova Science Publishers, Inc.: New York, 2015.

[28] J. G. Croissant, X. Cattoën, J.-O. Durand, M. Wong Chi Man, N. M. Khashab, *Nanoscale* **2016**, *8*, 19945.

[29] W. Wang, J. E. Lofgreen, G. A. Ozin, *Small* **2010**, *6*, 2634.

[30] K. Landskron, B. D. Hatton, D. D. Perovic, G. A. Ozin, *Science* **2003**, *302*, 266.

[31] M. P. Tate, V. N. Urade, J. D. Kowalski, T. C. Wei, B. D. Hamilton, B. W. Eggiman, H. W. Hillhouse, *J. Phys. Chem. B* **2006**, *110*, 9882.

[32] M. Cypryk, Y. Apeloig, *Organometallics* **2002**, *21*, 2165.

[33] A. Monnier, F. Schüth, Q. Huo, D. Kumar, D. Margolese, R. S. Maxwell, G. D. Stucky, M. Krishnamurty, P. Petroff, A. Firouzi, M. Janicke, B. F. Chmelka, Cooperative formation of inorganic-organic interfaces in the synthesis of silicate mesostructures. *Science* **1993**, *261*, 1299–303.

[34] Q. Huo, D. I. Margolese, U. Ciesla, P. Feng, T. E. Gier, P. Sieger, R. Leon, P. M. Petroff, F. Schüth, G. D. Stucky, *Nature* **1994**, *368*, 317.

[35] A. Firouzi, D. Kumar, L. Bull, T. Besier, P. Sieger, Q. Huo, S. Walker, J. Zasadzinski, C. Glinka, J. Nicol, A. Et, *Science (80-.).* **1995**, *267*, 1138.

[36] S. H. Tolbert, C. C. Landry, G. D. Stucky, B. F. Chmelka, P. Norby, J. C. Hanson, A. Monnier, *Chem. Mater.* **2001**, *13*, 2247.

[37] C. J. Brinker, *J. Non. Cryst. Solids* **1988**, *100*, 31.

[38] H. Kozuka, Y. Ishikawa, N. Ashibe, *J. Sol-Gel Sci. Technol.* **2004**, *31*, 245.

[39] A. D. Ross, K. K. Gleason, *J. Appl. Phys.* **2005**, *97*, 113707.

[40] G. Dubois, W. Volksen, T. Magbitang, R. D. Miller, D. M. Gage, R. H. Dauskardt, *Adv. Mater.* **2007**, *19*, 3989.

CHAPTER 8. PERIODIC MESOPOROUS ORGANOSILICA FILMS FOR LOW-K APPLICATION: PROMISES AND CHALLENGES

As we have shown in Chapter 7, the synthesis of 2D hexagonal PMO films using cetyltrimethylammonium chloride (CTAC) is independent of the ambient conditions during deposition. Therefore, it is the most compatible with IC manufacturing. Nevertheless, we show that the PMO films with a 2D hexagonal pore organization have 1.7 GPa lower Young's modulus than a film with disordered porosity at a dielectric constant of 2.30. Furthermore, CTAC is an ionic surfactant and ionic surfactants are considered detrimental to the low-k's electrical reliability. However, we demonstrate CTAC-templated PMO low-k films with low leakage current of 1.6×10^{-9} A/cm^2 at 1 MV/cm and a breakdown field of 5.5 MV/cm both of which are comparable to low-k films reported in literature. Additionally, we discuss challenges depositing the PMO films in 45 nm trenches. We demonstrate that the high surface energy of the substrate is important in order to obtain ordered porosity.

8.1. Introduction

Periodic mesoporous organosilica (PMO) films are considered to be a promising low-k candidate for future generation ultra-large scale integration. Compared to the traditional low-k films, one of the main advantages of the PMOs is the control over the pore structure and the ability to obtain an ordered porosity. The films with ordered porosity have been shown theoretically[1–3] and experimentally[4] to possess an improved Young's modulus as compared to films with disordered pores. An additional advantage of the PMO films is that porosity values higher than 50% without a pore collapse can be obtained.[5] Finally, PMOs have been shown to self-hydrophobize at T>300°C[6] and we have shown that the process initiates at even lower temperatures (Chapter 5). The self-hydrophobization can result in a hydrophobic film which is stable against moisture adsorption[7,8] and therefore with stable dielectric properties against atmospheric effects without the need for an additional hydrophobization treatment.

In order to deduce the effect of the pore organization on the film properties, it is beneficial to be able to obtain films with ordered and disordered pore organizations from the same solution. In contrast, films obtained as a result of differing processing conditions might result in a differing hydrolysis and condensation kinetics leading to significantly different organosilicate oligomer distribution affecting the observed film properties. For instance, it has been shown that the abundance of small 3-memebred siloxane rings in the film would lead to a film with higher elastic modulus as compared to a film with larger siloxane cyclic species.[4] Even less reliable and challenging would be to attempt to deduce the role of the pore order between films obtained via sol-gel and PECVD, for instance, because of the extensive bond rearrangement characteristic of the PECVD method. Therefore, in this study, we compare films obtained from the same solution but having different pore organization (mesophase).

Ionic surfactants are considered incompatible with microchip manufacturing.[9] Even though no elaboration has been provided for why they are unsuitable, it is probably due to an expected detrimental effect on the electrical reliability of the low-k films obtained using an ionic surfactant. Nevertheless, it has been demonstrated that the addition of a salt as a catalyst, part of which inevitably gets incorporated in the final film, results in low-k films with good electrical reliability.[10] However, the amounts of catalyst in the solution were 30 wt ppm or lower which is expected to be much lower than the remaining ions if an ionic surfactant is employed as a structure-directing agent (SDA). Indeed, Ting et al.[11] have reported that the use of the ionic surfactant cetyltrimethylammonium bromide (CTAB) leads to porous films with a leakage current density so high that they could not quantify it with the available equipment. Additionally, in contrast to the films templated by non-ionic surfactants, they showed a positive flat-band voltage (V_{FB}) for the low-k film templated by CTAB which was attributed to the abundance of remaining Br^- ions. Nevertheless, in that study, there are several observations which have not

been observed in the films prepared in our laboratory. For instance, the authors have reported a very high refractive index of 1.428 for a film with a pore volume of 42% which they have attributed to the ionic contribution to the dielectric function of the Br^- ions in the film even if an ionic response is usually not expected in the optical frequency range.[12] In comparison, we have obtained films with a similar pore volume and their refractive index is ca. 1.255. Additionally, in a previous study detailed in Chapter 4, we showed that the V_{FB} of the low-k films templated by an ionic surfactant was negative similar to the films templated by a non-ionic surfactant indicating the lack of a significant contribution from the chlorine ions to the V_{FB}. Given that the ionic surfactants are the SDAs which result in the mesoporous films with the smallest pore diameter of about 2 nm, it is important to clarify whether the ionic surfactants are indeed incompatible with the back-end of line processing and whether they deteriorate the low-k reliability. Therefore, we evaluated the electrical reliability of PMO films templated with an ionic surfactant in comparison to a non-ionic surfactant and to a commercial k2.2 spin-on film by performing current-voltage (I-V) measurements of a PMO low-k deposited in a 45 nm trench. In order to achieve the latter, we took advantage of a low-k replacement integration scheme which allows[13] avoiding the plasma-induced damage which is one of the biggest challenges for the integration of porous low-k dielectrics and therefore, allows studying the intrinsic low-k properties in technologically relevant structures and dimensions.

8.2. Experimental Section

The coating solution was synthesized using a modified synthesis procedure of Landskron et al.[14] In a typical synthesis ethanol (1.44 ml), HCl (0.71 ml 10^{-3}M), cetyltrimethylammonium chloride (0.85 ml 25% aqueous solution), and 1,1,3,3,5,5-hexaethoxy-1,3,5-trisilacyclohexane (0.93 ml) were mixed and stirred at room temperature. Following the stirring, the solution was spin-coated at 2500 rpm for 60 s on a 100 Si substrate on which a native oxide had been grown. The deposition was performed from the same solution following an aging at RT for 50 min and 100 min. The films were deposited at a lab humidity which was not actively controlled and is usually in the range between 40 and 50%. Finally, the CTAC was thermally decomposed at 400°C in an inert N_2 atmosphere for 2 h.

Alternatively, PMO films were deposited on a patterned structure which was obtained following the processing procedure shown schematically in Figure 8.1. The details of the processing steps can be found elsewhere.[13,15] In short, instead of a low-k, a sacrificial "template" is deposited and

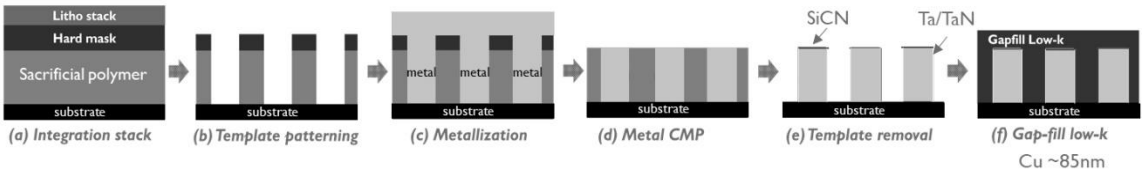

Figure 8.1. The template-replacement integration scheme

patterned which is followed by the copper electroplating and polishing. Thus far, these steps describe the usual damascene integration processing. Next, the template is removed by a plasma processing optimized not to oxidize the exposed metal and thin metal barrier. As a result, "standing" metal lines are obtained with gaps which can be filled with the ultra-low-k film. Three gap sizes are available – 45, 50, and 55 nm. The height of the metal lines is about 85 nm. The effect of the surface energy of SiCN, the interface on which the PMO is deposited, on the PMO film was investigated. The gap fill structures on which 6 nm SiCN had been deposited was exposed to a short CO_2 plasma in order to increase the surface energy of the SiCN. The deposition on a hydrophilized SiCN mimics the deposition on the hydrophilic SiO_2 reported in the previous chapters, i.e. by creating similar surface energy conditions, the surfactant self-assembly is ensured to be reproduced. Alternatively, the high surface energy SiCN was additionally treated with the vapors of the silylation agent dimetilaminotrimethylsilane (DMATMS) at 250°C in order to obtain a low surface energy SiCN.

To compare the stress-induced leakage current (SILC) density between PMO low-k films templated by an ionic and a non-ionic surfactant, we deposited a CTAC-templated and a BrijS10-templated PMO films in the gap-fill structures. Instead of 2 hours, the as-deposited films were annealed for only 20 min in order to avoid potential oxidation of the Cu lines with the longer annealing at 400°C. The films were additionally silylated by a vapor phase exposure to DMATMS at 250°C in order to exclude the detrimental effect on the leakage current of the Si-OH groups present in the PMO film templated by the ionic surfactant.

8.3. Results and Discussion

8.3.1. Effect of pore order on Young's modulus

As shown in Chapter 7, the synthesis procedure described in the experimental section results in a 2D hexagonal film if the solution is aged for longer than 40 min but shorter than 70 min. Also, the pore organization is relatively independent of ambient humidity which for these experiments could not be controlled precisely. On the other hand, if the solution is aged for 70 min or longer then a film with a disordered worm-like pore organization is obtained. The difference in pore organization was established by XRD and GISAXS (Figure 8.2). Additionally, a TEM investigation of the film with ordered porosity revealed a long range order (Figure 8.3a) which is punctuated by relatively small disordered regions which separate domains of ordered pores with different orientations (Figure 8.3b). Both of the domains with ordered channels in Figure 8.3b) seem to belong to the p6mm space group oriented parallel to the substrate but they are oriented perpendicular to each other. The disordered pore organization in the film aged for 100 min can be deduced from the GISAXS pattern shown in Figure 8.2 b) where no

diffraction spots are observed but only a Debye ring indicating the wormlike pore structure characterized by a narrow pore size distribution similar to the films with ordered porosity.

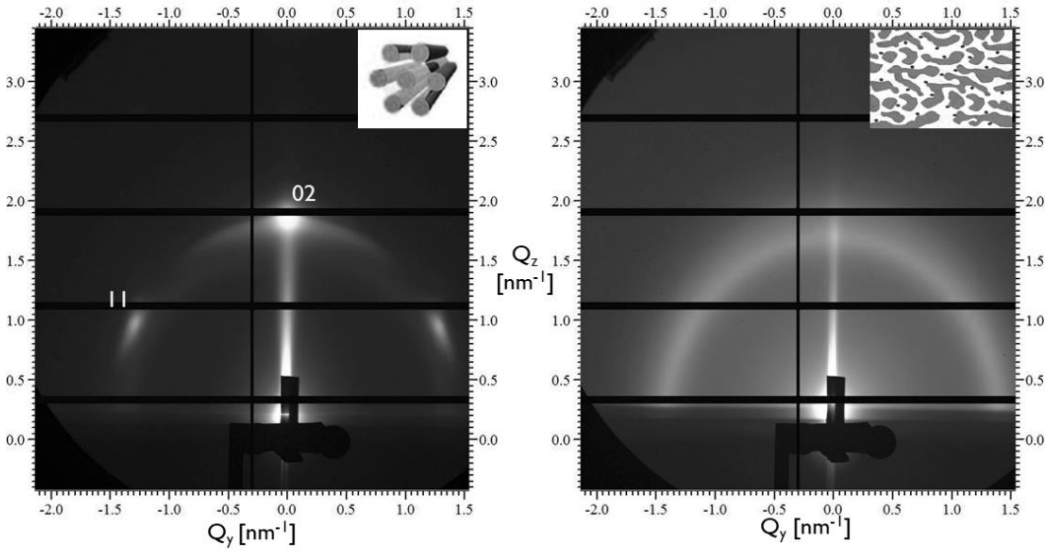

Figure 8.2. GISAXS patterns showing the a) 2D hexagonal organization in the film obtained from a solution aged for 50 min and b) the wormlike pore organization in the film obtained from the same solution aged for 100 min

Due to the similar synthesis conditions, the films being compared have a very similar pore size with a diameter centered on 2 nm calculated from the toluene adsorption isotherms (not shown). Importantly, comparing films obtained from the same solution ensures that there are no significant differences in the size distribution of the siloxane oligomers. Therefore, the films are expected to have similar to each other matrix connectivity which is known to affect the Young's modulus.[16] Admittedly, the fact that following a 50 min solution aging, a film with ordered pores is obtained while a longer aging results in wormlike pores indicates that there are differences in the siloxane oligomer size. Nevertheless, in both cases, the shared pH of ca. 3.0 favors the formation of weakly branched oligomers which grow longer with the solution aging time.[17] Furthermore, the annealing at 400°C following the deposition removes any differences in the siloxane population in the final ordered and disordered films. This conclusion

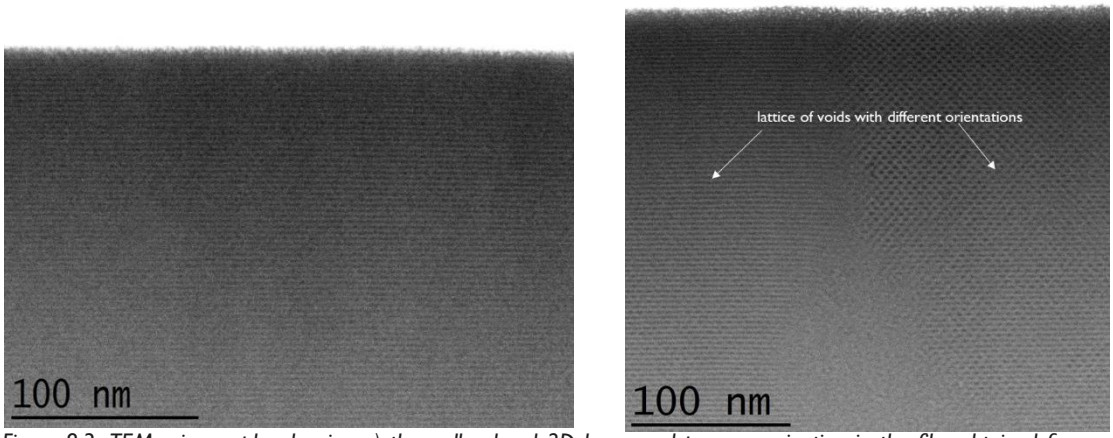

Figure 8.3. TEM micrographs showing a) the well-ordered 2D hexagonal pore organization in the film obtained from a solution aged for 50 min and b) the ordered pores are organized in domains as a result of which some channels are perpendicular to others

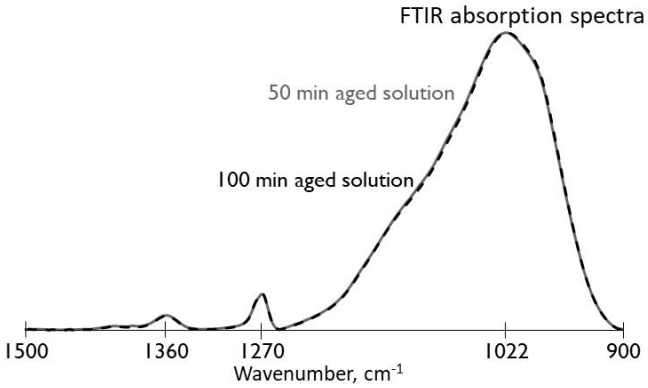

Figure 8.4. FTIR spectra of the films obtained following 50 and 100 min solution aging.

is based on the films' FTIR spectra (Figure 8.4) in the region between 900 and 1250 cm^{-1} which contains information about the distribution of siloxane bond angles and lengths which vary among the various cyclic siloxane units. In this region, the spectra overlap showing that the organosilica matrices of the films are composed to a large extent of the same bond configurations.

A drawback of the current experimental design is that the porous films have different densities due to the lower surfactant incorporation in a more polycondensed gel. Indeed, compared to the film with ordered porosity, the disordered porosity film has 0.05 g/cm^3 higher density, deduced form XRR measurements, and 3.5 percentage points lower open porosity, calculated from toluene EP measurements (Figure 8.5a). As a result, the observed difference in Young's modulus is partly explained by the difference in density. In particular, the film with a 2D hexagonal pore organization, which is also the more porous film, has a YM 1.7 GPa lower than the film with wormlike pores. When compared with literature where systematic syntheses and characterization of YM as a function of density were performed,[18,19] the density difference seems to explain about half of the difference in YM that we observe. In order to explain the remaining difference, we take into account the anisotropy characteristic of films with a pore organization belonging to a wallpaper space group such as the p6mm. In films with p6mm pore order in which the pores are parallel to the substrate, it is well-known that the axis normal to the substrate is the weakest mechanically.[5] Furthermore, the nanoindentation, employed to

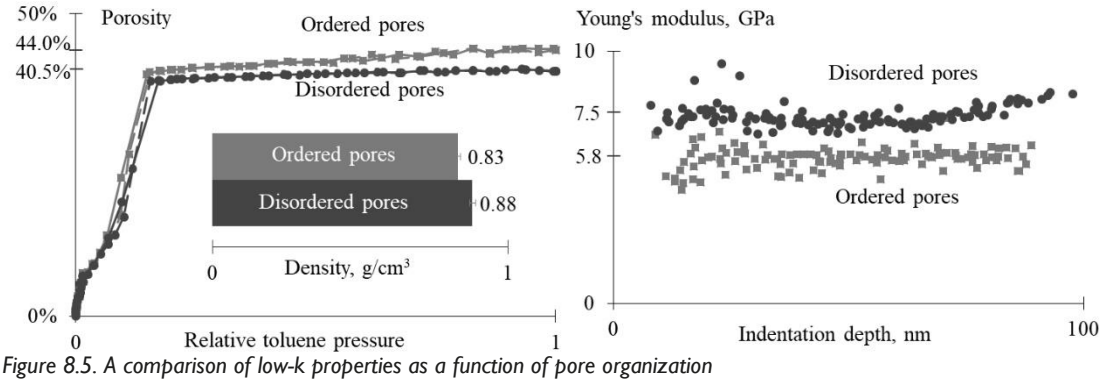

Figure 8.5. A comparison of low-k properties as a function of pore organization

obtain the elastic modulus, provides information mainly about the mechanical properties normal to the substrate.[20] On the other hand, the film with disordered pores is expected to have largely isotropic mechanical properties. Therefore, effectively, we are comparing the weakest YM component of the film with the ordered pores to the average elastic response of the film with disordered pores. Consequently, for the same density, we would expect a higher YM for the film with disordered pores than for the film with 2D hexagonal pores. Employing FEM calculations, Michalak et al.[5] have shown (FIG. 13 in ref.[5]) that a film with random spheroid pores would have a higher YM than the transverse YM components of the ordered porosity film. At a porosity of ca. 55%, the disordered porosity film has about 2 GPa higher YM than the YM component normal to the substrate. Nevertheless, the YM component parallel to the channels can be three times higher than each of the transverse components, 15 vs 5 GPa (FIG. 13 in ref.[5]). Therefore, the lower YM for the ordered film as compared to the disordered seems reasonable even if on average the YM of the ordered porosity film is expected to be higher than that of a disordered porosity film. However, these results seem to contradict a previous report where employing nanoindentation, films with hexagonally ordered pores were reported to have a significantly higher YM as compared to a film with a disordered porosity.[4]

The small difference in density between the films obtained from a 50 min and a 100 min aged solution results in a small difference in the dielectric constant. When the capacitance of a metal-insulator-semiconductor (MIS) structure is measured at room temperature at 100 kHz,[21] a k value of 2.30 is calculated for both of the films. When the capacitance measurement is performed at 200°C at 100 kHz, ensuring the evaporation of any physisorbed water, k-values of 2.27 and 2.29 are calculated for the films obtained from a 50 and 100 min aged solution, respectively. The difference with the value obtained at room temperature is not statistically significant indicating that the hydrophilicity of the films, reported in Chapter 7, has not led to a significant physisorption of moisture within the one week storage duration in a clean room environment.

8.3.2. PMO film deposition in 45 nm trenches

A PMO film with larger ordered domains is obtained when the film is deposited on a hydrophilic SiCN rather than a hydrophobic SiCN. The latter was deduced from an XRD study of the PMO film deposited on a hydrophilic and a hydrophobic SiCN (Figure 8.6). The diffraction peak from the film deposited on the hydrophilic SiCN is about 10 times more intense than if the coating solution is spun on a hydrophobic SiCN. Additionally, the full-width-at-half-maxima (FWHM) are 0.21° and 0.10° when the SiCN is hydrophobic and hydrophilic, respectively. According to Scherrer's formula,[22] the smaller FWHM indicates the larger ordered domains in the film deposited on the hydrophilic SiCN. The difference in pore organization can also be seen in the TEM images in Figure 8.7. The higher quality of the PMO on the hydrophilic SiCN can clearly be seen. Nevertheless, the pore order is disrupted in the space between the metal lines where no

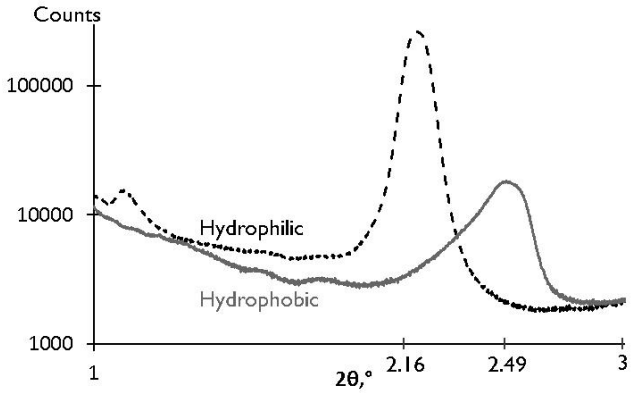

Figure 8.6. XRD diffractograms showing the better ordered PMO film on the hydrophilic SiCN as compared to the hydrophobic SiCN

clear pore organization is observed (Figure 8.7 a). Additionally, since the hydrophobized SiCN does not have any anchoring chemical functionalities to which the PMO can adhere, the film shrinkage during the thermal template removal causes delamination of the PMO from both the side-walls and the bottom of the trench (Figure 8.7 b). Therefore, it is important to ensure the presence of –OH groups on the substrate when the PMO is deposited in terms of both adhesion and pore organization.

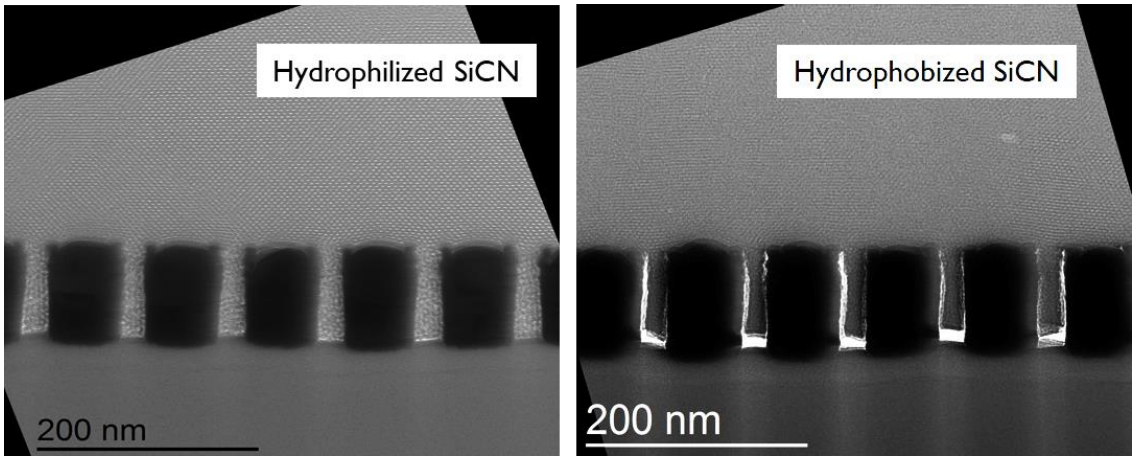

Figure 8.7. TEM micrographs showing the gap-fill structures deposited with PMO on a) hydrophilic SiCN and b) hydrophobic SiCN

To understand why the pore order is disrupted between the metal lines we examined wider gaps on the gap-fill structure. The hydrophilic SiCN is beneficial for the pore order since both on the Cu lines and between the Cu lines in the 450 nm gap, the pores immediately on top of the SiCN are not disrupted (Figure 8.8). On the other hand, next to the sidewalls of the metal lines, no pore order is observed. Therefore, the surface energy of the sidewalls seems to be disrupting the pore order and as a result, disordered pore regions of at least 25 nm to the left and the right of the metal lines are created (Figure 8.8b). This is why no ordered porosity is observed in the narrow 45 nm trenches. Two possible explanations are considered. First, the disordered pores next to the sidewalls might be due to a different surface energy at the sidewall as compared to the surface of the trenches. The differing surface energy might be due to a non-

conformal SiCN deposition which does not cover fully the sidewalls.[15] As a result, the sidewalls consist of an oxidized TaN. Second, the disordered porosity might be the result of the topology. In particular, the sidewalls might promote the tubular micelles to grow perpendicular to the silicon substrate, i.e. parallel to the walls. However, no such alignment is observed, probably, due to the conflicting driving force for the micelle to align parallel to the substrate. As a result, the conflicting driving forces lead to disordered porosity.

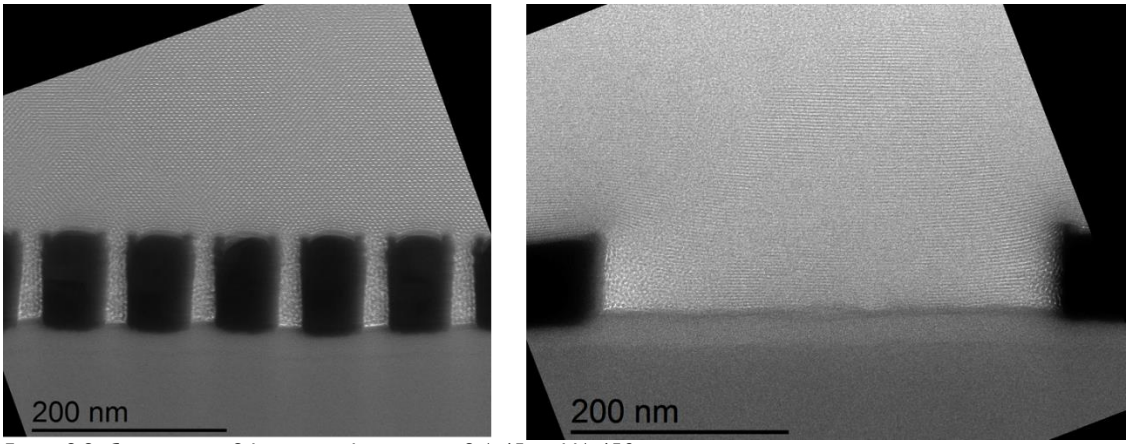

Figure 8.8. Comparison of the pore order in gaps of a) 45 and b) 450 nm

8.3.3. Effect of the template on the electrical reliability of PMO films

The current-voltage (I-V) curves shown in Figure 8.9 reveal that following the thermal template removal, in the PMO film, there are numerous leakage paths which lead to a wide distribution of breakdown fields (E_{BD}) from 2.8 to 5.7 MV/cm. The shown I-V curves are those observed for the BrijS10-templated film but the CTAC-templated film display a similar response. However, a consequent silylation improves the I-V behavior by eliciting a more consistent leakage current density as a function of the applied electric field. Therefore, the leakage paths before the silylation are attributed to the presence of Si-OH groups. According to the Poole-Frenkel emission mechanism,[23] under an applied electric field, the Coulomb potential energy of the proton from the silanol groups is reduced increasing the probability that the bound proton will become free

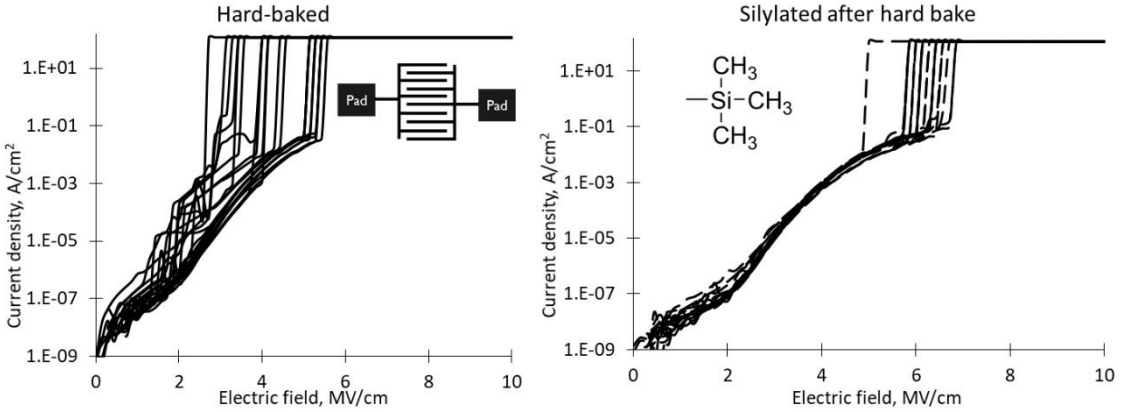

Figure 8.9. Stress-induced leakage current for a PMO a) annealed at 400°C for 20 min and b) additionally silylated by DMATMS. The inset in a) shows schematically the metal lines and the contact pads. The inset in b) shows the trimethylsilane functionality which gets incorporated into the films as a result of the silylation treatment

and contribute to the leakage current. The leakage current has been further shown to increase with the higher amount of adsorbed water[24] which is facilitated by the presence of the Si-OH groups. The silylation replaces the O-H groups with C-H-terminating functionalities. In spite of the fact that the C-H bond has a smaller dissociation energy as compared to the O-H, the methyl functionalities prevent the water adsorption which has a major role in the proton conduction contributing to the leakage current.[24] Similarly, the E_{BD} distribution becomes narrower, i.e. between 5.1 and 7.0 MV/cm as compared to the E_{BD} before the silylation and its average value increases from 4.2 to 6.3 MV/cm. Therefore, the next comparisons between the films templated by the ionic and non-ionic surfactants are for silylated films.

Following the hydrophobization treatment, the CTAC-templated film has a lower breakdown field of 5.7 MV/cm than the BrijS10-templated film which has an E_{BD} of 6.3 MV/cm (Figure 8.10). At a high electric field, E=4 MV/cm, the leakage current is about two times larger, 1.8×10^{-3} A/cm^2, for the film templated by the ionic surfactant as compared to the film templated by the non-ionic template. Nevertheless, it is comparable to the leakage current observed in the commercial spin-on SOG2.2 low-k. On the other hand, the leakage current measured for the CTAC-templated PMO at 1 MV/cm of 1.6×10^{-9} A/cm^2 is close to the tool's sensitivity level and an order lower than that of the BrijS10-templated film. These observations differ from a previous report where the use of an ionic surfactant, CTAB, resulted in films with very high leakage current.[11] The high leakage was attributed to the presence of excessive amount of bromine ions following the template removal. Therefore, we compared the chlorine content in the BrijS10- and CTAC-templated films. Indeed, there is on average about 3 to 4 times more chlorine in the CTAC-templated film as compared to the BrijS10-templated (Figure 8.10 b). The source of chlorine ions in the BrijS10-templated film is the HCl acid catalyst. Consequently, while we have ascertained the presence of chlorine ions in the CTAC-templated film, the observed I-V curves demonstrate that the ions do not deteriorate significantly the electrical reliability. Therefore, in terms of dielectric reliability, the ionic surfactants are a suitable templating agent for PMO films intended for a low-k application.

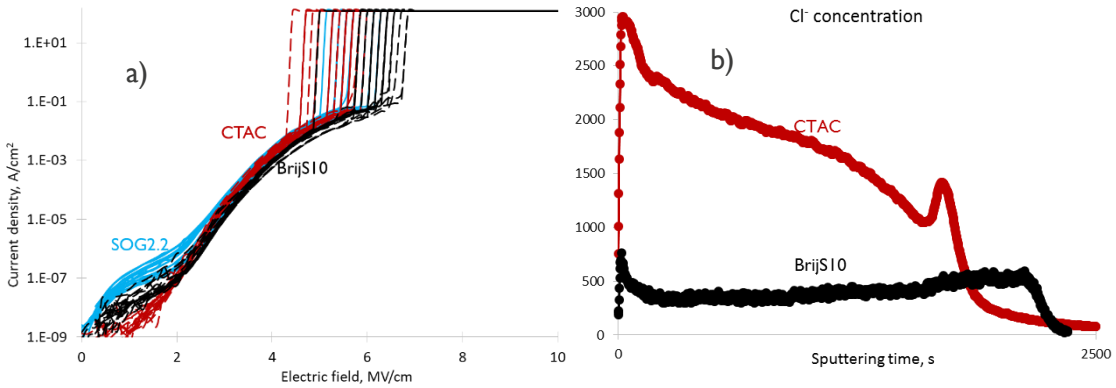

Figure 8.10. Films templated by ionic and non-ionic surfactants: a) comparison of the SILC; b) ToF-SIMS results showing the difference in Cl⁻ content in the CTAC and BrijS10-templated films

8.4. Conclusions

A PMO film with a 2D hexagonal pore order has been shown to possess 1.7 GPa lower Young's modulus than a film with a disordered porosity. This has been explained by a small difference in density and by the anisotropy of the PMO with a 2D hexagonal mesophase. A comparison of the electrical reliability of PMO films templated by an ionic surfactant, CTAC and a non-ionic surfactant, BrijS10, demonstrates that the CTAC is a suitable templating agent for low-k films. The use of CTAC does not result in a significantly higher leakage current density or lower breakdown field when compared to the film with a non-ionic surfactant. In particular, the leakage current density of the CTAC-templated film at 1MV/cm is 1.6×10^{-9} A/cm^2 while the breakdown field is 5.7 MV/cm. At the same time, CTAC-templated PMO films have a small pore size of about 2 nm and a narrow pore size distribution both of which are very important for a low-k application. High surface energy of the substrate is shown to be required in order to obtain a well-ordered PMO and reduce the size and number of domains with disordered porosity. The latter is not expected to affect the electrical properties, e.g. permittivity and reliability, but it will result in variability in the mechanical properties, to the extent that they are determined by the pore organization.

8.5. References

[1] H. Miyoshi, H. Matsuo, Y. Oku, H. Tanaka, K. Yamada, N. Mikami, S. Takada, N. Hata, T. Kikkawa, *Jpn. J. Appl. Phys.* **2004**, *43*, 498.

[2] H. Miyoshi, K. Yamada, K. Kohmura, N. Fujii, H. Matsuo, H. Tanaka, Y. Oku, Y. Seino, N. Hata, T. Kikkawa, *Japanese J. Appl. Physics, Part 1 Regul. Pap. Short Notes Rev. Pap.* **2005**, *44*, 5982.

[3] D. Jauffrès, R. Dendievel, M. Verdier, *Thin Solid Films* **2011**, *520*, 430.

[4] H. Fan, C. Hartshorn, T. Buchheit, D. Tallant, R. Assink, R. Simpson, D. J. Kissel, D. J. Lacks, S. Torquato, C. J. Brinker, *Nat. Mater.* **2007**, *6*, 418.

[5] D. J. Michalak, J. M. Blackwell, J. M. Torres, A. Sengupta, L. E. Kreno, J. S. Clarke, D. Pantuso, *J. Mater. Res.* **2015**, *30*, 3363.

[6] T. Asefa, M. J. MacLachlan, H. Grondey, N. Coombs, G. A. Ozin, *Angew. Chemie Int. Ed.* **2000**, *39*, 1808.

[7] F. Goethals, I. Ciofi, O. Madia, K. Vanstreels, M. R. Baklanov, C. Detavernier, P. Van Der Voort, I. Van Driessche, *J. Mater. Chem.* **2012**, *22*, 8281.

[8] W. Wang, D. Grozea, S. Kohli, D. D. Perovic, G. A. Ozin, *ACS Nano* **2011**, *5*, 1267.

[9] G. Dubois, W. Volksen, In *Advanced Interconnects for ULSI Technology*; John Wiley & Sons, Ltd: Chichester, UK, 2012; pp. 1–33.

[10] T. Kikkawa, Y. Kayaba, K. Kohmura, S. Chikaki, *IEEE Int. Reliab. Phys. Symp. Proc.* **2011**, 130.

[11] C.-Y. Ting, H.-S. Sheu, W.-F. Wu, B.-Z. Wan, *J. Electrochem. Soc.* **2007**, *154*, G1.

[12] P. S. Ho, J. Leu, W. W. Lee, *Low Dielectric Constant Materials for IC Applications*; Ho, P. S.; Leu, J.; Lee, W. W., Eds.; Springer-Verlag Berlin Heidelberg 2003, 2003.

[13] L. Zhang, J.-F. de Marneffe, N. Heylen, G. Murdoch, Z. Tokei, J. Boemmels, S. De Gendt, M. R. Baklanov, *Appl. Phys. Lett.* **2015**, *107*, 92901.

[14] K. Landskron, B. D. Hatton, D. D. Perovic, G. A. Ozin, *Science* **2003**, *302*, 266.

[15] L. Zhang, J.-F. de Marneffe, A. Lesniewska, P. Verdonck, N. Heylen, G. Murdoch, K. Croes, J. Boemmels, Z. Tokei, S. De Gendt, M. R. Baklanov, *Appl. Phys. Lett.* **2016**, *109*, 232901.

[16] D. D. Burkey, K. K. Gleason, *J. Appl. Phys.* **2003**, *93*, 5143.

[17] C. J. Brinker, G. W. Scherer, *Sol-Gel Sci.* **1990**, 96.

[18] G. Dubois, W. Volksen, T. Magbitang, M. H. Sherwood, R. D. Miller, D. M. Gage, R. H. Dauskardt, *J. Sol-Gel Sci. Technol.* **2008**, *48*, 187.

[19] G. Dubois, W. Volksen, T. Magbitang, R. D. Miller, D. M. Gage, R. H. Dauskardt, *Adv. Mater.* **2007**, *19*, 3989.

[20] A. Delafargue, F. J. Ulm, *Int. J. Solids Struct.* **2004**, *41*, 7351.

[21] I. Ciofi, M. R. Baklanov, Z. Tokei, G. P. Beyer, *Microelectron. Eng.* **2010**, *87*, 2391.

[22] S. Förster, A. Timmann, M. Konrad, C. Schellbach, A. Meyer, S. S. Funari, P. Mulvaney, R. Knott, *J. Phys. Chem. B* **2005**, *109*, 1347.

[23] F.-C. Chiu, *Adv. Mater. Sci. Eng.* **2014**, *2014*, 1.

[24] Y. Kayaba, K. Kohmura, T. Kikkawa, *Jpn. J. Appl. Phys.* **2008**, *47*, 8364.

CHAPTER 9. GENERAL CONCLUSIONS AND OUTLOOK

9.1. General conclusions

9.1.1. Conclusions on electromagnetic activation of the C-bridged low-k

In oxycarbosilanes films, the UV and VUV irradiation has a more detrimental effect on the ethylene bridges as compared to the methylene groups. Photons with energy lower than 6.2 eV (e.g. λ =222 nm) do not have a detrimental effect on the bridging methylene groups. In contrast, the concentration of the bridging ethylene groups is reduced by the 222 nm light. When the films are exposed to 172 nm light, the ethylene groups are depleted by more than 75% while methylene loss is limited to only 40%. The experimental results are qualitatively supported by DFT quantum chemical calculations.

After 1 min 172 nm and 20 min 222 nm irradiations, comparable dielectric constant and Young's modulus values ($k \leq 2.3$, YM $\geq$ 7.5 GPa) are observed, but the latter produces superior low-k films because of a better template removal and higher hydrophobicity. The longer UV cure densifies the film, while making the matrix less dense. This is due to the self-hydrophobization reaction. If the 20 min of 222 nm UV cure is applied on a film with a larger template content, a dielectric film with an YM of 5.5 GPa and a k of 2.07 is obtained.

Laser anneal increases the Young's modulus as a result of the high activation energy achieved due to the high temperatures around and in excess of 1000°C which ensures the condensation of the silanol groups and the densification of the matrix. High laser power corresponding to a surface temperature of ca. 1000°C is required in order to achieve complete template removal. To obtain an -OH-free low-k film, the laser anneal needs to be performed in an inert atmosphere. Around 1000°C, there exists a processing window which allows for a 13% higher Young's modulus value as compared to the reference films annealed in a furnace at 400°C, with no impact on the dielectric constant calculated to be 2.25. However, extensive bond rearrangements, mostly related to the removal or reorganization of the organic content of the organosilicate matrix, make this approach rather unattractive.

9.1.2. Conclusions on the replacement of siloxane bonds by alkylene groups

The replacement of some of the Si-O-Si by Si-CH_2-Si functionalities in a self-assembly-based porous organosilica film results in a smaller improvement of the YM than previously thought. For instance, at a density of ~0.87 g cm^{-3}, the film containing methylene groups has an YM of 6.6 GPa, while the one without – 5.3 GPa. Concurrently, a higher dielectric constant is measured for the films containing methylene groups – 2.27 with and 2.12 without the Si-CH_2-Si groups at the same density since replacing Si-O-Si by Si-CH_2-Si groups leads to a denser matrix. Therefore,

in an integration scheme where the processing damage to the low-k can be avoided, low carbon content dielectrics are more suitable for microchip production since lower porosity is required to achieve ultra-low dielectric constant.

9.1.3. Conclusions on PMO hydrophobicity

The self-hydrophobization reaction in which a bridging methylene group is transformed into a methyl group can occur at a temperature as low as 200°C, significantly lower than previously reported in literature. Additionally, the self-hydrophobization reaction is sterically hindered in the presence of a template requiring higher activation energy than in a porous material. Furthermore, in methylene-bridged organosilica films, the degree of self-hydrophobization depends on the employed template since surfactants containing polyethylene oxide chains block the silanol condensation making the Si-OH groups available for self-hydrophobization reactions. The films templated by cetyltrimethylammonium chloride (CTAC) are more hydrophilic when compared to films templated by BrijL4 and BrijS10.

9.1.4. Conclusions on Gemini-templated PMO

An ethane-PMO film templated with the ionic Gemini 16-12-16 surfactant has been shown to meet the material specifications for low-k dielectrics. Following a thermal template removal, the PMO film has a distorted 2D hexagonal pore organization with a pore size distribution centred at 2 nm. The Gemini surfactants are an exciting class of templating molecules because their packing parameter can be relatively easily controlled, opening the possibility for a systematic engineering of the mesopore structure of PMO films with a small pore size.

9.1.5. Conclusions on PMO for low-k

In spin-coated PMO films, there exists a tunable steady state in which the surfactant self-assembly can be directed by the ambient conditions, such as humidity and temperature, resulting in a desired mesopore structure. For instance, at a relative humidity of 70%, films with 3D or 2D hexagonal phases depending on the surfactant to organosilica molar ratio have been obtained. However, the high humidity has competing effects on the mesophase formation. On the one hand, the water adsorption increases the micelle surface curvature, while on the other hand, the H_2O molecules cause hydrolysis of the siloxane bonds favoring the decrease of the micelle surface curvature. The surfactant self-assembly is also affected by the degree of polycondensation of the organosilica oligomers. For instance, 3D hexagonal phase is favored after 20 min solution aging, 2D hexagonal after 40 min aging and no ordered mesophase is obtained if the solution is aged for longer than 70 min. When the water to organosilica molar ratio is reduced from 30 to 14 affecting the kinetics of hydrolysis, cubic mesophases are observed. A PMO film with a 2D hexagonal pore order possesses 1.7 GPa lower Young's modulus than a film with a disordered

porosity while both have the same dielectric constant of 2.30. High surface energy surface is required in order to obtain a well-ordered PMO film in 45 nm trenches.

9.1.6. Conclusions on the suitability of ionic surfactants as a low-k template

Contrary to expectations, the ionic surfactant CTAC is a suitable templating agent for low-k films. When compared to a film templated by a non-ionic surfactant, the use of CTAC results in a comparable leakage current density and breakdown field. In particular, the leakage current density of the CTAC-templated film at 1MV/cm is 1.6×10^{-9} A/cm^2 while the breakdown field is 5.7 MV/cm. At the same time, CTAC is an interesting templating molecule for low-k application since it results in films with small pore size of ca. 2 nm and narrow pore size distribution.

9.2. Outlook

9.2.1. Concerning PMO for low-k application

When PMOs are considered for low-k application, one of the main concerns is the uniformity of the pore order across the 300 mm wafer, i.e. the PMO film needs to have the same well-ordered pore structure in every structure. Such a good and consistent pore organization is not always observed in self-assembly based glasses. This issue can be approached in two somewhat distinct ways – kinetic and thermodynamic. The kinetic approach relies on control of the self-assembly during the whole extent of the tuneable steady state up to the moment when the mesophase is completely fixed. Ideally, this approach would employ a chamber with very well controlled ambient conditions (humidity, relative solvent pressure, temperature) as well as appropriate methods for in-situ monitoring of the self-assembly, e.g. GISAXS. However, since any gradients of the controlled parameters can affect the self-assembly adversely, the thermodynamic approach might be more suitable for a technological application. In a thermodynamic control over the mesopore structure, the synthesis conditions which favour the formation of a particular mesophase need to be identified. In particular, the surfactant packing parameter needs to be engineered for the desired surfactant assembly. Concurrently, the degree of organosilica polycondensation favouring the wanted mesophase needs to be controlled. Ideally, with this approach, very limited kinetic control will result in PMO films with long range and uniform pore order. An example of such a PMO synthesis which is relatively independent of deposition conditions is described in Chapter 7 of this thesis. However, that synthesis results in a PMO film with the anisotropic 2D hexagonal pore structure while isotropic cubic or 3D hexagonal mesostructures are preferred.

For the applicability of the kinetic approach in the microchip manufacturing, the effect of the high relative humidity on the metallization structures needs to be evaluated. The metal lines will need to be well-capped by a material which is thick enough not to allow for metal corrosion. This might be challenging given the trend for miniaturization.

Even if a suitable thermodynamic approach is identified, the surface energy of the material on which the PMO is deposited will still have a profound effect. As shown in Chapter 8, even if the synthesis conditions strongly favour the formation of long-range well-ordered PMO, the inappropriate surface energy can result in a PMO film with significantly disrupted pore organization. Therefore, when considering the technological relevance of a PMO material, it is important to take into account the surface energy of the substrate on which the PMO is grown. Alternatively, the PMO formation needs to be investigated on the capping layers established in the IC industry.

Due to the attractive small pore size and size distribution resulting from the use of ionic surfactants, it is important to ensure the hydrophobicity of the resulting films. The latter can be accomplished by the incorporation of a methyl-containing precursor, such as MTES, as shown in Chapter 4. However, a different synthesis approach will need to be employed if the pore order is to be maintained following the inclusion of MTES. As explained in the introduction to Chapter 4, such an approach is the late addition of MTES to the solution just before deposition.

In spite of their small size, one significant drawback of one-tailed ionic surfactants like CTAC is the fact that they have small head area which favours high surfactant packing parameter (g) values. In contrast, low g values of <1/3 are required in order to obtain spherical micelles which can form cubical or 3D hexagonal phases. Surfactants with high g values of higher than ½ can also result in cubical mesophase but those belong to bicontinuous phases with high network connectivity which is to be avoided in low-k films. The bicontinuous phases might be suitable in a low-k integration scheme in which the damage to the low-k is completely avoided. Therefore, surfactants with larger head size are required. Two broad classes of surfactants can be considered – Gemini surfactants and non-ionic surfactants. In Gemini surfactants, the head size can be easily controlled by the length of the hydrocarbon chain between the two N-atoms. However, such control is limited since it has been shown that a hydrocarbon chain longer than 6 carbon atoms does not lead to larger head size.[1] On the other hand, the non-ionic surfactants seem to offer larger flexibility since their head size can be controlled by the length of the polyethylene oxide chain. In Chapter 4, we showed that BrijL4 results in films with a small pore size comparable to that of CTAC-templated film. Therefore, surfactants with a hydrocarbon chain similar to that of BrijL4 but larger head seem interesting for further investigation.

9.2.2. Area-selective deposition of low-k

9.2.2.1. Introduction

With the downscaling of interconnect dimensions, the prospect of multiple patterning and etching steps in the standard top-down integration approach entails a tremendous increase in complexity and cost.[2,3] As a result, bottom-up approaches are more intensively researched.[4,5] In one such approach,[6,7] following a copper CMP and a copper clean step, a thiol-functionalized self-assembled monolayer (SAM) is deposited exclusively on the exposed metal lines while avoiding a deposition on the dielectric surface. Next, a metal oxide dielectric is deposited via an atomic layer deposition (ALD) exclusively on the exposed dielectric while the nucleation on the SAM-functionalized copper surface is delayed sufficiently to avoid a deposition of the dielectric. Finally, the SAM layer is removed and a dielectric barrier, e.g. SiCN, is deposited (Figure 9.1).

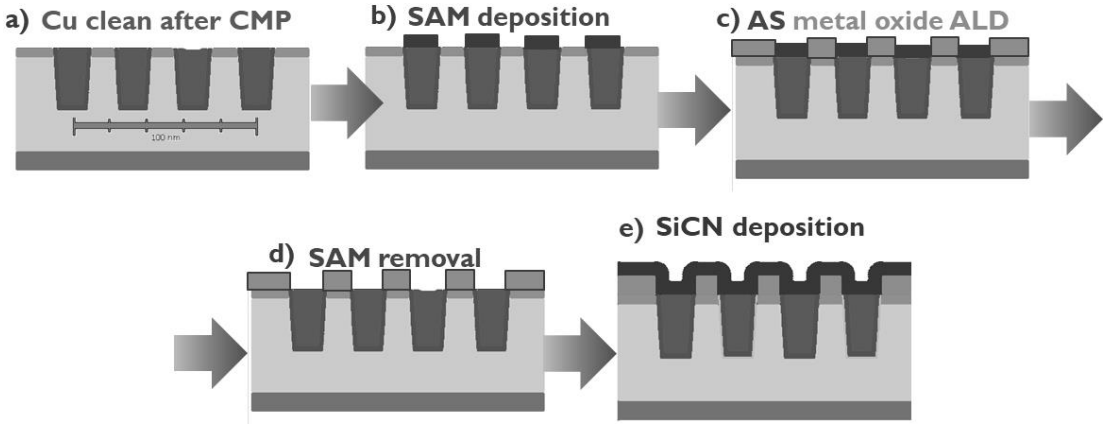

Figure 9.1. Integration scheme taking advantage of a selective SAM deposition followed by a selective ALD of a metal oxide

There are several challenges with the proposed method. First, the SAM needs to be dense enough in order to prevent effectively the ALD nucleation of the dielectric. In comparison to a liquid-phase SAM deposition, the vapor phase SAM deposition produces an organic monolayer which is more efficient in blocking the growth of the ALD dielectric layers.[7] Second, the ALD conditions are not necessarily compatible with the SAMs thermal and/or oxidative stability.[6] The SAM molecules can be thermally decomposed at the high temperatures required for the ALD or they can be oxidized by the oxidizing conditions employed in the ALD cycles. One of the options to reduce the deposition temperature of the ALD, the plasma-enhanced ALD, can also be incompatible with the stability of the SAMs due to an increased reactivity of the oxidizing reagents.[8]

Therefore, we propose an alternative approach which reduces the number of integration steps necessary to obtain the required pattern and avoids the mentioned issues. In this scheme, if necessary, the Cu clean is followed by a surface engineering which ensures different surface energies on the metal and the dielectric. Next, a low-k film is spin-coated resulting in a deposition

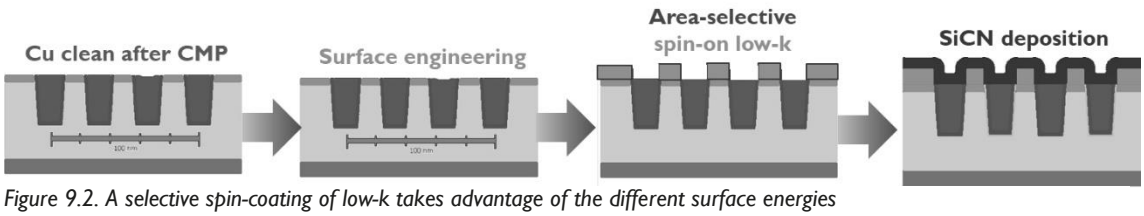

Figure 9.2. A selective spin-coating of low-k takes advantage of the different surface energies

only on the underlying dielectric avoiding a deposition on the metal surface (Figure 9.2). After a deposition of a dielectric barrier, the processing can continue with the metal deposition.

9.2.2.2. Experimental Section

Various synthesis conditions have been investigated in order to optimize the parameters leading to the best area-selective deposition. Acid-catalyzed (organo)silica polycondensation conditions have been employed. The investigated (organo)silica precursors have been tetraethoxysilane (TEOS) and methyltriethoxysilane (MTES). The most extensively investigated surfactant has been the 25wt% aqueous solution of cetyltrimethylammonium chloride (CTAC). The investigated parameters include 1) the surfactant to precursor molar ratio; 2) the acid concentration; 3) the synthesis temperature; 4) the solvent boiling point; 5) the solvent to precursor molar ratio; 6) the deposition spin speed. A synthesis procedure which resulted in one of the best selectivity results consists of preparing a matrix solution by mixing 2 ml ethanol, 0.56 ml 0.02M HCl and 1.2 ml MTES in a 100 ml round-bottom flask and stirring and refluxing the solution for 1 h at 60°C. After removing the flask from the heating plate, the mixture is transferred into a polyethylene bottle following a 5 min cooling in ambient conditions. In parallel, a template solution is prepared by mixing 0.5 ml CTAC aqueous solution with 7.6 ml 1-methoxy-2-propanol and stirring at room temperature for 50 min. Finally, the template solution is added to the matrix solution and stirred at RT for 15 min. The solutions are dispensed and spun on a native SiO_2 layer grown on a silicon substrate and a Si substrate from which the SiO_2 layer has been etched away by dipping in 5 wt% HF for 5 min which results in a surface terminated by Si-H bonds. The SiO_2 surface is hydrophilic with water contact angle (WCA) of ca. 20° while the Si-H terminated is more hydrophobic with a WCA of ≈80°. Additionally, the solution was spun on polished copper samples with and without a citric acid dip for 5 min which is a standard copper clean following the CMP intended to remove organics and restore the hydrophilicity of the Cu surface.

9.2.2.3. Results and Discussion

When an optimized low-k solution is spun on a hydrophilic SiO_2 surface at 1000 rpm for 60 s, no deposition of a film is observed. Alternatively, if the solution is spun on a Si-H-terminated surface then a film is present on the substrate following the spinning. The presence or absence of a film on the substrate can be ascertained visually and it can be demonstrated by FTIR and SE measurements (Figure 9.3). The FTIR spectra shown on Figure 9.3a are obtained following a

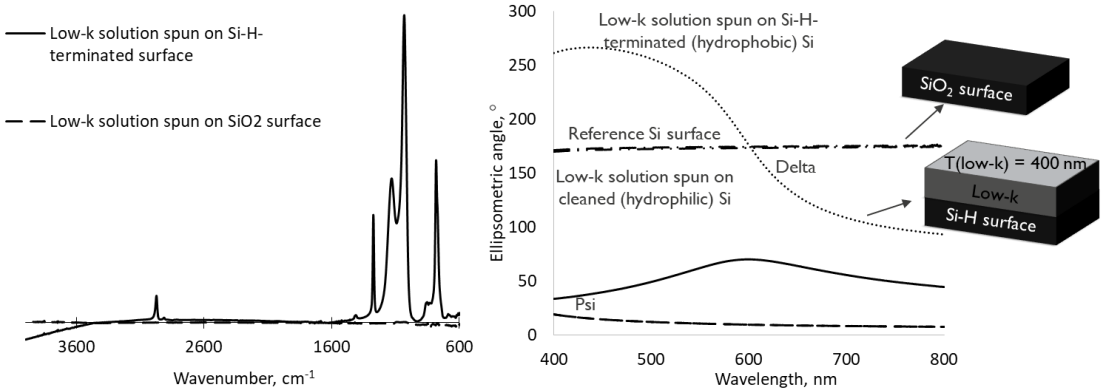

Figure 9.3. Spectroscopic evidence showing the presence of a low-k film on a Si-H terminated substrate while no film is present on the SiO_2 surface: a) FTIR spectra and b) dispersion of the raw ellipsometric angles

subtraction of the absorption observed for a silicon substrate on which no low-k solution had been spun. This is why the spectrum of the sample with an oxide surface does not have any absorption peaks. On the other hand, the spectrum of the sample with the Si-H surface contains the peaks characteristic of a low-k film obtained from the MTES precursor. Furthermore, the dispersions of the ellipsometric angles shown on Figure 9.3b demonstrate the lack of a film deposited on the oxide surface since the Psi and Delta dispersions obtained before and after the spinning of the low-k solution overlap. In contrast, the Si-H-terminated sample has a clearly different optical response after the spinning of the solution as compared to before it. Modelling of the raw data with a Cauchy function reveals that a 400 nm low-k has been deposited on the Si-H terminated substrate.

The selective deposition is observed within a selectivity window which is determined by the deposition spin speed. In general, the lower the spin speed, the better is the selectivity. At spin

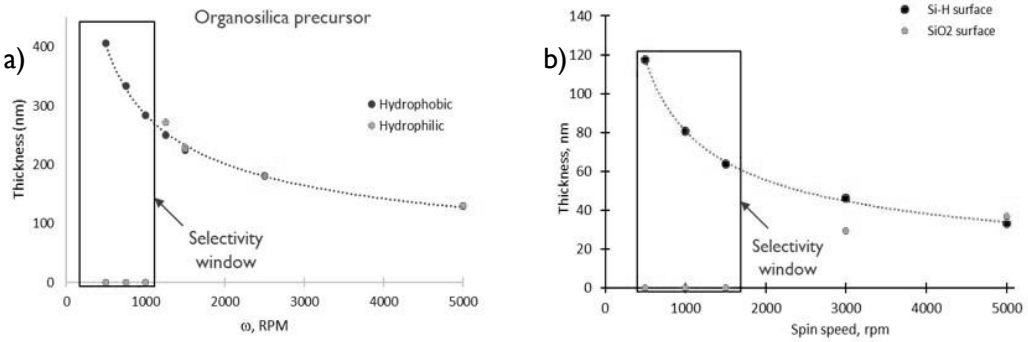

Figure 9.4. The selectivity window is limited up to a spin speed of a) 1000 rpm when organosilica precursor is present; and b) 1500 rpm when a surfactant solution is spun

speeds higher than a critical speed, films are deposited on both the SiO_2 and the Si-H surface (Figure 9.4). Nevertheless, often, the films observed on the SiO_2 surface de-wet within 5 minutes leaving behind "droplets" of organosilica. The remaining "droplets" clearly consist of organosilica molecules since upon an anneal at 400°C, they are not removed which would be expected if they were surfactant molecules. The "droplets" were not investigated further. Importantly, the de-wetting behavior is observed only if the spun solution contains MTES, i.e. no de-wetting is observed when a surfactant solution is spun. The surfactant solution contained all components

of a low-k solution but the organosilica precursor. Employing the surfactant solution, the largest selectivity window extending to a spin speed of at least 1500 rpm was observed (Figure 9.4 b). The best results for solutions containing organosilica precursors have been observed up to a spin speed of 1000 rpm.

The results described so far have been observed for solutions containing CTAC which is employed as the templating molecule. A single test which consisted of replacing the CTAC with other surfactants did not result in a selective deposition. The solution contained methoxypropanol, HCl, ethanol, and a surfactant in the same molar ratios as in the low-k coating solution. When the CTAC was replaced by Gemini 16-12-16, ammonium lauryl sulphate, or BrijS10, films were observed both on Si-H surface and on SiO_2 surface, i.e. no selective deposition was evident. On the other hand, replacing the CTAC by BrijL4, poly(ethylene glycol) (12) tridecyl ether, or poly(ethylene glycol) (18) tridecyl ether did not result in a film on either of the surfaces. However, further experiments are required before these surfactants can be considered unsuitable for the purposes of an area-selective deposition. This is because no selectivity to the surface energy was also observed for the 25 wt% aqueous CTAC solution which independent of the spinning speed formed a film on both the oxide surface as well as the Si-H-terminated surface. Therefore, the observed selective deposition on a Si-H-terminated surface with respect to an oxide surface is the result of an interplay between the solution components rather than determined solely by the surfactant. Deeper understanding of the role of each solution component is required.

Selective deposition on a low-energy surface with respect to a high-energy surface has been observed when MTES is employed as the organosilica source. In contrast, when the MTES is replaced by equimolar amount of TEOS, no selectivity of the resulting solution with respect to the surface energy of the substrate has been observed. The solution is deposited on the low- and high-energy surfaces independent of spinning speed. The solution pH of 1.95 and the TEOS-to-H_2O molar ratio of 1-to-5 entail complete hydrolysis of the TEOS while the polycondensation is promoted by the one hour treatment at 60°C. However, the degree of polycondensation, i.e. the molecular size of the polymers might play an important role for the area-selective deposition of the solution. Therefore, other degrees of polycondensation of TEOS need to be investigated before TEOS can be considered unsuitable for the purpose of area-selective spin-coating.

9.2.2.4. Selectivity mechanism

In the pursuit of identifying the underlying mechanism of the observed area-selective spin-coating, several factors have been recognized to be critical. First, the presence of a surfactant, CTAC, is essential but not sufficient. Second, the presence of MTES is not critical for selectivity but its presence results in de-wetting of already deposited films on high-energy surfaces, a phenomenon which is not observed on low energy surface. Since the latter does not result in a

completely material-free surface, it is not considered suitable for the purpose of area-selective deposition but it provides insight into the interaction between the organosilica precursor, the surfactant molecules and the high-energy surface. Third, the area-selective deposition is favored at lower deposition speeds. Based on these observation, the area-selective deposition is postulated to be based on the wetting properties of the coating solutions. Given that the high-energy surface "repels" the coating solution, taken as a whole, the solution seems to be hydrophobic. The hydrophobicity of the solution is reduced when the organic solvents are removed, i.e. when the aqueous CTAC solution is spin-coated, explaining the lack of selectivity towards the surface energy. Furthermore, in contrast to the TEOS, the higher hydrophobicity of the oligomers formed by the MTES explains the de-wetting of the deposited films. On the other hand, the deposition speed dependence indicates that the conditions which favor the slow solvent evaporation and the solution flow are those that lead to selectivity to the substrate surface energy. The high spin speeds lead to fast solvent evaporation which results in a solution enriched in the organosilica oligomers whose flow is strongly impeded leading to the formation of a film. This explanation predicts that apart from the hydrophobicity of the solvent, its boiling point and its viscosity are important properties which will determine the deposition speed to which the area-selective deposition will be observed.

9.2.2.5. Conclusions and outlook

The area-selective spin-coating of low-k films on a low-surface energy silicon substrate, WCA>80°, with respect to a high-surface energy, WCA<20°, has been demonstrated. While the mechanism of selectivity has not been entirely clarified, several important factors have been recognized such as the spin-speed, the presence of the surfactant CTAC, and the hydrophobicity of the organosilica oligomers at the time of deposition. The wetting interaction between the coating solution and the substrate is the main candidate to explain the observed area-selective deposition.

However, the area-selective spin-coating of low-k needs considerable amount of further investigation. While surfactants are supposed to be surface active molecules which enable the wetting of surfaces with different surface energy, instead, the CTAC seems to enable selectivity which is not otherwise observed. To aid fundamental understanding, molecular dynamics simulations might provide a better insight into the synergistic effects between the various components of the solutions for which the area-selective deposition has been observed.

At the same time, deeper insight can be gained from additional experiments. For instance, the better selectivity observed with the lower spin speed suggests that dip coating or blade coating might be even more suitable for area-selective deposition of organosilica films. More importantly, identifying other surfactants for which the effect is observed should provide insight into the molecular characteristics of CTAC which enable the area-selective coating. Given that the

(organo)silica precursor also plays a role in the de-wetting of as-deposited films, its role needs to be understood. The degree of polycondensation and the type of oligomers, branched or linear, together with the hydrophobicity of the precursor can be varied. The properties of the solvents are also postulated to play an important role for the selectivity. Higher boiling point solvents which are more hydrophobic are expected to increase the selectivity window.

9.3. References

[1] H. I. Lee, C. Pak, S. H. Yi, J. K. Shon, S. S. Kim, B. G. So, H. Chang, J. E. Yie, Y.-U. Kwon, J. M. Kim, *J. Mater. Chem.* **2005**, *15*, 4711.

[2] K. Mistry, Leading at the edge 10 nm technology leadership **2017**.

[3] R. Kim, J. Ryckaert, P. Raghavan, Y. Sherazi, P. Debacker, D. Trivkovic, W. Gillijns, L. E. Tan, Y. Drissi, V. Blanco, J. Bekaert, M. Mao, S. Larivière, G. McIntyre, **2017**, *10148*, 101480V.

[4] R. Gronheid, J. Doise, J. Bekaert, B. T. Chan, I. Karageorgos, J. Ryckaert, G. Vandenberghe, Y. Cao, G. Lin, M. Somervell, G. Fenger, D. Fuchimoto, *Proc. SPIE* **2015**, *9423*, 942305.

[5] Y. Badr, P. Gupta, *J. Micro/Nanolithography, MEMS, MOEMS* **2017**, *16*, 13505.

[6] F. S. M. Hashemi, S. F. Bent, *Adv. Mater. Interfaces* **2016**, *3*.

[7] F. S. Minaye Hashemi, B. R. Birchansky, S. F. Bent, *ACS Appl. Mater. Interfaces* **2016**, *8*, 33264.

[8] R. W. Johnson, A. Hultqvist, S. F. Bent, *Mater. Today* **2014**, *17*, 236.

APPENDIX A. METHODOLOGY

A1. Spectroscopic Ellipsometry (SE)

The polarization state of a light wave is modified by the reflection from a planar surface. Reflection ellipsometry determines the state of polarization of a reflected wave with suitably prepared polarization state of an incident wave. A general elliptic polarization of the incident and reflected waves can be resolved into the two basic linear polarizations, parallel (r_p) and perpendicular (r_s) to the plane of incidence. The ratio of the amplitude reflectivities (ρ) is the basis for the interpretation of reflection ellipsometry measurements. The fundamental ellipsometric equation is usually written in the form:

$$\tan \Psi \, e^{i\Delta} = \frac{\tilde{r}_p}{\tilde{r}_s} = \rho \text{ [1]}$$

In this work, the film thickness and refractive index (RI) values were obtained by modelling the experimentally measured dispersion of the ellipsometric angles Ψ and Δ using the Cauchy dispersion relation given by:

$$RI = A + \frac{B}{\lambda^2} + \frac{C}{\lambda^4},$$

where A, B and C are constants fitted during the modelling. The measurements were carried out using a spectroscopic ellipsometer SENTECH801 (350–800 nm). The RI values are reported at λ =632.8 nm.

A2. Ellipsometric Porosimetry (EP)

In-situ ellipsometric measurements during exposure of a porous material to the vapours of an adsorbate, toluene or water, results in an isotherm which is a function of the accessible pore volume and the pore size distribution of the porous material. Toluene is a suitable adsorbate for the hydrophobic low-k materials while water is useful in determining the degree of hydrophilicity, i.e. damage, as a result of the processing steps to which the low-k is exposed during integration. Open (accessible) pore volume (V) is calculated according to:

$$V = \left(\frac{n_{eff}^2-1}{n_{eff}^2+2} - \frac{n_p^2-1}{n_p^2+2}\right) \Big/ \left(\frac{n_{ads}^2-1}{n_{ads}^2+2}\right), \text{ [2,3]}$$

where n_{eff} is the refractive index of the film filled with the adsorbate, n_p is the refractive index of the porous film, and n_{ads} is the refractive index of the adsorbate. The pore size distribution in the mesopore size range is calculated according to the Kelvin equation:

$$\ln\left(\frac{P}{P_0}\right) = -\frac{f\gamma V_L \cos\theta}{r_k RT}, \text{ [2–4]}$$

where (P/P_0) is the relative pressure, γ and V_L are surface tension and molar volume of the liquid adsorptive, respectively. θ is the wetting angle of the adsorptive, f=1 for slit-shaped pores and f=2 for cylindrical pores. The pore size distribution is obtained by plotting adsorbed volume as

a function of pore size. The adsorbed volume is calculated based on the change in RI. If the radius of a cylindrical pore is r, then $r=r_k+t$ where t is the thickness of the layer adsorbed on the pore walls. In the micropore size range, i.e. below 2 nm, a method based on a theory developed by Dubinin and Radushkevich (DR) is used. According to DR, the adsorption potential A and characteristic adsorption energy E_0 are a function of the micropore size and the amount of adsorption W at the relative pressure P/P_0:

$$W = W_0 e^{-(\frac{A}{E})^2},$$

where $E = \beta E_0$ and $A = RTln(\frac{P}{P_0})$, W_0 is the micropore volume, β is the affinity coefficient and the E_0 gives the average pore width.[4]

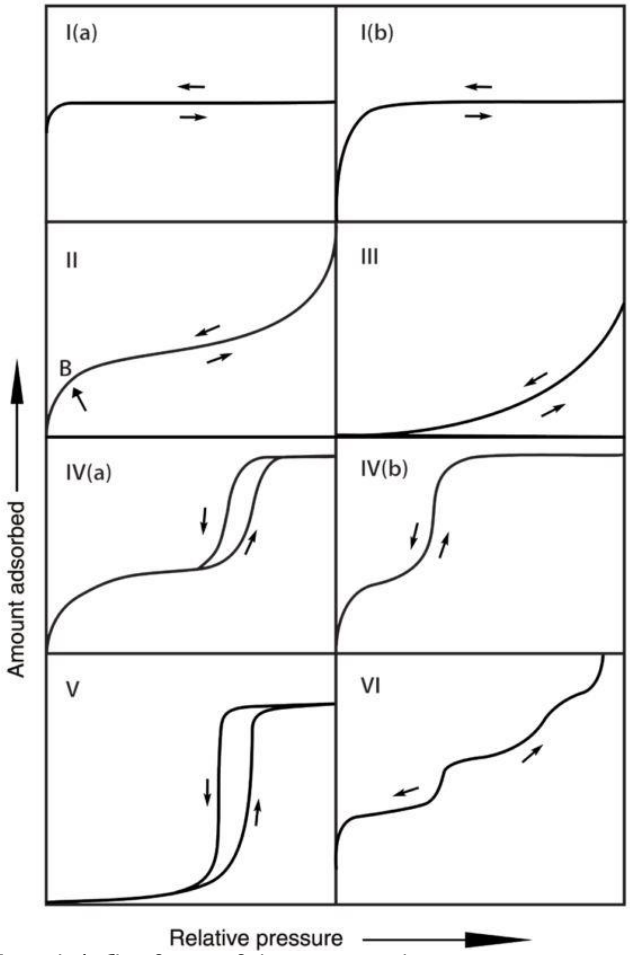

Figure A. 1. Classification of physisorption isotherms

The adsorption isotherms are divided into six main types (Figure A.1).[5] Of these, two have been observed for the materials investigated in this work. Type I isotherms are given by microporous materials. Type I(a) isotherms are given by microporous materials having narrow micropores (<~1 nm) while Type I(b) isotherms are observed for materials with pore size distributions over a broader range including wider micropores and possibly narrow mesopores (< ~ 2.5 nm). On the other hand, Type IV isotherms are given by mesoporous adsorbents. In the case of a Type IVa isotherm, capillary condensation is accompanied by hysteresis. This occurs

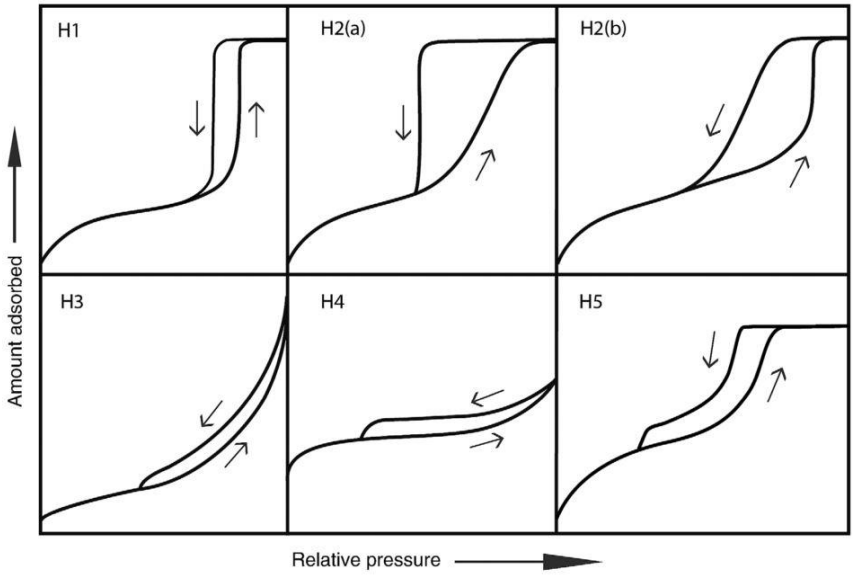

Figure A. 2. Classification of hysteresis loops

when the pore width exceeds a certain critical width, which is dependent on the adsorption system and temperature. Type IVb isotherms have not been observed for our materials. Hysteresis loops appear as a result of adsorption metastability and/or network effects. In an open-ended pore, delayed condensation is the result of metastability of the adsorbed multilayer. In more complex pore structures, the desorption path is often dependent on pore blocking. These phenomena occur if wide pores have access to the external surface only through narrow necks (e.g., ink-bottle pore shape). If the neck diameters are not too small, the network may empty at a relative pressure corresponding to a characteristic percolation threshold providing information about the neck size. On the other hand, if the neck diameter is smaller than a critical size, the mechanism of desorption from the larger pores involves cavitation in which case no quantitative information about the neck size can be obtained. The two types of hysteresis loops observed in this work are H1 and H2(a) (Figure A.2). The Type H1 loop is found in materials which exhibit a narrow range of uniform mesopores. Usually, network effects are minimal and the steep, narrow loop is a sign of delayed condensation on the adsorption branch. Hysteresis loops of Type H2 are given by more complex pore structures in which network effects are important. The very steep desorption branch, which is a characteristic feature of H2(a) loops, is attributed either to pore-blocking/percolation in a narrow range of pore necks or to cavitation-induced evaporation.

A3. Fourier-Transform Infra-Red Spectroscopy (FTIR)

The interactions of infra-red radiation with matter may be understood in terms of changes in molecular dipoles associated with vibrations and rotations. In a basic model, a molecule can be considered as a system of masses joined by bonds with spring-like properties. The stiffness of a bond can be characterized by a proportionality constant termed the force constant, k. On the

other hand, the reduced mass, μ, combines the individual atomic masses, and may be expressed as follows:

$$\mu = \frac{m_1 m_2}{m_1 + m_2},$$

Where m_1 and m_2 are the masses of the atoms at the ends of the bond. Thus, the equation relating the force constant, the reduced mass and the frequency of absorption is:

$$\vartheta = \frac{1}{2\pi}\sqrt{\frac{k}{\mu}}.$$

A molecule can only absorb radiation when the incoming infra-red radiation is of the same frequency as one of the fundamental modes of vibration of the molecule. For a vibration to give rise to the absorption of infra-red radiation, it must cause a change in the dipole moment of the molecule. Therefore, infra-red spectroscopy allows the determination of the chemical structure of a material. In our experiments, the FTIR analysis (Thermo Scientific, Nicolet 6700) was performed on spectra collected in the region 400–4000 cm^{-1} with a resolution of 2 cm^{-1} and averaged over 100 scans. The experimental spectra were treated by base-line correction and normalised to the thickness deduced from SE.

A4. Nanoindentation (NI)

During a nanoindentation test, the indentation probe is driven into a sample and then withdrawn. The applied load [P] and depth of penetration [h] into the sample are continuously monitored. A load-displacement curve is generated from the collected data. In our experiments, a nano-indenter (Nanoindenter XP) with a dynamic contact module and a continuous stiffness measurement option under the constant strain rate condition (0.05 s^{-1}) was employed. A standard three-sided pyramid diamond indenter tip (Berkovich) was used. Based on the load-displacement curves the reduced elastic modulus (E_r) can be calculated. The reduced modulus is related to the modulus of elasticity (E), i.e. Young's modulus (YM), through:

$$\frac{1}{E_r} = \left(\frac{1-\vartheta^2}{E}\right)_{sample} + \left(\frac{1-\vartheta^2}{E}\right)_{indenter},$$

where ϑ is the Poisson ratio. The Poisson ratio of the low-k films was assumed to be 0.25. In order to reduce the substrate effect,[6] which leads to overestimation of the YM of the low-k film, the elasticity was calculated at an indentation depth of less than 10% of the film thickness. Using a wedge indenter, when the indentation depth reaches 50% or more of the film thickness, a pop-up event appears in the load-displacement curve, i.e., the indentation depth increases suddenly at approximately a constant load. This feature of the curve has been associated with an interfacial delamination allowing the quantification of the interfacial adhesive energy.[7] The indentations were conducted using a TI950 triboindenter (Hysitron).

A5. Impedance Spectroscopy

The dielectric constant (k) of the films at 100 kHz was calculated from the measured capacitance using the formula of the parallel plate capacitance:

$$C = \frac{Ak\varepsilon_0}{d},$$

where C is the measured capacitance, A is the gate area, d is the film thickness, and ε_0 is the permittivity of free space (8.85×10^{-12} F/m). The capacitance was measured by impedance analysis (HP4284A-LCRmeter) of a metal–insulator-semiconductor-type capacitor obtained by e-beam evaporation of Pt through a contact mask to form Pt dots on the low-k film. Additionally, the samples were provided with an ohmic back contact, realised by Ga–In alloy paste.[8]

A6. Grazing-Incidence Small-Angle X-Ray Scattering (GISAXS)

X-ray scattering allows probing nanostructures by exploring the so-called reciprocal space, or the Fourier space. Since the interaction of hard X-rays with matter is weak, the kinematical approximation of single scattering, the so-called Born approximation (BA), or its application for grazing incidence geometry, the Distorted Wave Born Approximation (DWBA), are valid in most cases. In DWBA, the refraction and reflection effects, which become significant in grazing incidence geometry, are handled by first-order perturbation theory. In essence, the scattering at the film interfaces is treated dynamically while the scattering from the internal structure of the sample is treated kinematically (single scattering).

In SAXS, the scattering intensity from N identical particles is given by:[9]

$$I(\boldsymbol{q}) = \frac{1}{N_p}\left|\sum_{l=1}^{N_p} F_l(\boldsymbol{q}) e^{-j\boldsymbol{q}\boldsymbol{r}_l}\right|^2$$

where **q** is the scattering vector, $F_l(\boldsymbol{q})$ and r_l are the form factor amplitude and position of particle l, respectively. The exponential term e^{-jqr_l} is called the phase factor. The form factor amplitude F(**q**) of a geometric object is given by:

$$F(\boldsymbol{q}) = \int_V \Delta\rho(\boldsymbol{r}) e^{-i\boldsymbol{q}\boldsymbol{r}} d\boldsymbol{r},$$

where $\Delta\rho(\boldsymbol{r}) = \rho(\boldsymbol{r}) - \tilde{\rho}$, and $\rho(\boldsymbol{r})$ and $\tilde{\rho}$ are the scattering length density at position **r** and the mean scattering length density, respectively. In turn, the form factor is $P(\boldsymbol{q}) = |F(\boldsymbol{q})|^2$. Therefore,

$$I(\boldsymbol{q}) = \frac{1}{N} P(\boldsymbol{q}) \left|\sum_{l=1}^{N} e^{-j\boldsymbol{q}\boldsymbol{r}_l}\right|^2$$

The absolute square of the sum of the phase factor is referred to as the structure factor S(**q**). Finally, for identical particles, i.e. monodisperse approximation (MA) with spherical symmetry:

$$I(q) = P(q)S(q)$$

When particles are neither identical nor spherical, however, it is not possible to split the intensity into a product of the form factor and the structure factor without employing approximations. The two most popular approximations ,the decoupling approximation (DA)[10,11] and the local monodisperse approximation (LMA),[12] assume decoupling of position and individual particle properties, such as shape and size. The DA assumes that particles' intrinsic properties are not correlated with their positions while the LMA assumes that all particles are identical at short distances. In our work, the MA and the LMA were found to model well the scattering patterns observed from the porous low-k films.

The GISAXS characterization was performed at the Austrian SAXS beamline at ELETTRA, Italy. The wavelength of the incident beam was 0.154 nm (8 keV), and the sample to detector distance was set to 1.99m. The GISAXS patterns were recorded with a 2D Pilatus 1M detector.

The position of each pixel on the SAXS image is converted into the scattering vector q. This conversion is accomplished using experimental parameters that include the sample-to-detector distance (SDD) and the pixel size of the detector. The conversion can be performed by using Fit2D or DPDAK.[13] The modelling of the SAXS images in which no diffraction spots were observed was accomplished by utilizing the FitGISAXS software package.[14] To model the obtained scattering patterns, the form factor was calculated within the DWBA applied to a 3D assembly of scatterers homogeneously distributed between the depths z_j and z_{j+1} of a semi-infinite medium (option *Buried layer* in FitGISAXS).

$$|F(\boldsymbol{q})|^2 = \left|t_{0,1}(\alpha_i)\right|^2 \left|t_{0,1}(\alpha_f)\right|^2 \frac{Z_+}{t_j}\left[e^{-\frac{z_j}{Z_+}} - e^{-\frac{z_{j+1}}{Z_+}}\right]|F(\tilde{\boldsymbol{q}})|^2$$

The geometrical shape for which the form factor was calculated was spheroid (fits in-plane diameter D_y and height H), random spheroid (fits in-plane diameter D_y and height H with random orientation), ellipsoid (fits in-plane diameters D_x and D_y and height H) or cylinder (fits in-plane diameter D_y and height H). On the other hand, the structure factor was calculated in the BA within the Percus-Yevick approximation for hard spheres with 3D short-range order (option *Percus-Yevick 3D* in FitGISAXS). The hard-sphere diameter, D_{hs}, is assumed to be proportional to D_y with a constant factor C (D_{hs} = C x D_y) and the hard-sphere volume fraction is η_{hs}.

$$S(q) = \left[1 + 24\frac{\eta_{hs}G(qD_{hs})}{qD_{hs}}\right]^{-1},$$

where

$$G(A) = \alpha\frac{\sin A - A\cos A}{A^2} + \beta\frac{2A\sin A + (2-A^2)\cos A - 2}{A^3} + \gamma\frac{-A^4\cos A + 4\left[\left(3A^2-6\right)\cos A + (A^3-6A)\sin A + 6\right]}{A^5},$$

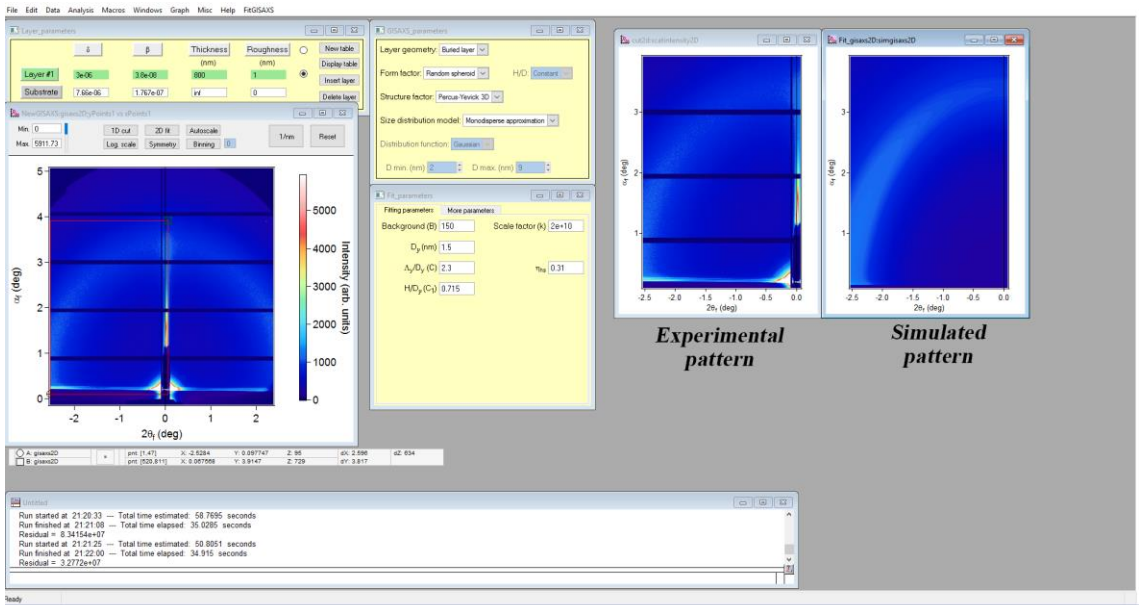

Figure A. 3. Screenshot from the fitting procedure performed using FitGISAXS. Experimental and simulated patterns are shown on the right side. The shown pattern is the one observed for MSQL4.

and

$$\alpha = \frac{(1 + 2\eta_{hs})^2}{(1 - \eta_{hs})^4}$$

$$\beta = -6\eta_{hs}\frac{(1 + \eta_{hs}/2)^2}{(1 - \eta_{hs})^4}$$

$$\gamma = \frac{\eta_{hs}\alpha}{2}$$

Within the LMA, the Gaussian distribution function was employed to model the pore size distribution.

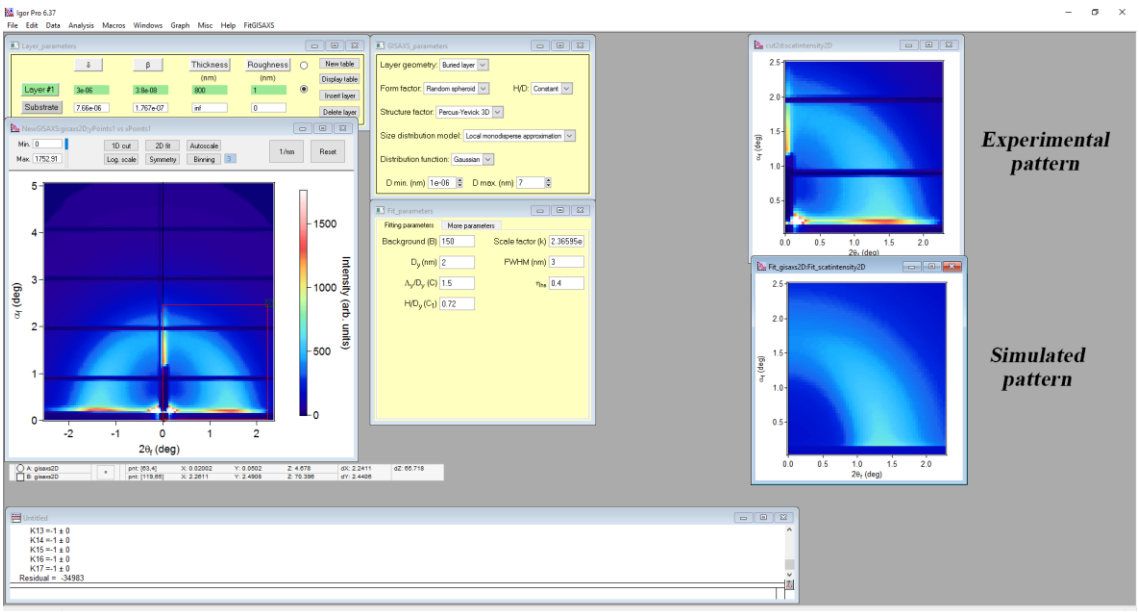

Figure A. 4. Screenshot from the fitting procedure performed using FitGISAXS. Experimental and simulated patterns are shown on the right side. The shown pattern is the one observed for MSQS10.

On the other hand, the scattering patterns containing diffraction spots were modelled using NANOCELL.[15] NANOCELL enables the simulation of the scattering pattern in both the BA and the DWBA. This is important since in GISAXS, at incidence angles close to the critical angle, reflection and refraction effects result in additional peaks which are not real features of the reciprocal space.[15] These peaks can also be identified during the data collection session by increasing the incidence angle which leads to the peaks being observed at a higher q_z with no change of their q_x coordinates.

A7. X-Ray Photoelectron Spectroscopy (XPS)

In an XPS experiment, an X-ray beam illuminates a sample from which electrons are ejected by the photoelectric effect. The kinetic energy of the ejected electrons is then determined. As the energy of the X-ray and of the ejected electron are known, the binding energy of the electron is determined. Knowing the binding energy allows for the identification of the elements from which the electron originates. Furthermore, chemical analysis is possible as a result of small variations of the binding energy. XPS is a surface sensitive technique. As the mean free path of the electron in the XPS-kinetic energy range is typically on the order of 2-3 nm, most of the information arises from the first 2-3 nm of the sample. The effective depth of analysis depends on the exit angle of measurement. A depth profile of the whole sample can be obtained by repeating cycles of sputtering by Ar^+ ions (0.5-2.0 keV) and analysis. In our work, depth-resolved XPS measurements were performed using an Al Kα X-ray source (1486.6 eV) with a spot size of 400 μm.

A8. Time-of-Flight Secondary Ion Mass Spectroscopy (TOF-SIMS)

The ion or molecule impact with a few keV of kinetic energy produces the emission of a variety of particles: photons, secondary electrons, radicals, neutral particles (atoms and molecules), secondary ions (positive and negative). These entire particles are characteristic of the sample. Secondary ions are extracted and mass analyzed. They only represent a minor part of the emitted particles. The neutral particles can be studied by postionization techniques. The required primary ion energy is on the order of a few keV (0.1 keV to 50 keV). The incidents primary ions produce a collision cascade on a few nanometers. This implantation depth fluctuates from 4 nm to more than 15 nm depending to the substrate and the primary ion nature. The collision cascade forwards the desorption of the secondary particles from the first atomic or molecular layer of the surface. So the SIMS is one of the most sensitive techniques at the outermost surface (1 nm). ToF-SIMS analyses were performed with a TOFSIMS IV instrument from ION-TOF GmbH. Negative ion profiles were measured in a dual beam configuration using a Bi (25 keV) gun for analysis and a Cs (500 eV) gun for sputtering.

A9. Chemical stability

Chemical stability tests were performed by immersion in an aqueous 0.5 wt.% HF solution. After the dipping, the samples were abundantly rinsed with deionized water and consequently, dried with N_2 flow.

A10. References

[1] *Handbook of Ellipsometry*; Tompkins, H. G.; Irene, E. A., Eds.; Springer New York, 2005.

[2] M. R. Baklanov, K. P. Mogilnikov, V. G. Polovinkin, F. N. Dultsev, *J. Vac. Sci. Technol. B Microelectron. Nanom. Struct.* **2000**, *18*, 1385.

[3] M. Baklanov, K. Maex, M. Green, *Dielectric Films for Advanced Microelectronics*; Baklanov, M. R.; Green, M. L.; Maex, K., Eds.; John Wiley & Sons, Ltd: Chichester, UK, 2007.

[4] M. R. Baklanov, K. P. Mogilnikov, *Microelectron. Eng.* **2002**, *64*, 335.

[5] M. Thommes, K. Kaneko, A. V. Neimark, J. P. Olivier, F. Rodriguez-Reinoso, J. Rouquerol, K. S. W. Sing, *Pure Appl. Chem.* **2015**, *87*, 1051.

[6] O. O. Okudur, K. Vanstreels, I. De Wolf, U. Hangen, *J. Appl. Phys.* **2016**, *119*, 25302.

[7] K. B. Yeap, K. Zeng, H. Jiang, L. Shen, D. Chi, *J. Appl. Phys.* **2007**, *101*, 123531.

[8] I. Ciofi, M. R. Baklanov, Z. Tokei, G. P. Beyer, *Microelectron. Eng.* **2010**, *87*, 2391.

[9] T. Li, A. J. Senesi, B. Lee, *Chem. Rev.* **2016**, *116*, 11128.

[10] A. Guinier, G. Fournet, *Small-angle scattering of X-rays*; Wiley, 1955.

[11] M. Kotlarchyk, S.-H. Chen, *J. Chem. Phys.* **1983**, *79*, 2461.

[12] J. S. Pedersen, *J. Appl. Crystallogr.* **1994**, *27*, 595.

[13] G. Benecke, W. Wagermaier, C. Li, M. Schwartzkopf, G. Flucke, R. Hoerth, I. Zizak, M. Burghammer, E. Metwalli, P. Müller-Buschbaum, M. Trebbin, S. Förster, O. Paris, S. V. Roth, P. Fratzl, *J. Appl. Crystallogr.* **2014**, *47*, 1797.

[14] D. Babonneau, *J. Appl. Crystallogr.* **2010**, *43*, 929.

[15] M. P. Tate, V. N. Urade, J. D. Kowalski, T. C. Wei, B. D. Hamilton, B. W. Eggiman, H. W. Hillhouse, *J. Phys. Chem. B* **2006**, *110*, 9882.